Seismic Response of Short Period Structures and the Development of a Self-Centering Truss Moment Frame with Energy-Dissipating Elements for Improved Performance

Scott C. Darling

Thesis submitted to the faculty of the Virginia Polytechnic Institute and State University in partial fulfillment of the requirements for the degree of

Master of Science
In
Civil and Environmental Engineering

Matthew R. Eatherton
Finley A. Charney
William J. Wright

August 6, 2012
Blacksburg, Virginia

Keywords: Seismic Behavior, Short Period Structures, Self-Centering Seismic Systems, Steel Moment Frame

Seismic Response of Short Period Structures and the Development of a Self-Centering Truss Moment Frame with Energy-Dissipating Elements for Improved Performance

Scott C. Darling

Abstract

Traditionally, earthquake engineering has focused on protecting the lives of building occupants by utilizing inelasticity in structural members and connections to dissipate seismic energy and provide protection against collapse. This design concept is partially based on the equal displacement concept, which states that peak drifts for an inelastic system will be approximately equal to the peak drifts of an elastic system with the same initial stiffness for a given dynamic loading. This is a concept that has been shown to work for structures with natural period greater than about 1.0 seconds, but does not hold true for shorter period structures. An additional consequence of this design methodology is that conventional seismic systems do not explicitly limit the amount of structural damage, or offer a repair method that allows continued use of a structure after an earthquake. In fact, the structural damage distributed throughout a building and permanent residual drifts can make a conventional structure difficult if not financially unreasonable to repair after a large earthquake. These are both concerns facing the seismic design community that are investigated as a part of this thesis.

First, a computational study was conducted on short period structural systems to investigate the relationship between initial structural period and collapse potential. The investigation utilizes a statistically based analysis methodology to investigate a study of single degree of freedom (SDOF) systems with periods between 0.1 seconds and 1.0 seconds. The SDOF models were developed using an elastic-linear hardening model with post-yield stiffness ranging between -10% and +10% of the initial stiffness. This part of the study was done to gain a general understanding of the influence of natural period and post-yield behavior on the collapse performance of structural systems and appropriate response modification factors. Next, a study of multi-degree of freedom (MDOF) masonry structures with short periods was conducted to examine how the SDOF trends

translated to realistic MDOF structures. Based on these two studies, recommendations were made for how current U.S. building codes could be modified to account for the behavior of short period structures.

Next, a new self-centering system that builds on the concepts of previous self-centering systems is developed. The self-centering truss moment frame (SC-TMF) was developed with the goal of providing self-centering capability while concentrating inelastic deformation in replaceable structural fuses. These goals are accomplished while mitigating a number of issues seen in other self-centering systems, such as deformation incompatibility with gravity framing, limited deformation capacity, and unusual field construction techniques. The development of the SC-TMF includes a set of preliminary monotonic pushover analyses and nonlinear time history analyses to confirm the expected behavior of the system. Next, a mechanics investigation was undertaken where static pushover analyses (monotonic and cyclic) were used to help derive equations to predict system behavior, such as strength and stiffness. Finally, a parametric study was conducted to gain a better understanding of how various design decisions influence structural behavior. It was shown that the SC-TMF was a viable seismic system for controlling residual drifts and concentrating inelasticity in replaceable fuse elements while mitigating the issues seen in other conventional self-centering systems.

Acknowledgements

It would have been impossible for me to complete my master's degree without the assistance and guidance of a number of individuals.

First, I must express my sincerest gratitude to my parents, Chris and Susan Darling. Without your continued support over the past 24 years I would not have been in the position to take on a task as difficult as pursuing a master's degree, much less seeing it through to the very end. It has been a process with many ups and downs, and you have been there in support of me every step of the way.

Next I would like to thank my advisor Dr. Matthew Eatherton for giving me the opportunity to work on the development of the SC-TMF and for the numerous hours helping me develop an understanding of the dynamic behavior of structures. It is a base that has already opened a number of doors for my future and one that I am excited to build on as I develop as an engineer.

I would also like to thank Dr. Finley Charney for giving me the opportunity to join his group on the short period project. It was in your classes that I first began working with the computer analysis of structures, which gained my interest in and opened up the opportunity to work on projects like this one.

I am grateful for many individuals who provided help while I was working this thesis. In particular, I would like to thank Andy Hardyniec for providing guidance on the programming and modeling questions that I had on a near daily basis throughout this project. Thank you to Dr. Plaut, who went out of his way to help me with a buckling problem that presented itself during the course of my work. Additional thanks go out to the other graduate students in the SEM department who have made my graduate studies a truly enjoyable experience.

I want to extend my thanks to the Applied Technologies Council, who provided funding for the short period study portion of this thesis as part of the ATC-84 project. I would also like to thank the National Science Foundation who have supported the work that the SC-TMF development is based on under Grant No. (CMMI-1200237*)*.

Finally, I would like to extend a final thank you to the Via Department of Civil and Environmental Engineering and Virginia Polytechnic Institute and State University as a whole. I have spent the past six years developing as an academic and human being in this great Hokie community and have enjoyed every minute of it.

Table of Contents

List of Figures

List of Tables

Notation – Short Period Study

The Short Period Study discussed in Chapter 3 uses the following symbols. Some definitions in the list have been simplified for brevity. In all cases, the definitions given in the body of this thesis govern.

$ACMR$	= adjusted collapse margin ratio
C_d	= deflection amplification factor currently employed by ASCE 7
C_{ds}	= short period deflection amplification factor
CMR	= collapse margin ratio
R	= response modification coefficient
R_M	= response modification coefficient for the MCE level ground motion
R_{Md}	= ductility component of the response modification factor
$R_{Md,max}$	= maximum value of the short period dependent ductility component of the response modification factor
$R_{Md,min}$	= minimum value of the short period dependent ductility component of the response modification factor
R_o	= overstrength component of the response modification factor
T_{max}	= natural period at which period dependent R_{Md} is at the maximum value
T_{min}	= natural period at which period dependent R_{Md} is at the minimum value but
T_n	= natural period of a structure
α	= post-yield stiffness ratio
δ_e	= elastic displacement computed under strength-level design earthquake forces
$\delta_{inelastic}$	= amplified inelastic displacements
Ω_o	= overstrength factor

Notation – Self-Centering Truss Moment Frame Development

The Self-Centering Truss Moment Frame investigations discussed in Chapters 4-9 use the following symbols. Some definitions in the list have been simplified for brevity. In all cases, the definitions given in the body of this thesis govern.

a	= width at the center of the link in a butterfly fuse plate
A	= cross sectional area of a given element
A_{ED}	= total cross sectional area of the energy-dissipating bars
A_{pt}	= total cross sectional area of the post-tensioning elements
b	= width of the ends of a link in a butterfly fuse plate
E	= modulus of elasticity of a given material
f_{axial}	= axial force in a given element
F_{IC}	= maximum compression force in the bottom chord inner tube
F_{IT}	= maximum tension force in the bottom chord inner tube
F_O	= maximum compressive force in the bottom chord outer tube
f_{pi}	= initial post-tensioning stress
f_{pu}	= ultimate post-tensioning stress
F_{TC}	= maximum compressive force in the top chord
F_{TT}	= maximum tension force in the top chord
f_{yED}	= yield stress of the energy dissipating bar material
h_{story}	= height of a single story of the building
h_{truss}	= height of the SC-TMF from centerline of the top chord to centerline of the bottom chord
$I(x)$	= moment of inertia of a link in a butterfly fuse plate at a given location along the length
K_1	= stiffness of the SC-TMF before gap opening
K_2	= stiffness of the SC-TMF after gap opening and before fuse yield
K_3	= stiffness of the SC-TMF after fuse yield and before post-tensioning yield
k_{axial}	= axial stiffness of a given element
K_{ED}	= stiffness provided by the energy-dissipating bar fuses

K_{ele} = stiffness contribution of a given element to the global behavior

K_{pt} = stiffness provided by the post-tensioning elements

K_{truss} = stiffness provided by the truss

L = length of a given element

L_{IC} = length of the bottom chord inner tube in compression

L_{IT} = length of the bottom chord inner tube in tension, equal to the length of the region connecting the inner tube to the column

L_{link} = length of the links in a butterfly fuse plate

L_{truss} = length of the SC-TMF

$M(x)$ = bending moment of a link in a butterfly fuse plate at a given location along the length

M_{ext} = moments applied externally to the SC-TMF

M_{fuse} = moment capacity provided by the fuse elements

M_{gap} = overturning moment where decompression occurs and gap openings begin to form

M_{int} = internal moment within the SC-TMF

M_n = Moment capacity of a SC-TMF measured at Fuse yield

= M_y

M_{pti} = moment capacity provided by the initial post-tensioning force

M_{ptu} = ultimate moment capacity provided by the post-tensioning elements

M_u = maximum moment capacity of the system at which post-tensioning reaches ultimate capacity

M_y = overturning moment at which the fuses yield

$P(X)$ = axial force in a member at a location, X

P_o = maximum compressive load at one end of the bottom chord outer tube

p_o = non-dimensionalized expression for the maximum compressive load

Q = shear force in the bottom chord outer tube

SC = self-centering ratio

= M_{pti}/M_{fuse}

t = thickness of a butterfly fuse plate

$w(x)$	= width of a link in a butterfly fuse plate at a given location along the length
X	= location along the length of the bottom chord outer tube
x	= non-dimensionalized ratio of the location X over the total length of the member
y	= non-dimensionalized ratio of the location Y over the total length of the member
Y	= out of plane location of the bottom chord outer tube in the buckled configuration
α	= ratio of the maximum compressive load at one end of the outer tube to the load at the far end
β	= ratio of the critical buckling load for the non-uniform loading to the Euler buckling load $= p_o/\pi^2$
γ_{pt}	= initial post-tensioning ratio $= f_{pi}/f_{pu}$
δ	= deformations in a given element
Φ	= truss or column rotation angle

Chapter 1. Introduction

1.1 State of the Practice in Earthquake Engineering

Traditionally, earthquake engineering has focused on protecting the lives of building occupants. For other forms of structural loading, such as gravity or wind, this is accomplished by requiring the building to remain elastic for the expected loads; however, the forces seen during a major seismic event are so large compared to other loading scenarios that it would be uneconomical to attempt to keep the building elastic during these events.

The conventional approach to the design of seismic force resisting systems uses inelasticity in structural members and connections to dissipate seismic energy and provide protection against collapse. This is accomplished in the U.S. building codes through the use of the Response Modification Factor, *R* (ASCE 2010). This factor is used to reduce the elastic forces from a seismic event to determine the design level forces. This design paradigm is partially based on the equal displacement concept, which implies that a structural system that is allowed to deform inelastically during a strong ground motion will result in peak displacements approximately equal to those experienced by the elastic system for the same ground motion. This concept is shown graphically in Figure 1.1.

There are some potential issues with a design paradigm that relies on the equal displacement concept for any portion of its basis. Newmark and Hall (1982) showed that the equal displacement concept was not valid for structures with a natural period, T_n, less than 1.0 seconds. For these structures, larger displacements are expected for the inelastic system than the elastic system. As the natural period of the structure continues to decrease, the ratio of the inelastic to elastic displacements continue to increase until it reaches a point where the response modification factor should be equal to 1.0. However, current design practice does not modify the response modification factor based on the natural period of the structure being designed, but are instead held constant for all values of natural period for a given structural system.

Historically, the response modification factors were largely based on qualitative judgments by a committee of experts in the field of seismic design. They have considered the ductility and overstrength that a structural system is expected to provide when setting the response modification factor. It is conceivable that the short period problem has been partially accounted for through a reduction in the response modification factor that is applied to the structural system for all values of natural period.

Recently, a quantitative method has been presented for setting the response modification factor for new structural systems (FEMA 2009). This methodology, known as the FEMA P-695 Methodology, utilizes a series of nonlinear dynamic analyses to determine an appropriate response modification factor for the system. Initial studies with this methodology showed that the response modification factor that was calculated based on the results could be highly dependent upon the natural period (NIST 2010). This fact created a need for an investigation into the short period problem so an appropriate procedure could be recommended for handling these concerns.

A second concern that comes out of a design paradigm that has a foundation in the equal displacement concept is the potential for residual displacement following a strong ground motion. This type of design approach relies on significant inelastic deformation during seismic loading to dissipate seismic energy in the system. However, as shown in Figure 1.1, when the system is unloaded from the deformed configuration it is unable to rebound fully and the structure may be left with significant residual displacements. It should be noted that the residual displacement shown in Figure 1.1 represents the maximum possible residual drift for a system. However, residual displacements of only a portion of the maximum possible can present significant problems for the continued use of a structure. While the energy dissipation may have helped the building reach the design goal of collapse prevention and life safety, the residual displacements can render a building unusable immediately following a strong ground motion and may make the structure economically unreasonable to repair for continued use. In order for conventional seismic systems to fully self-center after a seismic event they may be required to remain elastic throughout the ground motion.

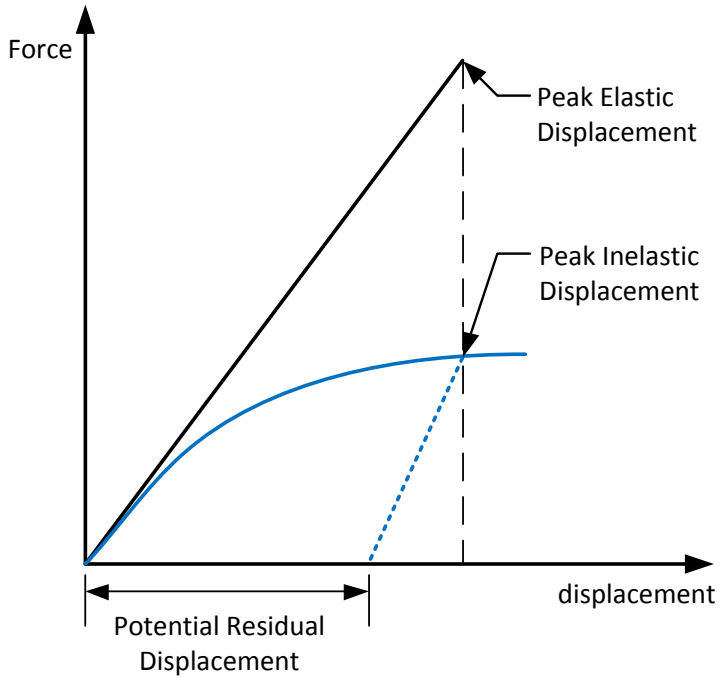

Figure 1.1: Equal Displacement Concept

Additionally, the conventional earthquake engineering design provisions are only focused on a life safety performance goal for a structure subjected to the design basis earthquake. This design approach does nothing to limit the inelastic deformations during smaller ground motions that may occur more frequently. In performance based earthquake engineering, a number of performance based goals can be identified, such as immediate occupancy, limited downtime, or limited repair costs. Similarly, a range of possible hazard levels can be considered for each performance goal, from frequent earthquakes up ones with very long return periods. Ultimately, the traditional life safety goal under the maximum considered earthquake must be met, but the additional goals allow for more predictable performance at all levels. However, the development of performance based earthquake engineering in the past two decades has highlighted some of the shortcomings of conventional structural systems in meeting performance goals beyond life safety.

The concern of residual drifts following a strong ground motion has led to development of self-centering seismic systems. These are systems which provide an internal restoring force which acts to eliminate residual drifts at the conclusion of a strong ground motion. In the past two

decades there have been significant advances in the development of self-centering seismic force resisting systems that satisfy performance criteria based on limiting costs associated with structural repair and business downtime. However, examples of self-centering systems used in practice are limited because difficult or complex field construction is required and there are challenges associated with deformation compatibility. An additional concern is that they are not expected to be economically competitive with conventional systems in an initial cost comparison, although a formal economic analysis could not be found that made such comparisons. The advantage of self-centering systems is expected to be seen when comparing the life-cycle costs to the conventional systems.

Even though a handful of self-centering systems have been developed, they will not have the ability to reduce earthquake losses until the performance advantages outweigh the associated costs and challenges leading to more widespread implementation in practice. In addition to satisfying performance goals related to structural repairability after earthquakes, self-centering systems need to be accessible to the construction industry, not cause deformation incompatibility, and be economically competitive with conventional systems.

This thesis addresses these two unique concerns with a design paradigm partially based on the equal displacement concept through two separate investigations that were discussed above. First, a short period study was conducted within the confines of the FEMA P-695 methodology (FEMA 2009). This investigation starts with a single degree of freedom (SDOF) parametric study to set a baseline for the expected results. Next, a multi-degree of freedom (MDOF) system study is conducted on masonry models with short natural periods. The results of these two studies are utilized to make recommendations on how the short period problem can be handled within the context of the FEMA P-695 methodology. The second investigation develops a new self-centering seismic system: the self-centering truss moment frame (SC-TMF). The development of this system addresses the concerns of previously developed self-centering systems. Additionally, strength and stiffness of the SC-TMF are decoupled, which allows for the system to fit within a performance based design procedure by being finely tuned for various criteria.

1.2 Description of the Short Period Study

A computational study was conducted on short period structural systems to investigate the relationship between initial structural period and collapse potential. The investigation utilizes the FEMA P-695 methodology (FEMA 2009) to complete a study of single degree of freedom (SDOF) systems with periods between 0.1 seconds and 1.0 seconds. The SDOF models were developed using an elastic-linear hardening model with post-yield stiffness ratio ranging between -10% and +10%. This part of the study was done to gain a general understanding of the influence of natural period and post-yield behavior on the collapse performance of structural systems and appropriate response modification factors. Next, a study of multi-degree of freedom (MDOF) masonry structures with short periods was conducted to examine how those trends translated to more complex structures. Based on these two studies, recommendations were made for how current U.S. building codes could be modified to account for the behavior of short period structures.

This investigation was part of Applied Technologies Council Project 84 (ATC-84). The core objective of this part of the project is to continue development of the FEMA P-695 methodology. Specifically, the objective of ATC-84 was to investigate the issues that have been seen in beta testing of the FEMA P-695 methodology and determine if adjustments in the formulation of these seismic parameters should be made.

1.3 Description of the Self-Centering Truss Moment Frame

This research investigates the development of a new high performance seismic force resisting system. The self-centering truss moment frame (SC-TMF), is a system that builds on previous forms of self-centering systems while mitigating a number of the major concerns related to those systems. Shown in Figure 1.2, the SC-TMF utilizes an innovative truss configuration with precompressed concentric tubes along the bottom chord. Structural fuses are incorporated to provide energy dissipation. Here, a butterfly fuse plate is included in a Vierendeel middle

section of the truss. Five primary components are labeled in Figure 1.2(a) to demonstrate their purpose:

1. A steel truss connects the top chord to the outer tube of the bottom chord. The outer tube of the bottom chord is not connected directly to the column at the height of the bottom chord. The truss forces the bottom chord outer tube to displace with the top chord movements. Here, a Pratt truss with cross web diagonals in the end panels and a Vierendeel middle panel is shown. However, a number of diagonal configurations could be employed provided sufficient stiffness is developed to ensure equal displacement of the top chord and bottom chord outer tube. The Vierendeel middle section is included to accommodate the butterfly fuse plates, but is not required for other fuse configurations that are investigated.

2. The bottom chord inner tube is connected to the columns at the height of the bottom chord. During lateral loading, the rotation of the column causes a relative horizontal displacement between the column at the height of the bottom chord and the column at the height of the top chord. Because the bottom chord outer tube displaces with the top chord, the inner tube and outer tube of the bottom chord move laterally relative to one another as the column rotates relative to the truss.

3. Post-tensioning strands precompress the concentric tubes. The post-tensioning acts to keep the inner and outer tube of the bottom chord in alignment. When a gap opening is created by the relative displacement of the two bottom chord tubes, the post-tensioning provides the restoring force that creates self-centering by bringing the two tubes back into alignment during unloading.

4. Free floating anchorage plates slide over the connectors at the end of the inner tube, but are held in place by the post-tensioning. During lateral loading, the inner tube bears on the anchorage plate at one end [the left end in Figure 1.2(a)] while the outer tube bears on the anchorage plate at the opposite end [the right end in Figure 1.2(a)]. This creates a gap

opening between the tubes and the anchorage plates at both ends which elongates the post-tensioning strands.

5. Structural fuses are utilized to dissipate seismic energy through inelastic deformations. Figure 1.2(a) shows a butterfly steel fuse plate that is connected to the top chord on one side and the bottom chord inner tube on the other. The relative displacements between these two members cause the formation of plastic flexural and shear deformations in the links of the butterfly fuse plate. In this configuration, the outer tube is slotted around the fuse plate to allow the butterfly fuse plate to move freely with the inner tube.

During a strong ground motion, gap openings form between the anchorage plates and the concentric tubes of the bottom chord, seismic energy is absorbed by the fuse element, and the post-tensioning provides a restoring force to bring the truss back to its original configuration after the loading ceases. Unlike currently available self-centering moment frames, the gap opening is internal to the truss, which ensures that the distance between the columns remain constant throughout the loading process.

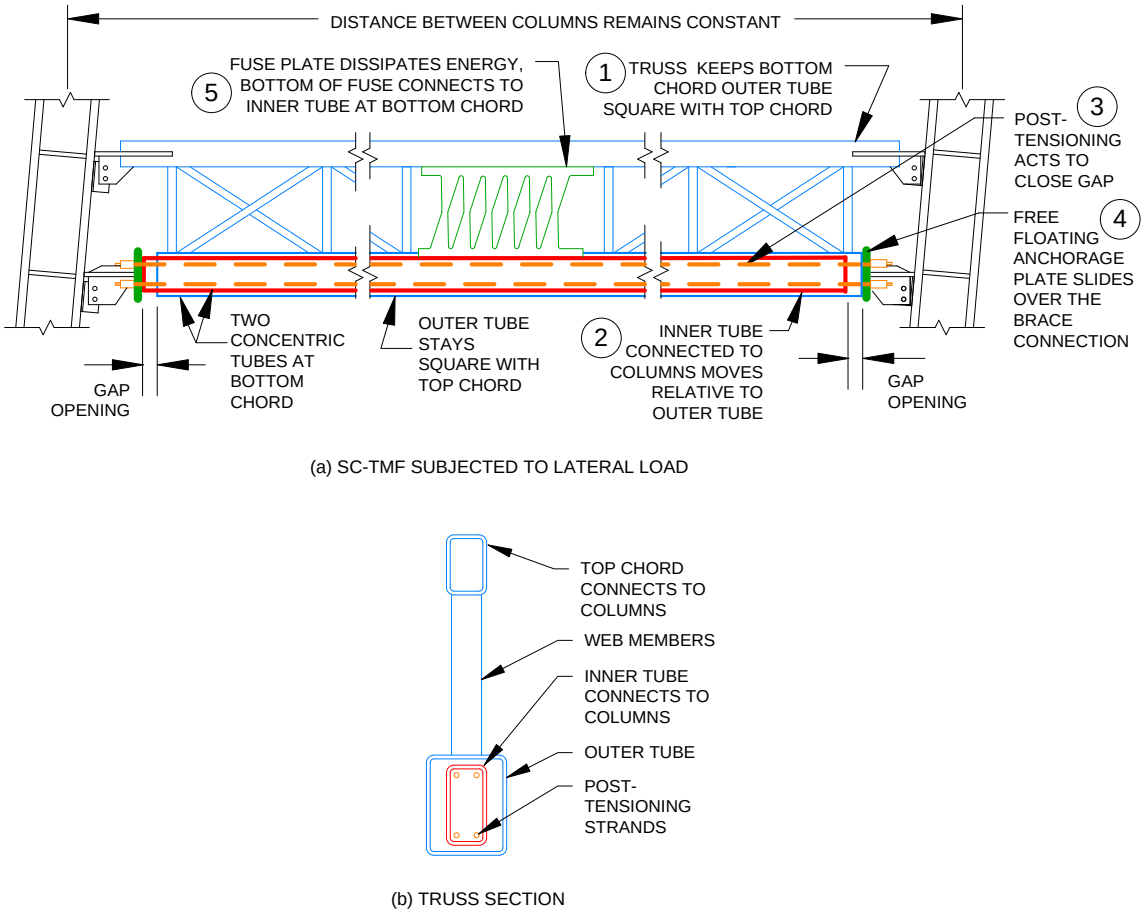

Figure 1.2: Proposed SC-TMF Configuration

1.4 Organization of Thesis

This thesis combines two somewhat separate research projects, both of which are intended to improve the performance of structures subjected to earthquakes. The investigation of the seismic performance of short period structures is presented first followed by several chapters related to the development of the self-centering truss moment frame. The thesis is organized as follows:

- Chapter 1 provides a brief introduction to the current state of the practice of earthquake engineering in the United States, the investigation into the short period structures, and the development of the self-centering truss moment frame.

- Chapter 2 presents a review of the literature that is relevant to the research projects that are in the thesis.

- Chapter 3 discusses the investigation of the seismic collapse potential of short period structural systems including both SDOF and MDOF computational simulations.

- Chapter 4 discusses the preliminary investigations into the self-centering truss moment frame. It has been presented in the format of a conference paper that was developed for the 2012 Conference on the Behavior of Steel Structures in Seismic Areas (STESSA), which was held in Santiago, Chile.

- Chapter 5 outlines a second configuration for the self-centering truss moment frame that was developed to improve on the behavior discussed in the STESSA paper. This chapter goes on to discuss the mechanics investigation which developed a series of equations to describe the strength and stiffness of the self-centering truss moment frame at various stages of its response.

- Chapter 6 discusses the parametric study that was performed to further develop an understanding of the behavior of the self-centering truss moment frame. It outlines the important input parameters as how they were expected to affect the important output parameters.

- Chapter 7 outlines the capacity based design procedure that was developed for the design of members that were intended to remain elastic throughout the loading. It also reviews the results of the parametric study with regards to the capacity based design procedure and makes conclusions regarding the adequacy of the proposed design procedures.

- Chapter 8 reports the parametric study results by presenting and analyzing the variation in key output parameters as the input design parameters change. The potential use of these results for future design methodologies is discussed.

- Chapter 9 discusses the conclusions that can be drawn from the self-centering truss moment frame portion of the thesis. It is broken into two parts. First, a recommended design procedure is outlined based on the results of the parametric study. Finally, conclusions that can be drawn from the study are discussed and recommendations for future work are outlined.

Chapter 2. Literature Review

This chapter presents a review of the literature relative to the self-centering truss moment frame (SC-TMF). A review of literature relevant to the short period study is included at the beginning of the next chapter.

There have been a number of studies conducted on the use of trusses in seismic applications. There have also been studies on the application of systems that provide self-centering capability during strong ground motion. This literature review first presents the available research on how trusses have been utilized in seismically active regions. The development of self-centering seismic systems is then discussed, starting with the prestressed concrete systems and moving on to self-centering steel moment resistant frames. Finally, the research on a number of energy dissipating fuse components is presented to provide context for the replaceable energy dissipating elements that are part of the SC-TMF system.

2.1 Seismic Applications of Trusses

Two applications of trusses that can be utilized in seismic resistant structures are discussed in this section. The first, the staggered truss, utilizes story tall trusses in a unique configuration to resist lateral forces applied to the structure. The second is the special truss moment frame. This system is configured similar to a traditional moment frame, but utilizes open web trusses in place of solid web members.

2.1.1 Staggered Truss

The staggered truss system was developed by a team of civil engineers and architects at MIT as a lateral wind resisting system for high rise steel frame buildings (MIT 1967). The system is designed to behave as a cantilevered beam. Columns, which are only located around the perimeter of the building, behave as the flanges of the system. The fact that interior columns are not needed allows for large open spaces on the first floor without the need for transfer columns. Story-high steel trusses are arranged in a staggered pattern in the transverse direction, essentially

acting as webs of the cantilevered beams and resisting lateral loading. The most efficient truss system is the Pratt truss with a Vierendeel middle panel to provide room corridors (Zhou et al. 2009). The staggered pattern between stories allows for open areas that are two bays wide with the floor system spanning from the top of one truss to the bottom of the adjacent truss (Scalzi 1971). The combination of open spaces and only exterior columns gives a great deal of flexibility in the floor plans for architectural arrangements.

The floor system is a critical structural component and must be designed to provide sufficient diaphragm action to transfer lateral shears from one column line to the next. This is especially important because each truss is carrying the loads for two bays for the entire structure above it. In this way, the floor system must be able to transfer half of that load in each direction from the bottom of one truss to the top of the trusses on the floor below. This unique load path allows the staggered truss to mobilize the entire building to resist the overturning moments from the lateral loads (Cohen 1986).

The staggered truss is also able to transfer loads axially through members, eliminating bending moments in nearly all structural components. This fact allows the columns to be oriented with their strong axis in the longitudinal direction of the building such that the staggered trusses are connected to the weak axis of the column. This detail enables the longitudinal lateral forces to be resisted by a traditional portal frame.

While the staggered truss was designed as a lateral force resisting system, it has yet to be designated as a basic-seismic-resisting system in current U.S. building codes (ASCE 2010). The seismic behavior of the staggered truss was first investigated as the first part of a two part paper published in 1974 (Hanson et al. 1974). Part I of the paper determined that this system was an efficient structural framing system for earthquake loads. It was able to provide drift control for wind and small earthquakes and sufficient ductility and inelasticity in the open middle panel to perform well under design level earthquakes. Part II of this paper provided a design procedure for elastic or ultimate limit state design that provided a predictable yielding mechanism: inelasticity of the chord members in the area of the central opening in the trusses.

The seismic performance of the staggered truss was further investigated through static push over analyses (Kim et al. 2007). This study compared the effectiveness of the staggered truss system for seismic loading to other conventional systems for low-, mid-, and high-rise applications. It found that the staggered truss performed as well as the conventional systems in low-rise structures, but mid- and high-rise structures failed in a brittle fashion. This failure occurred as the result of the formation of plastic hinges in the horizontal and vertical members of the Vierendeel panels. This study also investigated seismic reinforcing for these panels to eliminate this problem.

More recently, Zhou et al. (2009) performed a parametric study of the staggered-truss to determine how various factors affect the seismic performance of this system. The results of the analyses were verified using an experimental analysis of an 8-story staggered truss frame. It was determined that the length of the Vierendeel middle panels should be minimized to improve seismic performance so long as it continues to meet all other structural and architectural requirements. The ductility of the system is greatly affected by structure height, increasing at first then decreasing with increasing height. Also, ductility of the system decreased with increasing height to width ratio and decreasing truss span-depth ratio (Zhou et al. 2009).

2.1.2 Special Truss Moment Frame

In mid to high-rise steel building design, it is often desirable to utilize open-web truss systems over solid web moment frames for a number of reasons. First, these truss systems are generally lighter and more economical than their solid web counterparts, particularly over longer spans. Additionally, the open web trusses provide openings for mechanical piping and duct work and the moment connections for these systems are easy to detail.

Before 1990, little research had been done on open-web truss systems for seismic loadings. Because of this lack of information, these systems were designed as Ordinary Moment Resisting Frames (OMRF) as part of a weak-column-strong-beam seismic system, which was considered undesirable by many engineers (Goel and Itani 1994b). In the early 1990s, an experimental and analytical study was undertaken at the University of Michigan to investigate the behavior of

OMRF open-web truss-moment frames in a weak-column-strong-beam system during seismic loading. This study found that these systems lost significant strength and stiffness as the result of buckling and fracture of the diagonal web members. This led to poor hysteretic behavior of the system and large story drifts.

In a companion paper, Goel and Itani (1994a) described the design and testing of a new open web truss moment frame configuration, the special truss moment frame (STMF). A special truss moment frame contains a special segment in the middle half of the truss that is designed to undergo significant inelastic deformations during earthquake loading (AISC 2010b). This allows for the more desirable strong-column weak-beam configuration. The study by Goel and Itani looked at a four story building with STMF with X-diagonals within the special segments. In this system, the X-diagonals buckle and yield and plastic hinges form in the chord members within the special segment. They found that this system showed superior hysteretic behavior and improved economy of material over traditional OMRFs (Goel and Itani 1994a). An additional configuration for the STMF that utilizes Vierendeel middle segments was investigated. It was determined that the Vierendeel configuration showed excellent performance during seismic loading with full and stable hysteretic loops. Additionally, this configuration provides added economy and larger openings for mechanical ductwork and piping when compared to the X-diagonal configuration (Basha and Goel 1995). These are still the only two configurations allowed by the AISC Seismic Provisions for Structural Steel Buildings.

In 2008, Chao and Goel (2008) introduced a performance based plastic design approach for STMFs that eliminated the need for an iterative process that was typical. Also, new configurations for the STMF have been investigated. One promising configuration proposes energy dissipating devices (EDD) be incorporated into the Vierendeel middle segments (Pekcan et al. 2009). Additionally, the ends of the chords in the special segment were pinned to allow for greater deformations along the diagonals of the special segment. In this study, buckling restrained braces (BRB) were utilized in order to show proof of concept. It was found that this configuration had a more predictable seismic response with improved performance with regards to story displacements, interstory drifts, story shears, overturning moments, and observed

damage to structural members. Additional studies have been conducted to investigate issues with the design of STMFs in practice (Valley and Hooper 2003; Ölmez and Topkaya 2010) .

2.2 Review of Steel Self Centering Systems

2.2.1 Precast and Prestressed Concrete Structures

The Precast Seismic Structural Systems (PRESSS) project was a 1990's program funded by the National Science Foundation (NSF), Precast/Prestressed Concrete Institute (PCI), and Precast/Prestressed Concrete Manufacturers Association of California in order to improve the seismic performance of precast and prestressed concrete buildings. The culmination of this research program was the experimental testing of a sixty percent scaled five-story concrete structure that incorporated a number of the design concepts that had been investigated during the program. The lateral force resisting system of this structure varied in the two primary directions. In the transverse direction, shear walls that took advantage of jointed construction were utilized. These jointed walls were increased the structure's natural period in the transverse direction, which helped to reduce the design base shear force. This design also took advantage of the concept of rocking by allowing the shear walls to lift off the ground and rock (Nakaki et al. 1999).

In the longitudinal direction of the building, moment frames along the exterior column lines were designed to resist the lateral forces. These frames were unique in that they incorporate four of the framing concepts that had been investigated previously during the PRESSS program, which are shown in Figure 2.1 (Priestley et al. 1999).

The first seismic resisting frame, the Pre-Tensioned Frame, consisted of hybrid frame construction along the first three floors and pretensioned frame construction for the top two floors. The hybrid framing system utilizes multistory columns with post-tensioning strands passing through the columns at mid-height of the beam and creating the connection. Mild steel is grouted in ducts at the top and bottom of the beam and is allowed to yield to provide energy dissipation while the post-tensioned strands provide re-centering capabilities. The pretensioned

frame is developed for single story columns where the beams are cast in standard casting beds with specific lengths of the pretensioning debonded. These beams are placed on top of the columns and reinforcing is passed through sleeves in the beams and spliced to the column above.

The second frame consisted of the TCY Gap Frame and TCY Frame, which allowed for tension and compression yielding (TCY) of predetermined components for energy dissipation. The TCY Gap frame is developed to leave a small gap between the end of the beam and the face of the column. The bottom of this gap is grouted to provide contact and post-tensioning clamps the connection together. Mild reinforcing is grouted into sleeves along the top of the beam and is debonded so that it can yield in tension and compression, providing energy dissipation. This system is unique because during deformations, the gap on one side of the column will open while the other side will close such that the frame length remains constant. Finally, the TCY Frame is designed to concentrate tension/compression yielding at the connection. To prevent premature fracture of the mild reinforcing at these locations, these bars are debonded over a specified length. Each of these framing connections is designed to provide improved response to seismic loadings for precast concrete construction (Nakaki et al. 1999).

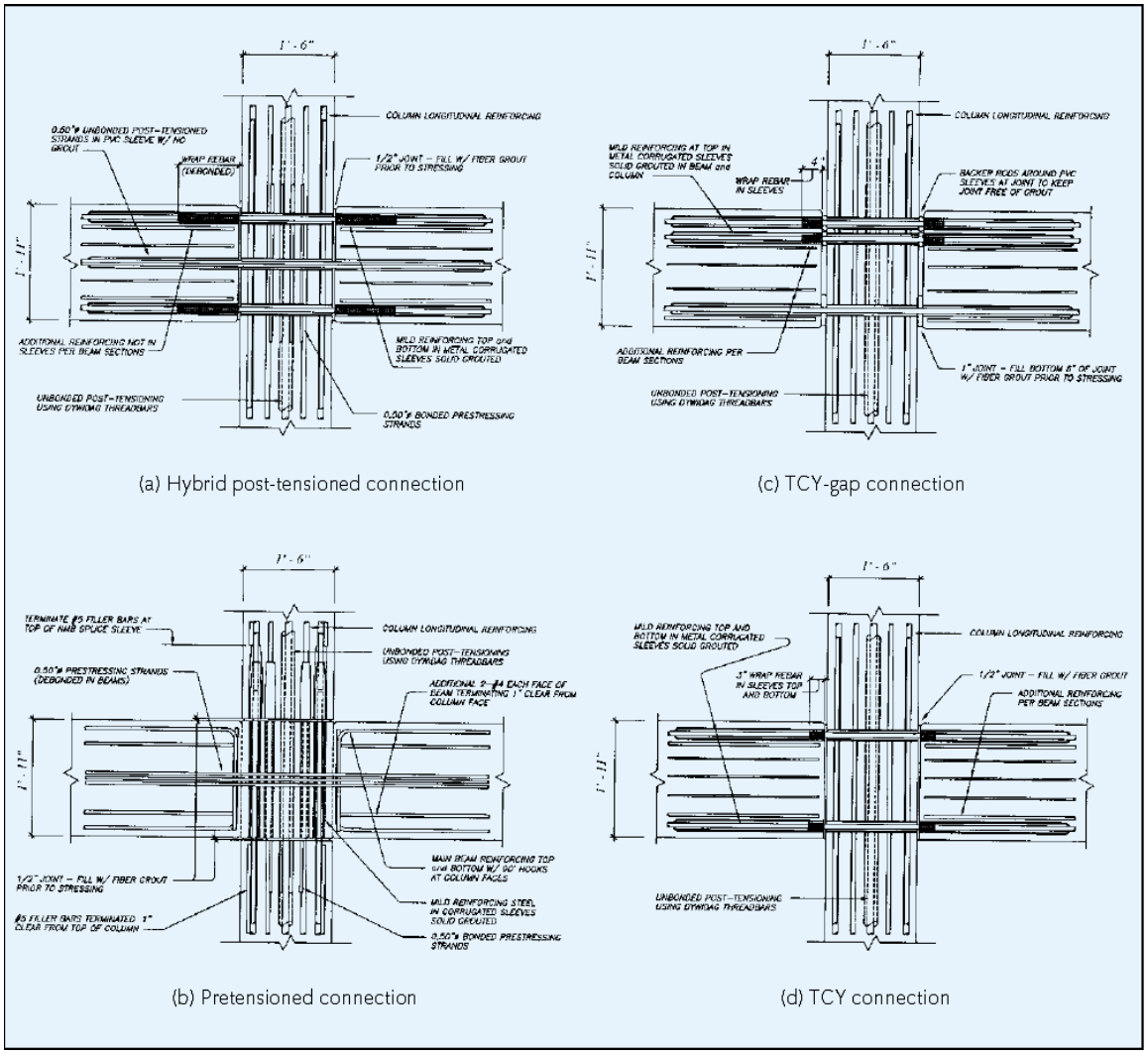

Figure 2.1: Seismic frame connection configuration investigated by PRESSS studies [from (Priestley et al. 1999)] [Used under fair use, 2012]

This five story scale model was tested in the Charles Lee Powell Structural Laboratory at the University of California at San Diego on August 9, 1999. The building was subjected to a series of loadings that corresponded to 33, 50, 100, and 150 percent of the design level earthquake. The results of the test showed that the shear wall configuration and the framing connections performed as anticipated even under the 150 percent of design level earthquake loading. When the structure was loaded in the transverse direction, the wall only experienced minor spalling at its base. Additionally, minor cracking in the floor system and column bases was seen during the

test, but closed up as the loading was removed. The residual drift in this direction was kept to 0.06 percent, just 3 percent of the maximum drift experienced.

When the structure was loaded in the longitudinal direction the performance of the two frames performed well with varied levels of damage. The prestressed frame performed exceptionally well and sustained a limited amount of concrete cover spalling in the beams. The non-prestressed frame did not perform as well despite the fact that it dissipated more energy. In particular, the TCY-gap connection showed damage at earlier stages as a result of an upward slip at the beam-column interface. Despite this fact, it was shown that all four connection details were viable concepts for precast/prestressed concrete structures in high seismic zones (Priestley et al. 1999).

2.2.2 Post-Tensioned Steel Moment Frames

Following the 1994 Northridge Earthquake brittle connection failures were found in 130 steel moment resisting frame buildings that utilized field welds. This fact greatly concerned engineers and owners, so new connection details were investigated. The self-centering and energy dissipation seen in post-tensioned connections in precast/prestressed concrete buildings made this an attractive connection concept for steel moment frames.

Ricles et al. (2001) introduced the first post-tensioned steel moment connection. In this connection detail, which is illustrated in Figure 2.2, the beams are not rigidly attached to the columns. Horizontal post-tensioned high strength steel strands or bars extend from one end of the moment frame to the other. These elements precompress the interface between the beams and columns. This precompression provides significant moment resistance in the connection, while friction at the contact surface is able to provide shear resistance. Shim plates are installed between the end of the beam and the column to aid in construction fit up and to ensure that only the beam flanges were in contact with the column. Reinforcing plates are installed on the beam flange to distribute stresses and prevent yield at these locations. Additionally, energy dissipating fuses are generally installed at the beam column interface. In Figure 2.2, top and seat angles are installed for this purpose (Ricles et al. 2001; Ricles et al. 2002).

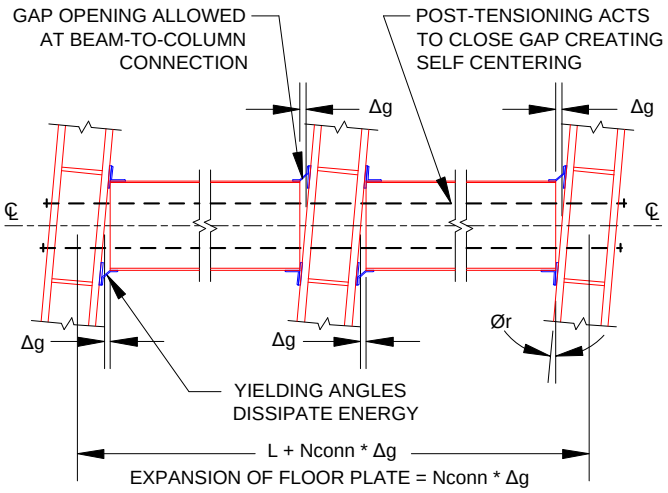

Figure 2.2: Post-Tensioned Steel Moment Frame Configuration

This connection has a similar initial stiffness as a conventional welded connection, but allows gap openings at the beam to column interface. Gap opening occurs when the the moment exceeds the decompression moment. A gap then opens between the beam tension flange and the column. The post gap opening system stiffness is reduced to that of the post-tensioning steel and the top and seat angles. This stiffness is again reduced when the angle on the tension side of the beam yields. The inelasticity in the angles dissipates seismic energy while the gap opening is closed by the post-tensioning.

This connection, in comparison with traditional field welded connections, has numerous advantages. In addition to utilizing only conventional materials, field welding is not required to create a connection with similar stiffness. The beams and columns remain elastic while inelastic deformation, which is confined to the angles, provides energy dissipation. These angles can then be replaced following a strong ground motion. Finally, the connection returns to near zero rotation when the moment is removed implying self-centering of the frame. Through an analytical model, experimental tests on subassemblages, and time history analyses, Ricles et al. (2001) was able to show that the post-tensioned moment connection provided improved response to strong ground motions, including decreased story shears, smaller maximum roof displacements, and reduced interstory drift. Additionally, the self-centering capabilities reduced

the residual drift in the system, although yielding of the base column left some residual drift in the building (Ricles et al. 2001). Similar results were seen for post-tensioned connections with wide flange steel columns and concrete filled HSS columns (Ricles and Sause 2007).

Garlock (2002) expanded on Ricles concept by further investigating the behavior of the post-tensioned steel moment resisting connection and frame. Her work took into account the interaction of the gravity system with the lateral load resisting system of the post-tensioned moment resisting frame. This was done through the modeling of collector beams that are used to transfer the inertial forces of the gravity system to the lateral load system. It was observed that gap openings caused the frame as a whole to expand. This expansion caused deformations in the collector beams and significantly changed the loads on the post-tensioned connection. Additionally, Garlock developed a simplified performance based design approach for the post-tensioned steel moment resisting frame. Testing showed that this design approach created buildings that responded as expected to strong ground motions (Garlock 2002; Garlock et al. 2005).

Garlock et al. (2005) expanded on previous research by conducting a series of experimental tests to examine the effects of the initial prestressing strand force, the number of strands present in the construction, and the length of the flange reinforcing plate. It was observed that as the initial prestressing force increased, the moment capacity for a given rotation also increased. However, if the initial prestressing force is too large it can cause beam local buckling to occur at relatively small story drifts. The number of strands has a great effect on the stiffness of the connection after the gap opens. As the number of strands increased, it was observed that the axial stiffness of the strands increased and the stiffness after decompression and angle yielding is increased. Additionally, the deformation capacity of the connection is increased as the number of strands is increased. This is because the initial force can be obtained at lower stress levels when more strands are present and there is more capacity for increasing the strand force before yield is reached. Finally, when beam local buckling was observed, it prevented the specimen from self-centering and decreased ductility of the system. For this reason, it was recommended that this limit state be avoided completely (Garlock et al. 2005).

Christopoulos et al. (2002a) also investigated the concept of the post-tensioned steel moment frame by combining it with the concept of the hybrid connection seen in precast concrete connections. The use of bolted angles in the previous configuration was difficult to model and analyze because it was highly dependent on geometric considerations and boundary considerations. Cristopoulos sought to simplify this through the use of energy dissipating (ED) bars to provide the necessary inelasticity, as had been seen in the hybrid connection for precast/prestressed structures. In this configuration, post-tensioning was placed at the neutral axis of the beam and stressed to create the contact stresses that produce self-centering capabilities. Then, four energy dissipating bars were installed using threaded couplers that were welded to the beam flange and column continuity plates. These ED bars were inserted into confining steel cylinders to limit buckling creating stable inelastic axial deformations in tension and compression. This concept was shown to be viable through analytical and experimental studies, and a simple design procedure was developed for this configuration (Christopoulos et al. 2002b).

Esposto et al. (2006) developed a numerical model of the post-tensioned steel moment frame connection utilizing angles as energy dissipating devices. The numerical model was developed and calibrated based on the experimental test results from Ricles and Garlock. The model was developed in two phases. First, the energy dissipating angles were modeled and subjected to a cyclic analysis. Then, the post-tensioned connection was created in the model and loaded cyclically. The model was used to gain an understanding of the finite element mesh properties as well as the component interaction in the connection. The model was in pretty good agreement with the experimental results, but could have been improved through improved characterization of the materials. Ultimately, the model showed that for large drift values, the beam undergoes inelastic deformations. This is of concern because if the beams and columns are not kept free of damage, the system will experience a loss of friction at the beam-to-column interface which reduces the shear capacity. Additionally, it was seen that the prestressing strands would make contact with the inside of the holes in the columns at large drift values. This could cause localized stresses in the strands and reduce their capacity (Esposto et al. 2006).

In 2009, Lin et al. proposed a new configuration for the post-tensioned steel moment frame connection. In this design, web friction devices are used to dissipate energy. The web friction devices consist of friction channels that are welded to the column flange and brass cartridge plates that are sandwiched between the web of the beam and the friction channels. The channels are then clamped to the beam using friction bolts, which pass through slotted holes in the web to allow the beam to move independent of the friction device. Aside from this change, all details of the post-tensioned connection remain the same as the configuration originally presented by Ricles. The post-tensioned moment frame connection with web friction devices was tested experimentally. The experimental model was a 0.6 scale model of a section of a frame that had been designed using performance based design approach. The results from this experiment showed that this connection performed well under design basis earthquake levels and that the web friction devices provided a reasonable amount of energy dissipation. Additionally, when loaded under the maximum considered earthquake level, the frame met the collapse prevention design level it had been designed for (Lin et al. 2009).

Although there has been significant development of the post-tensioned steel moment resisting frame, it is unclear that this system has ever been implemented in practice. It is reasonable to believe that this fact can be attributed to the challenges that are associated with the implementation of this system as well as the potential increase in initial cost. These challenges are discussed further in Section 4.1 of this thesis. How the SC-TMF is able to overcome these challenges is also discussed at that time.

2.3 Energy Dissipating Structural Fuses

The concept of allowing structural elements to deform inelastically in order to dissipate energy is widely employed in seismic design of structures. It allows for structural systems to be designed for significantly lower forces, which ultimately reduces the cost of the initial structure. In these configurations, it may make a structural system very expensive, if not economically unreasonable, to repair after an earthquake.

The concept of replaceable structural fuses is one solution to the concern of these high repair costs. A structural fuse is a disposable, easy to repair structural element where damage can be

concentrated while the rest of the structure remains mostly elastic (Vargas and Bruneau 2006). This can significantly reduce repair costs when compared to systems where major structural components are allowed to yield. Structural fuses have been utilized in a number of self-centering frames because they create energy dissipation while allowing the rest of the system to remain elastic and fully self-center.

There are numerous configurations for replaceable structural fuses in the literature, but one of the most promising fuses is the steel plate fuse with specific cut-outs (Deierlein et al. 2009; Deierlein et al. 2010; Ma et al. 2010b). Figure 2.3 shows two configurations for these steel plate fuses. The first, type "B", utilizes diamond shaped cut-outs to produce hour-glass shaped links that develop flexural plastic hinges at the quarter points along the length. The second, type "S" use slits in the steel plate to develop links with constant cross section.

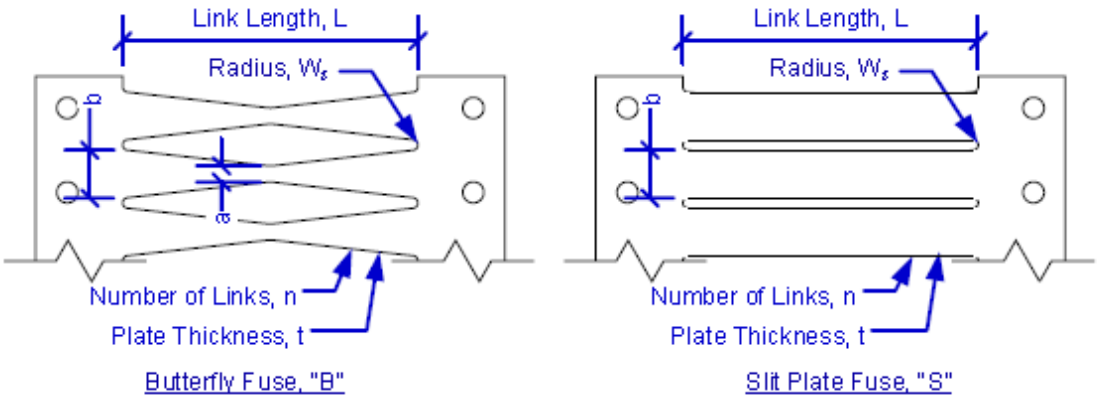

Figure 2.3: Steel Plate Fuse Configurations [from (Eatherton 2010)] [Used with kind permission of M. Eatherton, 2012]

Both configurations were experimentally tested at Stanford University. Figure 2.4(a) shows the experimental setup for a sample butterfly fuse plate in its deformed configuration. As this picture depicts, the links form flexural plastic hinges to dissipate energy. Figure 2.4(b) shows the hysteretic response for the sample butterfly fuse plate. It is evident that the butterfly fuse plates have very stable hysteretic response up to shear strains approaching 40 percent.

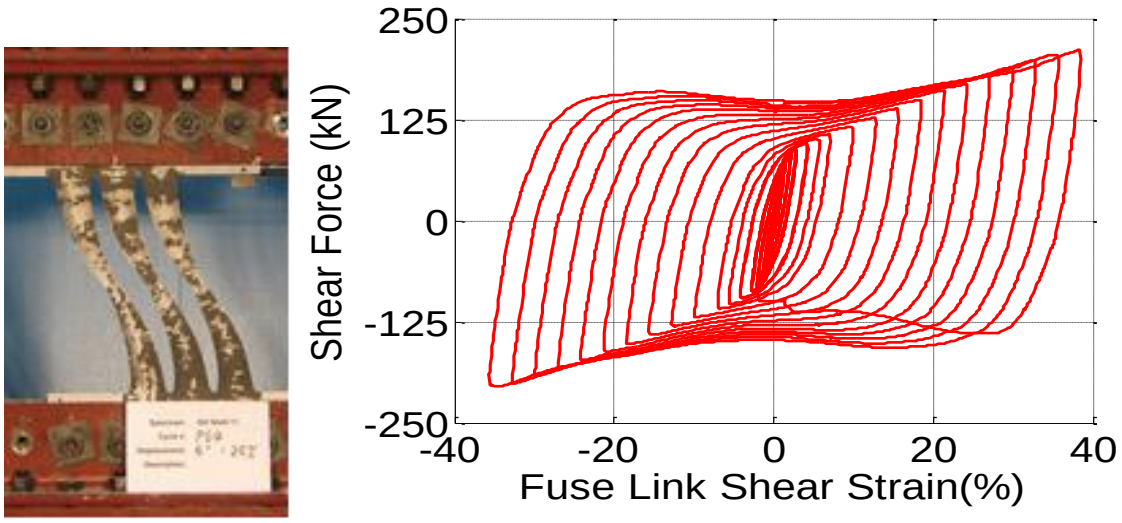

(a) (b)

Figure 2.4: Butterfly Fuse Plate B02-14 (a) Experimental Setup and (b) Hysteretic Response [from (Eatherton 2010)] [Used with kind permission of M. Eatherton, 2012]

The full and stable hysteretic response of the butterfly fuse plates can be attributed to the shape of the cutouts, which have been designed to allow for distributed yielding that initiates away from locations where stress concentrations are likely to occur. For a butterfly link, the ends and middle of the link have stress concentrations due to the changes in geometry at these locations. Because of this, the ideal location for the butterfly fuses to initiate yielding is at the quarter points of each link, which can be ensured by controlling the ratio of the width at the center of the link, *a*, to the width at the ends, *b*. The following derivation shows that a ratio of 1/3 for these dimensions will ensure this behavior.

The bending moment, *M*, width, *w*, and moment of inertia, *I*, of the link at location *x* along the length of the link, are described by the following equations (Ma et al. 2010a):

$$M(x) = \frac{2M_0}{L_{link}} x \qquad 1.1$$

where

L_{link} = link length

x = location along the length of the link

M_0 = maximum moment at the end of the butterfly fuse link

$$w(x) = \frac{2(b-a)}{L_{link}} x + a \tag{1.2}$$

$$I(x) = \frac{w(x)^3 t}{12} = \frac{1}{12}\left[\frac{2(b-a)}{L_{link}} x + a\right]^3 t \tag{1.3}$$

where

t = plate thickness

The stress at the extreme fibers of the cross section, σ, is described by the equation

$$\sigma = \frac{M(x)}{I(x)}\frac{w(x)}{2} = \frac{12M_0}{L_{link}t}\frac{1}{\left[2(b-a)\sqrt{x}/L + a/\sqrt{x}\right]^2} \tag{1.4}$$

The maximum bending stress can be determined by setting dσ/dx equal to zero. This results in the maximum bending stress, $\sigma_{\max}$

$$\sigma_{\max} = \frac{3M_0}{2(b-a)at} \tag{1.5}$$

which occurs at the location x_m of

$$x_m = \frac{a}{b-a}\frac{L_{link}}{2} \tag{1.6}$$

Assuming x_m occurs at $L_{link}/4$, the required ratio of a/b is 1/3. Provided each link in the butterfly fuse plate is designed to these parameters, it is expected that the full and stable hysteretic response depicted in Figure 2.4(b) will be achieved.

The steel plates with straight slits did not produce the same level of energy dissipation as the shown in the butterfly fuse plates. The behavior of the links in this fuse were characterized by yielding at the ends of the links, initiation of out-of-plane buckling, initiation of cracks at the link ends, tearing of the links, and full link fracture. During the experimental investigation, the cracks were initiated at shear strains between 5.6 percent and 10.0 percent. These cracks progressed until fracture occurred between 18.6 percent and 30 percent. This resulted in significant strength losses which greatly reduced the energy dissipation capacity of this fuse. The inability of this fuse to initiate yielding away from stress concentrations ultimately led to the diminished performance of this configuration. The butterfly fuse plate provides much more stable and predictable behavior and is expected to be a superior option as a structural fuse.

Chapter 3. Short Period Structural Systems

3.1 Introduction

3.1.1 Description of the Short Period Problem

The short-period problem refers to an issue that is caused by the design codes use of the equal displacement design concept as part of its foundation. The equal displacement concept, which is based on the idea that peak displacements for an inelastic system are approximately equal to the peak displacements for an elastic system with the same initial stiffness, is not valid for structural systems with natural periods less than about 1.0s (Newmark and Hall 1982). Being partially based on the equal displacement concept, current design equations determine the inelastic design forces by reducing the elastic forces by a response modification factor, *R*. Conceptually, *R* is a combination of a reduction based on the ductility and overstrength provided by a structural system. A number of researchers have developed period dependent expressions for *R* [eg (Veletsos et al. 1965)], but the value of *R* in the design equations are currently constant for all values of natural period. Historically, the values of *R* used in the codes have not been calculated explicitly, but have instead been agreed upon by consensus.

The FEMA P-695 methodology (FEMA 2009) was developed by ATC-63 to provide a quantitative method for determining the appropriate value of *R* for a particular structural system. This method utilizes nonlinear dynamic analyses of structural archetypes for 44 ground motions at incrementally increasing scale levels. The scale level that causes collapse of the archetype for half of the ground motions normalized by the scale level of the maximum considered earthquake (MCE) is defined as the collapse margin ratio, CMR. The CMR is adjusted based on a number of factors to arrive at the adjusted collapse margin ratio, ACMR, which can be compared to the acceptable value for a probability of collapse given the MCE level ground motion. Prior studies employing the FEMAP-695 methodology (FEMA 2009; NIST 2010) have found that short-period systems (structures with natural periods less than 0.6sec) consistently had lower ratios of calculated ACMR to acceptable ACMR than similar structural systems with longer periods.

While not all of these short period archetypes failed the acceptance criteria, they generally had the lowest ratio of computed *ACMR* to the acceptable *ACMR*. With the movement towards a quantitative method, it has become necessary to explicitly address the difference in structural behavior for systems with periods less than about 1.0.

There are a number of theories on how the code writers should approach this problem. The first approach is to eliminate the traditional design paradigm where energy is dissipated solely through inelastic material behavior for structures with periods less than 0.6 seconds. A separate set of design recommendations would need to be developed that were not founded in the equal displacement design concept. Instead, the system would need to be designed to allow for alternative mechanisms, such controlled sliding or rocking. For these systems, it would be important to limit the allowable displacements in order to protect the non-structural components.

One of the main concerns with the first approach is that it changes the design paradigm when compared to structures with longer natural periods. In order to keep the design approach consistent across the full range of structural periods, a second recommended approach suggests that a period based response modification coefficient, *R*, be developed which decreases as the natural period of the system decreases. This approach would allow for a consistent design methodology that reduces elastic forces by a factor *R* while accounting for the difference in behavior exhibited by short period structures.

In addition to reducing the *R* factor, it may also be necessary to increase the deflection amplification factor, C_d, as the fundamental period of the structure decreases. C_d amplifies the displacements determined by elastic analysis with reduced forces to estimate the expected inelastic deformations. Current values of C_d are equal to or slightly less than *R* due to the amplification being partially based on the equal-displacement concept. However, these constant values of C_d are only applicable to longer period systems and are likely unconservative for short period systems. A new term, C_{ds} is proposed in this chapter that would act as a multiplier on current values of C_d to accompany the adjustments made to the *R* factor.

Another approach to this problem is to achieve acceptable performance by increasing the ductility requirements of these short period systems through stricter detailing requirements. By increasing the ductility capacity, the structure is better able to accommodate the increased deflections that system will undergo and maintain the life safety performance criteria during strong ground motions.

The final approach to solving the short-period problem is to do nothing. This approach is based on the fact that there is little post-earthquake or experimental evidence for the short period problem. This approach is supported by the fact that analytical models and non-simulated collapse metrics used in the FEMA P-695 analyses of previous studies did not fully encompass the behavior of the entire structure. For example, computational models may ignore a number of factors that would increase the flexibility of the structure and push the natural period outside the realm of the short-period problem. Some examples of possible increased flexibility could come from flexibility of the connections, flexibility from soil structure interaction, diaphragms modeled as excessively rigid, foundation flexibility, or inaccurately locating the masses in a 3D model.

Additionally, there is concern over how non-simulated collapse should be defined when employing the FEMA P-695 methodology. Non-simulated collapse occurs when potential modes of collapse failure that have not been explicitly modeled are evaluated through measurement of a physical mechanism (such as peak strain of a reinforcing bar exceeding a predetermined limit). The results of the study can be very sensitive to the definition of non-simulated collapse parameters. However, the FEMA P-695 does not currently provide sufficient guidance on how to define these parameters to ensure that the mechanism being measured would actually cause structural collapse.

3.1.2 Context for this Study

The investigation into short period structural systems was completed as part of Applied Technologies Council Project 84 (ATC-84). The core objective of this project is to continue development of a procedure for determining seismic performance factors (i.e. the system

response modification factor, R, the deflection amplification factor, C_d, and the overstrength factor, Ω_o).

When the response modification factors were first introduced in 1978 as part of the ATC-3-06 report, Tentative Provisions for the Development of Seismic Regulations for Buildings (ATC 1978), the values were based on a consensus of the committee members of that project. These factors, which were originally listed for 21 systems, were not developed by any quantitative methods.

In contrast to the qualitative method that was previously employed, the Applied Technologies Council Project 63, ATC-63, looked to develop a quantitative method for developing a number of seismic performance factors for the 84 systems currently listed in ASCE/SEI 7-10 and for newly developed system. The resulting FEMA P-695 report, Quantification of Building Seismic Performance Factors (FEMA 2009), outlined a methodology for accomplishing this goal through the use of non-linear incremental dynamic analyses. Preliminary analyses of a number of structural systems indicated that the system collapse performance could be significantly affected by the natural period of the structure. Further testing of the methodology on a variety of structural systems was performed as a part of ATC-76 project. The resulting report, NIST GCR 10-917-8 Evaluation of the FEMA P-695 Methodology for Quantification of Building Seismic Performance Factors (NIST 2010), highlighted similar issues with regards to the effect of natural period.

The objective of ATC-84 was to investigate the issues that have been seen in beta testing of the FEMA P-695 methodology and determine if adjustments in the formulation of these seismic parameters should be made. The investigation discussed in this chapter examines issues observed with very short period structures and makes recommendations on how these issues could be resolved.

3.1.3 Approach

A computational study was conducted on short period structural systems to investigate the relationship between initial structural period and collapse potential. The investigation utilized

the FEMA P-695 methodology (FEMA 2009) to complete a study of single degree of freedom (SDOF) systems with periods between 0.1 seconds and 1.0 seconds. The SDOF models were developed using an elastic-linear hardening model with post-yield stiffness ratio ranging between -10% and +10%. This part of the study was done to gain a general understanding of the influence of natural period and post-yield behavior on the collapse performance of structural systems and appropriate response modification factors. Next, a study of multi-degree of freedom masonry structures with short periods was conducted to examine how those trends translated to more complex structures. Based on these two studies, recommendations were made for how current U.S. building codes could be modified to account for the behavior of short period structures.

3.2 Single Degree of Freedom Study

In this part of the project, single degree of freedom (SDOF) models were analyzed using the FEMA P-695 Methodology to investigate the relationship between initial structural period and the response modification factor, *R*. These models were developed in OpenSees (Mazzoni et al. 2005) and analyzed using the Toolkit for Automated Implementation of FEMA P-695 Methodology that was developed as part of the ATC-84 project.

The computational models for this parametric study consisted of simple bilinear models with varying natural periods, yield strength (as defined by a trial response modification factor, *R*), and post-yield slopes. The yield strength for each model was calculated using the trial *R* factor and the lateral forces associated with seismic design category (SDC) D_{max}. The models used ten natural periods that ranged from 0.1 seconds to 1.0 second, in 0.1 second increments. This was accomplished by adjusting the initial stiffness of each model and keeping the mass the same. Next, the models were given design strengths corresponding to trial *R* values of 1, 2, 4, 6, 8 and 10. These six coefficients were selected because they account for the full range of values currently allowed by ASCE-7, starting with a system that is designed to remain elastic and increasing to one with one-eighth the strength of the elastic system. Post-yield stiffness ratios, which followed a kinematic strain hardening rule, were set to -0.10, -0.05, -0.01, 0.0, 0.01, 0.05, and 0.10. These parameters result in 180 models (10x6x3) that are presented subsequently.

Figure 3.1 shows the results from an example full set of incremental dynamic analyses for a model with a natural period of 0.5s, post-yield stiffness ratio of +0.10, and an *R* value of 4. The vertical axis is the ground motion scale factor, where a scale factor of 1.0 corresponds to the maximum considered earthquake (MCE). On this plot, each point represents the peak displacement from a single nonlinear time history analysis divided by the yield displacement for that model. Incremental dynamic analyses were run for 44 ground motions at scale levels from 0.2 to 8.0 by increments of 0.2. This results in 40 nonlinear time history analyses per ground motion incremental dynamic analysis (IDA), 44 IDAs per model, and 1760 nonlinear time-histories per IDA plot. These analyses were run for all 180 models that are discussed subsequently.

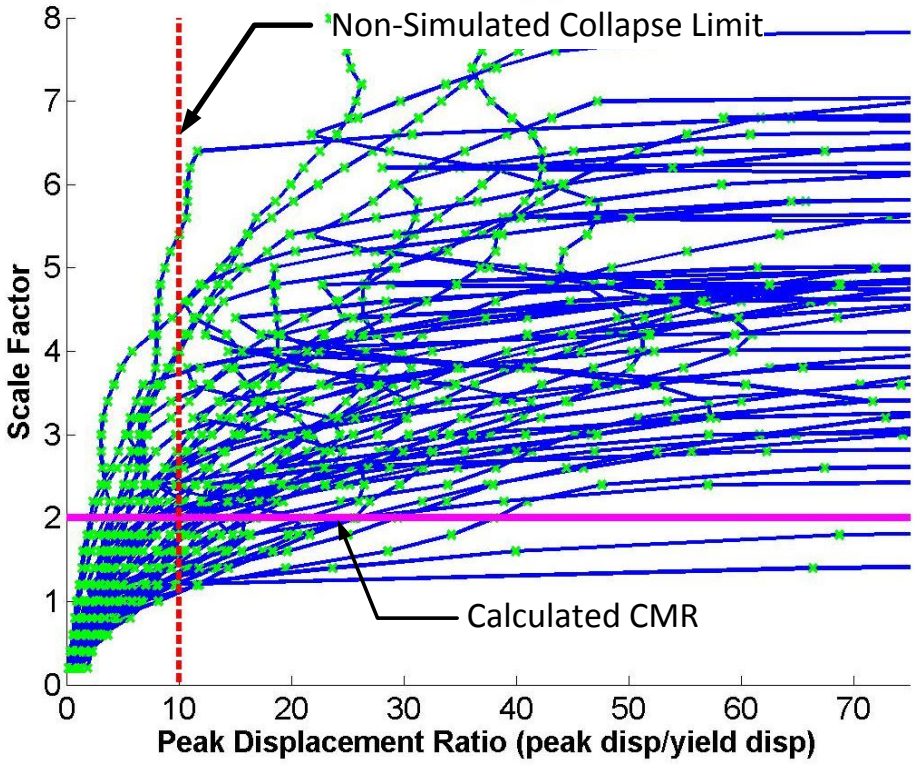

Figure 3.1: Example SDOF Incremental Dynamic Analysis Curve

The FEMA P-695 methodology was applied to each of the models and the resulting adjusted collapse margin ratio (ACMR) was calculated. The collapse margin ratio (CMR) is calculated by determining the ground motion scale level that causes collapse in 50% of the models and dividing that scale level by the scale level that indicates the MCE level ground motion. Collapse can be defined in two separate ways within the context of the FEMA-P695 methodology. First, simulated collapse occurs when a small increase in the scale factor applied to the ground motion causes a large increase in the peak displacement of the model. The second, non-simulated collapse, is defined when a physical property of the model exceeds a predetermined limit. Examples of these limits include yielding a certain percentage of reinforcing steel in a masonry wall or exceeding a force in a steel brace that would be expected to cause rupture. For this study, the collapse of the system was defined as when the ductility demand exceeded 10. This was somewhat arbitrarily defined because a true physical mechanism for a SDOF system could not be determined. Non-simulated collapse limits were also run for ductility demands of 20, 30, and 40 to see the influence of this arbitrarily defined limit. It was seen that the definition had a significant effect on the value of ACMR for each model, but that the same trends were shown for all each non-simulated collapse definition. Because the trends were the same, only the results from the ductility demand of 10 are reported. This ductility limit is shown in Figure 3.1 as vertical line at the appropriate ductility. The CMR for the IDA shown in Figure 3.1 is approximately 2.0. This CMR is calculated based on the worse of these two collapse criteria and then adjusted to determine the ACMR by multiplying the CMR by a spectral shape factor (SSF). Details for calculating the ACMR can be found in the FEMA P-695 report (FEMA 2009). Additionally, the qualitative parameters for design, test data, and analysis uncertainties were set to a value of "B" or "Good."

The computed ACMR for each model was then compared to the acceptable value for the 10% and 20% probability of collapse. The 20% probability of collapse is the level that, according to the FEMA P-695 methodology, must be met by each individual archetype. According to the FEMA P-695 document, an archetype is "a prototypical representation of a seismic-force-resisting system configuration that embodies key features and behaviors related to collapse performance when the system is subjected to earthquake ground motions" (FEMA 2009). The 10% level must be met by a given performance group that encompasses a number of individual

archetypes. Performance groups are subdivided based on major differences in configuration, design gravity, seismic load intensity, structural period, or other factors that may significantly affect seismic behavior. In general, the results that have been shown are compared to the 10% probability of collapse because it is assumed that each SDOF system could represent an entire performance group with similar parameters.

Figure 3.2 shows the plots for the elastic perfectly plastic (EPP) systems (post-yield stiffness ratio = 0.0). Figure 3.2(a) shows the ACMR ratio versus the natural period. In order to develop each ACMR ratio, an IDA was run for the archetype that required non-linear time history analyses for 44 ground motions at 40 scale levels (0 to 8, in increments of 0.2). This results in 1760 individual time history analyses for each model to develop a single ACMR. The ACMR ratio is given as the calculated value versus the accepted value for the 10% probability of collapse. Values less than one indicate that the model has failed to meet the performance criteria. These curves show a trend of increasing ACMR ratio as the natural period of the system increases.

The calculated *R* value was then computed for each fundamental period as the value that produces the desired collapse probability. This is the *R* value which would approximately result in an ACMR ratio of 1.0 and is computed by interpolating between trial *R* values that result in ACMR ratios on either side of 1.0. The calculated *R* values for the data shown in Figure 3.2(a) were computed for each fundamental period and are shown in Figure 3.2(b). These *R* values are based on the 10% probability of collapse and as expected, show a positive trend of increasing calculated *R* value as the natural period of the system increases.

For a period of 0.1 seconds, a target *R* value could not be calculated because all of the ACMR ratios at that period were less than 1.0. This is shown in Figure 3.2(b) by a downward pointing triangle, which shows the expected target *R* would be less than 1.0 if models with *R* values less than 1.0 had been evaluated. Figure 3.2(b) shows the calculated *R* values range from less than 1 for a natural period of 0.1 seconds to approximately 4 for a natural period of 1.0 seconds.

Figure 3.2(c) shows the probability of collapse versus the natural period of the system. This figure shows a negative trend of decreasing probability of collapse as the natural period increases. At a period of 0.1 seconds, only the system that has been designed to remain elastic during the design basis earthquake (DBE) (trial R=1) had a probability of collapse of less than 20%, which is the level needed for a single archetype to pass the performance criteria of FEMA P695 (FEMA 2009). This value is also just above the 10% level which is required for an entire performance group to pass.

Finally, the ratios of the median inelastic to elastic drift for the maximum considered earthquake (MCE) level ground motion are shown in part (d) of Figure 3.2. These plots show that for the very short period structures, the inelastic drift greatly exceeds the elastic drift for that system. As the natural period of the system increases, these ratios approach 1.0. This illustrates that the equal displacement concept is not met by the very short period systems and is more closely adhered to as the natural period increases. In general, archetypes with a natural period greater than or equal to 0.6 seconds produce median displacements that follow the equal displacement concepts.

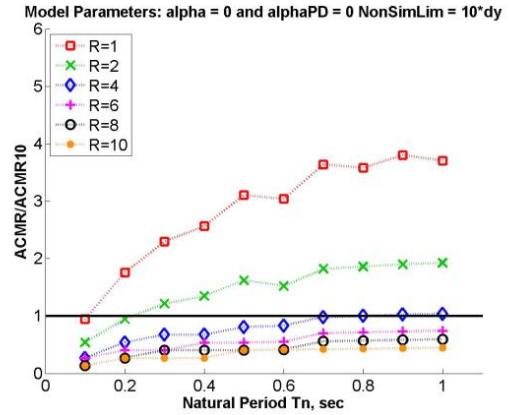

(a) ACMR Ratios for 10% Prob. of Collapse

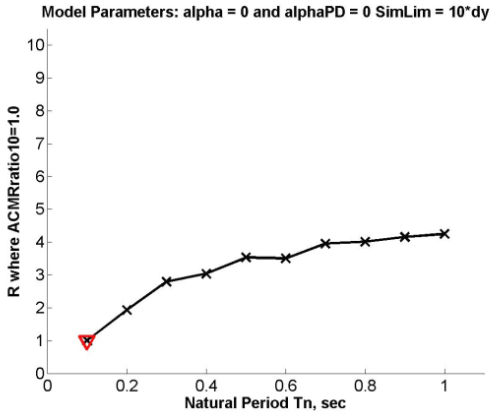

(b) Calculated *R* Values for 10% Prob. of Collapse

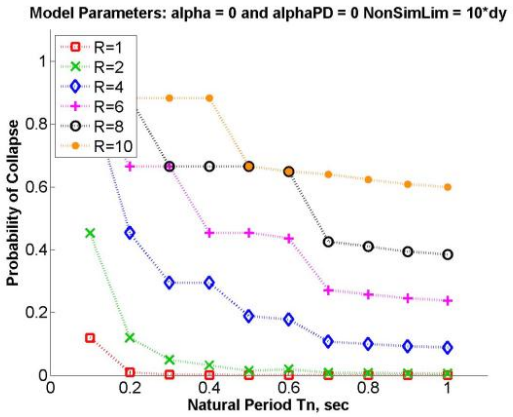

(c) Probability of Collapse

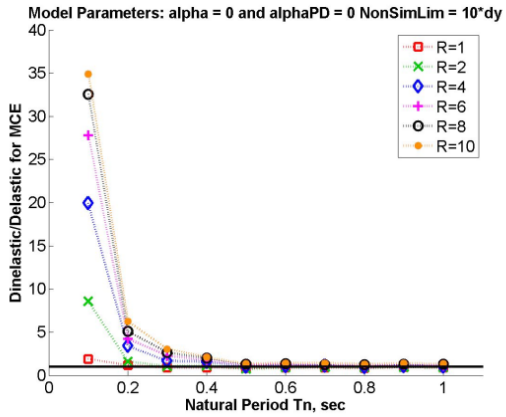

(d) Inelastic to Elastic Drift Ratios

Figure 3.2: Results for SDOF systems with 0% strain hardening and a ductility limit of 10

Figure 3.3 shows the plots for ACMR ratio and target *R* values when the collapse limit is increased from a ductility of 10 to a ductility of 20. When compared to Figure 3.2, the ACMR ratios and the calculated *R* values have increased. This illustrates two concepts well: first, it shows that the results of a FEMA P-695 analysis can be greatly affected by the selected collapse criteria. Additionally, this shows that if systems are designed to have a greater level of ductility, they can be designed for greater *R* values. This supports the third approach to the short period structure problem in which short period structures must be designed for greater ductility than longer period versions of the same system.

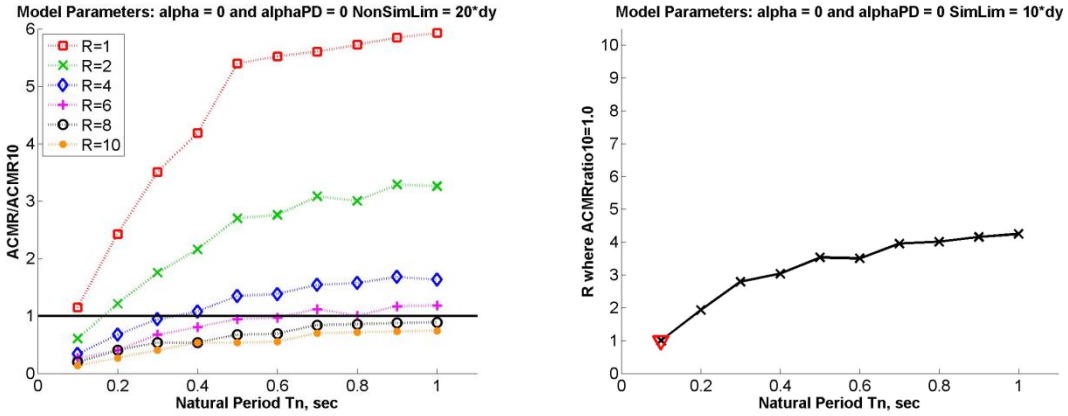

(a) ACMR Ratios for 10% Prob. of Collapse

(b) Calculated *R* Values for 10% Prob. of Collapse

Figure 3.3: Results for SDOF systems with 0% strain hardening and a ductility limit of 20.

Figure 3.4 shows the same set of curves for the system with positive 10% strain hardening and the trends are similar to those seen for the systems with 0% strain hardening. The curve in part (b) again shows the calculated *R* values will be approximately 1 for a natural period of 0.1 seconds. However, the target *R* value for natural periods greater than 0.6 seconds have increased from approximately 4 to between 5 and 6. In Figure 3.4(c), similar to the EPP systems, only the system that has been designed to be elastic (*R*=1) has a probability of collapse that is less than the levels required for an individual archetype (20%) at a natural period of 0.1 seconds. In contrast to the EPP model, this *R*=1 model is also less than 10% and meets the requirements for an entire performance group. Part(d) again shows that the inelastic drift greatly exceeds the elastic drift at very short periods and then the ratio approaches 1.0 as the natural period increases. This again illustrates that the inelastic drift is not well approximated by the elastic drift at very short periods, as is assumed by the equal displacement concept.

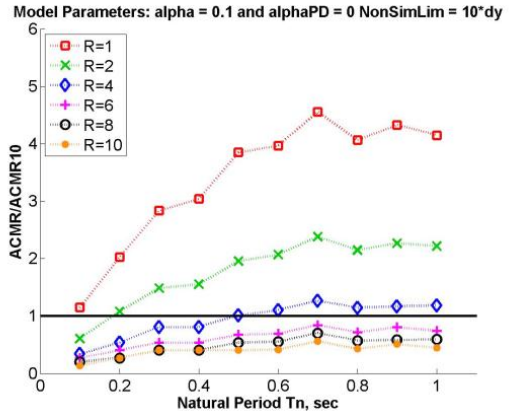

(a) ACMR Ratios for 10% Prob. of Collapse

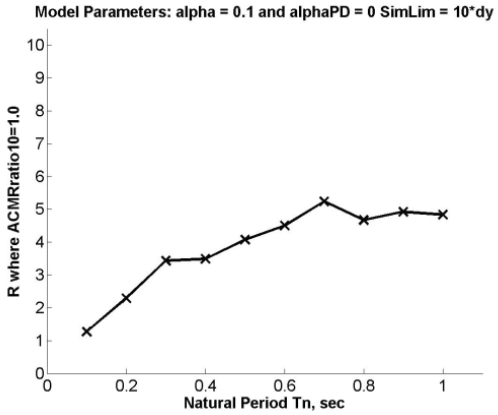

(b) *R* Values for 10% Prob. of Collapse

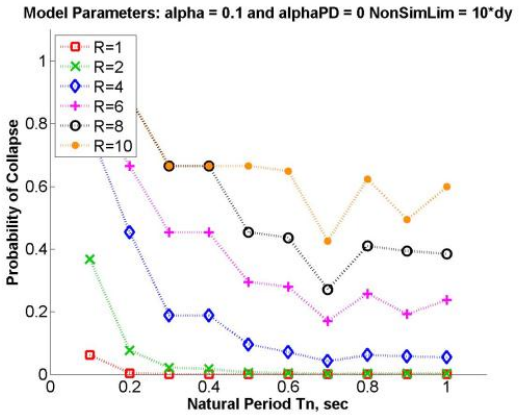

c) Probability of Collapse

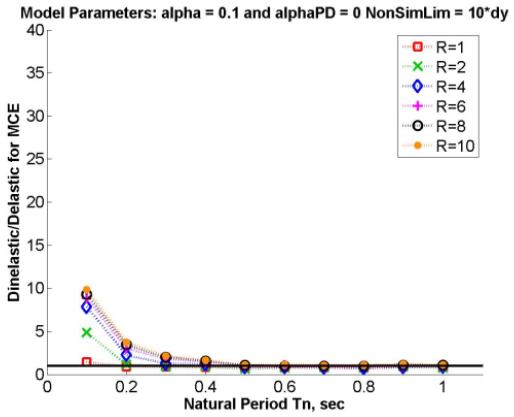

(d) Inelastic to Elastic Drift Ratios

Figure 3.4: Results for the SDOF systems with 10% strain hardening and a ductility limit of 10

Figure 3.5 shows the same set of curves for the system with negative 10% strain hardening. The curves in Figure 3.5(a) show greatly decreased performance when compared to the curves for 0% and positive 10% strain hardening and result in only the R=1 curve having ACMR ratios greater than 1.0. This fact is highlighted in Figure 3.5(b) where the target R values are expected to be less than 1 for all models with periods less than or equal to 0.4 seconds. Even the systems with longer natural periods have target R values that are very low and fall between 1 and 2. Figure 3.5(c) shows significantly higher probability of collapse for the full range of periods considered.

The ductility demands in Figure 3.5(d) do not appear to follow any typical patterns, which can be attributed to the fact that dynamic instability appears to dominate for models at every natural

period. This fact is illustrated in Figure 3.6, which shows sample time histories for the system with a natural period of 0.1 seconds and a design *R* value of 1 at two different IDA levels. Figure 3.6(a) shows the response due to the TMZ000 component of the 1976 Friuli, Italy scaled to 60% of the MCE level ground motion and Figure 3.6(b) shows the response at the MCE level. These plots clearly indicate that at one level, the system undergoes the "ratcheting" that is commonly seen for short period structures, but then stabilizes and is able to finish the ground motion. However, for a relatively small increase in ground motion intensity, the system becomes dynamically unstable and the displacements shoot off to very high values. Similar behavior was seen for every natural period for the systems with negative 10% post-yield stiffness ratio. This shows how systems that immediately transfer to a negative post-yield stiffness and have no positive post-yield stiffness section are very susceptible to collapse if inelastic deformations are allowed to form. In contrast to the systems with a positive post-yield stiffness, the susceptibility to collapse does not appear to be dependent upon the natural period of the system, but instead applies across the board.

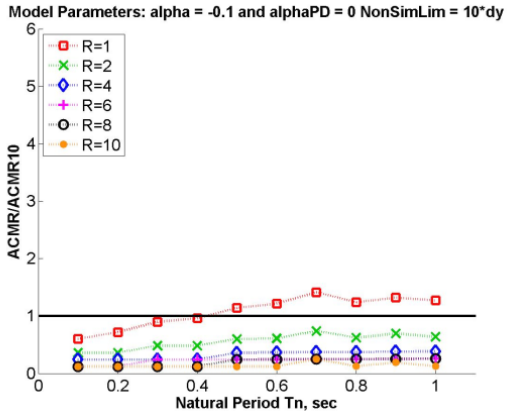

(a) ACMR Ratios for 10% Prob. of Collapse

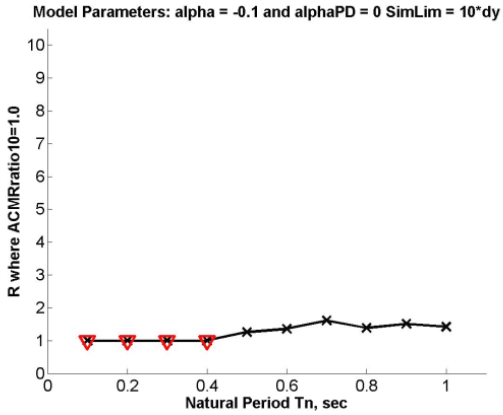

(b) *R* Values for 10% Prob. of Collapse

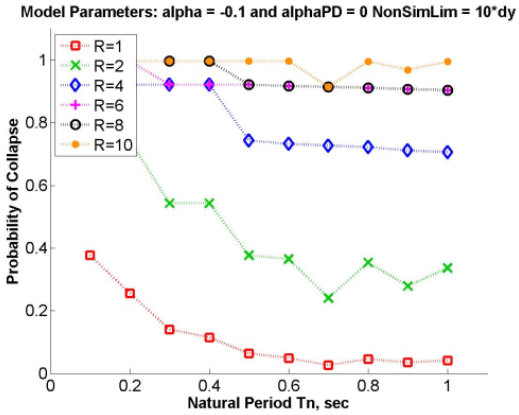

(c) Probability of Collapse

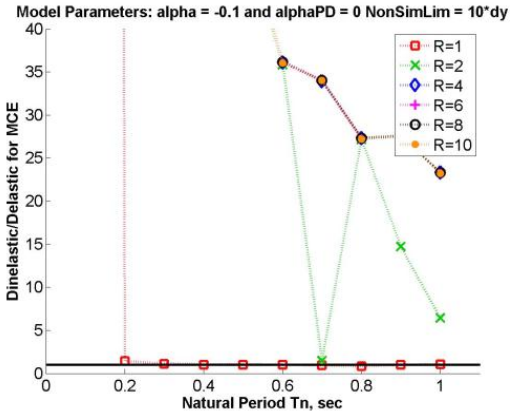

(d) Inelastic to Elastic Drift Ratios

Figure 3.5: Results for SDOF systems with -10% strain hardening and a ductility limit of 10

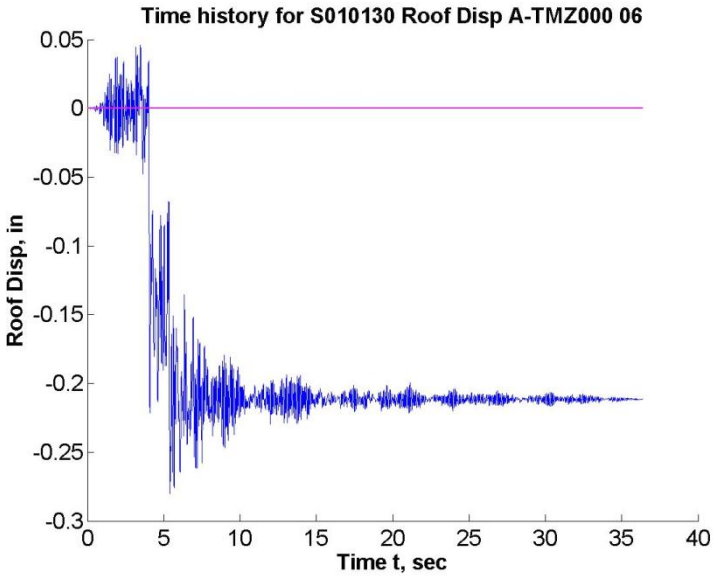

(a) Response at IDA Increment 06

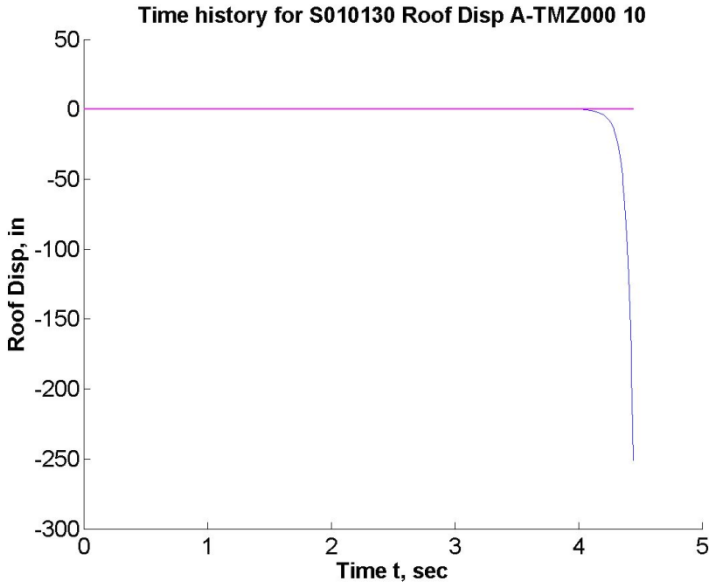

(b) Response at IDA Increment 10

Figure 3.6: Example response histories for -10% strain hardening at two IDA increments

3.3 Masonry Model Study

The SDOF studies indicated a strong relationship between the calculated *R* and the system period for structures with a natural period less than 0.5 seconds. However, bilinear models constitute a very simple, idealized representation of structural load deformation behavior. To better understand the effects of period on calculated *R*, it was necessary to investigate multi-degree of freedom structures that better represented building behavior. Reinforced masonry systems were studied as part of the NIST GCR 10-917-8 report (NIST 2010) and a study was developed to analyze a set of buildings based on the designs produced as part of that investigation. The results from the NIST report are summarized in Table 3.1. These archetypes were designed with R=5.0; and, per the recommendations of FEMA P-695, C_d was taken as equal to *R* and set to 5.0. The results shown in Table 3.1 indicate that all of the 1-story and some of the 2-story archetypes did not meet the required ACMR for individual archetypes with and ACMR ratio less than 1.0. This was believed to be the result of the short period problem that was being investigated and because of this, special reinforced masonry shear wall systems were selected to be further investigated in this study.

Table 3.1: Summary of Results for Special Reinforced Masonry Shear Wall Systems

Archetype	NS	SDC	Grav.	T (sec.)	T_1(sec.)	Ω	ACMR	$ACMR_{20\%}$	ACMR/ $ACMR_{20\%}$
S1	**1**	**D_{max}**	**High**	**0.25**	**0.10**	**1.84**	**0.66**	**1.56**	**0.42**
S2	**2**	**D_{max}**	**High**	**0.26**	**0.13**	**2.28**	**1.52**	**1.56**	**0.97**
S3	4	D_{max}	High	0.45	0.21	1.87	2.06	1.56	1.32
S4	8	D_{max}	High	0.75	0.55	1.89	1.76	1.56	1.13
S6	**1**	**D_{min}**	**High**	**0.25**	**0.14**	**1.62**	**1.19**	**1.56**	**0.76**
S7	2	D_{min}	High	0.28	0.19	2.61	2.18	1.56	1.40
S8	4	D_{min}	High	0.48	0.35	1.65	1.88	1.56	1.21
S9	8	D_{min}	High	0.80	1.12	1.63	2.03	1.56	1.30
S11	**1**	**D_{max}**	**Low**	**0.25**	**0.10**	**1.84**	**0.66**	**1.56**	**0.42**
S12	2	D_{max}	Low	0.26	0.13	1.82	2.27	1.56	1.46
S13	4	D_{max}	Low	0.45	0.26	1.73	2.19	1.56	1.40
S14	8	D_{max}	Low	0.75	0.61	1.59	1.82	1.56	1.17
S16	**1**	**D_{min}**	**Low**	**0.25**	**0.14**	**1.62**	**1.19**	**1.56**	**0.76**
S17	2	D_{min}	Low	0.28	0.21	1.80	2.71	1.56	1.74
S18	4	D_{min}	Low	0.48	0.43	1.41	1.88	1.56	1.21
S19	8	D_{min}	Low	0.80	1.16	1.64	2.05	1.56	1.37

NS=Number of Stories

In order to gain a better understanding of the short period problem, a study of special masonry shear walls was developed with an expanded set of short period archetypes. The study consisted of 1-, 2-, and 4-story structures that were designed for SDC D_{max} and SDC D_{min}. These structures were also designed according the recommendations in FEMA P-695 for trial *R* values of 1, 2, 4, 6, and 8. This array of *R* values was selected because it encompasses all of the values currently allowed by ASCE 7 and, similar to the results from the SDOF study, so that the effect of *R* value on the collapse margin ratio could be studied.

Table 3.2 through Table 3.8 summarizes the designs of each of the shear wall archetypes. These designs, which were developed by the San Francisco office of the structural design firm Rutherford and Chekene, utilize the gravity loads that were given in the NIST GCR 10-917-8 (NIST 2010) study and have been designed according the Masonry Standard Joint Committee design standard (MSJC 2008).

Table 3.2: Basic Design Parameters for All Special Reinforced Masonry Walls

Number of Stories	f_m'	Wall length	Total Wall height	Nominal Thickness
1 at 12'	1.5	24 ft.	12 ft.	8.0 in.
2 at 10'	2.5	32 ft	20 ft	8.0 in.
4 at 10'	3.0	32 ft.	40 ft.	8.0 in.

Table 3.3: Reinforcement for Four-Story Wall designed for SDC Dmax

Design *R* Value	System Designation	Story Level	Reinforcement
1	M4DmaxR1	4	#4 at 16”
		3	#5 at 8”
		2	#7 at 8”
		1	#9 at 8”
2	M4DmaxR2	4	#4 at 32”
		3	#4 at 16”
		2	#6 at 16”
		1	#8 at 16”
4	M4DmaxR4	4	#4 at 32”
		3	#4 at 32”
		2	#4 at 32”
		1	#4 at 16”
6	M4DmaxR6	4	#4 at 32”
		3	#4 at 32”
		2	#4 at 32”
		1	#4 at 32”
8	M4DmaxR8	4	#4 at 32”
		3	#4 at 32”
		2	#4 at 32”
		1	#4 at 32”

Table 3.4: Reinforcement for Two-Story Wall designed for SDC Dmax

Design *R* Value	System Designation	Story Level	Reinforcement
1	M2DmaxR1	2	#4 at 8”
		1	#7 at 8”
2	M2DmaxR2	2	#4 at 16”
		1	#4 at 8”
4	M2DmaxR4	2	#4 at 32”
		1	#4 at 32”
6	M2DmaxR6	2	#4 at 32”
		1	#4 at 32”
8	M2DmaxR8	2	#4 at 32”
		1	#4 at 32”

Table 3.5: Reinforcement for One-Story Wall designed for SDC Dmax

Design *R* Value	System Designation	Story Level	Reinforcement
1	M1DmaxR1	1	#6 at 8”
2	M1DmaxR2	1	# 5 at 16”
4	M1DmaxR4	1	#4 at 16”
6	M1DmaxR6	1	#4 at 32”
8	M1DmaxR8	1	# 4 at 32”

Table 3.6: Reinforcement for Four-Story Wall designed for SDC Dmin

Design *R* Value	System Designation	Story Level	Reinforcement
1	M4DminR1	4	#4 at 32”
		3	#4 at 32”
		2	#4 at 16”
		1	#8 at 16”
2	M4DminR2	4	#4 at 32”
		3	#4 at 32”
		2	#4 at 32”
		1	#6 at 16”
4	M4DminR4	4	#4 at 32”
		3	#4 at 32”
		2	#4 at 32”
		1	#4 at 16”
6	M4DminR6	4	#4 at 32”
		3	#4 at 32”
		2	#4 at 32”
		1	#4 at 32”
8	M4DminR8	4	#4 at 32”
		3	#4 at 32”
		2	#4 at 32”
		1	# 4 at 32”

Table 3.7: Reinforcement for Two-Story Wall designed for SDC Dmin

Design *R* Value	System Designation	Story Level	Reinforcement
1	M2DminR1	2	#4 at 16”
		1	#4 at 8”
2	M2DminR2	2	#4 at 32”
		1	#4 at 32”
4	M2DminR4	2	#4 at 32”
		1	#4 at 32”
6	M2DminR6	2	#4 at 32”
		1	#4 at 32”
8	M2DminR8	2	#4 at 32”
		1	#4 at 32”

Table 3.8: Reinforcement for One-Story Wall designed for SDC Dmin

Design *R* Value	System Designation	Story Level	Reinforcement
1	M1DminR1	1	#5 at 16”
2	M1DminR2	1	#4 at 16”
4	M1DminR4	1	#4 at 32”
6	M1DminR6	1	#4 at 32”
8	M21minR8	1	#4 at 32”

Analysis of the masonry walls was completed using the open source software *Open System for Earthquake Engineering Simulation* (OpenSees), (Mazzoni et al. 2005). The models that were used for nonlinear analysis in this study are based on the OpenSees models that were developed as part of the NIST GCR 10-917-8 report which were provided by Professor Benson Shing at the University of California San Diego (UCSD). The nonlinear models were developed as individual cantilever walls using displacement-based beam column elements with a fully fixed base. The fiber cross section consisted of a concrete material to model the masonry blocks,

mortar and grout as well as a steel material to represent the reinforcing. The concrete material was the OpenSees uniaxial material "Concrete01", which utilizes a Kent-Park constitutive relationship in compression and has zero strength in tension. The "Hysteretic" uniaxial material was utilized to develop the reinforcing steel fibers which were assumed to be ASTM A615 Grade 60 steel. Based on this, the yield stress for the steel material was defined as 60ksi. This material was able to account for rupture in tension and buckling in compression by independently defining points on the stress-strain curve in each direction. In order to account for localization issues that can occur in the beam column elements, both the concrete and the steel material were regularized according to the method outlined in Appendix A of NIST GCR 10-917-8 (NIST 2010).

The displacement-based beam-column elements were discretized into two elements at the first floor and a single element at each subsequent floor. The length of the lower element in the first floor was set to be equal to effective length of the plastic hinge, which, based on the discussion in NIST GCR 10-917-8, was set as 20% of the wall height. At the time these models were developed, flexure-shear interaction could not be accounted for in a single beam column element in OpenSees. In order to account for shear deformations a horizontal elastic spring was added at the top of each story. The vertical and rotational degrees of freedom between the two nodes were constrained together and the elastic spring controlled horizontal deformations. Inelastic shear behavior was not taken into account. An example two story model is shown in Figure 3.7.

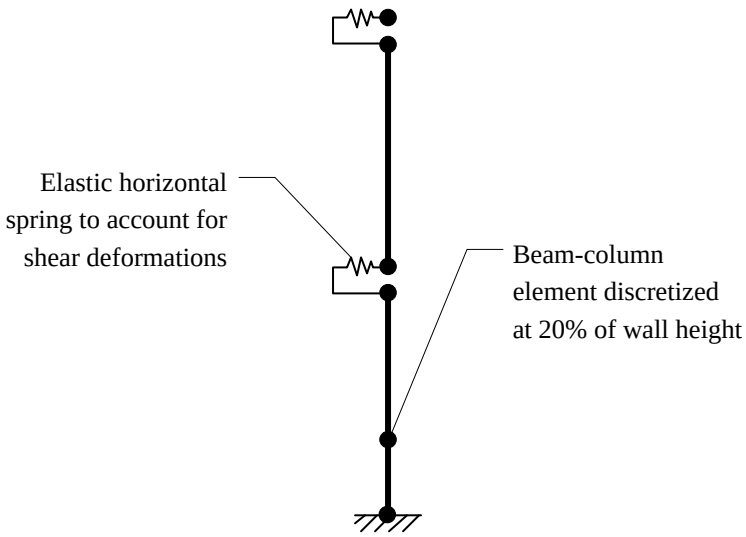

Figure 3.7: Representative model configuration for Masonry Shear Wall Archetype

The gravity loading on the structure was taken from the NIST GCR 10-917-8 report and is summarized in Table 3.9 (NIST 2010). These models are the same as those provided by UCSD with a couple key distinctions: first, leaning column loads were added for all analyses. Next, live load was not included when developing the seismic mass of the system. Finally, the masonry elements were modeled as uncracked.

Table 3.9: Gravity load assumptions for Special Reinforced Masonry Shear Walls

Description	Load
Roof Loading	
Typical Dead Load (single-story)	30 psf
Typical Dead Load (multi-story)	85 psf
Typical Live Load	20 psf
Floor Loading	
Typical Dead Load	100 psf
Typical Live Load	28 psf
Corridor Dead Load	73 psf
Corridor Live Load	60 psf
Masonry Walls	
Masonry Walls	120 pcf

One of the key assumptions that must be made when performing a FEMA P-695 analysis is determining what defines collapse. There are two types of collapse that can occur. First, a simulated collapse occurs when the incremental dynamic analysis (IDA) curves flatten out and begin to show a large increase in drift for a small increase in ground motion intensity. This phenomenon can only be captured when the computational model appropriately accounts for items like buckling, fracture, or instability that cause system softening.

The second type of collapse is a non-simulated collapse, which defines a specific mechanism that would result in collapse of the structure. These mechanisms are unique for each type of structure. In this study, non-simulated collapse was defined to have occurred when either material reached a limiting strain 30% into the cross section from the extreme fiber. For the masonry, this non-simulated collapse occurred when 30% of the cross section reached the end of the softening branch of the constitutive relationship which represented a point where a significant portion of the cross section had crushed. For the reinforcing steel, non-simulated collapse occurred when 30% of the steel fibers had lost their tensile strength due to rupture or had lost their compressive strength due to buckling.

Instead of relying on tracking and recording the strains at every fiber for every analysis during the IDA, displacements were determined for each masonry shear wall configuration where these strains would be exceeded. This was done by performing a static monotonic pushover analysis for each structure and determining which displacement would cause a non-simulated collapse to occur. The pushover curves are given in Figure 3.8 through Figure 3.10. An asterisk (*) is shown on each curve to indicate the point at which non-simulated collapse would occur.

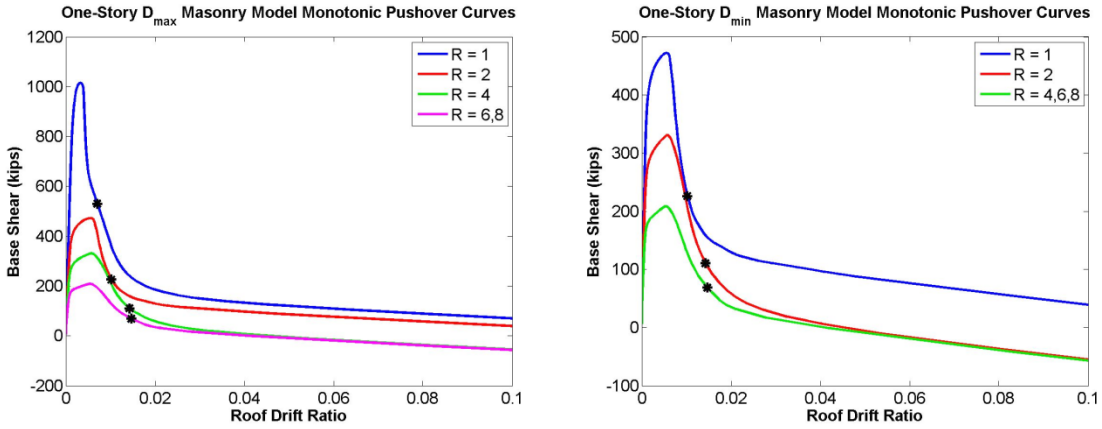

Figure 3.8: Monotonic pushover curves for the 1-story systems.

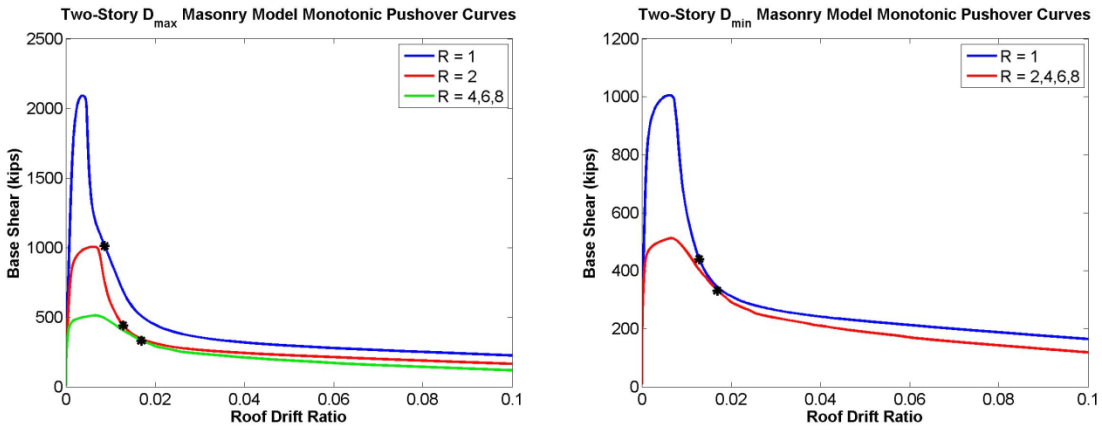

Figure 3.9: Monotonic pushover curves for the 2-story systems.

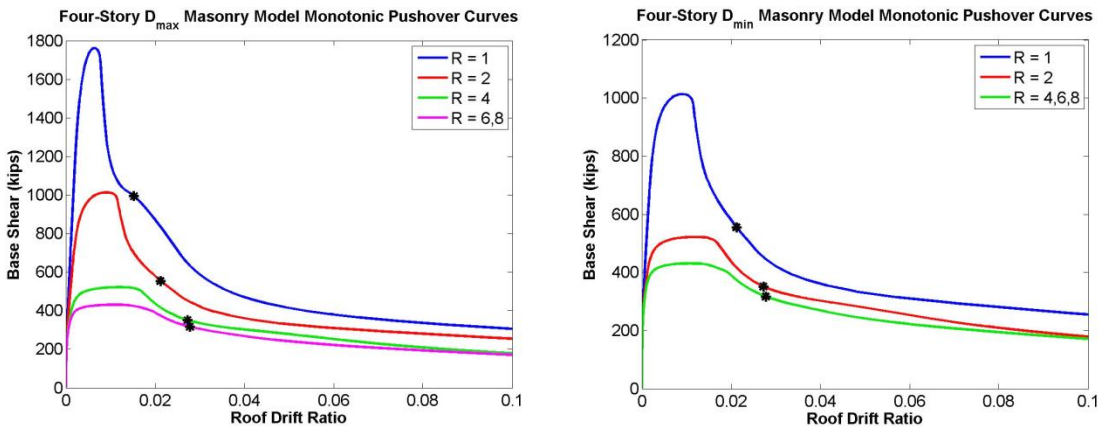

Figure 3.10: Monotonic pushover curves for the 4-story systems.

In addition to running the monotonic, static pushover curves, cyclic pushover curves were also run for each structural configuration prior to starting the IDA. This was done to gain a better understanding of the hysteretic behavior of the system as a whole and sample results are shown below. Figure 3.11 and Figure 3.12 show the cyclic pushover curves for the 2-story, SDC D_{max} structures at R=2 and R=6, respectively. Figure 3.13 and Figure 3.14 show the curves for the 4-story, SDC D_{max} shear walls at R=2 and R=6, respectively. The R=2 configurations acted as would generally be expected; however, the R=6 models show a flag shaped hysteretic response. This type of response is typical of self-centering systems and indicates that a rocking mechanism is occurring at the base of these structures with relatively little reinforcement. During the design of these structures it is important to understand that this mechanism may be occurring and that these walls must be appropriately detailed if this is allowed to happen.

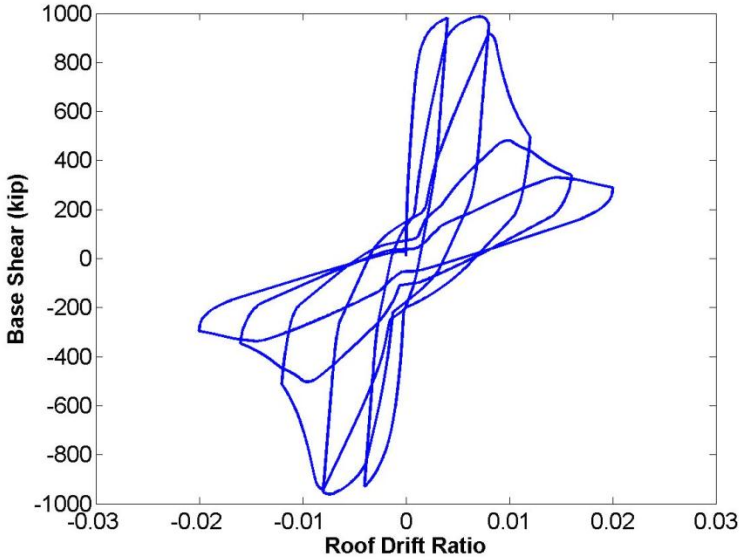

Figure 3.11: Cyclic pushover curve for the 2-story *R*=2 Dmax system.

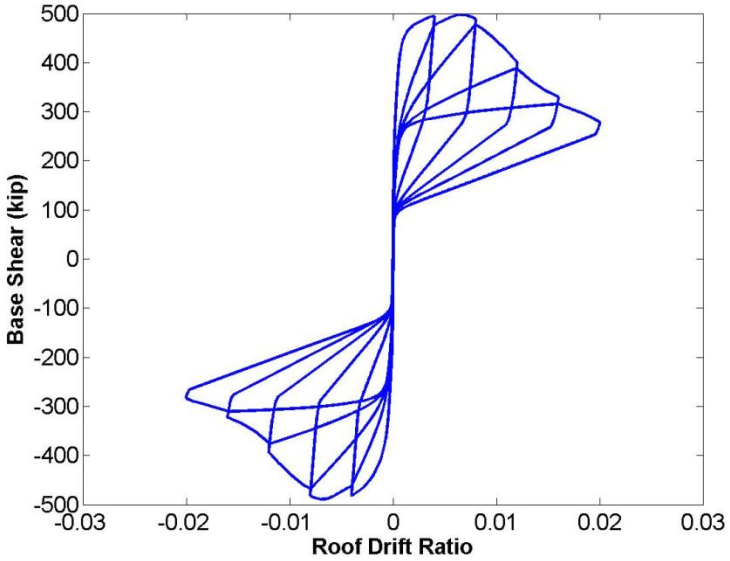

Figure 3.12: Cyclic pushover curve for the 2-story *R*=6 Dmax system.

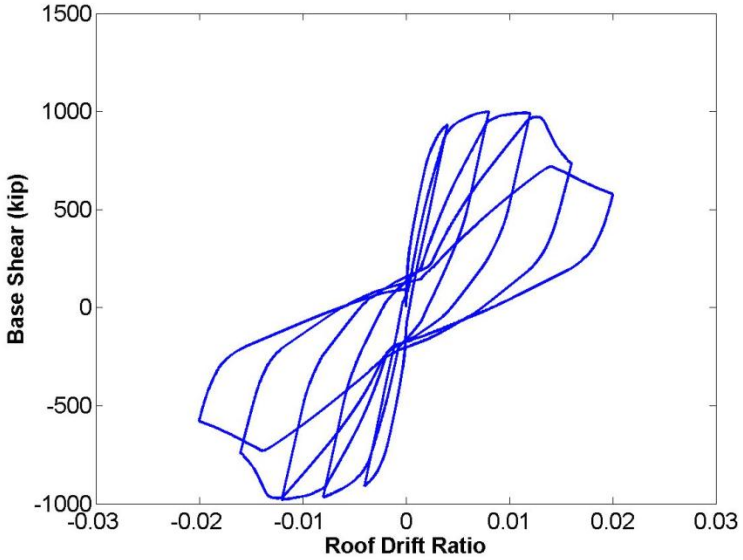

Figure 3.13: Cyclic pushover curve for the 4-story Trial *R*=2 Dmax system.

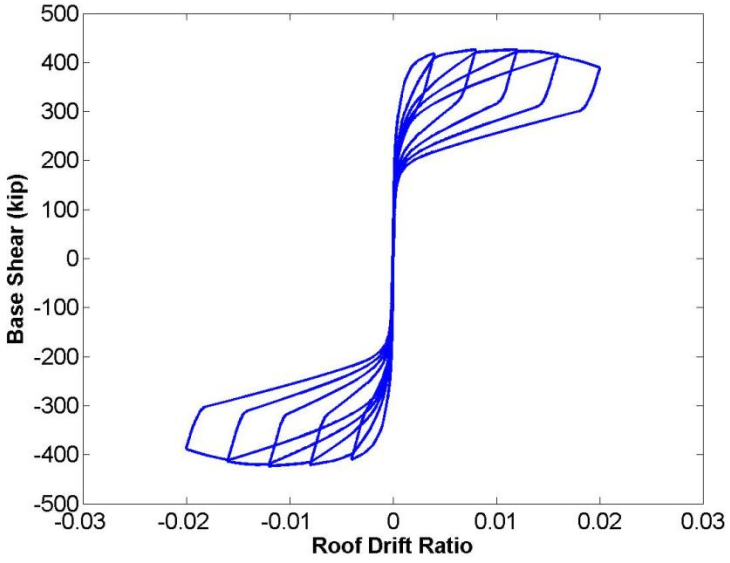

Figure 3.14: Cyclic pushover curve for the 4-story *R*=6 Dmax system.

After these preliminary analyses were run to understand the system behavior and to define collapse parameters, a full FEMA P-695 analysis was conducted for each structural configuration. The analyses include nonlinear response history analyses starting at 20% of the MCE level ground motion and then incrementally increasing the intensity by 20% until reaching

400% of the MCE. This resulted in 20 time history analyses for each of the 44 ground motions, or 880 unique time history analyses per masonry archetype. The collapse level was defined as the level at which simulated collapse or non-simulated collapse first occurred. No attempt was made to pinpoint the exact collapse point through a bisection method or other methodology. A factor of four times the MCE level ground motion was considered large enough to encompass the collapse of all structures and this fact was confirmed during post-processing of the data.

An overview of the results from the FEMA P-695 analysis is given in Table 3.10. Further explanation of how each of these variables is calculated can be found in the FEMA P-695 report (FEMA 2009). This table gives values from a number of steps during the analysis, including the calculated fundamental period, T_1, the static overstrength factor, Ω, the period based ductility, μ_T, and the spectral shape factor, SSF. Finally, ACMR, accepted ACMR for an individual archetype, and ACMR ratios are given. It is immediately apparent that each of the single story SDC D_{max} structures with trial $R>1$ fail to meet the accepted ACMR for an individual archetype. This indicates that these structures have greater than a 20% probability of collapse during the MCE level ground motion.

Table 3.10: Analysis Results for all Special Reinforced Masonry Archetypes

No. of stories	SDC	R	T (sec)	T1 (sec)	Static Ω	CMR	μ_T	SSF	ACMR	Accept. ACMR ≥ 20%	ACMR / AACMR 20%
1	Dmax	8	0.25	0.108	2.58	0.8	6.4	1.29	1.03	1.56	0.66
		6	0.25	0.108	1.93	0.8	6.4	1.29	1.03	1.56	0.66
		4	0.25	0.108	2.04	1.0	4.2	1.23	1.23	1.56	0.78
		2	0.25	0.108	1.46	1.2	2.5	1.15	1.39	1.56	0.92
		1	0.25	0.106	1.57	1.6	0.7	1.00	1.60	1.56	1.14
1	Dmin	8	0.25	0.108	2.58	1.6	6.4	1.12	1.80	1.56	1.15
		6	0.25	0.108	1.93	1.6	6.4	1.12	1.80	1.56	1.15
		4	0.25	0.108	1.29	1.6	6.4	1.12	1.80	1.56	1.15
		2	0.25	0.108	1.02	1.9	4.2	1.09	2.08	1.56	1.33
		1	0.25	0.108	0.73	2.2	2.5	1.07	2.35	1.56	1.56
2	Dmax	8	0.26	0.099	6.33	1.4	8.0	1.33	1.86	1.56	1.19
		6	0.26	0.099	4.75	1.4	8.0	1.33	1.86	1.56	1.19
		4	0.26	0.099	3.17	1.4	8.0	1.33	1.86	1.56	1.19
		2	0.26	0.099	3.10	1.8	2.9	1.18	2.12	1.56	1.36
		1	0.26	0.097	3.23	2.5	0.8	1.00	2.50	1.56	1.79
2	Dmin	8	0.28	0.099	6.33	2.8	7.3	1.13	3.17	1.56	2.03
		6	0.28	0.099	4.75	2.8	7.3	1.13	3.17	1.56	2.03
		4	0.28	0.099	3.17	2.8	7.3	1.13	3.17	1.56	2.03
		2	0.28	0.099	1.58	2.8	7.3	1.13	3.17	1.56	2.03
		1	0.28	0.099	1.55	3.4	2.5	1.07	3.64	1.56	2.40
4	Dmax	8	0.45	0.161	5.32	2.4	8.0	1.33	3.19	1.56	2.04
		6	0.45	0.161	3.99	2.4	8.0	1.33	3.19	1.56	2.04
		4	0.45	0.160	3.22	2.4	8.0	1.33	3.19	1.56	2.04
		2	0.45	0.158	3.13	2.6	2.6	1.16	3.01	1.56	1.98
		1	0.45	0.153	2.72	3.0	1.0	1.00	3.00	1.56	2.14
4	Dmin	8	0.48	0.161	5.32	5.5	8.0	1.14	6.27	1.56	4.02
		6	0.48	0.161	3.99	5.5	8.0	1.14	6.27	1.56	4.02
		4	0.48	0.161	2.66	5.5	8.0	1.14	6.27	1.56	4.02
		2	0.48	0.160	1.61	5.7	7.1	1.13	6.45	1.56	4.13
		1	0.48	0.158	1.56	6	2.3	1.07	6.39	1.56	4.28

Table 3.11 shows the results of the FEMA P-695 analysis with the 1- and 2-story SDC D_{max} when they are organized by performance group. The average ACMR is taken for each performance group and then compared for the $ACMR_{10\%}$ value. Performance groups with an average ACMR less than the $ACMR_{10\%}$ have greater than a 10% probability of collapse at the MCE level ground motion for the performance group as a whole. Based on the ACMR ratios, all of the performance groups fail with the exception of the R=1 performance group. While the 1-story archetypes generally brought the average of the performance group down significantly, many of the 2-story structures would not have met the $ACMR_{10\%}$ requirement on their own. The only systems that did meet the $ACMR_{10\%}$ limit independently were the R=1 and R=2 systems. Because of this, even if the 4-story structures were included in the data (which generally had higher computed ACMR values), the only performance group that would have passed was the trial R=1 performance group.

Table 3.11: Analysis Results for 1- and 2-Story SDC Dmax Masonry Archetypes Arranged into Performance Groups

R	SDC	No. of stories	T (sec)	T1 (sec)	Static Ω	CMR	μ_T	SSF	ACMR	AACMR	ACMR/AACMR
8	Dmax	1	0.25	0.108	2.58	0.8	6.4	1.29	1.03	1.56	0.66
		2	0.26	0.099	6.33	1.4	8.0	1.33	1.86	1.56	1.19
		Avg			4.45				1.45	1.96	0.74
6	Dmax	1	0.25	0.108	1.93	0.8	6.4	1.29	1.03	1.56	0.66
		2	0.26	0.099	4.75	1.4	8.0	1.33	1.86	1.56	1.19
		Avg			3.34				1.45	1.96	0.74
4	Dmax	1	0.25	0.108	2.04	1.0	4.2	1.23	1.23	1.56	0.78
		2	0.26	0.099	3.17	1.4	8.0	1.33	1.86	1.56	1.19
		Avg			2.60				1.54	1.96	0.79
2	Dmax	1	0.25	0.108	1.46	1.2	2.5	1.15	1.39	1.56	0.92
		2	0.26	0.099	3.10	1.8	2.9	1.18	2.12	1.56	1.36
		Avg			2.28				1.75	1.96	0.89
1	Dmax	1	0.25	0.106	1.57	1.6	0.7	1.00	1.60	1.56	1.14
		2	0.26	0.097	3.23	2.5	0.8	1.00	2.50	1.56	1.79
		Avg			2.40				2.05	1.96	1.05

Finally, Table 3.12 summarizes the results for the 1- and 2-story D_{min} archetypes when they are arranged into performance groups. Every performance group for these systems passes the $ACMR_{10\%}$ requirement.

Table 3.12: Analysis Results for 1- and 2-Story SDC Dmin Masonry Archetypes Arranged into Performance Groups

R	SDC	No. of stories	T (sec)	T1 (sec)	Static Ω	CMR	μ_T	SSF	ACMR	AACMR	ACMR/AACMR
8	Dmin	1	0.25	0.108	2.58	1.6	6.4	1.12	1.80	1.56	1.15
		2	0.28	0.099	6.33	2.8	7.3	1.13	3.17	1.56	2.03
		Avg			4.45				2.49	1.96	1.27
6	Dmin	1	0.25	0.108	1.93	1.6	6.4	1.12	1.80	1.56	1.15
		2	0.28	0.099	4.75	2.8	7.3	1.13	3.17	1.56	2.03
		Avg			3.34				2.49	1.96	1.27
4	Dmin	1	0.25	0.108	1.29	1.6	6.4	1.12	1.80	1.56	1.15
		2	0.28	0.099	3.17	2.8	7.3	1.13	3.17	1.56	2.03
		Avg			2.23				2.49	1.96	1.27
2	Dmin	1	0.25	0.108	1.02	1.9	4.2	1.09	2.08	1.56	1.33
		2	0.28	0.099	1.58	2.8	7.3	1.13	3.17	1.56	2.03
		Avg			1.30				2.62	1.96	1.34
1	Dmin	1	0.25	0.108	0.73	2.2	2.5	1.07	2.35	1.56	1.56
		2	0.28	0.099	1.55	3.4	2.5	1.07	3.64	1.56	2.40
		Avg			1.14				3.00	1.96	1.53

Similar to the method that was used to develop the plots for the SDOF study, curves were developed for the masonry shear wall models to describe the effect of design period, C_uT_a, and design R value on the probability of collapse and the inelastic versus elastic displacement ratios for the MCE level ground motion. Figure 3.15 and Figure 3.17 shows the probability of collapse for the D_{max} and D_{min} configurations, respectively. From these curves, it evident that as the

design period decreases, the probability of collapse increases. This tends to confirm the trends observed in the SDOF study described above. The probability of collapse drastically increases when going from the 2-story to the 1-story archetypes.

Figure 3.16 and Figure 3.18 show the ratio of inelastic to elastic roof displacements for the D_{max} and D_{min} configurations, respectively. Again, these curves show similar trends to those seen in the SDOF study, with the displacement ratios increasing as the design period decreases. These ratios also undergo a drastic spike when going from the 1-story to the 2-story archetypes. This would indicate that these systems do not follow the equal displacement concept.

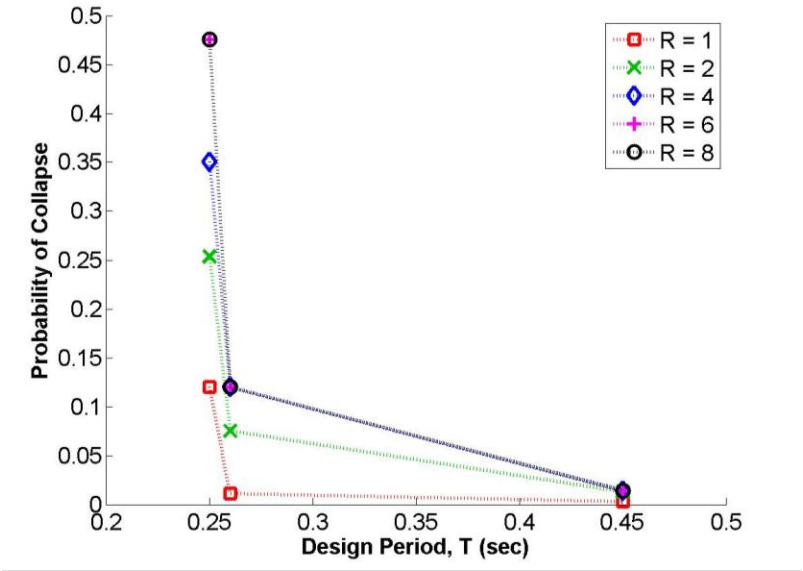

Figure 3.15: Probability of collapse for Dmax archetypes.

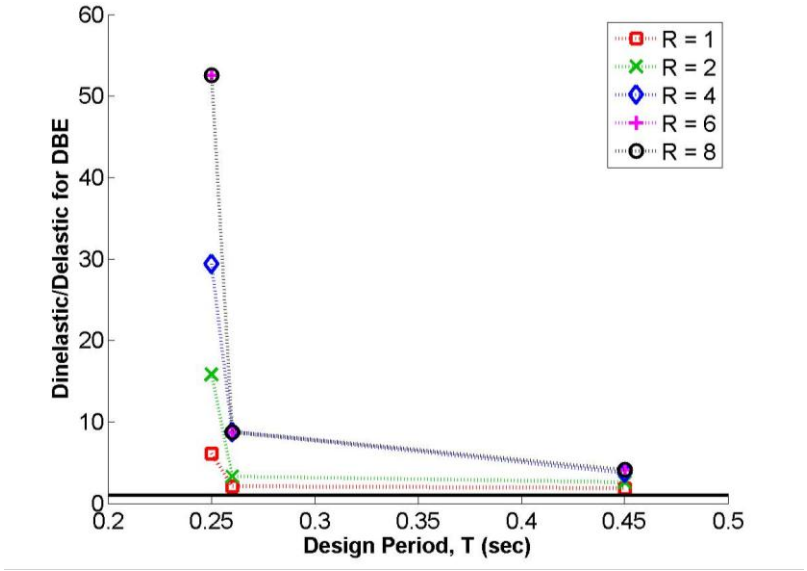

Figure 3.16: Roof displacement ratios for Dmax.

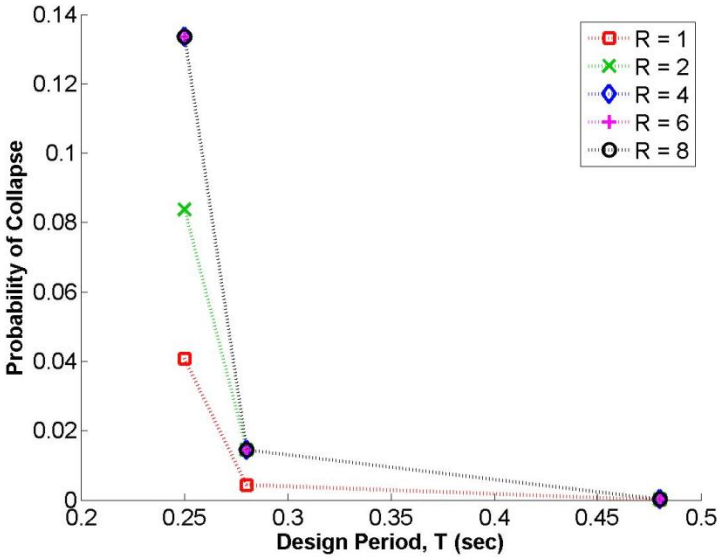

Figure 3.17: Probability of collapse for Dmin.

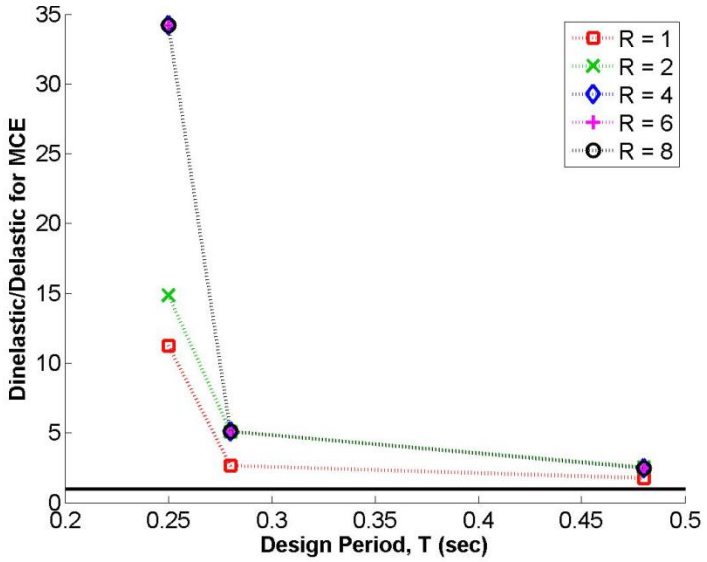

Figure 3.18: Displacement ratios for Dmin.

3.4 Conclusions

Previous studies using the FEMA-P695 methodology found that short period systems tended to have a greater probability of collapse than longer period archetypes of the same system. The SDOF study and the Masonry Study were performed to build on the understanding of the behavior of these short period systems and to establish general trends based on the period of vibration. These two studies yielded very similar results, which are summarized below:

1. In general, both studies showed that the probability of collapse increases as the natural period decreases for systems designed for the same response modification factor, *R*.

2. For archetypes with natural periods less than 0.6 seconds, the ratio of inelastic displacement to elastic displacement for the system exceeded 1.0. This shows that short period systems do not follow the equal displacement concept. Even further, as the natural period fell below 0.3 seconds, this ratio reached 10 or greater, indicating inelastic drifts were a full order of magnitude greater than expected.

3. Systems with natural periods larger than 0.6 seconds had calculated *R* values that plateaued and remained relatively consistent. This signified that a single design *R* value

could be used independent of the natural period for systems with natural periods greater than 0.6 seconds. These findings were generally supported by the masonry study results as well.

4. In order to maintain a probability of collapse of 10% in 50 years or better, the *R* value needs to vary with the natural period of the system at very short natural periods. The SDOF study showed that this *R* value should be 1.0 for systems with natural periods less than or equal to 0.2 seconds and transition up to the structural system's long period value at periods of 0.6 seconds.

These results tend to indicate that the response modification factor for structures with natural periods less than 0.6 seconds should be decreased as the natural period decreases. However, at this stage in the development of the FEMA P-695 methodology, there are concerns with its implementation that should be addressed prior to making wholesale changes to the design paradigm for seismically resistant structures. Chief among these concerns is the determination of the collapse parameters for a structural system. As has been noted in the NIST GCR 10-917-8 (NIST 2010), some of the collapse parameters that were defined occurred well before that system would actually collapse. In other cases, significant losses in system strength that could lead to a progressive collapse were not identified as a collapse parameter. Because the probability of collapse determined by the FEMA P-695 methodology is very sensitive to the definition of the collapse parameters, these issues should be further investigated before significant changes are made to the design process.

Another concern stems from the fact that all of these models assume a fully rigid foundation. This is an unrealistic boundary condition that could be playing a significant role in the behavior of these short period systems. If foundation flexibility were considered, some of the archetypes may experience an elongation in natural period that pushes these configurations outside of the short-period range. This concern falls in line with the argument that the short period problem has only been identified by computational analyses and that there is little experimental or post-earthquake findings to support the problem. Foundation flexibility may be one of the factors that

contribute to this fact. Because of this, further studies should be conducted to understand how foundation flexibility affects the behavior of systems with very short periods.

3.5 Recommendations for *R* Factor Reformulation

The NIST report that resulted from the ATC-84 project, GCR 11-916-16 (NIST 2011), presents a reformulation for the development of *R* factors. In this formulation, a value of *R* is determined for the MCE level ground motion based on a product of a ductility component and an overstrength component. This version of *R*, designated R_M, is given by the following equation:

$$R_M = R_{Md} R_o \qquad 2.1$$

The recommended changes to the *R* factor for structures at short periods that are presented here were developed by Dr. Finley Charney at Virginia Tech. These changes would be applied to the ductility portion of this formulation, R_{Md}. A reduction in R_{Md} would be made to accommodate the fact that the masonry investigation indicated that a design value of R=1 is required for systems with an extremely short period (T_1 < 0.1 seconds). However, it has been recognized that there are a number of limitations associated with this study that would need to be further investigated prior to the implementation of these recommendations. These limitations include:

- Approximations used in modeling masonry shear walls, such as the horizontal springs that were used to account for shear displacements, need to be validated through experimental investigation.

- Improved methods for defining non-simulated collapse need to be developed. The definition of these limits can have a significant effect on the results of a FEMA P-695 study and current definitions do not always represent a situation that would cause collapse of a building structure.

- The influence of additional forms of system flexibility needs to be incorporated into the model. These include, but are not limited to, structure soil interaction, diaphragm

flexibility, and foundation flexibility. Incorporation of one or more of these items may pull some of the structures with short period behavior outside of realm where it is truly an issue.

For these reasons, the following formulation is recommended in a general sense, but would require further investigation with more robust models and collapse criteria before they should be implemented in design.

Figure 3.19 shows five possible curves for period dependent values of R_{Md}. The current design approach, where the same value for the response modification factor is applied for all periods, it represented by the flat line at $R_{Md,max}$. The first approach to short period adjustments assumes that a uniform probability of collapse across all periods is desired. If this is the case, the value of R_{Md} would follow a curve similar to the two that vary with the natural period of the structure. When the natural period falls below T_{min}, R_{Md} would be set equal to 1.0. This would imply that the structure is designed to remain elastic during a strong ground motion. Then, R_{Md} could transition up to $R_{Md,max}$ at a natural period equal to T_{max}. The first curve, shown with a solid line, indicates that $R_{Md,max}$ would be set equal to the current design value such that there would be no change to the design of structures with a natural period longer than T_{max}. However, it was recognized that for all design values of R, the masonry models showed very low probability of collapse for the four story designs. This indicates that the current values may be conservative and that these FEMA P-695 studies could lead to an increase in the design R value for longer period structures.

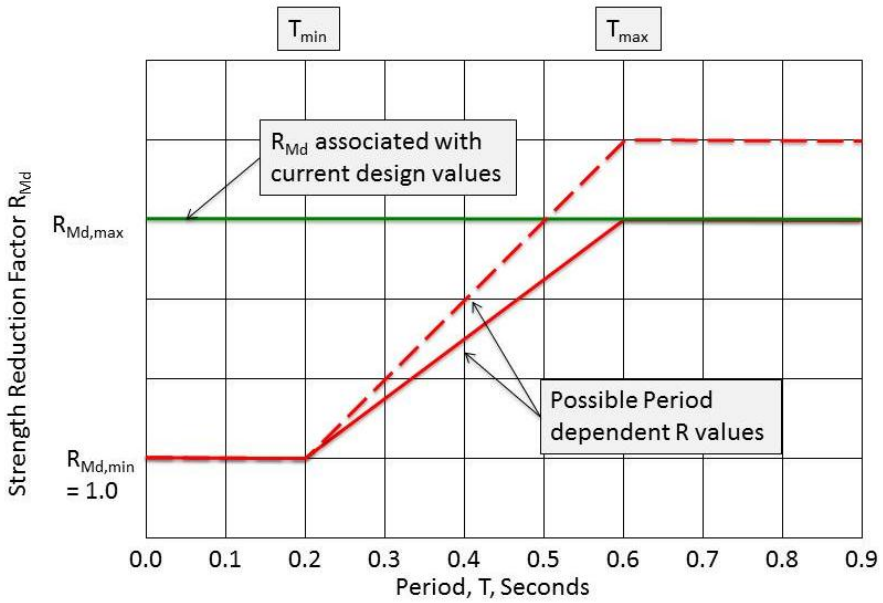

Figure 3.19: Period Dependent Values of R_{Md}

The lines in Figure 3.19 are defined mathematically as:

For $T \leq T_{min}$ $$R_{Md} = R_{Md,\min} \quad (2.2)$$

For $T_{min} \leq T \leq T_{min}$ $$R_{Md} = R_{Md,\min} + [R_{Md,\max} - R_{Md,\min}]\frac{T - T_{\min}}{T_{\max} - T_{\min}} \quad (2.3)$$

For $T \geq T_{min}$ $$R_{Md} = R_{Md,\max} \quad (2.4)$$

In Figure 3.19, values are given based on values of T_{min} = 0.2 seconds and T_{max} = 0.6 seconds. These values are used here because these are the periods where significant changes in behavior were seen during these analyses, however further investigation overcoming the limitations listed above could lead to a shift in these values.

In addition to the recommended adjustment to the response modification factor, it is also necessary to formulate a short period deflection amplification factor, C_{ds}. This would be an additional factor used to amplify the calculated elastic drifts according to the equation:

$$\delta_{inelastic} = C_{ds} C_d \delta_e \qquad 2.5$$

where.

$\delta_{inelastic}$ = amplified inelastic displacements

δ_e = elastic displacement computed under strength-level design earthquake forces

C_d = deflection amplification factor currently employed by ASCE 7

C_{ds} = short period deflection amplification factor

Figure 3.20 shows the possible curves for this new factor. If one of the period dependent curves in Figure 3.19 is utilized to determine the response modification factor for a system, the system would be designed to behave elastically at periods less than T_{min}, which would correspond to a displacement modification factor of 1.0. Similarly, C_{ds} for systems with periods greater than 0.6 seconds would also be 1.0. In this way, the flat curve in Figure 3.20 gives the displacement magnification that would be required for systems that have been designed using using a period dependent value of R_{Md}.

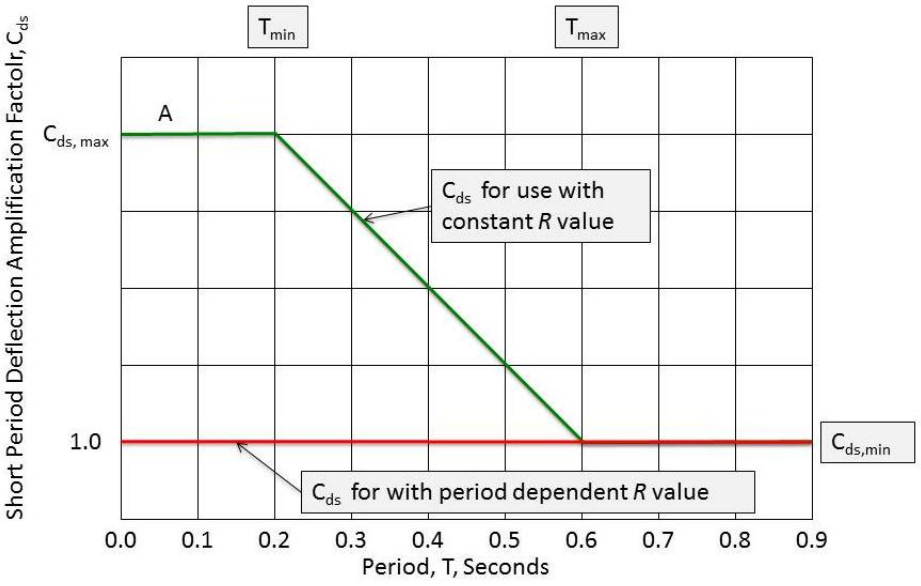

Figure 3.20: Period dependent values for C_{ds}

However, if R_{Md} is held constant regardless of period (the current design practice shown in Figure 3.19), it is necessary to increase the displacement magnifier for systems with short periods ($T < T_{min}$). This increase is given by curve A in Figure 3.20 and is described mathematically using the following equations.

For $T \leq T_{min}$ $$C_{ds} = C_{ds,\max}$$ 2.6

For $T_{min} \leq T \leq T_{min}$ $$C_{ds} = C_{ds,\max} - [C_{ds,\max} - C_{ds,\min}] \frac{T - T_{\min}}{T_{\max} - T_{\min}}$$ 2.7

For $T \geq T_{min}$ $$C_{ds} = C_{ds,\min}$$ 2.8

The use of a period dependent response modification factor in design could have significant impacts on the economy of the design of structures with very short periods because the system is being designed to remain elastic. This severe of a penalty may not be justifiable at this stage due to the limitations in the modeling and definition of collapse criteria in these studies. In these cases, intermediate combinations of decreased response modification and increased deflection amplification may be employed. This would allow for more economical designs because R_{Md} would not be reduced to the minimum value of 1.0, but it would decrease the probability of collapse for structures at these natural periods. However, appropriate intermediate values are not clear at this stage because of the research limitations and further research is required before any approach is worked into the code. This additional research would also need to focus significant efforts on the development of the upper and lower bounds of R_{Md} and C_{ds}.

3.6 Future Studies

For future studies into the handling of the short period problem within the confines of the FEMA P-695 methodology, it is recommended that more robust mathematical models be developed to fully describe the behavior of the system. These models need to be experimentally verified to ensure that they are accurately representing additional forms of system flexibility and that any assumptions made are valid. Additionally, collapse metrics should be improved upon for the FEMA P-695 methodology. System performance can be very sensitive the limits defined for

non-simulated collapse and there is currently not a significant amount of guidance on how to define them. This has resulted in a subjective decision process where limits used may not represent a time where the physical system would have collapsed. Continued development and use of the FEMA P-695 methodology will help define guidelines for developing these metrics for all systems.

Chapter 4. Preliminary SC-TMF Investigations (STESSA Paper)

The following paper was developed for the 2012 Conference on the Behavior of Steel Structures in Seismic Areas (STESSA) which was held from January 8, 2012 to January 12, 2012 in Santiago, Chile. This paper describes the preliminary investigations into the SC-TMF that provided a basis for the mechanics investigation that is described in the next chapter. This paper has been reformatted for this document, but can be found in its original format in the STESSA 2012 Conference Proceedings.

Self-centering truss moment frame with replaceable energy-dissipating elements

S.C. Darling & M.R. Eatherton
Charles E. Via Department of Civil and Environmental Engineering, Virginia Polytechnic Institute and State University, Blacksburg, VA, USA

ABSTRACT: A self-centering steel truss moment frame (SC-TMF) has been developed that is capable of resilient performance during large earthquakes, virtually eliminating residual drifts, concentrating structural damage in replaceable elements, allowing design flexibility to separately tune strength, stiffness, and ductility, and can be shop fabricated allowing conventional field construction methods all while utilizing approximately the same amount of steel as conventional moment frames. The truss chords consist of precompressed concentric tubes that allow for gap openings as the truss undergoes racking deformations. Post-tensioning strands act to close the gaps while replaceable fuse elements dissipate seismic energy. The SC-TMF was investigated by subjecting a nonlinear prototype building model to a suite of ground motions. The results show that the SC-TMF is a viable seismic force resisting system for reducing structural damage due to large earthquakes and can limit cost and time required to make a building operational following a strong ground motion.

4.1 Introduction

4.1.1 Context

Traditionally, earthquake engineering has focused on protecting the lives of building occupants. Conventional seismic force resisting systems use inelasticity in structural members and connections to dissipate seismic energy and provide protection against collapse. A consequence of this design methodology is that conventional seismic systems do not explicitly limit the amount of structural damage, or offer a repair method that allows continued use of a structure after an earthquake. In fact, the structural damage distributed throughout a building and permanent residual drifts can make a conventional structure difficult if not financially unreasonable to repair after a large earthquake.

In the past two decades there have been significant advances in the development of self-centering seismic force resisting systems that satisfy performance criteria based on limiting costs associated with structural repair and business downtime. However, examples of self-centering systems used in practice are limited [e.g. (Mar 2010)] because difficult or complex field construction is required, there are challenges associated with deformation compatibility, or they are not economically competitive with conventional systems. Even though a handful of self-centering systems have been developed, they will not have the ability to reduce earthquake losses until the performance advantages outweigh the associated costs and challenges leading to more widespread implementation in practice. In addition to satisfying performance goals related to structural repairability after earthquakes, self-centering systems need to be accessible to the construction industry, not cause deformation incompatibility, and be economically competitive with conventional systems.

4.1.2 Self-Centering Seismic Systems

Self-centering (SC) seismic systems found in the literature may be categorized into three primary groups: SC rocking frame systems, SC moment frames, and SC braces. SC moment frames and butterfly fuse plates are examined further here for their relationship to the self-centering truss system.

SC moment resisting frame (MRF) systems with horizontal post-tensioned elements have been studied for concrete MRFs and coupled walls and for steel MRFs [e.g. (Ricles et al. 2001)]. As shown in Figure 4.1, the horizontal post-tensioning elements clamp the beams to the columns. During an earthquake, the post-tensioned connections decompress and develop a gap-opening that leads to effective softening of the system without structural damage. The SC capability is provided by the post-tensioning elements acting to close the gap and energy dissipation is provided using supplemental elements, such as yielding angles or friction dampers.

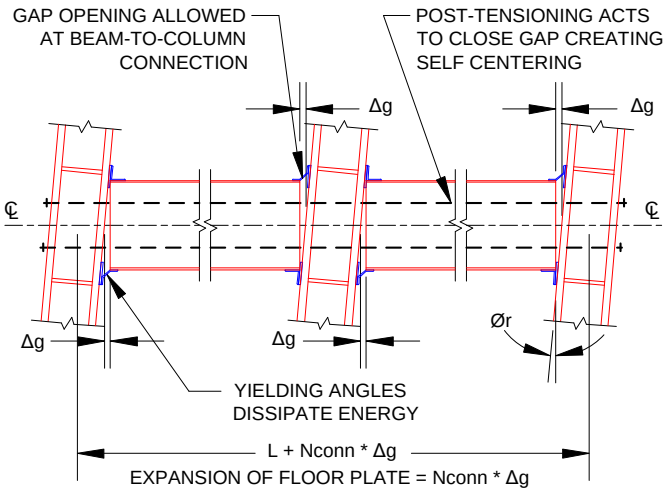

Figure 4.1: Self-Centering Steel Moment Frame with Horizontal Post-Tensioning

However, the gap opening at the beam-to-column connection causes the centerline of the beam to displace relative to the face of the column, Δ_g. As shown in Figure 4.1, the gap openings have the cumulative effect of increasing the width of the moment frame by $\Delta_g * N_{conn}$, where N_{conn} is the number of beam-to-column connections. Schemes for accommodating the expansion of the floor plate [e.g. (Garlock and Li 2008)], require the SC moment resisting frames to be located at the building perimeter, the diaphragm to be disconnected along large lengths of the moment resisting frame, and special detailing to allow horizontal frame expansion.

Steel butterfly fuse plates were designed and tested as part of a controlled rocking steel frame system [e.g. Ma 2010 (Ma 2010)]. The plates employ diamond shaped cutouts leaving butterfly shaped links as shown in Figure 4.2. The butterfly fuse plates were shown to have stable full

hysteretic behavior without fracture up to shear strains across the link length of 30% to 46% (Ma 2010).The significant ductility without fracture is attributed to the geometry which causes the initiation of yielding and plastic hinging at the link quarter points, away from areas of discontinuity, and smooth cut surfaces achieved using water jet or laser cutting. Furthermore, thicker non-buckling fuse plates were shown to have little degradation in strength or stiffness after being subjected to deformation histories consistent with multiple large earthquakes(Eatherton et al. 2010). It was concluded that fuse plates that resist buckling and do not experience shear strains in excess of 15% across the link length will not need to be replaced even after large earthquakes (Eatherton 2010).

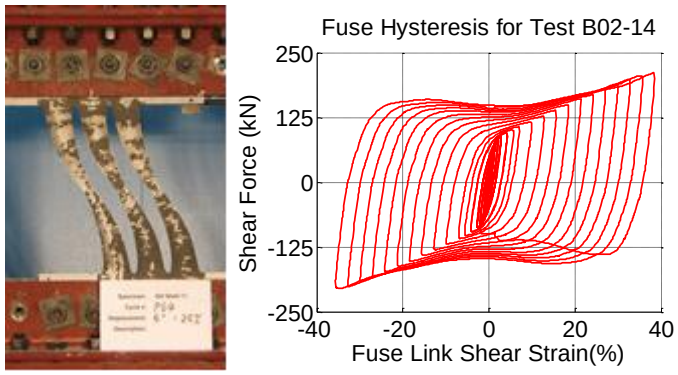

Figure 4.2. Deformed Butterfly Fuse Plate and Resulting Hysteretic Response [from (Eatherton 2010)] [Used with kind permission of M. Eatherton, 2012]

4.1.3 Scope of Paper

A self-centering truss moment frame (SC-TMF) has been devised which offers advantages in constructability, seismic performance, and competitiveness over most currently available self-centering systems. Preliminary design and analyses presented below demonstrate that the SC-TMF eliminates residual drifts, concentrates structural damage in fuse plates which will not need to be replaced after most earthquakes, allows design flexibility to separately tune strength, stiffness, and ductility, can be shop fabricated allowing conventional field construction methods, and utilizes approximately the same amount of steel as conventional moment resisting frames.

This paper describes the concepts related to the design and behavior of the system, development of a computational model, and a computational study used to investigate the application of the system to a prototype building.

4.2 Self-centering truss moment frame configuration and behavior

4.2.1 Concept and Configuration

The SC-TMF uses a truss configuration with precompressed concentric tubes in conjunction with highly ductile and resilient steel butterfly fuse plates to create a moment resisting frame with superior seismic performance. The SC-TMF system is shown in Figure 4.3 as subjected to lateral loads (bending deformations have been neglected for clarity). The elements inside the bottom chord are shown in Figure 4.3 to demonstrate the five main components:

1. A Pratt truss with X-web diagonals in the end panels and a Vierendeel middle panel. The web members connect the top chord to the outer tube at the bottom chord. The truss causes the bottom chord outer tube, which is not connected to the columns, to move laterally in unison with the top chord.

2. The bottom chord inner tube is connected to the columns and moves laterally relative to the outer tube as the column rotates relative to the truss.

3. Post-tensioning strands precompress the concentric tubes and acts to keep the inner and outer tube in alignment.

4. Free floating anchorage plates slide over the end connections, but are held in place by the post-tensioning force. During lateral loading, the inner tube bears on the anchorage plate at one end (the left end in Figure 4.3), while the outer tube bears on the anchorage plate at the other end (the right end in Figure 4.3) creating gap openings between the tubes and anchorage plates at both ends.

5. Butterfly steel fuse plates dissipate seismic energy through plastic flexural and shear deformations in the links. The bottom of the fuse plate connects to the inner tube and thus moves laterally relative to the top chord. The outer tube is slotted around the fuse plate to allow the fuse to move freely with the inner tube.

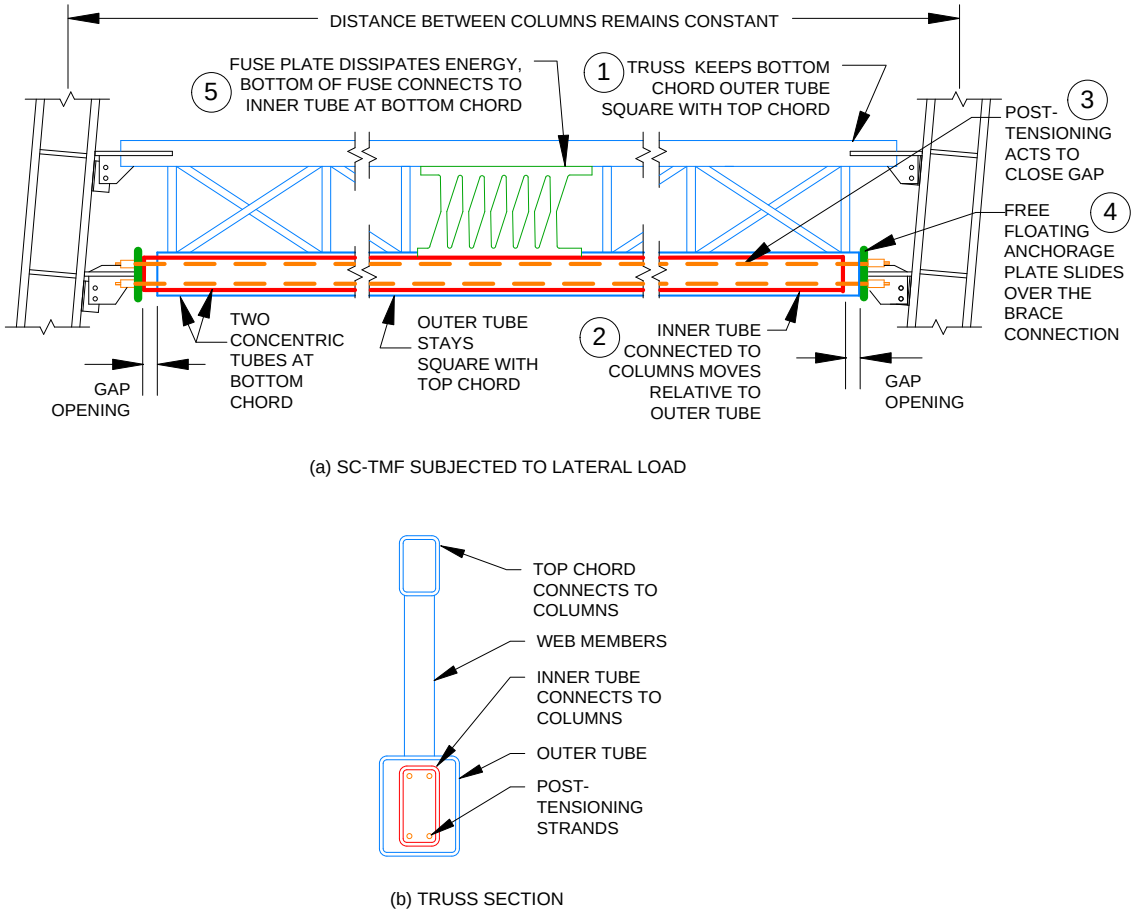

Figure 4.3: Drawing of SC-TMF Configuration

As shown in Figure 4.4, during earthquake loading, gap openings form between the anchorage plates and the tubes, seismic energy is absorbed by the fuse plate, and the post-tensioning acts to

bring the truss back to its original configuration. Unlike currently available SC moment frames, the distance between the columns remains constant throughout the loading process.

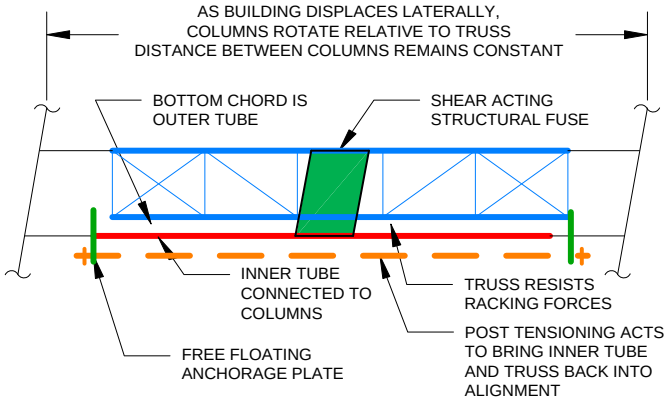

Figure 4.4. Schematic Diagram of SC-TMF Behavior

4.2.2 Preliminary Design Concepts

A preliminary design methodology has been developed for the design of the SC-TMF. First, a 2D elastic model with trusses replaced by frame elements is used to determine the moment demand in the truss and required moment of inertia to meet deflection criteria.

The post-tensioning and fuse elements are then proportioned to possess the required moment capacity from the 2D elastic model. The contribution to moment capacity from the post-tensioning elements is equal to the chord centerline to centerline depth of the truss times the total pretension force. The contribution to moment capacity from the fuse element is equal to the shear capacity of the fuse times the depth of the truss. The total moment capacity of the system is equal to the combination of these two contributions.

Because the stiffness of the system prior to gap openings is governed by the elastic stiffness of the tubes, the three tubes can be directly proportioned to develop the required moment of inertia. Additionally, the tubes must be designed to resist buckling due to initial post-tensioning (completely unbraced) and peak post-tensioning force (shorter unbraced length).

The fact that the strength and stiffness are developed in different elements of the cross-section represents a departure from design of conventional moment frames in which the beams are typically overdesigned for strength because deflections control. The ability to tune strength and stiffness separately allows efficient use of materials.

4.3 Expected Global Behavior

The expected behavior of the system as subjected to cyclic loading is shown in Figure 4.5 through Figure 4.7. The truss rotation shown on the horizontal axis is defined as the angle of the truss relative to the columns. Figure 4.5 shows an idealized elastic plastic contribution of the fuse element. The post tensioned truss contribution is shown in Figure 4.6 to exhibit a bilinear elastic response. When the two contributions are combined in parallel, the resulting hysteretic behavior is a flag shape shown in Figure 4.7 which is characteristic of SC systems. When the load is removed, the truss rotation returns to a near zero state. Points in the response associated with stiffness changes or events in the response are labeled with letters and summarized in Figure 4.7.

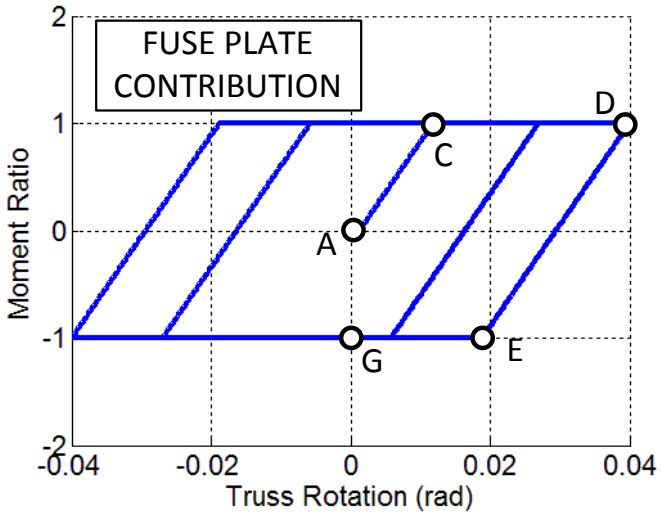

Figure 4.5. Fuse Plate Response Due to Cyclic Loading

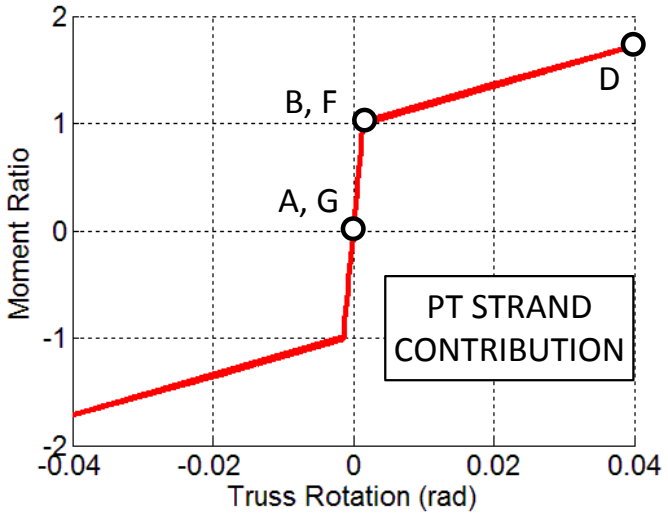

Figure 4.6. Post-Tensioning Response Due to Cyclic Loading

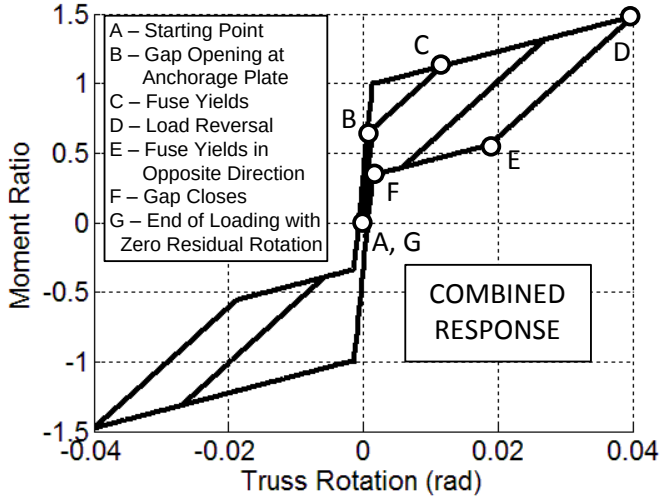

Figure 4.7. Combined Response of the SC-TMF System

4.4 Computational model

The computational model shown in Figure 4.8 was created using OpenSees software (Mazzoni et al. 2005) and was constructed in three stages. First, the columns, truss, and concentric tubes were created using elastic beam-column elements with six degrees of freedom (DOF)g to simulate fully welded connections. Post-tensioning strands were modeled using an elastic truss element with an initial stress representing the pretension force. Gap elements that are stiff in

compression, but have zero stiffness in tension were placed between the ends of the bottom chord tubes and the ends of the post-tensioning element to simulate the behavior of the free floating anchorage plates. The butterfly steel fuse plate with the hysteretic shear behavior shown in Figure 4.5 was simulated with an elastic-perfectly plastic spring.

Initially, the right column is able to move horizontally relative to the left column. Next, the pretension force is allowed to equilibrate throughout the system. Finally, the boundary conditions of the right column are redefined to represent the boundary conditions of the system after the truss is installed.

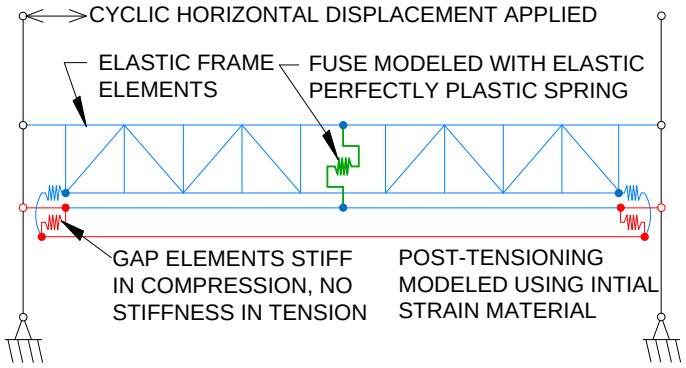

Figure 4.8. Schematic Diagram of SC-TMF OpenSees Model

4.5 Prototype building

The prototype building is shown in Figure 4.9 and Figure 4.10. This prototype was used in research to evaluate the FEMA P-695 (FEMA 2009) methodology for special steel moment frames (SMRF) (NIST 2010). Utilizing this prototype will provide a basis for comparison between the SC-TMF and conventional moment frames already analyzed. Seismic loads were calculated with an equivalent lateral force design procedure. Following the procedures in FEMA P-695, the value for C_d was set equal to R which was assumed to be 8. A 2D elastic analysis was performed using commercially available software with frame elements to calculate truss moments and required moment of inertia to limit deflections.

The required moment capacity and moment of inertia were used with the design concepts discussed above to develop SC-TMF 1 and 2. SC-TMF 1 is 61cm (24in) deep from chord centerline to centerline and consists of a HSS6x6x3/8 top chord, a HSS 8x8x3/8 bottom chord inner tube, and a HSS10x10x1/4 bottom chord outer tube. It has (9) ½" 7-wire post-tensioning strands, initially stressed to 40% of ultimate, and a fuse with 535kN (120 kip) shear capacity. SC-TMF 2 is 56cm (22in) deep from chord centerline to centerline and consists of a HSS6x6x1/4 top chord, a HSS 7x7x3/8 bottom chord inner tube, and a HSS9x9x1/4 bottom chord outer tube. It has (8) ½" 7-wire post-tensioning strands, initially stressed to 33% of ultimate, and a fuse with 360kN (80 kip) shear capacity.

It is emphasized that the tubes are intended to have the same moment of inertia as the SMRF beam in the NIST report and as a result the area of steel was similar between the SMRF and SC-TMF. It is expected that the amount of steel and therefore the cost of the SC-TMF will be similar to that of a conventional moment frame.

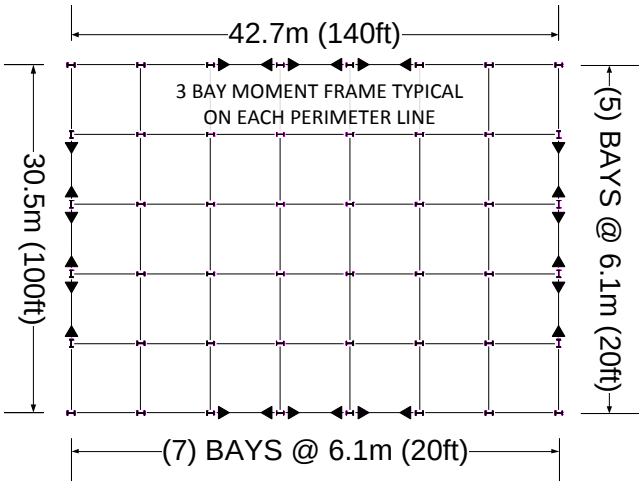

Figure 4.9. Prototype Building Plan View

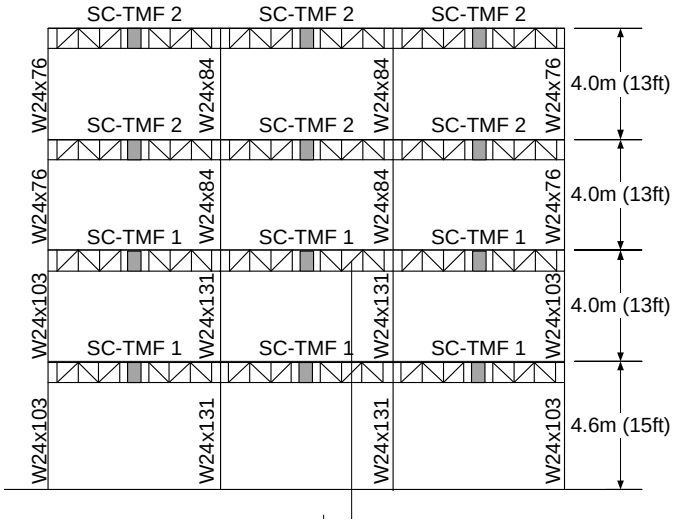

Figure 4.10. 4-Story Prototype Building Elevation View

4.6 Prototype building performance

The center bay of the resulting design was modeled using OpenSees. The truss at each floor was modeled as shown in Figure 4.8 and described above. The model was then subjected to the ATC-63 suite of ground motions and the behavior was analyzed.

The behavior of the prototype frame during a sample earthquake is presented in Figure 4.11 and Figure 4.12. The sample earthquake ground motion is from the 1994 Northridge Earthquake record from the Beverly Hills-Mulholland recording station and has been scaled to the 10% in 50 recurrence level at a period of 1 second using the FEMA P-695 scaling procedure. Figure 4.11 shows the roof drift ratio with respect to time. The self-centering behavior of the system is depicted by the fact that at the end of the ground motion the roof drift is centered about zero.

The hysteretic behavior of the first floor truss is shown in Figure 4.12 by plotting the gap opening ratio against the moment ratio. The gap opening ratio is the ratio of the gap opening to the depth of the truss between chord centerlines. The moment ratio is the ratio of the applied moment to the moment capacity calculated using the preliminary procedures outlined above. The hysteretic behavior of the system is the flag shaped that is characteristic of systems with energy dissipating and self-centering capabilities.

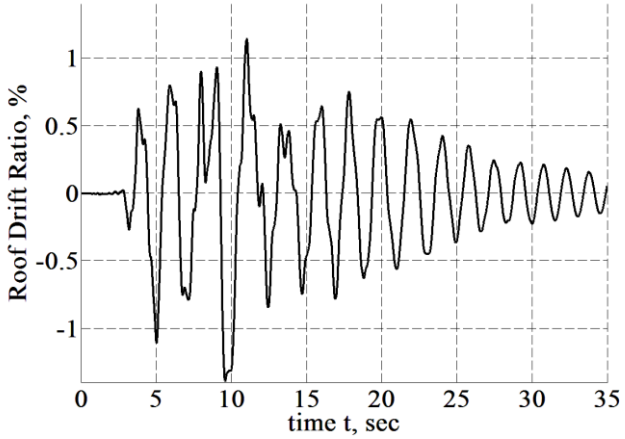

Figure 4.11. Roof Drift Ratio for Sample Time History Analysis

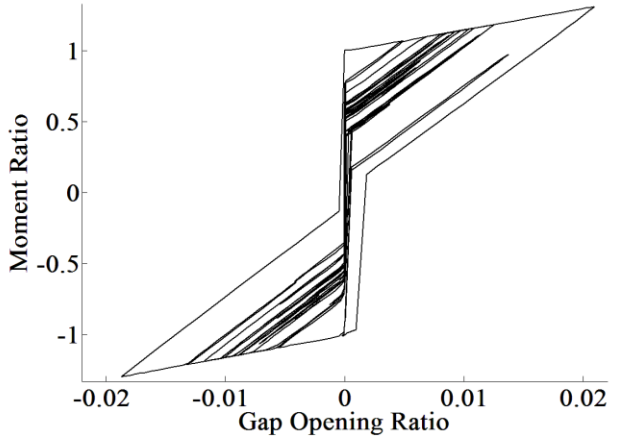

Figure 4.12. First Floor SC-TMF Response to Sample Time History Analysis

The prototype building model was subjected to the full ATC-63 far field ground motion suite. The 44 ground motion set was scaled using the FEMA P-695 methodology based on 1 second period for the earthquake that has a 10% probability of exceedance in 50 years. The resulting response spectra are shown in Figure 4.13 for each ground motion and the median of the ground motions as compared to the design response spectrum.

Figure 4.14 shows the median drift ratio and median residual drift ratio at each floor for the time history analyses. The drift ratio is the drift divided by the height at that level. Figure 4.14 demonstrates that the peak drift ratios are similar to that expected for conventional moment frames, but the residual drifts are near zero. It is shown that residual drifts one standard deviation

above the median is about 0.3% drift ratio at upper floors. This falls below the limit at which structures are generally not economical to repair.

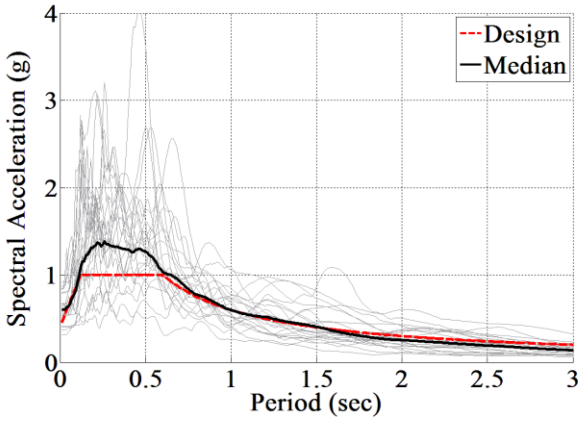

Figure 4.13. ATC-63 Response Spectrum Scaled to T = 1sec for a 10% in 50yr EQ

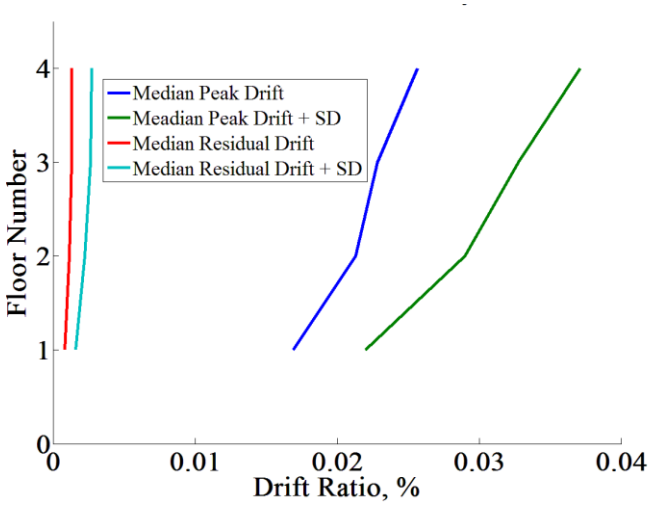

Figure 4.14. Median Peak Drift Ratio and Residual Drift Ratio for ATC63 Ground Motion Set Scaled to 10% in 50 Year

4.7 Conclusions

The self-centering truss moment frame is a new self-centering seismic force resisting system. It utilizes concentric tubes at the bottom chord to create gap openings during a strong seismic event. Post-tensioning is utilized to precompress the bottom chord and provide restoring force after gap openings occur. Replaceable butterfly fuses are used to provide energy dissipation and stable hysteretic behavior.

The SC-TMF utilizes a similar amount of steel while providing numerous benefits as compared to conventional moment frames. It produces a self-centering force that essentially eliminates residual drifts in the system. It also concentrates inelastic deformations into elements which can be replaced following a strong ground motion but may not need to be replaced after most earthquakes. Finally, during design, the strength and stiffness of the SC-TMF can be independently tuned to meet all necessary criteria allowing an efficient use of material.

A significant advantage of the SC-TMF system over other self-centering systems is that it does not develop deformation incompatibility common in other systems. Additionally, this system can be shop fabricated so that conventional construction techniques can be utilized in the field.

This research developed a preliminary design procedure for the SC-TMF which was in turn used to design a prototype building. A computational model of the system was developed using OpenSees and was subjected to time history analyses for the full ATC-63 ground motion set. These analyses confirmed that the SC-TMF provides the expected self-centering seismic performance.

4.8 References

Eatherton, M. *R.* and Hajjar J. F. 2010. Large-Scale Cyclic and Hybrid Simulation Testing and Development of a Controlled-Rocking Steel Building System with Replaceable Fuses. *Newmark Structural Engineering Laboratory Report Series*, Report No. NSEL-025..

Eatherton, M., Hajjar, J. F., Deierlein, G. G., Krawinkler, H., Billington, S., and Ma, X. 2010. Hybrid Simulation Testing of a Controlled Rocking Steel Braced Frame System. *9NCEE / 10CCEE,* Toronto, July 25, 2010.

FEMA. 2009. Quantification of Building Seismic Performance Factors. *FEMA P-695.* prepared by Applied Technology Council for the Federal Emergency Management Agency, Washington, D.C.

Garlock, M.E.M., and Li, Jie. 2008. Steel Self-Centering Moment Frames with Collector Beam Floor Diaphragms. *Journal of Constructional Steel Research.* Vol. 64, No. 5, pp. 526-538.

Ma, X. 2010. *Seismic Design and Behavior of Self-Centering Braced Frame with Controlled Rocking and Energy Dissipating Fuses.* Ph.D. Dissertation. Department of CEE, Stanford University, Stanford, California.

Mar, D. 2010. Design Examples Using Mode Shaping Spines for Frame and Wall Buildings. *9th National Conference of Earthquake Engineering.* Toronto, Canada, July 25-29.

Mazzoni, S., McKenna, F., Scott, M. H., and Fenves, G. L. 2005. *Open System for Earthquake Engineering Simulation User Command-Language Manual*, Berkeley, California.

NIST. 2010. Evaluation of the FEMA P-695 Methodology for Quantification of Building Seismic Performance Factors. *GCR 10-917-8*. Prepared by NEHRP Consultants Joint Venture for the National Institute of Standards and Technology

Ricles J., Sause *R.*, Garlock M., and Zhao C. 2001. Post-tensioned Seismic-Resistant Connections for Steel Frames. *ASCE Journal of Structural Engineering* Vol. 127, No. 2, pp. 113-121.

Chapter 5. System Refinement and Mechanics Investigation

The models discussed in Chapter 4 provided a great deal of insight into the behavior of the SC-TMF. In order to gain more in depth understanding of the system behavior, an investigation into the mechanics of how forces are transferred through the system was required. The purpose of this investigation was in part to develop equations to describe the system strength and stiffness throughout its different regimes of behavior. Prior to the mechanics investigation, the results of the preliminary modeling presented in Chapter 4 are analyzed and refinements are made to the system configuration and to the computational model.

5.1 Refinements in the Computational Model and Comparison with Conventional Moment Frames

The first challenge related to the preliminary modeling described in Chapter 4 dealt with the order in which members were modeled in OpenSees. As described above, these models were developed such that every member in the system was initialized prior to applying the post-tensioning force. Once the post-tensioning was applied, the boundary conditions were adjusted to their final configuration and the system was analyzed for earthquake loading. This had the unintended consequence of causing initial force in the members outside of the concentric tubes. Most notably, the end members along the bottom chord where resisting a substantial level of the prestressing force. This contradicted the expected behavior of the system because it is expected that the post-tensioning would be applied as part of the truss pre-fabrication process. This fact dictates that these end members would remain unstressed because there would be no column connection at the time of stressing.

In order to address this inconsistency between the model and the expected construction sequence, it was determined that a staged development of the model was required. To do this, the left column was first created in the model to provide boundary conditions for the truss during post-tensioning. Next, the full truss was built and connected to the left column and the post

tensioning was applied. A static analysis with zero external force was run to allow the post-tensioning to equilibrate into the concentric tubes. Then, the right column was connected to the truss at its deformed location. This staged construction worked as intended and prevented the forces in the system from transferring to the members outside of the concentric tubes. This fact is confirmed later in this chapter by Figure 5.11 through Figure 5.13, which show how forces develop in each chord member during a monotonic pushover analysis.

A second challenge came out of prototype building analysis described in Chapter 4. It was shown that the median displacements of SC-TMF during the nonlinear dynamic time history analyses reached levels similar to those allowed for Special Moment Resisting Frames (SMRF); however, many of the maximum displacements significantly exceed the expected levels. In order to gain a better understanding of why these excessive displacements occurred, an SMRF model was developed to allow comparison. This model utilized the member sizes that were reported in the NIST GCR 10-917-8 report (NIST 2010) for the prototype building for which the SC-TMF was designed. This system was modeled using concentrated plasticity frame elements with plastic hinge regions defined with cross sectional properties of the middle of the reduced beam section (RBS). Although this is a very simplified model for a SMRF with RBS connections, it provided a baseline comparison for the SC-TMF. This model was run for the same ground motions that the SC-TMF was analyzed for and example comparative response histories were developed.

Figure 5.1 shows a sample response history for one component from the 1992 Cape Mendocino ground motion recorded at the Rio Dell Overpass recording station (RIO360) scaled to the design basis earthquake (DBE) level. This is an example of the SC-TMF and SMRF with relatively similar levels of maximum displacement. Additionally, the SMRF begins to cycle about a displaced location and results in a large residual drift. In contrast, the SC-TMF cycles are centered about the origin and will self-center when the oscillations damp out. This figure clearly illustrates the advantages of the SC-TMF while maintaining similar levels of maximum displacement.

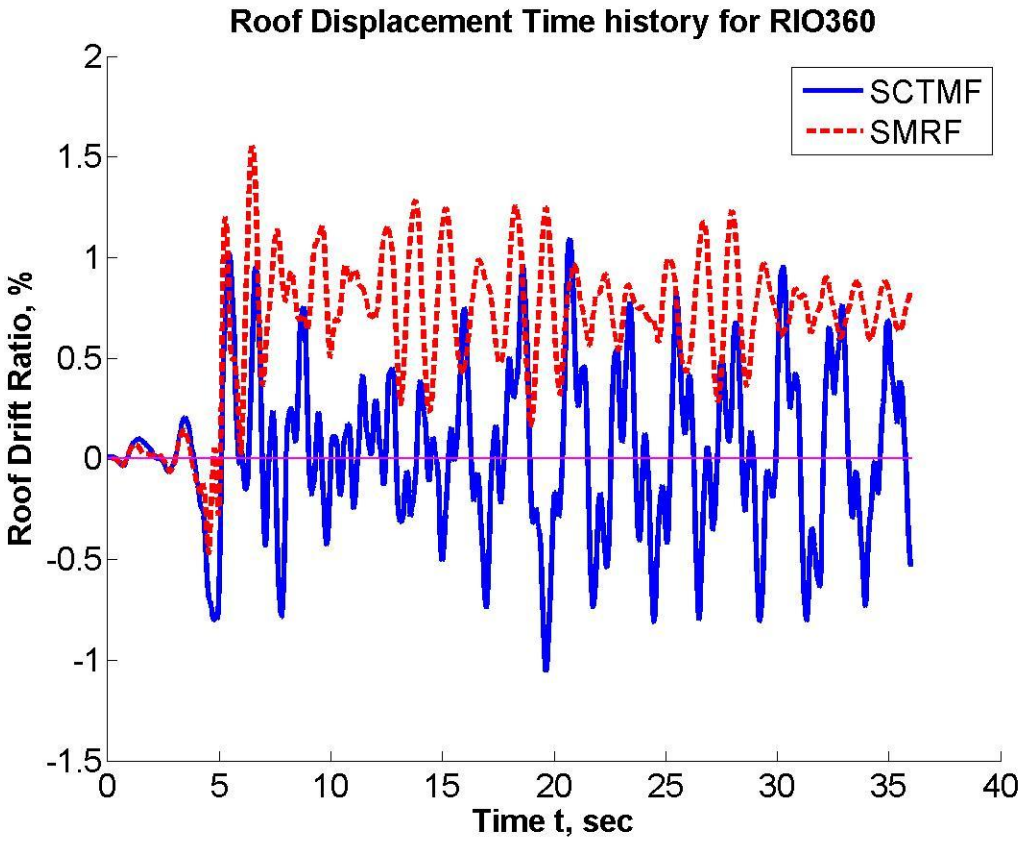

Figure 5.1: Response Histories for RIO360 Ground Motion Scaled to the DBE Level

Figure 5.2 shows the response history for one component of the 1999 Kocaeli, Turkey ground motion that was recorded at the Arcelik recording station (ARC000) scaled to the DBE level. In this figure, the SC-TMF displacements greatly exceed those of the SMRF. Here, the SMRF displacements remain rather small with limited residual drift. While the SC-TMF remains centered about the origin and would be expected to self-center, the maximum displacements are nearly three times those in the SMRF.

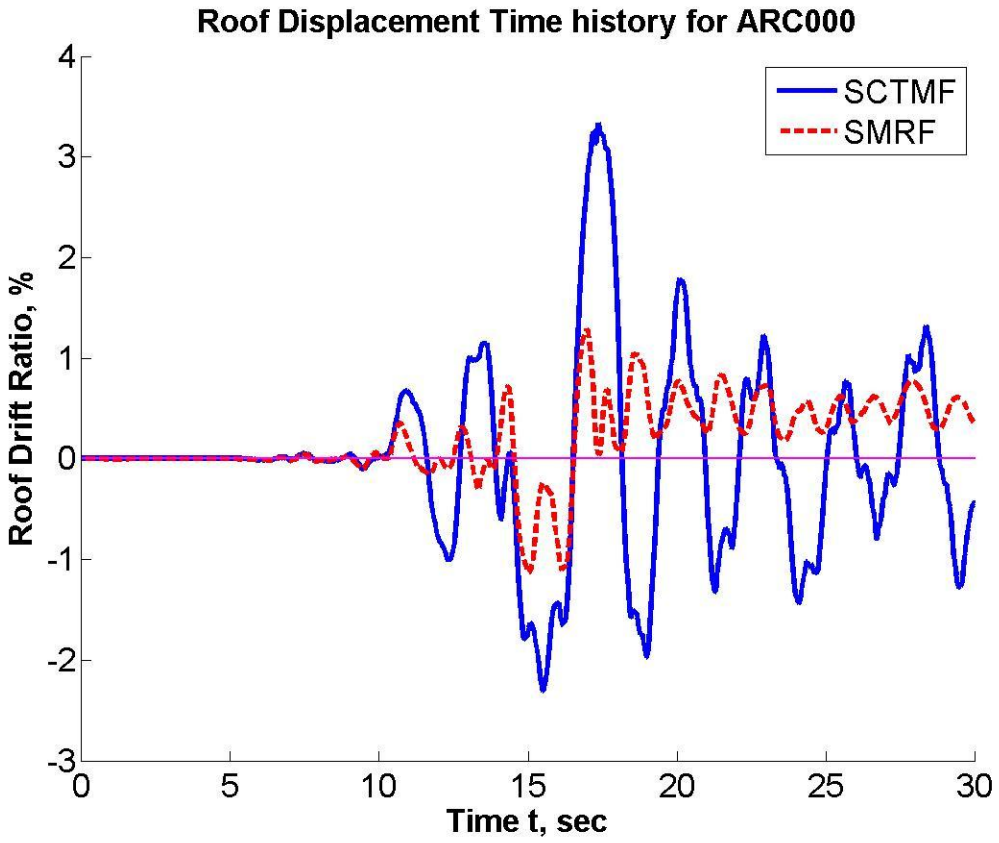

Figure 5.2: Response Histories for ARC000 Ground Motion Scaled to the DBE Level

By analyzing these comparative time histories, it was determined that the excessive deformations observed in the SC-TMF response could be explained by the relatively small secondary stiffness exhibited by the system. The initial stiffness of the SC-TMF is dependent upon the size of the truss members and is equivalent to the stiffness of a truss with no gap opening or post-tensioning. The SC-TMF and SMRF systems provide similar initial stiffness because the SC-TMF has been designed to have similar moment of inertia as the original SMRF design. The secondary stiffness of the SC-TMF is the stiffness of the system after gap opening occurs and is significantly less than the stiffness of the SMRF at the same point during the loading. Because of this, it was determined that providing a greater secondary stiffness would improve the global behavior of the SC-TMF and reduce earthquake related drifts.

A description of how the stiffness of the SC-TMF changes during loading is fully described in Section 5.6. Simply stated, the secondary stiffness in the SC-TMF is dictated by the size of the post-tensioning strands and the stiffness of the fuse elements in the system. The stiffness contributed by the post-tensioning is small relative to the stiffness contributed by the fuse elements. This means the only reasonable way to increase the secondary stiffness is to increase the contribution of the fuse elements. It was determined that efficiency of the butterfly-fuse plates in contributing stiffness to the overall system was being compromised by the elastic deformations within the truss. This fact created a need for a new configuration for the SC-TMF fuses that could eliminated the effect of the elastic truss deformations on stiffness contribution.

5.2 Alternative Fuse Configuration – Energy Dissipating Bars

The most promising fuse configuration was fuses at the ends of the bottom chord. This concept was based on the configuration for the SC-MRF, which places fuses at the beam to column connections and created more favorable stiffness behavior than the initial configurations of the SC-TMF. At each end of the bottom chord of the SC-TMF, there is relative movement between the outer tube and the column that is equal to the length of the gap opening at that location. By using a fuse to connect the outer tube to the column, these fuses allowed the stiffness of the SC-TMF to more closely mimic the stiffness behavior of the SMRFs. An additional advantage of this configuration is that the fuse is connected to the outer tube along the bottom chord. In contrast, the butterfly fuse plate was connected to the inner tube, which required a slot in the outer tube to provide access. By changing the fuse connection point, the truss fabrication process became significantly easier and the fuse is simpler to replace.

One such fuse that could span the gap between the outer tube and the column and that has been shown to provide stable hysteretic behavior is the buckling-restrained energy-dissipating (ED) bar. This fuse, which was first proposed by Christopoulos et al. (2002b), was developed for use at the end of the SC-MRF and behaves similar to a scaled version of the buckling restrained braces. Figure 5.3 shows a sample configuration of the ED bars that was tested by Christopoulos. The ED bars consist of a post-tensioning bar that is encased by a restraining

cylinder. The restraining cylinder is meant to prevent buckling of the post-tensioning bar and provide stable hysteretic behavior in tension and compression. In this case, the post-tensioning bar was a Dywidag No. 7 bar that restrained by a 1 inch diameter cylinder. Dywidag couplers are used to connect the bar at each end and would make it simple to replace these bars after a strong ground motion. In this component test, one ED bar was placed on each side of the plates to avoid eccentricities and the plates were pulled apart to simulate a gap opening. Only gap openings with tensile strains (as shown in Figure 5.3) were tested because these are the only type of strains that gap openings in a SC-MRF can develop.

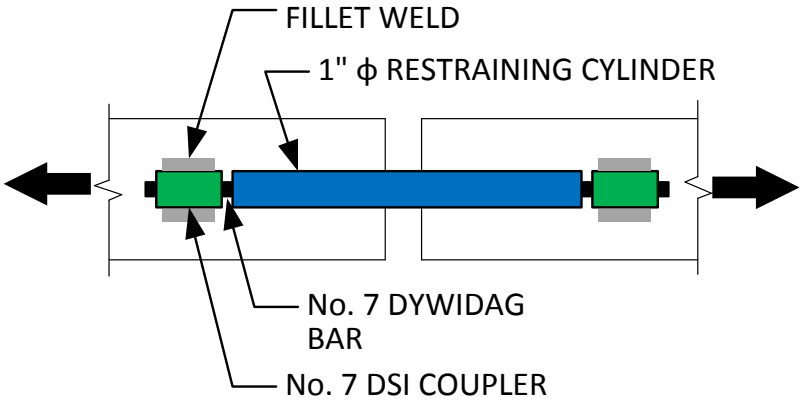

Figure 5.3: Sample ED Bar Configuration

Figure 5.4 shows the results from the component test. This system shows full, stable hysteretic behavior for both tensile and compressive forces. In contrast to the SC-MRF, the SC-TMF will develop strains in both the tensile and compressive direction. It was assumed, because of the expected behavior of the restraining tube, that the stable hysteretic behavior shown in Figure 5.4 would be exhibited for positive and negative strains. Additionally, the yield force and yield displacement shown closely matched value predicted by simple mechanics equations (320 kN and 2.6 mm, respectively). This provided a reasonable level of confidence that these ED bars would provide sufficient energy dissipation as a fuse in the SC-TMF.

One concern from the results of the component test is the flat portion in the curve that is seen in Figure 5.4 between points B and C. This occurs because of a slip in the coupler bar connection,

and the size of the slip increases as the inelastic deformation in the threads increases. In order to limit this slip, it is necessary to keep the threads fully elastic throughout the deformation of the fuse. It should be noted that the ED bars tested had a constant diameter through the threading; to keep the threads elastic, the ED should have a reduced section between the couplers to control where inelastic deformation occur.

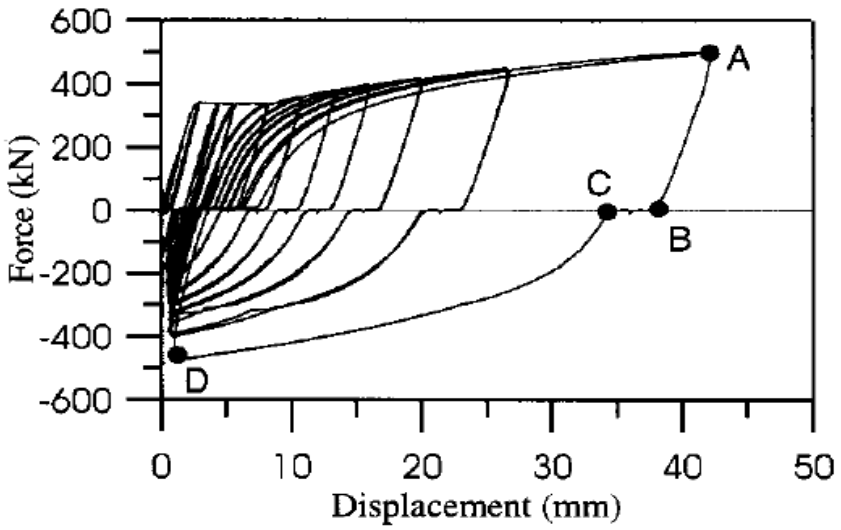

Figure 5.4: ED Bar Component Test Results [from (Christopoulos et al. 2002b)] [Used under fair use, 2012]

Figure 5.5 shows the fuse configuration for the SC-TMF with ED Bars. This installation is very similar to the installation that has been tested for the SC-MRF (Christopoulos et al. 2002b), with the exception being that the right side of the fuse is connected to the outer tube rather than to the flanges of the beam in the moment frame.

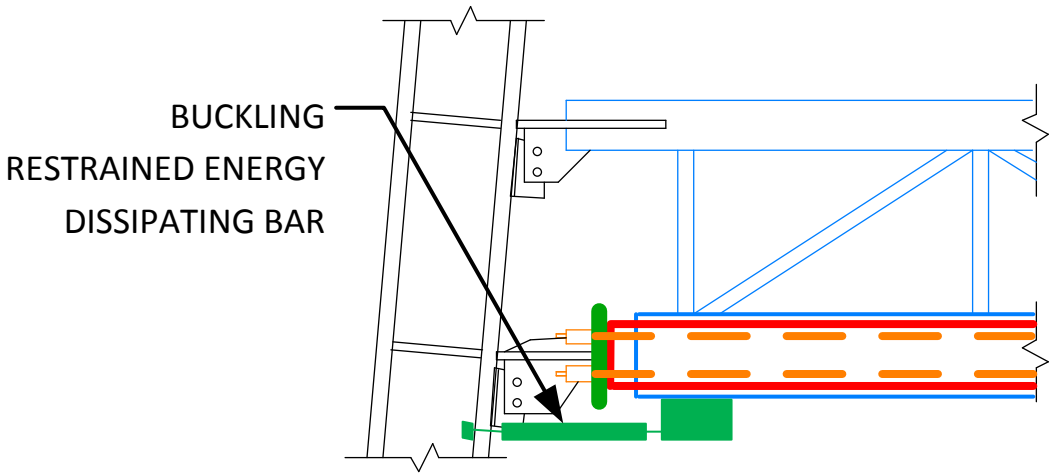

Figure 5.5: Fuse Configuration for SC-TMF with ED Bar Fuse

The buckling restrained ED bars are just one of the energy dissipating devices that could be utilized along the bottom chord of the SC-TMF. A number of other fuses have been developed for use in steel structures for seismic applications and could be adapted for use in this location. For example, Vasdravellis et al. (2012) investigated web hourglass pins for use as energy dissipating devices in the SC-MRF. A similar fuse was investigated by Tirca et al. (2012),which utilized single pins to dissipate energy at a the brace-to-column connection in concentrically braced frames. Finally, Gray et al. (2012) developed a cast steel connecter with yielding fingers for use in a concentrically braced frame that could be adapted to the needs of the SC-TMF. Each of these fuses provides stable hysteretic behavior similar to that of the energy dissipating bar.

The updated model for the SC-TMF with ED bar fuses is shown in Figure 5.6. In this model, the ED bars are modeled as elastic perfectly-plastic springs between the ends of the outer tube and the columns. An EPP load-deformation behavior was utilized for simplicity and to produce distinct yielding and stiffness changes in the results. Additionally, the simple EPP model can conceptually represent any fuse with stable full hysteretic behavior. Because the fuse is now at the ends of the truss, the Vierendeel middle section is no longer required and has been removed. Outside of these changes, the computational model for the ED bar configuration is exactly the same as the SC-TMF with the butterfly fuse plate described in Section 4.4.

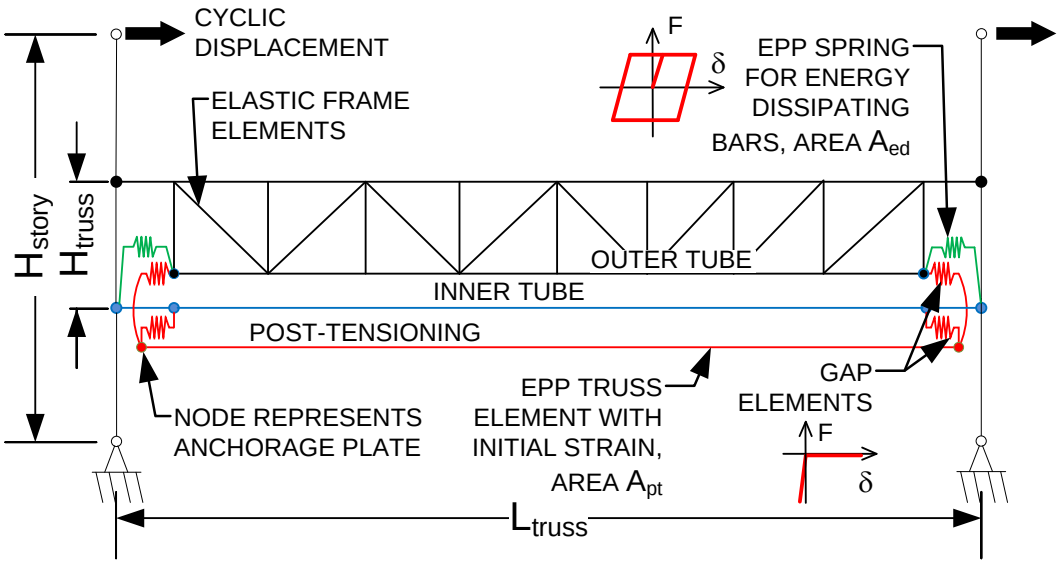

Figure 5.6: Computational model for SC-TMF with ED Bar Fuse

5.3 Fuse Comparison

The single story, single bay models described in Section 4.4 were used to do a preliminary comparison of behavior between the two fuse configurations. A model named SCTMF11bf has butterfly fuse plate at the middle panel of the truss. A second model named SCTMF11ed has energy dissipating bars between the column and the outer tube. Outside of the different fuses, all other elements in these two models are exactly the same. Additionally, the fuses were designed to have nearly the same self-centering ratio.

Figure 5.7 shows the monotonic pushover curves for the two fuse configurations. Initially, both models have approximately the same stiffness. This is because the stiffness of the system before gap opening is controlled by the size of the members within the truss and the stiffness of the truss as a whole. This fact is confirmed in Figure 5.8, which shows the stiffness at each point of the monotonic pushover analysis. The butterfly fuse configuration has a slightly higher initial stiffness, which can be attributed to the fact that the butterfly fuse is acting as a web member in this configuration. Additionally, the vertical web members of the butterfly fuse configuration are

spaced closer together to allow for the Vierendeel middle panel. This will shorten the diagonal members and increase their stiffness.

It is evident that gap openings occur at the same location in both models; however, the pushover curves clearly show that the stiffness after this point is drastically different. This is because after gap opening occurs, the stiffness of the system is governed only by the size of the post-tensioning and the stiffness of the fuse elements. Even though the fuses have the same capacity, and therefore self-centering ratio, the energy dissipating bars are able to provide a greater amount of stiffness to the overall system. This fact is again confirmed in Figure 5.8, which shows the stiffness of the butterfly fuse configuration drops to 20 percent of its initial stiffness after gap opening, while the energy dissipating bar configuration is able to retain over 60 percent of its initial stiffness.

The third region of behavior starts at a moment approximately equal to 600 kip-ft for this configuration. This corresponds to fuse yield and the stiffness is controlled only by the size of the post-tensioning strands. Both systems have the same size strands, which is why both systems have the same stiffness during this region of response. Finally, the fourth part of the curve represents a drift where the post-tensioning has yielded and there is nearly zero stiffness in the system. This point does not occur until the system has undergone a drift of nearly 6 percent, which is well above the maximum inelastic drift allowed by current U.S. building codes for moment frames equal to 2% (ASCE 2010) and the required drift to prequalify a special moment connection (AISC 2010b).

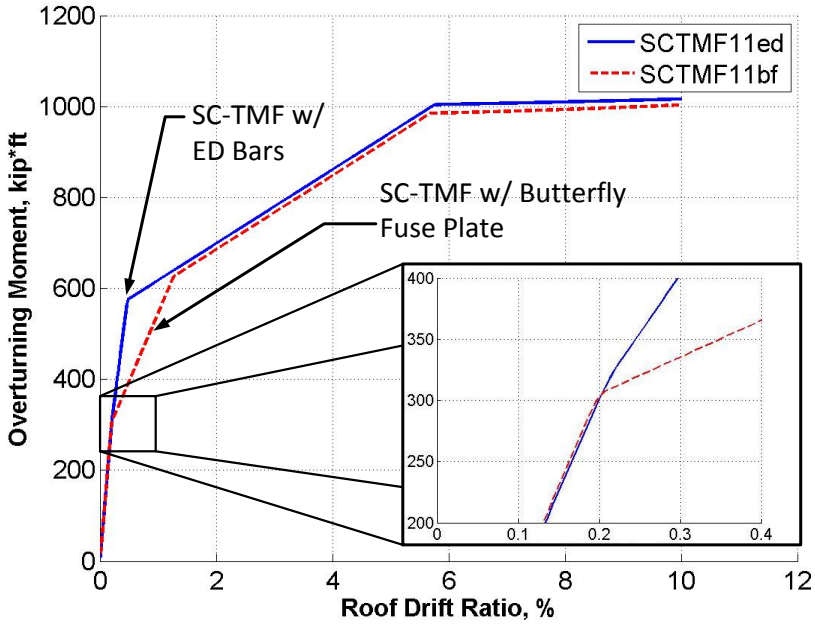

Figure 5.7: Monotonic Pushover Curves for Two Fuse Configurations

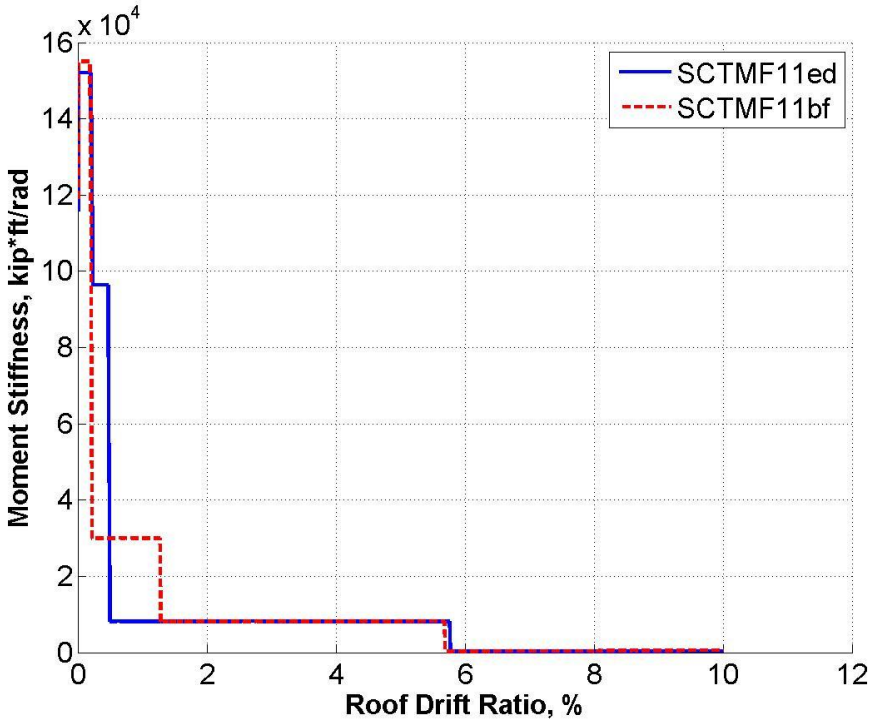

Figure 5.8: Stiffness versus Roof Drift Ratio for Two Fuse Configurations

Figure 5.9 shows the cyclic static pushover curves for the two fuse configurations. In this figure, it is evident that both systems are showing the flag-shaped hysteretic curve that is typical of self-centering systems. However, a major difference can be seen in the path that the two systems take during the unloading phase. The system will unload along their secondary stiffness. This is why the energy-dissipating bar system is unloading along a much steeper slope. This has the benefit of providing a more full global hysteretic behavior that is capable of greater levels of energy dissipation.

The added energy dissipation and the increased secondary stiffness of the energy-dissipating bars are expected to improve the behavior of the system and limit excessive drifts observed during earlier analyses. In addition to these performance benefits, the energy-dissipating bar configuration is expected to allow simpler detailing and easier replaceability. This is because the butterfly fuse is connected to the inner tube at the bottom chord, which would require a slot in the top of the outer tube to allow access. In contrast, the energy dissipating bars could simply be connected to the outer tube at each end, which decreases detailing and fabrication requirements and improves the repairability of these elements. For these reasons, the rest of this thesis uses the energy-dissipating bar configuration

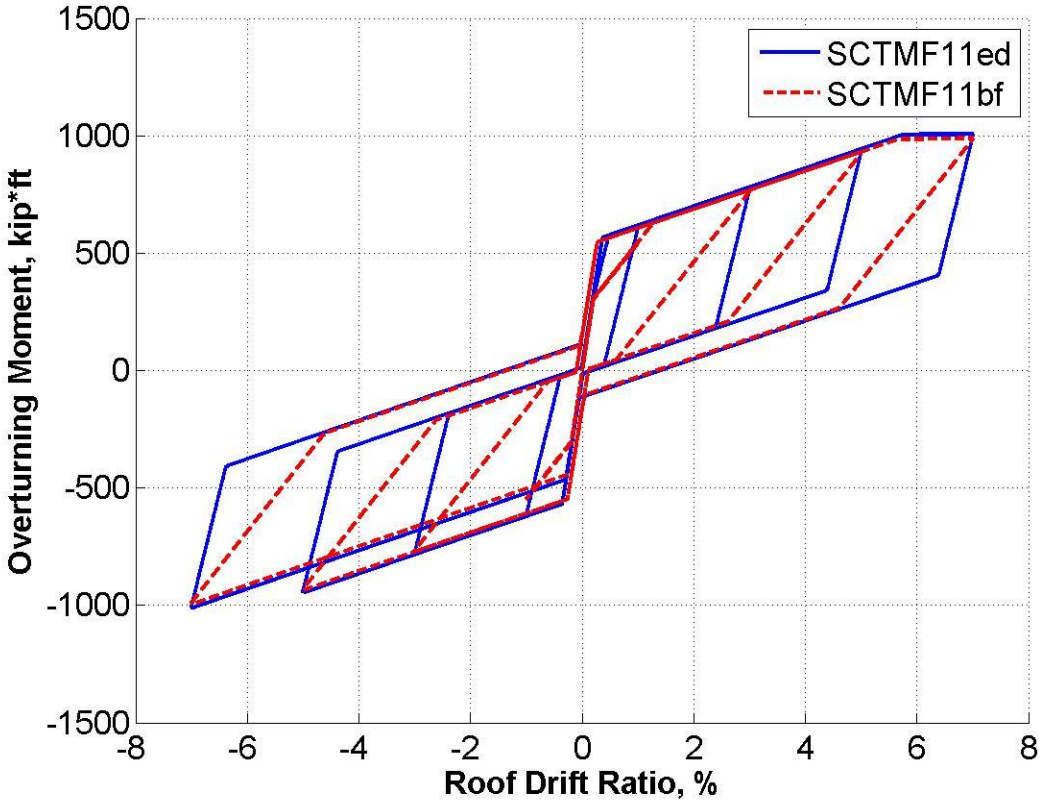

Figure 5.9: Cyclic Static Pushover Curves for Two Fuse Configurations

5.4 Progression of Internal Forces

In this portion of the mechanics investigation, the objective was to investigate how the forces flow through the components of the SC-TMF. For these investigations, the configuration with energy dissipating bars, shown in Figure 5.6, is utilized. In this section, the force in each of the members, including the post-tensioning, energy dissipating bars, and top and bottom chord components, are analyzed. This information was then utilized to develop the design method used in the parametric study as described in Chapter 6. However, after the parametric study, the preliminary design method is reassessed and updated in Chapter 7.

Figure 5.10 through Figure 5.13 show the forces in each element during the static pushover analysis plotted against the roof drift ratio. Figure 5.10 shows the moment resisted by the post-tensioning (PT) and the fuses. This is determined by multiplying the force in that element by the height of the truss, which was 24 inches. Fuse 1 is the fuse at the left end of the truss and Fuse 2 is the fuse at the right end of the truss. During this analysis, the truss is pushed to the right, which causes Fuse 1 to go into tension and Fuse 2 to go into compression. The plot shows that the post-tensioning elements begin the analysis with an initial stress, while the two fuses have zero-force initially. As the truss begins to deflect, the energy-dissipating bars begin to take some force and the post-tensioning force remains constant. Then, once gap openings occur, all three elements begin to take on a significant amount of force. As expected, one of the fuses is going into tension while the other is being compressed. Buckling of the energy-dissipating bars is restrained, which allows both bars to take on an equivalent level of force. Next, the energy-dissipating bars yield and are no longer able to take more force. At this point, the forces directed to the post-tensioning elements drastically increases. These forces continue to increase until the post-tensioning ultimately yields and can no longer accept greater levels of force. Figure 5.10 also shows the pushover curve for the total truss overlaying the element moment curves. This is done to show how the stiffness in the total moment-deformation relationship is changed when there is a change in the stiffness of one of the self-centering elements. This plot is able to confirm the progression of forces that occurs within the post-tensioning and fuse elements.

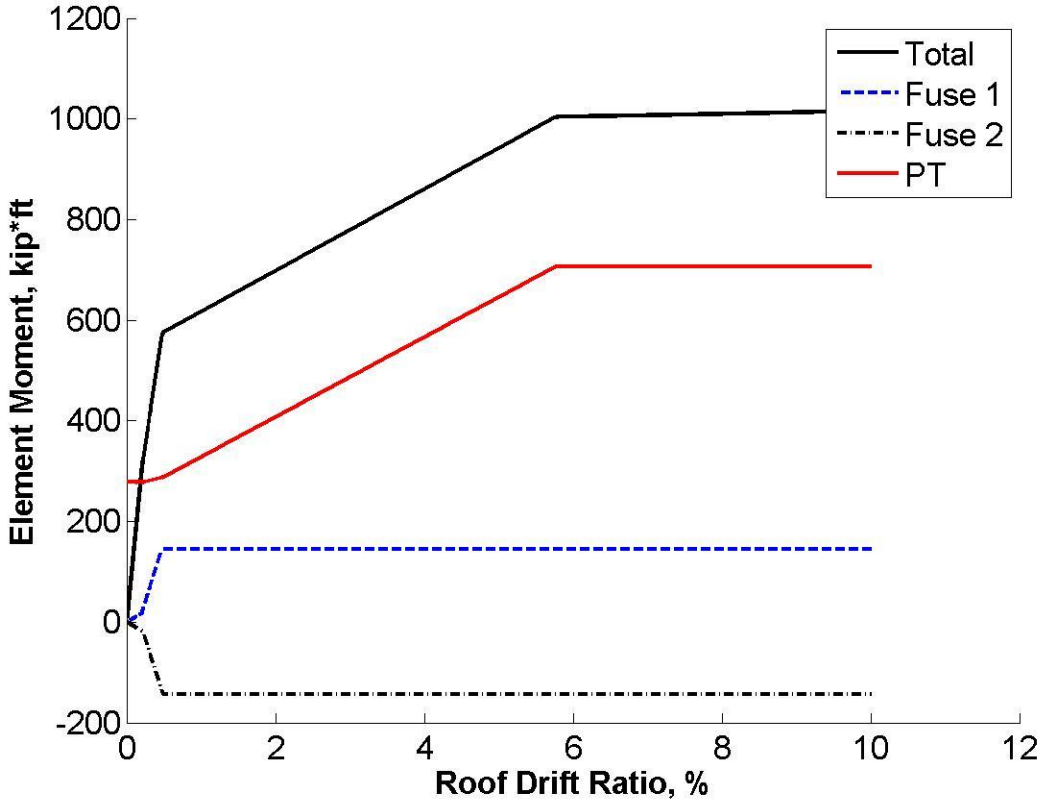

Figure 5.10: Force Development in Self-Centering Elements during Monotonic Static Pushover Analysis.

The development of forces in the inner tube is shown in Figure 5.11. The elements are numbered from left to right such that element two represents the entire HSS member that is precompressed by the post-tensioning. Elements 1 and 3 are the end connection pieces that fall outside the precompressed zone and connect the inner tube to the column at the bottom chord elevation. The initial force shown in the plot for each of these members confirms the fact that the model is behaving as expected and is not transferring any of the precompression to the connecting members. When force is initially applied, these end members begin taking on force while the force in element 2 remains constant. Element 1, which is at the left end, goes into tension while element 3 goes into compression with equal and opposite force. Once the force in element 3 is equal to the precompression in element 2, gap opening occurs and the force in each element increases proportionately as the external forces increase.

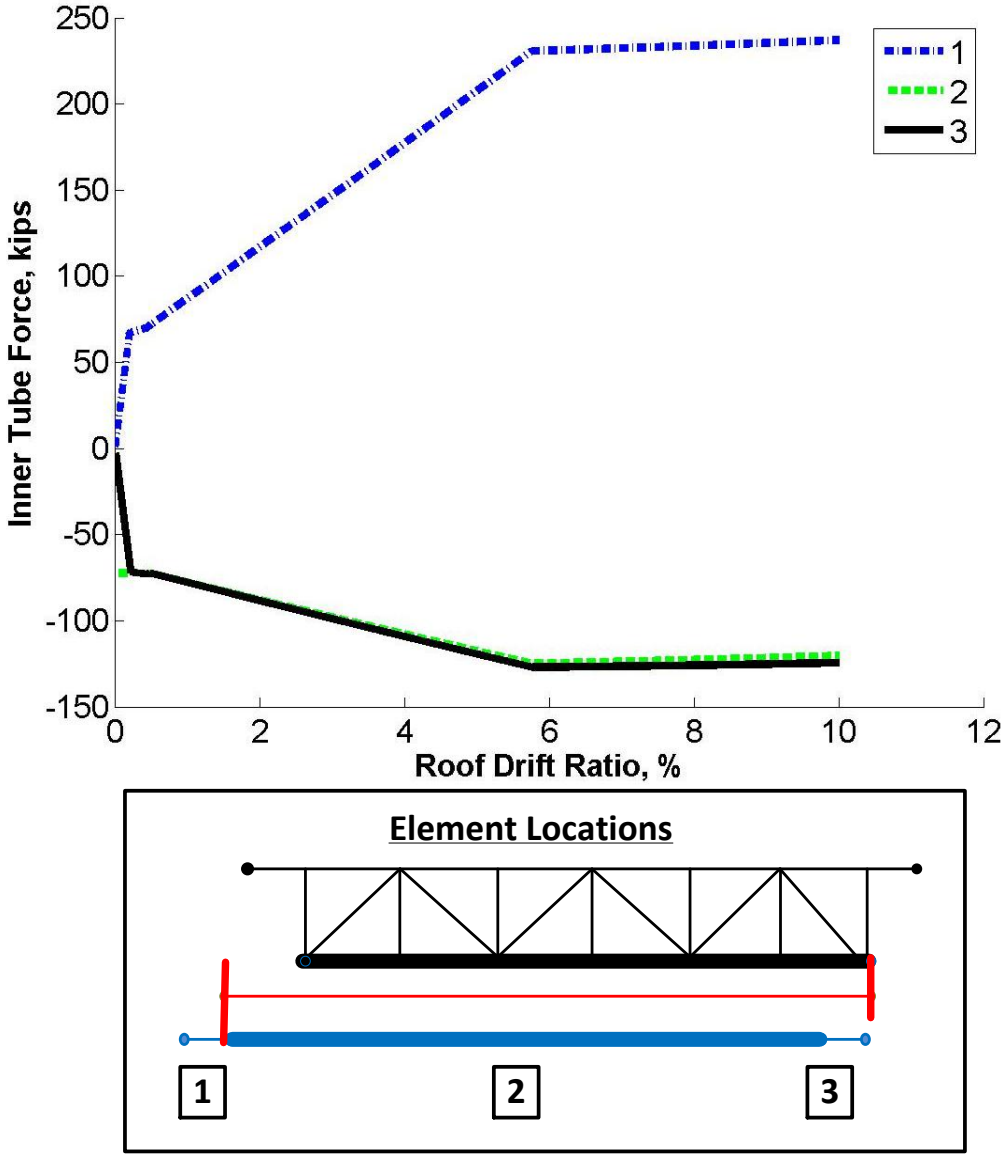

Figure 5.11: Force Development in Inner Tube Elements during Monotonic Static Pushover Analysis.

Figure 5.12 shows how the forces in the outer tube develop during the monotonic static pushover analysis. The outer tube is split into 6 elements to create nodes for web members to connect to and all six sections fall within the precompressed zone. All of these elements start with an initial compression of 60.5 kips. This results in an initial stress in the member of 6.7 ksi, which is

approximately equal to initial stress in the inner tube. As the pushover analysis progresses, the elements at the right of the system begin to take more compression while the members at the left go into tension. This is because the web members are transferring force to the top chord, which is transferring some of the force to the left column in tension and some of the force to the right column in compression. This fact is illustrated in Figure 5.13. This figure shows that the top chord is initially unstressed. However, as soon as force is applied to the system, the elements at the right begin to go into tension while the elements at the left begin to go into compression.

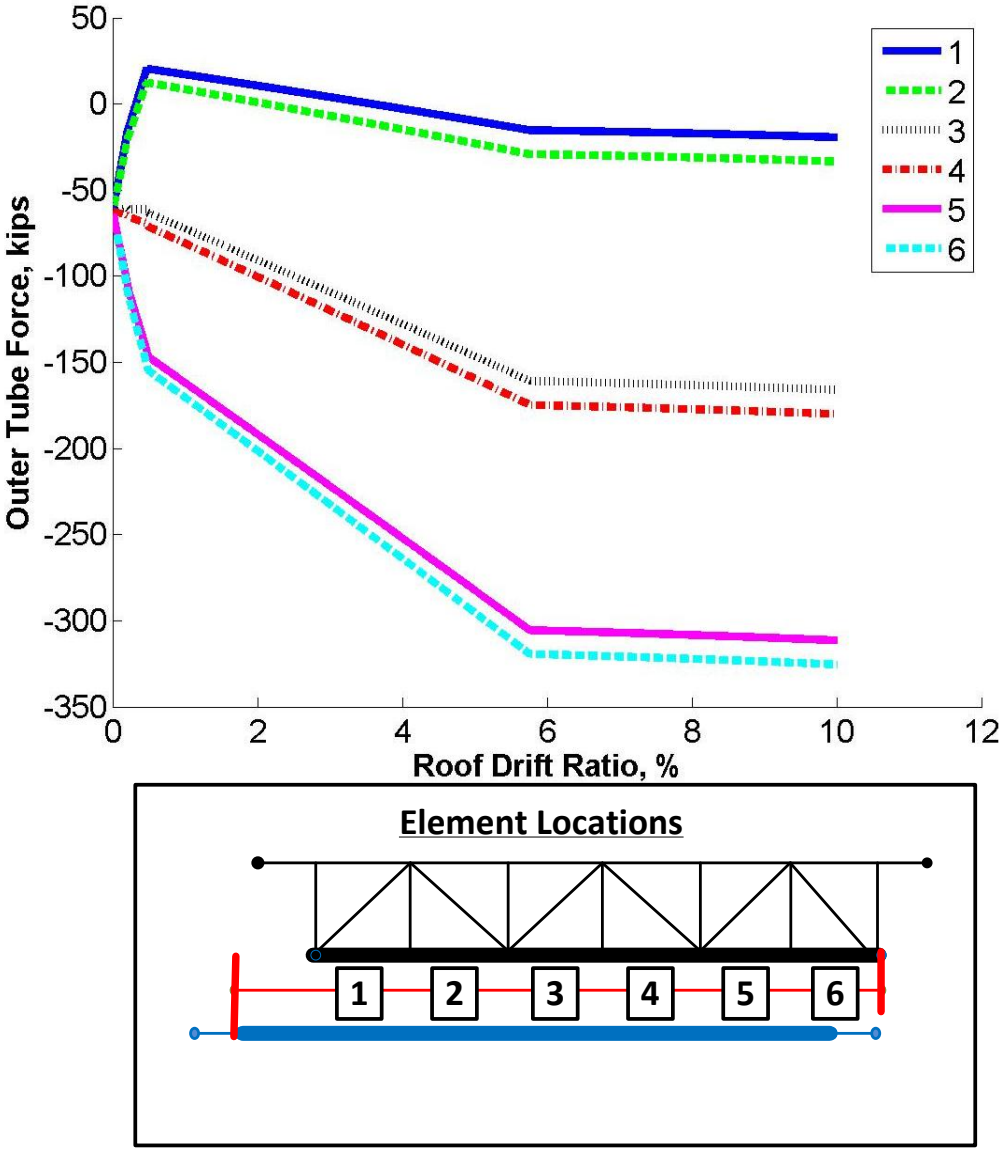

Figure 5.12: Force Development in Outer Tube Elements during Monotonic Static Pushover Analysis.

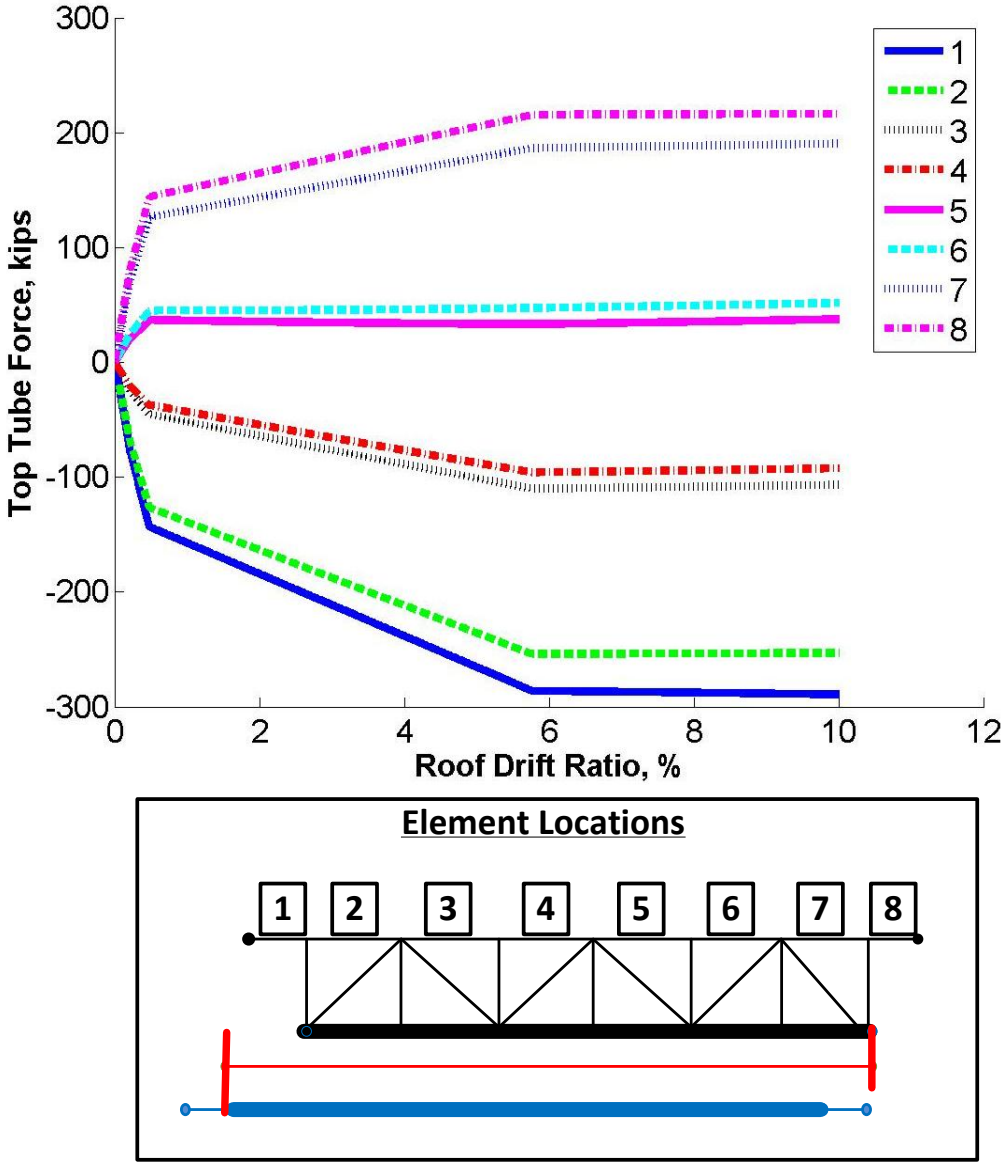

Figure 5.13: Force Development in Top Chord during Monotonic Static Pushover Analysis.

5.5 Equations to Describe System Strength

A simple design procedure was developed to describe the behavior of the SC-TMF. For this procedure, moment capacities were developed for each of the elements at various times during

loading. The moment at which the initial post-tensioning force is exceeded, M_{pti}, and decompression occurs is given by the equation:

$$M_{pti} = A_{pt} f_{pi} h_{truss} \quad 4.1$$

Where

A_{pt} total cross sectional area of the post-tensioning

f_{pi} initial post-tensioning stress

h_{truss} the height of the SC-TMF from centerline to centerline of the top and bottom chords

The maximum moment the post-tensioning members can develop, M_{ptu}, is given by the equation:

$$M_{ptu} = A_{pt} f_{pu} h_{truss} \quad 4.2$$

where

f_{pu} = ultimate post-tensioning stress

The yield moment of the energy dissipating bar fuse is

$$M_{fuse} = A_{ED} f_{yED} h_{truss} \quad 4.3$$

where

A_{ED} total cross sectional area of all energy dissipating bar fuses

f_{yED} yield stress of the energy dissipating bar material

The behavior of the self-centering truss moment frame can be partially characterized by three moments in the pushover backbone. The first, M_{gap}, is the moment where decompression occurs and gap openings begin to form. The second, M_y, is the point at which the fuse fully yields. Finally, M_u, is the maximum moment capacity of the system and occurs when the post-tensioning reaches its ultimate capacity. These three points are given by the following equations:

$$M_{gap} = M_{pti} \quad 4.4$$

$$M_y = M_{pti} + M_{fuse} \quad 4.5$$

$$M_u = M_{fuse} + M_{ptu} \quad 4.6$$

The strength parameters for the SCTMF11ed model were predicted using this set of equations. The moment at which decompression occurs, M_{gap}, was predicted to be 297 kip-ft. The moment at which all bars yield, M_y, was predicted to be 585 kip-ft. Finally, M_u, was predicted to be 1032 kip-ft. The pushover curve for this model is shown in Figure 5.14, where it is evident that the values are very closely matched.

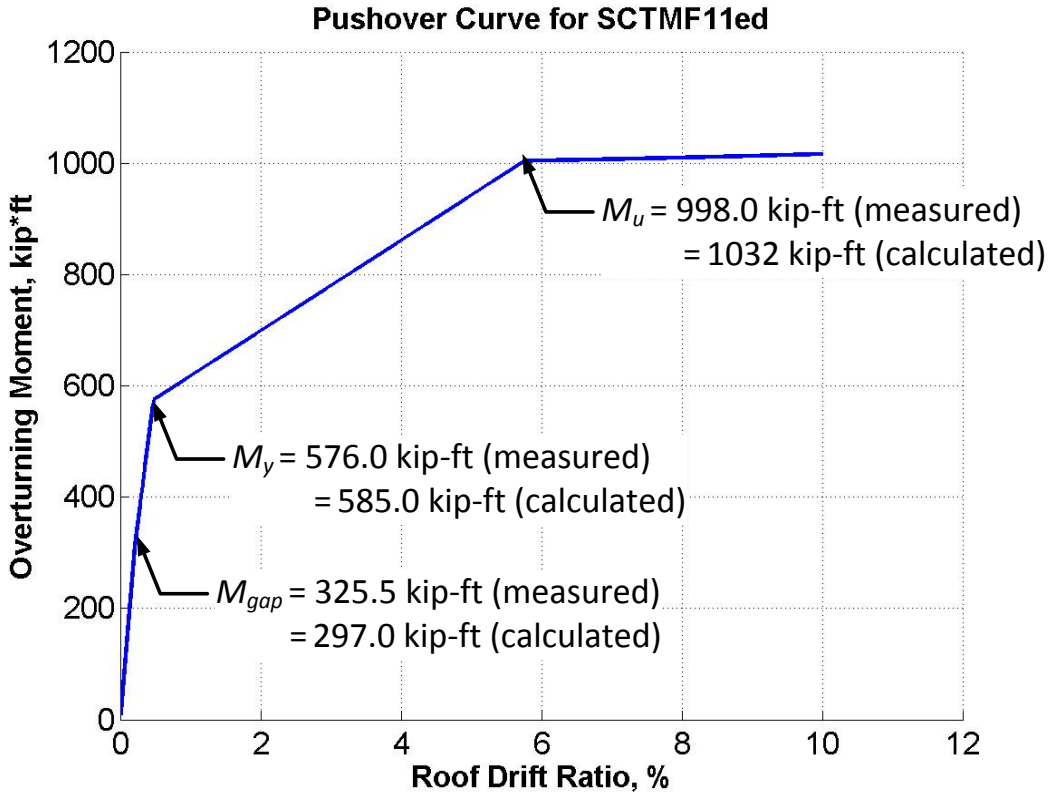

Figure 5.14: Monotonic Pushover Curve for SCTMF11ed

5.6 Equations to Describe SC-TMF System Stiffness

One of the unique benefits of the SC-TMF is that the strength and stiffness can be independently tuned. Because of this, stiffness equations were also developed. The stiffness of the SC-TMF can be characterized by three quantities: the stiffness of the truss, K_{truss}; the stiffness of the post-tensioning, K_{pt}; and the stiffness of the energy dissipating bar fuse, K_{ED}. Each stiffness was developed based on the applied overturning moment and the truss rotation, and therefore have units of [moment*radian^{-1}].

The stiffness of the truss, K_{truss} can be developed analytically using a simple frame analysis program. The stiffness of the remaining two elements requires a simple derivation to relate the axial stiffness of each element to its contribution to the global stiffness of the system. This derivation is given below.

The axial stiffness of each element is given as:

$$k_{axial} = \frac{AE}{L} \qquad 4.7$$

where

A = cross sectional area of the element

E = modulus of elasticity of the material

L = length of the element

The axial force that causes a deformation of δ within the truss is

$$f_{axial} = k_{axial}\delta = \frac{AE}{L}\delta \qquad 4.8$$

The associated internal moment resulting from the axial force in an element deformed by an amount, δ, and acting at the centerline of the chord is given by the following equation, where h_{truss} was defined in the previous section as the centerline to centerline distance between the top and bottom chords:

$$M_{\text{int}} = f_{axial} h_{truss} = \frac{AE}{L} \delta h_{truss} \qquad 4.9$$

The external moment, M_{ext}, must be equal to the internal moment, M_{int}. A geometric relationship between the truss rotation relative to the column, ϕ, and the deformation of an element, δ, at the chord centerline is then developed as:

$$\sin\theta = \frac{\delta}{h_{truss}} = \frac{\Delta}{h_{story}} = \phi \qquad 4.10$$

$$\phi = \frac{\delta}{h_{truss}} \qquad 4.11$$

where h_{story} is the total height of the story. These relationships can then be used to determine the stiffness contribution of each element to the global moment – displacement behavior.

$$K_{ele} = \frac{M_{ext}}{\phi} = \frac{\frac{AE}{L}\delta h_{truss}}{\frac{\delta}{h_{truss}}} = \frac{AE}{L} h_{truss}^{\ 2} \qquad 4.12$$

Using this relationship, the stiffness contributions of the post-tensioning and the energy-dissipating bar fuse are given by the equations, respectively.

$$K_{pt} = \frac{A_{pt}E}{L_{truss}} h_{truss}^{\ 2} \qquad 4.13$$

$$K_{ED} = \frac{A_{ED}E}{L_{ED}} h_{truss}^{\ 2} \qquad 4.14$$

The stiffness of each element in the system can then be combined to describe the stiffness of the truss for three regions of behavior. The first, K_1, is the stiffness before gap openings form. This stiffness is controlled by the stiffness of the truss alone. The second, K_2, is the stiffness after gap openings occur but before the point at which the fuse fully yields. The equation for K_1 is developed assuming that the post-tensioning and fuse are acting in parallel and that those two elements are working in series with the stiffness of the truss. Finally, K_3, is the stiffness of the system after the fuse yields but before the post-tensioning reaches its ultimate capacity. It is calculated assuming the fuses provide zero stiffness after they yield (no strain hardening) and that the post-tensioning and truss are acting in series. These are described by the following equations.

$$K_1 = K_{truss} \qquad 4.15$$

$$K_2 = \frac{1}{\frac{1}{K_{truss}} + \frac{1}{K_{pt} + K_{ED}}} \qquad 4.16$$

$$K_3 = \frac{1}{\frac{1}{K_{truss}} + \frac{1}{K_{pt}}} \qquad 4.17$$

Following the yielding of the post-tensioning, it is assumed that the system has zero stiffness because strain hardening of the materials is not taken into account in these initial investigations.

The stiffness parameters for the SCTMF11ed model were predicted using this set of equations. The stiffness before gap opening was assumed to be 152,880kip-ft/rad. The stiffness after gap opening, K_2, was predicted to be 99,840 kip-ft/rad. Finally, the stiffness after the fuse yields, K_3, was predicted to be 8,424 kip-ft/rad . When these values are compared to the plot of stiffness versus drift ratio that is shown in Figure 5.15, it is evident these equations predict the system stiffness well.

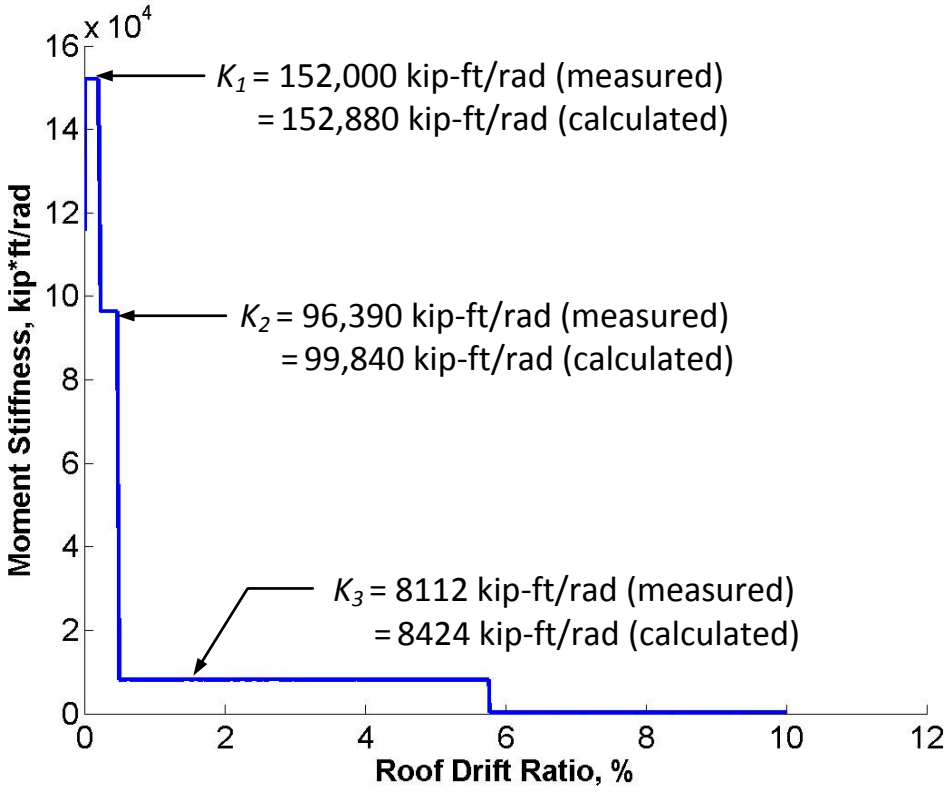

Figure 5.15: Stiffness versus Roof Drift Ratio for SCTMF11ed

Chapter 6. Parametric Study

6.1 Parametric Study Plan

A parametric study was designed to build on the concepts of the initial mechanics investigation and evaluate how design parameters affect the behavior of the system. In this parametric study, the one bay, one story configuration that was shown in Figure 5.6 was utilized with a variety of changes to design variables. Figure 6.1 shows the computational model with the important parameters for the study labeled. Monotonic and cyclic static pushover analyses were conducted. These analyses followed the cyclic Loading Sequence for Beam-to-Column Connections outlined in Chapter K of AISC 341-10 (AISC 2010b). The loading protocol, which is described in Table 6.1, follows a saw-toothed pattern and is shown graphically in Figure 6.2.

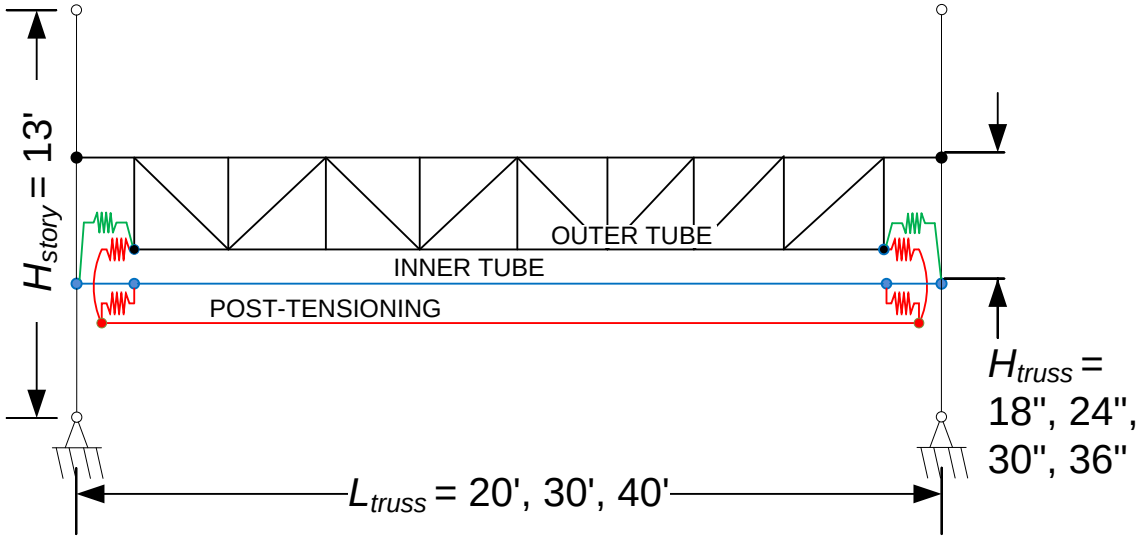

Figure 6.1: Parametric Study Computational Model

Table 6.1: AISC Loading Sequence for Prequalification of Beam-to-Column Connections

Interval	Number of Cycles	Story Drift Angle, θ
1	6	0.00375 rad
2	6	0.005 rad
3	6	0.0075 rad
4	4	0.01 rad
5	2	0.015 rad
6	2	0.02 rad
7	2	0.03 rad
8	2	0.04 rad

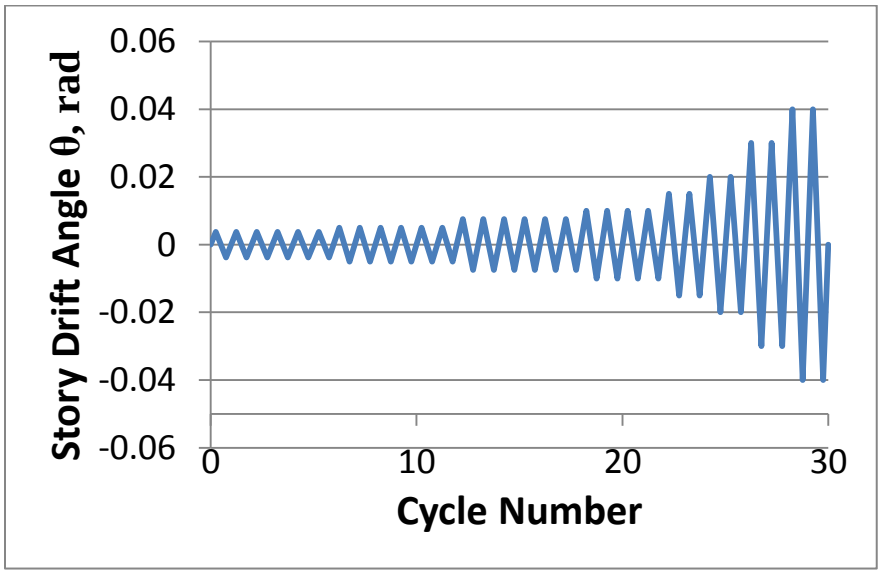

Figure 6.2: AISC Loading Sequence for Prequalification of Beam-to-Column Connections

The parameters that were studied are outlined in Table 6.2. The parameters, which were individually varied such that every combination was analyzed, included 4 values for truss depth, 3 values for moment capacity, 3 values for bay width, 5 values for initial pretension level, and 5 values for self-centering ratio. This resulted in 900 permutations that were analyzed as a part of the parametric study.

Table 6.2: Input Parameters to be varied during Parametric Study

Parameter	Notation	Description	Values
Truss Depth	h_{truss}	Truss depth measured centerline to centerline of chord.	18 in, 24 in, 30 in, 36 in
Moment Capacity	M_n	Moment capacity relative to W-Shapes with equivalent depths	Low, Med, High
Bay Width	L_{truss}	Distance from column line to column line	20 ft, 30 ft, 40 ft
Initial Pretension Level	γ_{pt}	Initial post-tension stress as percentage of ultimate, F_{pu}	20%, 35%, 50%, 65%, 80%
Self-Centering Ratio	SC	Ratio of initial post-tensioning moment to fuse yield moment	0.50, 0.75, 1.0, 1.25, 1.5

Truss depth was selected as a parameter because it is one of the controlling factors that must be considered when designing a moment frame. Member depth can be influenced by the desired floor-to-floor height, the clearance relative to mechanical piping or ducts, and by the required moment capacity/stiffness of the member. W-shapes are utilized in a variety of depths in order to meet this combination of requirements and it was desired to show how the SC-TMF compares to the beams that are currently used in SMRFs. In order to make this comparison, a range that is representative of the beam depths used in SMRF was selected.

The moment capacity of the system is another important factor to investigate as part of the parametric study. In a typical beam in a moment frame, the moment capacity can be closely tied to the depth of that member. The SC-TMF moment capacity is similarly affected by the depth of the truss; however, it has been shown that the moment capacity of the SC-TMF can be more finely tuned by altering the size of its post-tensioning and fuse components. Because of this, it is important to see how a design is affected by the combination of moment capacity and truss depth. In Table 6.2 the moment capacity variables are described as "Low, Med, and High." This means that a range of moment capacities will be selected for the SC-TMF based on the capacity

of beams with similar depths. Table 6.3 gives the design values for each truss depth and each moment design level.

Table 6.3: Design Moment Capacities

	Moment Level					
	Low		**Medium**		**High**	
Depth	**Size**	M_n	**Size**	M_n	**Size**	M_n
in		kip-ft		kip-ft		kip-ft
18	W18x55	420	W18x119	983	W18x192	1660
24	W24x62	574	W24x131	1390	W24x250	2790
30	W30x99	1170	W30x173	2280	W30x261	3540
36	W36x150	2140	W36x231	3610	W36x302	4800

The third parameter was bay width. This parameter is generally controlled by the architectural layout of the building but can have a significant effect on the behavior of the system. In the SC-TMF, the bay width is expected to have a significant effect on the deformation capacity of the post-tensioning elements. Longer post-tensioning strands will undergo less strain to accommodate a unit interstory drift. Because of this, it is expected that longer bay widths will increase the ultimate deformation capacity of the system because it will take greater levels of interstory drift for the post-tensioning to reach its ultimate strain. This is very important because reaching the ultimate capacity of the post-tensioning is a limit state that needs to be avoided because the behavior of the system is less controlled.

Initial pretension level is an important factor to consider for two main reasons. First, as shown in the previous chapter, the initial pretension level affects the moment that will cause decompression. Second, the larger levels of initial pretension leave less strain capacity in the post-tensioning elements and will limit the deformation capacity of the entire system. Therefore, it is important that the initial pretension is large enough that it does not allow for gap openings

during wind loads or frequent earthquakes while it leaves a sufficient amount of deformation capacity.

Self-centering ratio was the final parameter considered. Self-centering ratio is the ratio of the initial post-tensioning moment to the fuse yield moment. It can be calculated using the equation:

$$SC = \frac{M_{pti}}{M_{fuse}} = \frac{A_{pt} f_{pi} h_{truss}}{A_{ED} f_{yED} h_{truss}} \qquad 5.1$$

This value describes the ability of the system to fully self-center. Self-centering ratios greater than 1.0 indicate that the initial post-tensioning force is able to create sufficient moment to cause the fuse to yield toward zero displacement, even if external forces are removed slowly. Values less than 1.0 indicate that the post-tensioning alone may not be able to overcome the fuse force and create the desired self-centering behavior.

The self-centering ratio also has a significant influence on the amount of energy dissipation that the system can provide when compared to a theoretical system with a full hysteresis that fully encompasses the flag hysteresis of the SC-TMF. Larger self-centering ratios cause the flag shape hysteresis to tighten up and become smaller, reducing the energy dissipation that is retained.

There are a number of important output variables that were be measured during the parametric study. The important outputs are outlined in Table 6.4.

Table 6.4: Important outputs measured during the Parametric Study

Output	Location	Stage of Loading	Reason
Interstory Drift Ratio	Global	Gap Opening	Understanding drift capacity of the SC-TMF
		Fuse Yield	
		Post-tensioning yield	
Max Element Force	Inner Chord	Post-tensioning yield	Capacity based design
	Outer Chord		
	Top Chord		
Moment Capacity	Global	Gap Opening	Compare the design capacities to the actual capacity for each event
		Fuse Yield	
		Post-tensioning yield	
Energy Dissipation	Global	Final cycle	Compared to an elastic linear hardening hysteretic
Interstory Drift at Zero Force	Global	After final cycle	At the end of the AISC loading protocol

The first output considered was the drift ratio at which gap opening, fuse yield, and post-tensioning yield occur. Each drift is important to describe the behavior of the system because they are associated with significant changes in stiffness. The drift at which gap opening occurs is particularly important because if this is too small, then gap openings may occur under frequent loading. Also, the drift at which post-tensioning yields is important because it needs to be sufficiently large to prevent collapse during large earthquakes. The post-yield behavior of post-tensioning strands is not well defined and should be avoided at this stage.

In order to determine the drift at which each event occurred, a flag was created that would identify the load step during the monotonic pushover at which each event happened. The post-tensioning flag recorded the load step at which the post-tensioning element force exceeded the

yield force for that component. Similarly, fuse yield was identified as the load step where the force in both energy dissipating bars had exceeded the yield force. Gap opening was harder to identify because small displacements were recorded for the gap opening before the associated change in stiffness occurred. For this reason, the flag could not be identified as the load step where a relative displacement between element end nodes was recorded. Instead, a script was developed to identify the first load step where a significant change in stiffness occurred. This load step was then checked against the load step where the measured gap opening change was more than twice the change of the previous load step. Logical operators were utilized to determine which load step most accurately described gap opening and the flag was set there. Then the interstory drift at each flag was recorded as the location where each event first occurred.

The next output considered is maximum force in the elements that are expected to remain elastic. This is important because the system must remain elastic outside the fuses in order to produce a repairable structural system. Because of this, a capacity based design approach is developed in the next chapter for the members outside the fuse and post-tensioning components. The maximum force experienced by the monotonic pushover protocol is used to refine the design approach in the next chapter.

The output is the moment capacity, which was measured at gap opening, fuse yield, and post-tensioning yield. The moment capacity was determined by multiplying the applied force at the flag for each event by the interstory height. This is a calculation of externally applied moment. These moments could then be compared to the equations that described the internal moment capacity of the system at each event.

Energy dissipation is another very important variable for seismic resistant systems. One of the concerns of utilizing a self-centering system is that the energy dissipation capacity is reduced when compared to a system with a full hystersis. This is because the flag-shaped hysteresis that is typical of self-centering systems can encompass significantly less area than the full hysteresis of a system that can be idealized as bilinear. In order to measure the level of energy dissipation, an energy dissipation ratio was developed.

Energy dissipation ratio is the ratio of the energy dissipated by the SC-TMF during the final loop of cyclic loading when compared to a theoretical, full hysteresis loop. This concept is illustrated in Figure 6.3 through Figure 6.5, which show the last hysteresis loop for the 24 inch SC-TMF with 20 ft bay width, initial post-tensioning ratio of 0.50, and self-centering ratios of 0.50, 1.0, and 1.5, respectively. Three lines are shown on each plot. The first hysteresis loop is the load-deformation response of the SC-TMF system during the last cycle of loading. The second loop is a bilinear hysteresis that is formed by matching the slope of the initial stiffness and the final stiffness of the SC-TMF. The final loop is an elastic, perfectly plastic (EPP) hysteresis that is found by matching the initial stiffness for unloading and assuming perfectly plastic behavior. The energy dissipation ratio is then computed as the ratio of the area under the load-deformation response to the area under one of the idealized curves.

In each of the self-centering curve, the energy dissipation has a tendency to decrease as the self-centering ratio increases. In order to create designs with larger self-centering ratio, the relative size of the self-centering component (post-tensioning) has to increase when compared to the energy dissipation component (ED bars). This has the resulting effect of creating flag shape hysteresis, which decreases the net area under the curve.

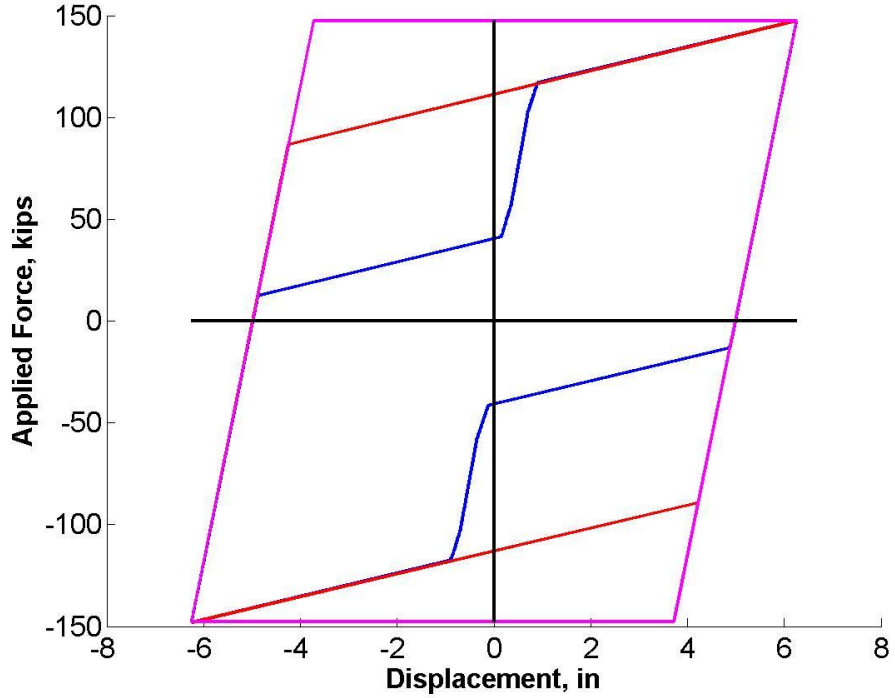

Figure 6.3: Hysteretic Curve for 24 inch SC-TMF with *SC* = 0.5, PT_i = 0.50, Length = 20ft

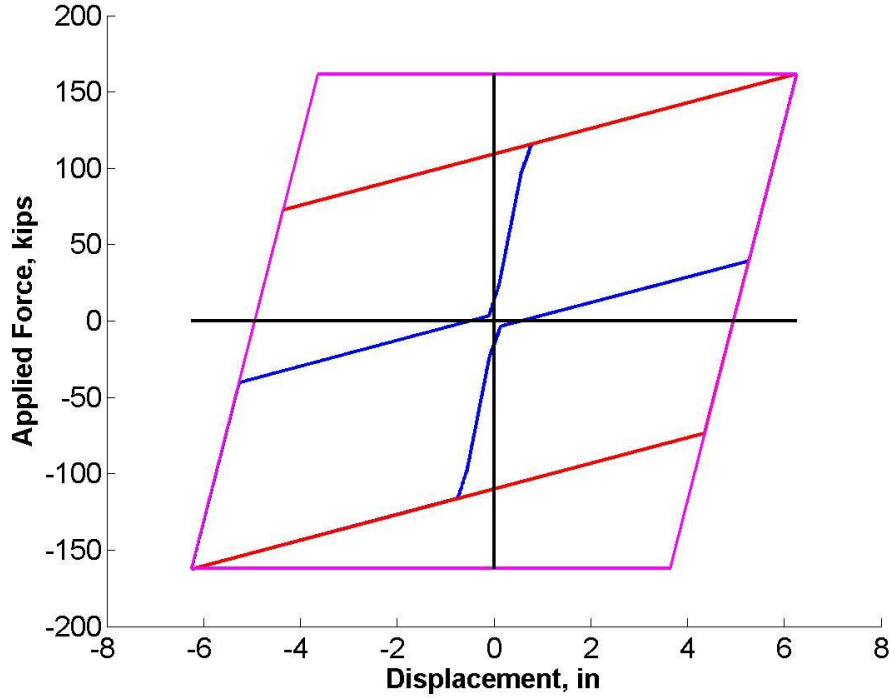

Figure 6.4: Hysteretic Curve for 24 inch SC-TMF with *SC* = 1.0, PT_i = 0.50, Length = 20ft

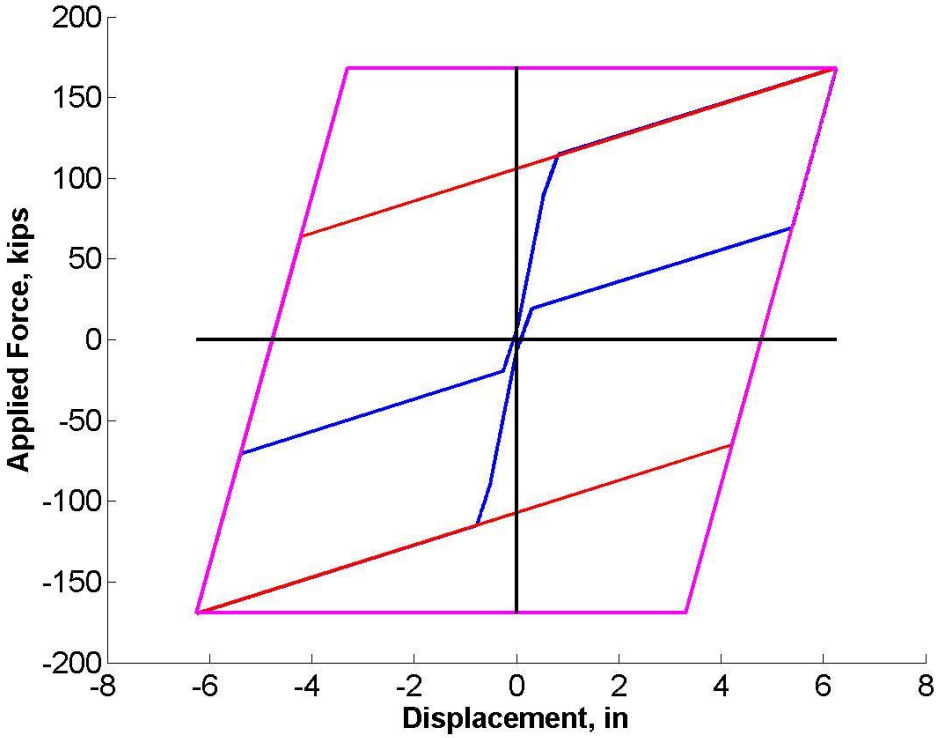

Figure 6.5: Hysteretic Curve for 24 inch SC-TMF with *SC* = 1.5, PT_i = 0.50, Length = 20ft

Currently there is a disparity between the ways energy dissipation of self-centering systems are reported in the literature. Some references report energy dissipation as normalized by an equivalent EPP system (ACI 2007). Others report energy dissipation normalized to an equivalent bilinear system. As discussed in the literature review, the concept for self-centering systems was born out of concrete systems that were post-tensioned across connections. The American Concrete Institute developed recommendations for the acceptance of moment frames based on structural testing (ACI 2007). The criteria outlined in this report utilized the energy dissipation ratio based on the EPP hysteresis loop. The criteria then required that the ratio developed must exceed 1/8, or 12.5%. However, research on steel self-centering systems has commonly reported energy dissipation ratio normalized to the bilinear systems and found possible limits of 25% (Seo and Sause 2005).

The bilinear hysteresis method of normalizing the energy dissipation ratio has been considered superior because the energy dissipation ratio can be correlated to system proportioning. For

instance, SC-TMF systems with self-centering ratios near 1.0 will have an energy dissipation ratio of approximately 0.5. That is, a SC-TMF system with equal parts initial post-tensioning force and fuse will dissipate approximately 50% of the energy of a bilinear system.

6.2 Typical Parametric Study Results

Figure 6.6 through Figure 6.8 show sample results from the cyclic static pushover analyses performed as part of the parametric study. Each plot shows the final hysteresis loop from the AISC prequalification loading sequence. These figures are split in plot (a) through (c) to give sense of how the results change with respect to a given input variable.

Figure 6.6 gives an idea of how the hysteretic behavior changes for each model as the self-centering ratio, *SC*, changes. These plots are taken from the models for the 24in SC-TMFs with an initial post-tensioning ratio of 0.50, bay width of 20ft, medium design moment, and self-centering ratios of 0.50, 1.0, and 1.5, respectively. In Figure 6.6(a), it is clear that the system with a self-centering ratio of 0.50 does not provide full self-centering behavior. Instead, the drifts do not begin to move toward zero until after the load has been fully reversed. Figure 6.6(b) shows that with a self-centering ratio of 1.0, the SC-TMF is able to provide a full self-centering behavior. Finally, Figure 6.6(c) shows that models with $SC = 1.5$ will have a much tighter flag shaped hysteresis. These models are still providing full self-centering behavior, but they are not able to dissipate as much energy as those with lower values of *SC*.

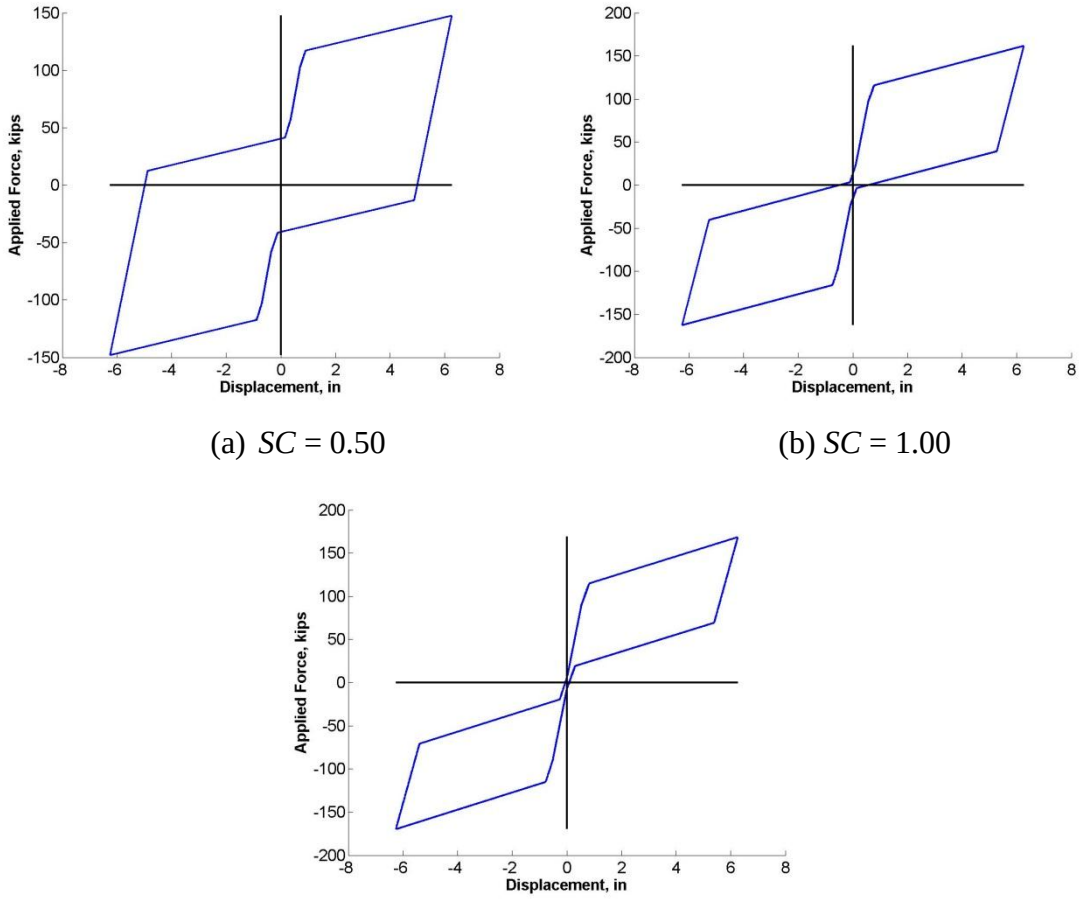

(a) *SC* = 0.50

(b) *SC* = 1.00

(c) *SC* = 1.50

Figure 6.6: Final Hysteresis Loop for 24in SC-TMFs with PT_i = 0.50, Length = 20 ft, and Medium Moment

Figure 6.7 gives an idea of how the hysteretic behavior changes for each model as initial post-tensioning ratio. These plots are taken from the models for the 36in SC-TMFs with a self-centering ratio of 1.0, a bay width of 20ft, medium design moment, and an initial post-tensioning ratio of 0.20, 0.50, and 0.80, respectively. The deepest truss and shortest bay width combination was selected because these values make the SC-TMF most susceptible to post-tensioning yield. Because the self-centering ratio is set to1.0, it is expected that these models would provide full self-centering behavior. This fact is true for Figure 6.7(a), which has the lowest initial post-tensioning ratio. Figure 6.7(b) begins to show a deviation from this behavior, and Figure 6.7(c) shows an even greater departure from full self-centering. This can be attributed to the fact that these two systems have experienced post-tensioning yield. The hysteretic curves do not show

the post-tensioning yield plateau because the post-tensioning yield would have happened during the first cycle at the maximum displacement (and the final cycle is the second cycle at the maximum displacement). The loss of post-tensioning force changes the hysteretic behavior and causes the departure from full self-centering. Comparing Figure 6.7(b) and (c), it is evident that the system with the higher initial post-tensioning ratio has experienced greater levels of inelastic behavior, which causes the more significant departure from the expected hysteresis.

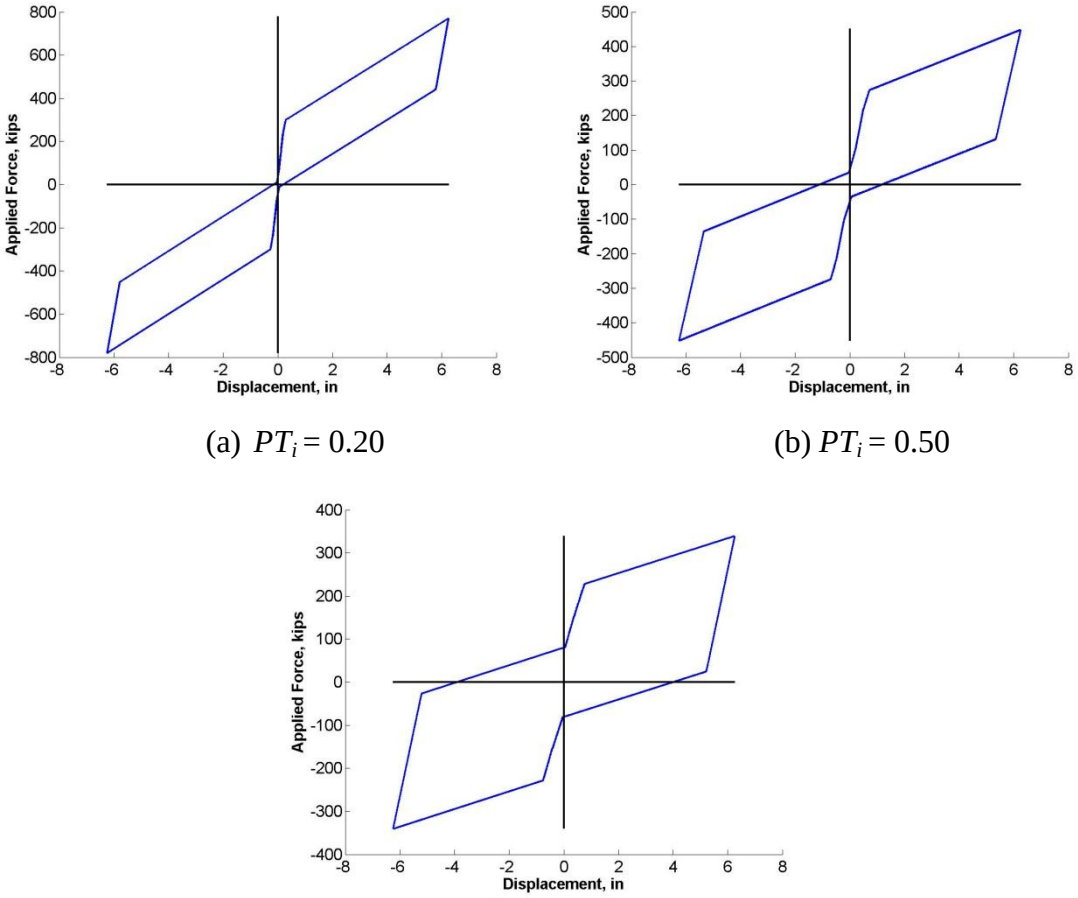

(a) $PT_i = 0.20$ (b) $PT_i = 0.50$

(c) $PT_i = 0.80$

Figure 6.7: Final Hysteresis Loop for 36in SC-TMFs with *SC* = 1.00, Length = 20 ft, and Medium Moment

Figure 6.8 gives an idea of how the hysteretic behavior changes for each model as the bay width increases. These plots are taken from the models for the 30in SC-TMFs with a self-centering

ratio of 1.0, an initial post-tensioning ratio of 0.50, medium design moment, and bay widths of 20ft, 30ft, and 40ft, respectively. There is very little difference seen in the three hysteretic behaviors. This indicates that the hysteretic behavior is not directly influenced by the bay width. However, the bay width can have an effect indirectly. For example, a shorter bay width may make a truss more susceptible to post-tensioning yield, which has been shown to have a significant effect on the hysteretic behavior.

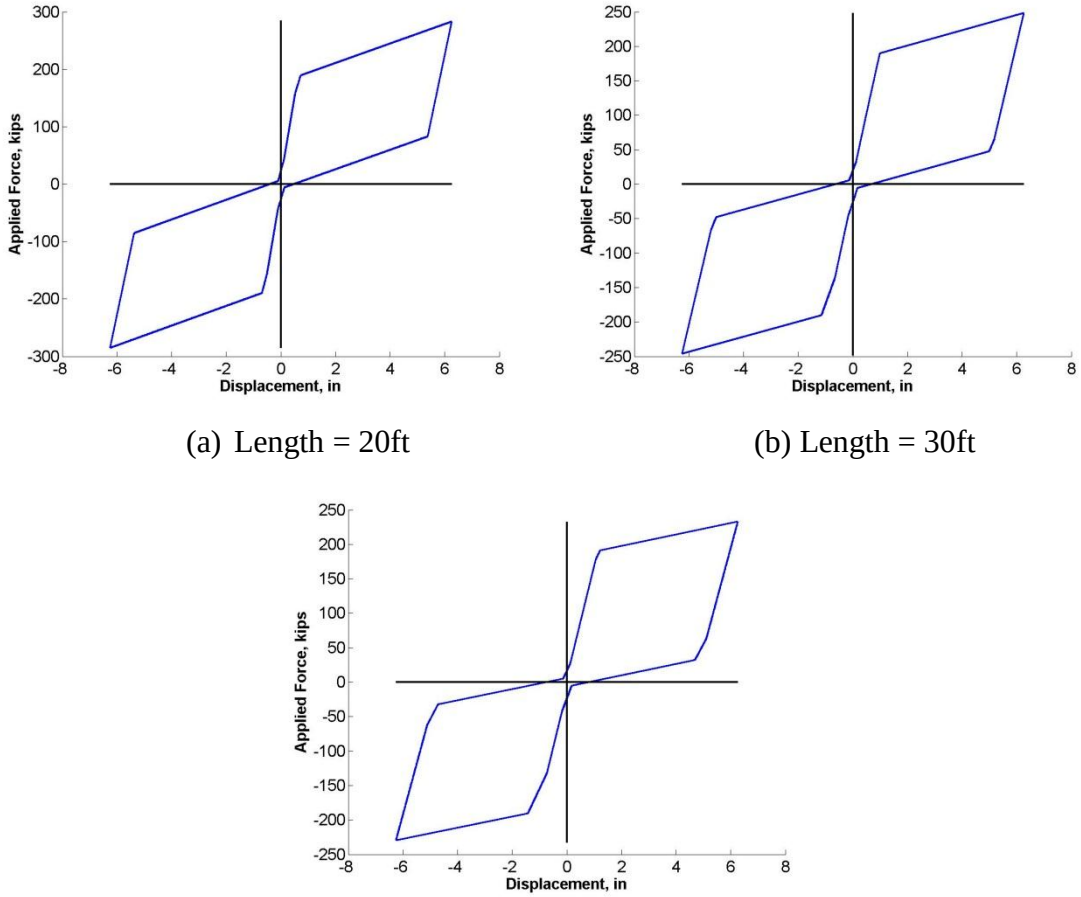

(a) Length = 20ft

(b) Length = 30ft

(c) Length = 40ft

Figure 6.8: Final Hysteresis Loop for 30in SC-TMFs with *SC* = 1.00, PT_i = 0.50, and Medium Moment

Chapter 7. Capacity Based Design

A preliminary capacity based design approach was developed to design the members outside of the post-tensioning and fuse components. This includes the top chord, bottom chord inner tube, and bottom chord outer tube. This was done to ensure these members to remain elastic during the imposed displacement protocol. If significant inelasticity occurs in the truss members, the SC-TMF may cease to function properly and the performance objectives related to repairability would be lost. The preliminary design approach described in this chapter was used to design the members included in the parametric study models. The parametric study results affecting the capacity design process are discussed in sections 7.3 and 7.4. Based on these results, updated equations are recommended as summarized in Chapter 9.

7.1 Top Chord and Inner Tube Capacity Design

The first step in developing the capacity based design was to develop a free body diagram of the system for the truss at ultimate moment from laterally applied forces. This occurs when the post-tensioning and ED bars are all yielding. Figure 7.1 shows the free body diagram for SC-TMF under ultimate loading. This diagram assumes zero gravity load for simplicity. For clarity, the post-tensioning and end plates have been left out and the forces they apply are shown instead.

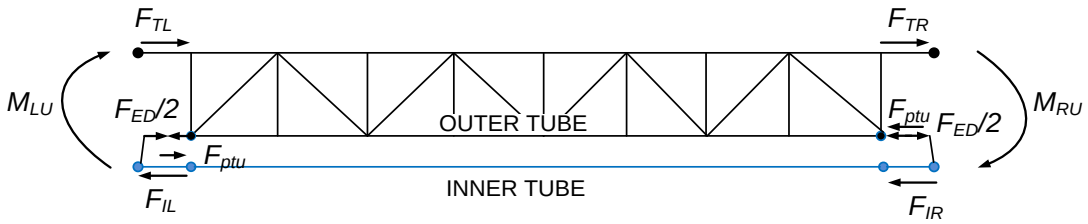

Figure 7.1: SC-TMF Capacity Design Free Body Diagram

M_{LU} and M_{RU} represent the moments applied to the SC-TMF at each end of the structure, respectively. It is assumed that the system is behaving symmetrically such that $M_{LU} = M_{RU}$. Based on this assumption, the moment applied at each end is given by the equation:

$$M_{LU} = M_{RU} = \frac{M_u}{2} \tag{6.1}$$

where M_u is the moment at which post-tensioning yields which is given by Equation 4.6. Decomposing this moment into the force couple shown at each end, the force at each end of the top tube can be determined.

$$F_{TL} = -F_{TR} = -\frac{M_{LU}}{h_{truss}} \tag{6.2}$$

The force at the location of the bottom chord must be equal and opposite to the force in the top tube to develop the force couple. However, in addition to the force in the inner tube, the force in the energy dissipating component is also contributing to the force at this level. Because of this, the force in the inner tube is given by the equation

$$F_{IL} = \frac{F_{ptu}}{2} \tag{6.3}$$

During design, it was assumed that the truss would provide sufficient bracing to prevent buckling of individual members in the plane of the truss. Therefore, the critical case that needed to be analyzed for the inner tube and top chord was out of plane buckling of each of these members. The trusses utilized the chord members set on their side (weak axis vertical). Because of this, weak axis buckling was braced by the web members and buckling was only considered for the strong axis of each member individually. The unbraced length was assumed to be the entire length of the truss for each of these members. Finally, it was assumed that each of these members was behaving as a pinned-pinned column. This resulted in an effective length factor equal to 1.0 for design.

7.2 Outer Tube Capacity Design

A capacity design procedure was also developed for the outer tube. First, a free body diagram of the outer tube by itself was developed. Figure 7.2 shows the displaced shape of the SC-TMF and the free body diagram of the outer tube.

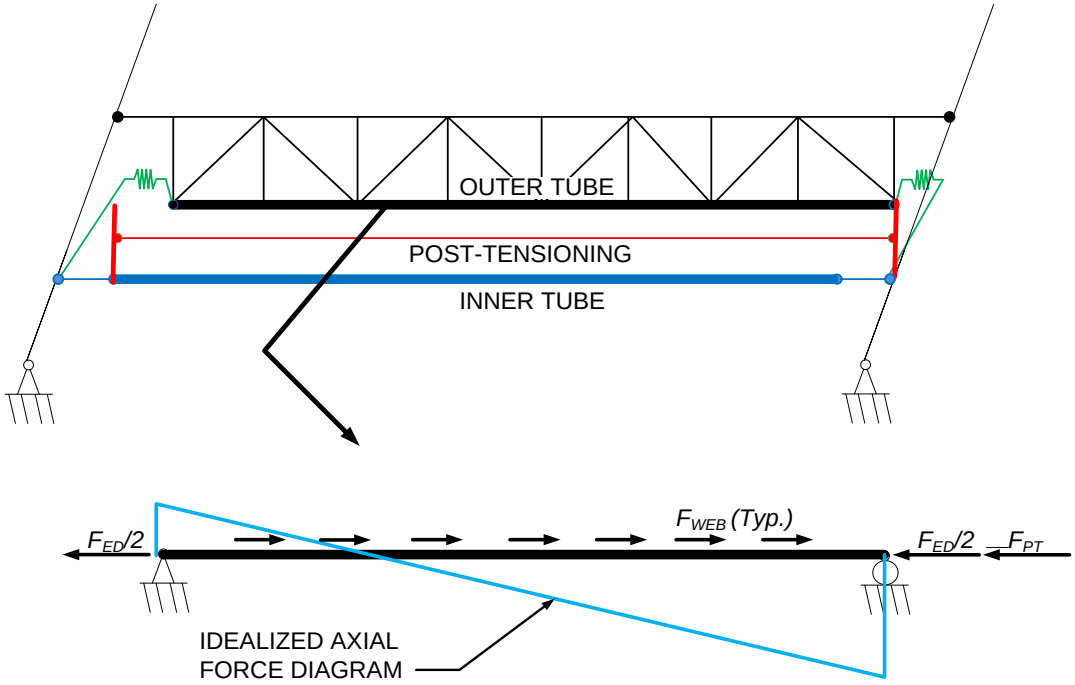

Figure 7.2: Outer Tube Capactiy Design Free Body Diagram

The maximum compression force in the outer tube is given by the equation

$$F_O = \frac{F_{ED}}{2} + F_{ptu} \qquad 6.4$$

During design, it was assumed that the truss would provide sufficient bracing to prevent buckling of outer tube in the plane of the truss. Therefore, the critical case that needed to be considered during design was out of plane buckling. The trusses utilized the outer tube set on its side (weak axis vertical), so buckling was considered for the strong axis of each member individually. The unbraced length was assumed to be the entire length of the outer tube because the truss did not

provide out of plane bracing. Finally, it was assumed that this member was behaving as a pinned-pinned column. This resulted in an effective length factor equal to 1.0 for design.

It was seen in preliminary designs (e.g. Chapter 4) that this equation resulted in forces that were larger than those used for the other two tubes. The free body diagram of the outer tube in Figure 7.2 is also overlaid by the axial force diagram. The force at each end of the tube is known from the free body diagram and the axial load is idealized as varying linearly across the length of tube.

It was expected that the non-uniform loading would allow a larger buckling load as compared with a member having constant compressive load. In order to take advantage of this fact, a fourth order ordinary differential equation (ODE) was formulated and solved for the capacity of a pin-pin column with a linearly varying load. The derivation of the ODE has a similar process as the equation developed for predicting the buckling capacity of a joist top chord that is laterally supported by a standing seam roof (Cronin and Moen 2012). Dr. Raymond H. Plaut of Virginia Tech assisted in the creation of a solution using the computational software package Mathmatica.

The boundary conditions for the ODE were set to zero deflection and zero moment at each end of the outer tube. This is based on the assumption that the outer tube is behaving as a pinned-pinned column. The equations that describe these boundary conditions are given below:

$$\begin{aligned} Y(0) &= 0 \\ Y(L) &= 0 \\ Y''EI(0) &= 0 \\ Y''EI(L) &= 0 \end{aligned} \qquad 6.5$$

Where

Y = lateral deflection in the outer chord

$Y''EI$ = the moment in the outer tube

L = total length of the outer tube (between the anchorage plates)

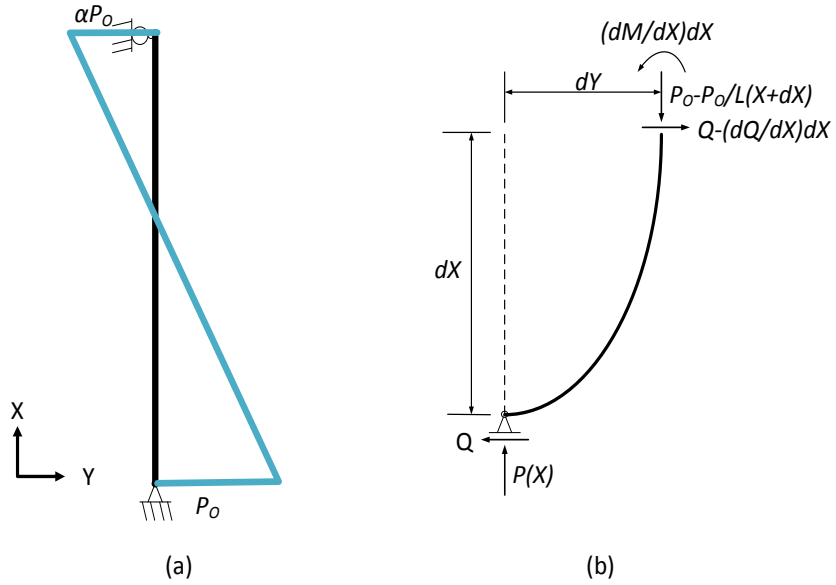

Figure 7.3: (a) Axial Load Diagram of Outer Tube (b) Cut in the Deflected Shape of the Outer Tube

The idealized axial load varies linearly along the length of the column and is represented by Equation 6.6. This load is shown graphically in Figure 7.3(a).

$$P(X) = P_o\left[1-(1-\alpha)\frac{X}{L}\right] \qquad 6.6$$

Where

P_o = The maximum compressive load in the outer tube (equal to F_O)

α = ratio of compressive load to tensile load

X = location along the length of the outer tube

The fourth order linear homogenous differential equation can then be derived using the following steps:

1. Sum the moments in the section about the pinned end of the column and solve for Q:

$$\sum M = 0 = -QdX + PdY + \frac{dM}{dX}dX \qquad 6.7$$

$$Q = \frac{dM}{dX} + P\frac{dY}{dX} = \frac{dM}{dX} + P_o\left[1-\left(1-\alpha\right)\frac{X}{L}\right]\frac{dY}{dX} \qquad 6.8$$

2. Take the derivative of Equation 6.8 with respect to *X*:

$$\frac{dQ}{dX} = \frac{d^2M}{dX^2} + \left[P_o\left[1-\left(1-\alpha\right)\frac{X}{L}\right]\frac{dY}{dX}\right]' \qquad 6.9$$

3. Sum the forces in the *Y*-direction:

$$\sum F_Y = 0 = -Q + Q - \frac{dQ}{dX}dX \qquad 6.10$$

$$\frac{dQ}{dX} = 0 \qquad 6.11$$

4. Substitute Equation 6.11 into Equation 6.9 and substitute the equation for curvature $\frac{M}{EI} = \frac{d^2Y}{dX^2}$:

$$\frac{d^2M}{dX^2} + \left[P_o\left[1-\left(1-\alpha\right)\frac{X}{L}\right]\frac{dY}{dX}\right]' = 0 \qquad 6.12$$

$$EIY'''' + \frac{d}{dX}\left[P_o\left[1-\left(1-\alpha\right)\frac{X}{L}\right]Y'\right] = 0 \qquad 6.13$$

The final equation can be made more valuable by placing the terms into non-dimensional quantities for all variables. X is normalized in Equation 6.14 as the percentage of the span that is represented by the location along the outer tube. Y is normalized in Equation 6.15 as the percentage of the span that is represented by the out of plane displacement. Finally, the maximum compressive load, P_o, is normalized by Equation 6.16.

$$x = \frac{X}{L} \tag{6.14}$$

$$y = \frac{Y}{L} \tag{6.15}$$

$$p_o = P_o \frac{L^2}{EI} \tag{6.16}$$

The following substitution can be utilized when the derivative of each variable needs to be non-dimensionalized:

$$\frac{d}{dX} = \frac{d}{dx}\frac{dx}{dX} = \frac{1}{L}\frac{d}{dx}$$

$$\frac{d^2}{dX^2} = \frac{d}{dX}\frac{d}{dX} = \frac{1}{L^2}\frac{d^2}{dx^2} \tag{6.17}$$

Using Equations 6.14-6.16, Equation 6.13 can be non-dimensionalized as follows:

$$EI\frac{d^4(Ly)}{L^4dx^4} + p_o\frac{EI}{L^2}\frac{1}{L}\frac{d}{dx}\left\{\left[1-(1-\alpha)x\right]\frac{d(Ly)}{Ldx}\right\} = 0 \tag{6.18}$$

$$y''''(x) + p_o \left\{ \left[1 - (1-\alpha)x \right] y'(x) \right\}' = 0 \qquad 6.19$$

Equation 6.19 can then be expanded using the chain rule to the following equation for use in Mathematica:

$$y''''(x) + p_o \left\{ -\left[(1-\alpha) y(x) \right] + \left[1 - (1-\alpha)x \right] y'(x) \right\} = 0 \qquad 6.20$$

The trivial solution to Equation 6.20 occurs when $y = 0$ everywhere; however, we are only concerned with the buckling solution where $y(x)$ does not equal zero. In conjunction with Dr. Raymond Plaut, a Mathmatica worksheet was utilized to solve for the buckling solution to the equation. The solution for p_o is given for a range of values of α in Table 7.1. In this worksheet, which can be found in Appendix A, the shooting method was employed. This method requires an initial guess for the first and third derivatives of $y(x)$ since these values are not defined by the boundary conditions. These values go through a series of iterations until the solution converges and all of the boundary conditions are satisfied.

One concern with the solution given by the worksheet is to verify that the correct buckling mode has been found. If the initial guesses were too large, the solution would converge on a capacity well above the capacity for the first buckling mode. This was checked by plotting the deflected shape of the tube, which can be seen in the middle of the worksheet in Appendix A.

The last step in solving the ODE was to convert the non-dimensional value p_o into a value that could readily be utilized during design. When solving for the buckling load for a given structural shape, the value of p_o needs to be converted to the dimensional quantity for the critical elastic buckling load of P_o. This conversion yields the equation:

$$P_o = \frac{p_o EI}{L^2} \qquad 6.21$$

It was immediately evident that this crucial elastic buckling load takes on a form very similar to the Euler Buckling Load used in design, which is given by the equation:

$$P_{Euler} = \frac{\pi^2 EI}{L^2} \qquad 6.22$$

To utilize the increased buckling capacity, it was important to convert the non-dimensional values into a form of Euler Buckling load for design. The resulting equation, which is shown in Equation 6.23, can then directly be implemented anywhere the Euler Buckling load is utilized in the design of the outer tube.

$$P_{cr} = \frac{\frac{p_o}{\pi^2}\pi^2 EI}{L^2} = \frac{\beta\pi^2 EI}{L^2} = \beta P_{Euler} \qquad 6.23$$

Where

β = the ratio of the critical buckling load to the Euler buckling load.

$\beta = p_o / \pi^2$

This solution method was completed for values of α between -1.0 and 1.0. Negative values of α indicate that the far end of outer tube is in tension, while positive values indicate that it is in compression. The results are summarized in Table 7.1 and Figure 7.4.

Table 7.1: ODE Solution Results

α	p_o	β
-1.0	41.58	4.21
-0.8	35.77	3.62
-0.6	30.46	3.09
-0.4	25.77	2.61
-0.2	21.80	2.21
0.0	18.56	1.88
0.2	15.98	1.62
0.4	13.93	1.41
0.6	12.29	1.25
0.8	10.96	1.11
1.0	9.87	1.00

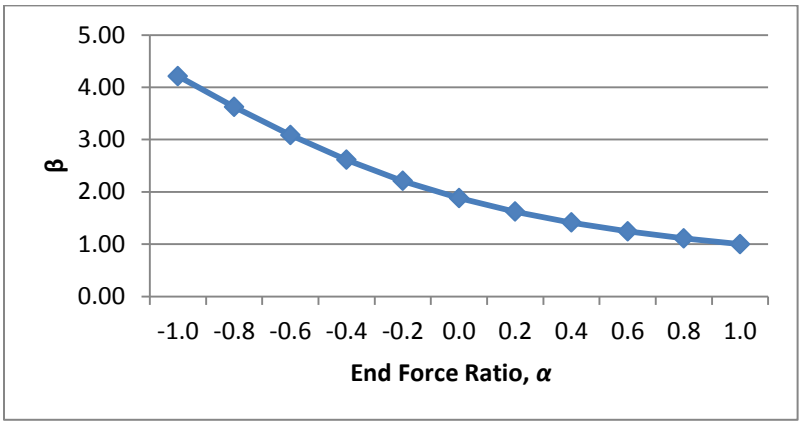

Figure 7.4: Euler Buckling Modification Factor for Varying Values of α

Figure 7.4 clearly shows that as the system approaches a constant load, the Euler Buckling Modification Factor, β, approaches 1; however, for the design of the outer tube, the capacity design indicated that the opposite end would be in tension. This results in a modification factor greater than 2 for all values of α. One problem with assuming a tension on the far end of the tube is that it assumes that the fuse at that end is applying the tensile force. If the energy dissipation bar is not installed properly or if it ruptures during loading, then that end of the outer tube would experience zero force and a design assuming any level of tension would be unconservative. Because of this, the outer tubes were designed using $\alpha = 0$ ($\beta = 1.88$).

7.3 Parametric Study Results: Capacity Design of Inner Tube and Top Chord

During the monotonic static pushover analysis, the forces in the top chord, bottom chord inner tube, and bottom chord outer tube were recorded. For each member, the maximum force occurred when the post-tensioning yielded. For a small subset of the models, post-tensioning yield did not occur prior to the analysis reaching its maximum roof drift ratio of 20%. In these cases, the maximum forces in the members were taken as the final forces from the monotonic pushover. Then, the force ratio was computed as the ratio of the maximum force to the design

force. Ratios less than or equal to 1.0 indicate that design equation is adequate or conservative, whereas values greater than one indicate an inadequate design.

Figure 7.5 and Figure 7.6 show the force ratios in 24 in SC-TMFs for the inner tube in peak compression forces and inner tube peak tension forces, respectively. In the initial capacity design approach, it was assumed that the loading would be symmetric such that the moments applied on each end were equal. This resulted in the tension force being equal to the compression force in the inner tube. However, Figure 7.5 clearly indicates that the compression force developed in the inner tube is significantly less than the force predicted by Equation 6.3. In contrast, the tension forces in the inner tube were grossly underestimated using the same equation. This was the first sign that the assumption that loading was symmetric was invalid and that the moment on the side of the truss where the inner tube was in tension was greater. Similar results are shown for the remaining truss sizes in Appendix B.1 and B.3.

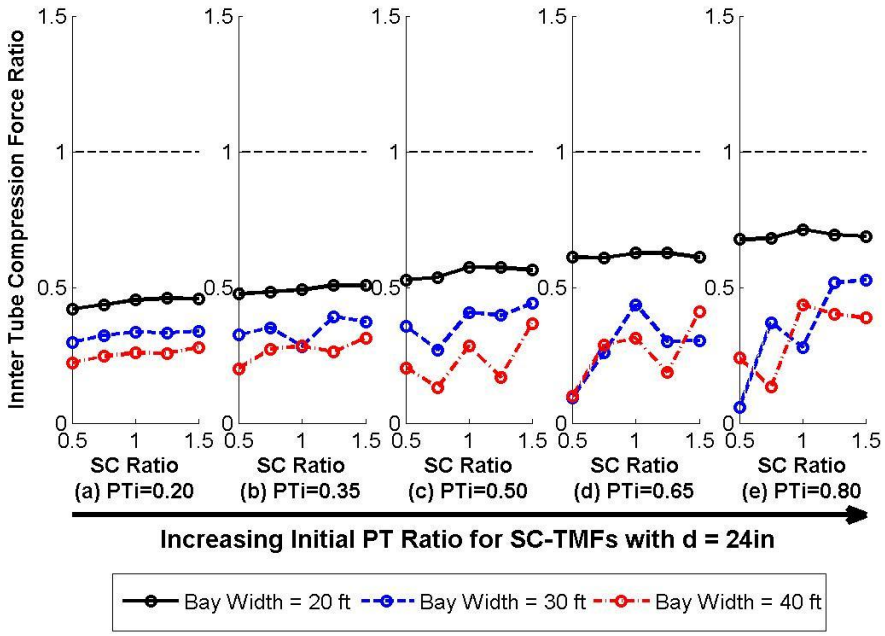

Figure 7.5: Inner Tube Compression Force Ratios for 24in SC-TMFs using Equation 6.3

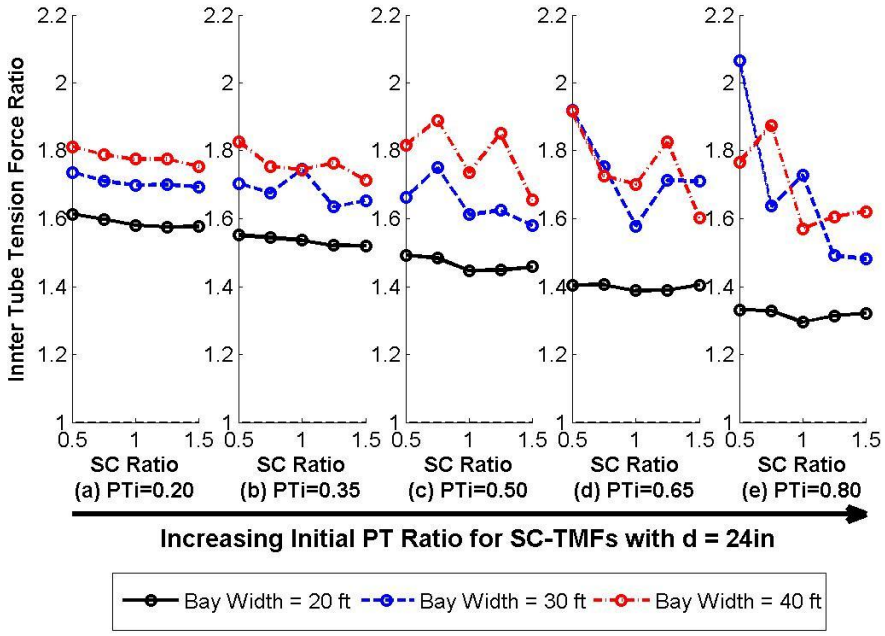

Figure 7.6: Inner Tube Tension Force Ratios for 24in SC-TMFs using Equation 6.3

Figure 7.7 and Figure 7.8 show similar results for the compression and tension force ratios in the top chord when compared to the values developed by Equation 6.2. Plots for additional depths can be found in Appendix B.5 and *B.7*. In the top chord, the tension forces have generally been overestimated, while the compression forces have been underestimated. This is the exact opposite of what occurred in the inner tube, which is logical because the compression in the inner tube develops a force couple with the tension in the top tube on one end of the truss while the tension in the inner tube develops a force couple with the compression in the top tube. The paired increase and decrease in the forces on each side of the truss confirms that the moments on each end are uneven. Based on this fact, it was necessary to develop new equations for the forces in the top and bottom chord that check for tension and compression separately.

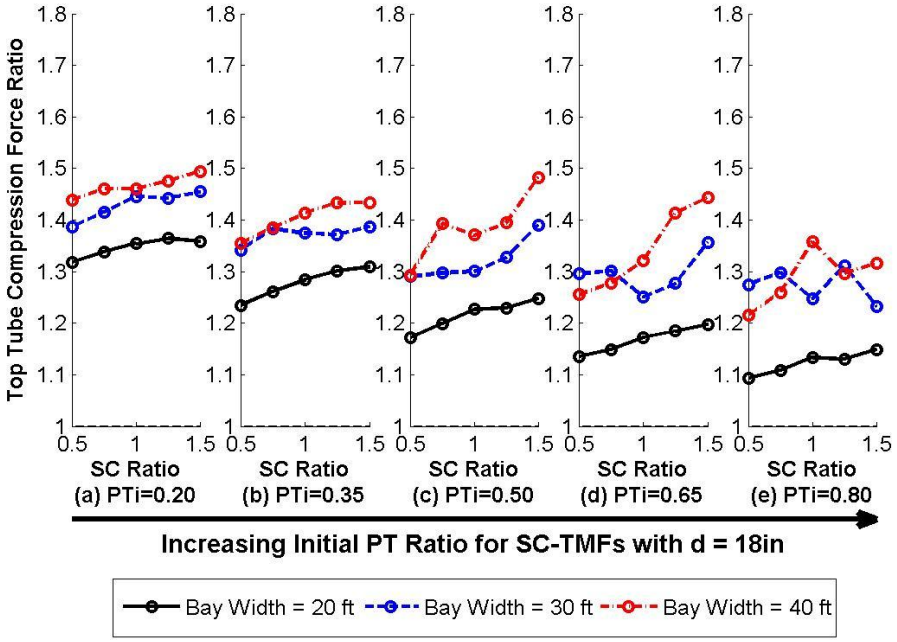

Figure 7.7: Top Chord Compression Force Ratios for 24in SC-TMFs using Equation 6.2

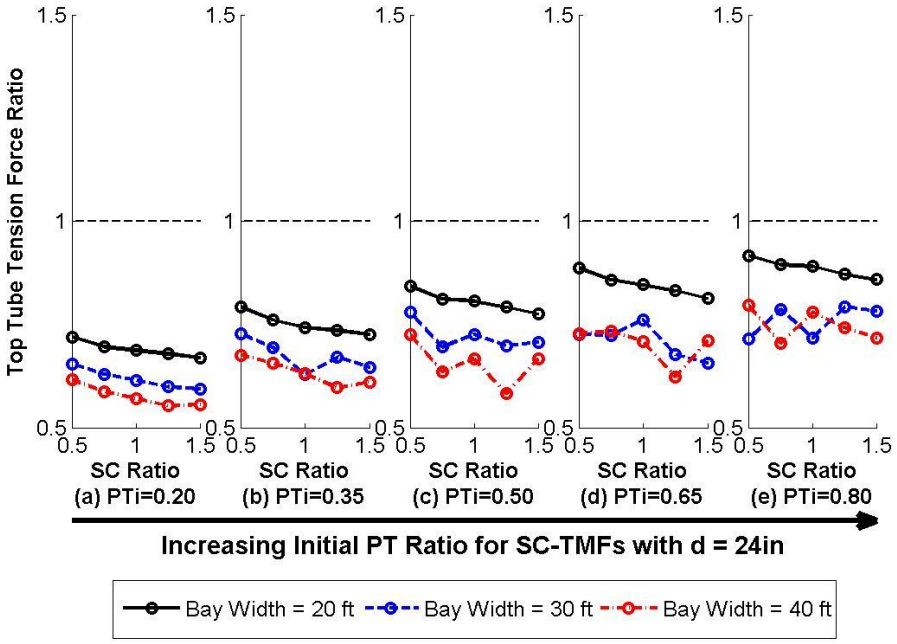

Figure 7.8: Top Chord Tension Force Ratios for 24in SC-TMFs using Equation 6.2

In order to develop new equations for capacity design, it was necessary to determine the mechanics that were causing the unbalanced loading. The results of that investigation determined that the unbalance was caused by the behavior of the inner tube and its connection to the column. Figure 7.9 shows a free body diagram of the forces applied to the inner tube. In this diagram, the only external force acting on the inner tube is the ultimate force developed in the post-tensioning, F_{ptu}. At this level in the truss, the forces in the energy dissipating components are being transferred directly into the column and do not affect the inner tube. The post-tensioning force is transferred into the inner tube by end plate that anchors the post-tensioning. This places the short end section at the left of the inner tube in tension, and the rest of the inner tube in compression.

Figure 7.9: Inner Chord Free Body Diagram

Based on the results from the parametric study, it was determined that the length of the tension and compression portions of the inner tube was causing an unbalance in the axial stiffness of these two portions of the inner tube. In general, axial stiffness can be calculated as AE/L, where A is the cross sectional area, E is the modulus of elasticity of the material, and L is the length of the element. The computational model includes the assumption that the connection regions at the ends of the inner tube have the same cross sectional area as the inner tube. This means that the only difference in the stiffness equation was caused by the length. Because the portion in tension is significantly shorter, it has higher axial stiffness and attracted greater levels of force.

An equation was developed to describe the tension in the inner tube, F_{IT}, that related the magnitude of the force to the ratio of the stiffnesses calculated using the equation above. Because it was assumed that the column connection region had the same area as the inner tube,

the ratio of stiffnesses simplified to the ratio of lengths seen in Equation 6.24. This method provided a more accurate estimate for the tension in the inner tube, but was generally too conservative. A ten percent reduction in this value gave more accurate estimates of the tension force and resulted in the following equation.

$$F_{IT} = 0.9\left(1-\frac{L_{IT}}{L_{IC}}\right)F_{ptu} = 0.9\left(1-\frac{L_{IT}}{L_{IC}}\right)\left(f_{pu}A_{pt}\right) \qquad 6.24$$

where

F_{IT} = ultimate tension force in the inner tube

L_{IT} = length of the connection region connecting the inner tube to the column

L_{IC} = length of the inner tube that is in compression

f_{pu} = ultimate stress for the post-tensioning material

A_{pt} = cross sectional area of the post-tensioning

Figure 7.11 shows the force ratios for the tension in the inner tube compared to the value predicted by the new equation for the 24in SC-TMFs. Plots for the remaining truss depths can be found in Appendix B.2. These plots show that the design equation (Equation 6.24) produces accurate if not slightly conservative estimates of the maximum forces delivered to the inner tube. It is evident that the data shows a greater scatter as the initial post-tensioning ratio is increased. This fact is not taken into account in the current design, but the influence of post-tensioning ratio should be investigated in future research into SC-TMFs. Despite the fact that the influence of initial post-tensioning ratio is not included, Equation 6.24 generally remains conservative and based on this study appears sufficient for a capacity based design approach.

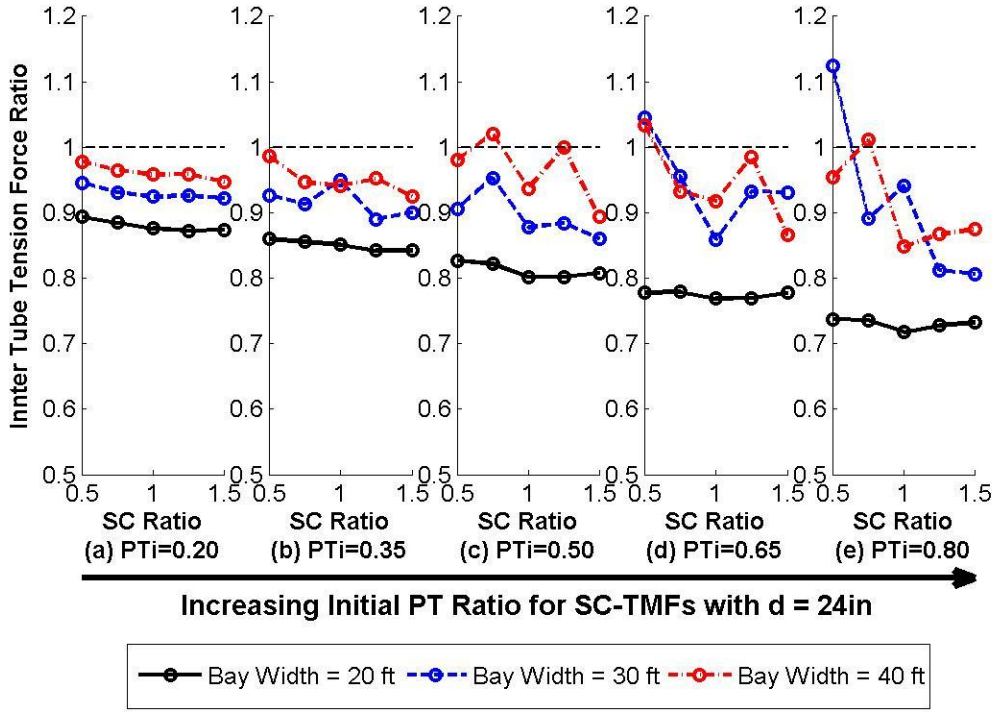

Figure 7.10: Inner Tube Tension Force Ratios for 24in SC-TMFs using Equation 6.24

In contrast to the tension force, using a ratio of the stiffnesses did not provide an accurate description of the compression force in the inner tube. Any rational attempt to utilize this method grossly underestimated the compression force. Absent of a full mechanics based explanation, a ratio of the ultimate post-tension force was calibrated based on the parametric study results. The following equation was developed to describe the maximum compression force in the inner tube, F_{IC}.

$$F_{IC} = -0.35F_{ptu} = -0.35\left(f_{pu}A_{pt}\right) \qquad 6.25$$

Figure 7.11 shows the force ratios for the tension in the inner tube compared to the value predicted by the new equation for the 24in SC-TMFs. Plots for the remaining truss depths can be found in Appendix B.4. These plots show the new equation is not very accurate, but it provides

a conservative estimate for use in the capacity based design. They again show the increase in scatter as the initial post-tensioning ratio increases.

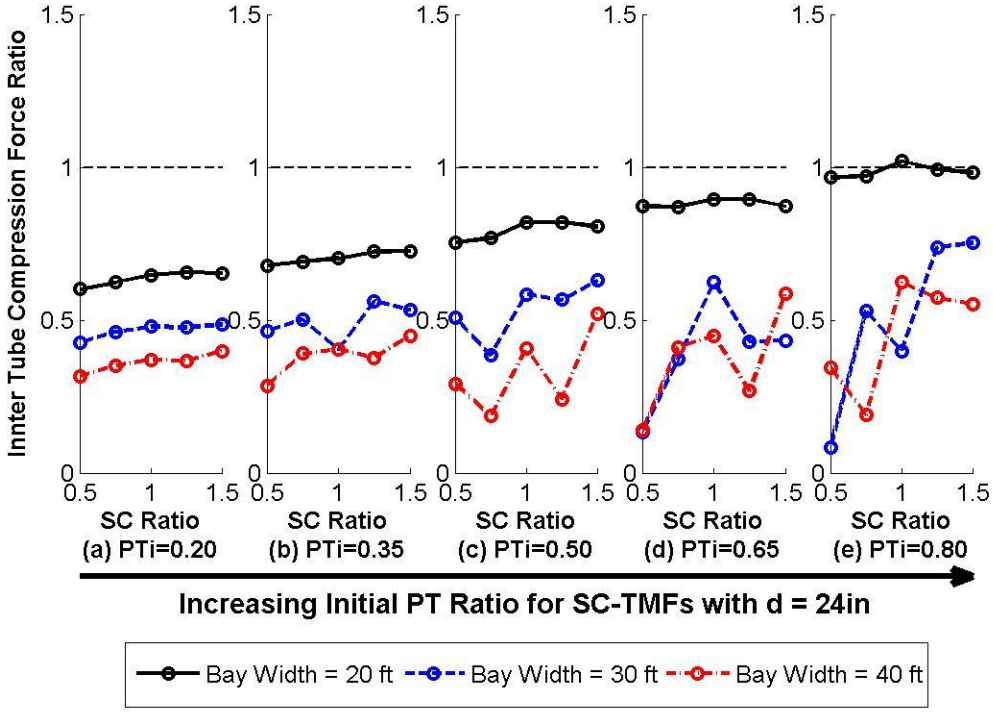

Figure 7.11: Inner Tube Compression Force Ratios for 24in SC-TMFs using Equation 6.25

Similar approaches are employed in developing new equations to describe the forces in the top chord. The compression force in the top chord, F_{TC}, is based on adding the design bottom chord inner tube tension force and the ED bar tension force that is transferred directly to the column. Since the top chord compression force makes a couple with the tension forces at the bottom chord level, the forces are assumed equal and opposite. Similar logic is used to obtain the top chord tension force, F_{TT}, as the opposite of the bottom chord inner tube design compression force added to the ED bar compression force. The resulting equations for F_{TC} is:

$$F_{TC} = -F_{IT} - \frac{F_{ED}}{2}$$
$$F_{TC} = -0.9\left(1 - \frac{L_{IT}}{L_{IC}}\right)F_{ptu} - \frac{F_{ED}}{2} \qquad 6.26$$
$$F_{TC} = -0.9\left(1 - \frac{L_{IT}}{L_{IC}}\right)\left(f_{pu}A_{pt}\right) - \frac{F_{ED}}{2}$$

The resulting equation for F_{TT} is:

$$F_{TT} = -F_{IC} + \frac{F_{ED}}{2}$$
$$F_{TT} = 0.35F_{ptu} + \frac{F_{ED}}{2} \qquad 6.27$$
$$F_{TT} = 0.35\left(f_{pu}A_{pt}\right) + \frac{F_{ED}}{2}$$

Figure 7.12 and Figure 7.13 depict the force ratios that result from the new equations for the forces in the top tubes of the 24in SC-TMFs. Plots of the additional depths can be found in Appendix B.6 and B.8, respectively. These figures show very similar trends to those seen for new inner tube equations. The new equations are generally conservative and, based on this study, are expected to provide adequate force predictions in a capacity based design approach.

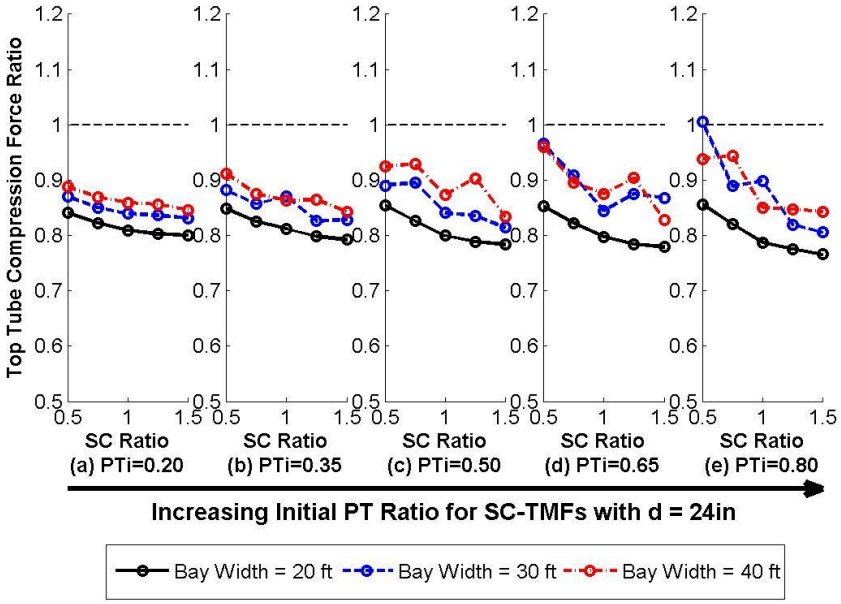

Figure 7.12: Top Chord Compression Force Ratios for 24in SC-TMFs using Equation 6.26

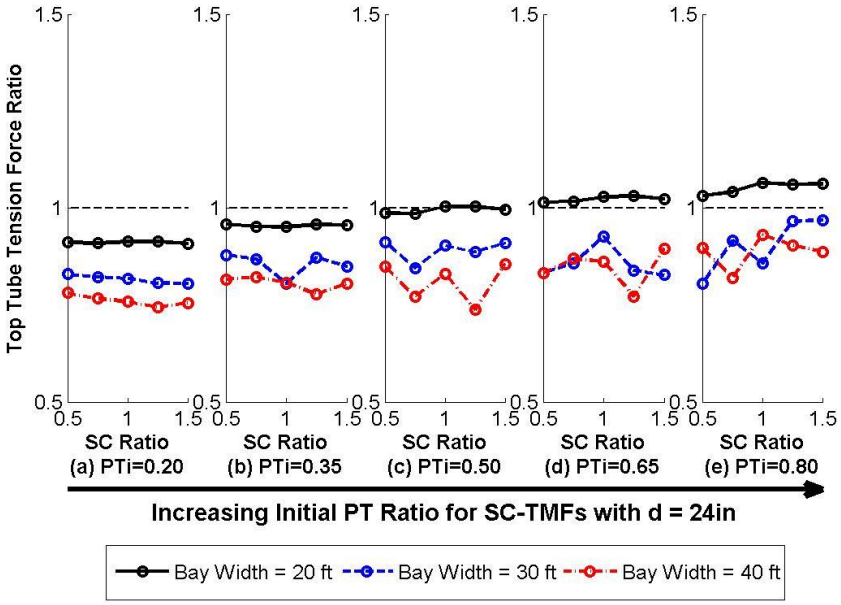

Figure 7.13: Top Chord Tension Force Ratios for 24in SC-TMFs using Equation 6.27

7.4 Parametric Study Results: Capacity Design of Outer Tube

Figure 7.14 shows an example of the force ratio measured in the outer tube for the 24 inch deep SC-TMFs. Plots for the additional truss depths can be found in Appendix B.9. Here it is evident that the Equation 6.4 is conservative for the trusses with a 20ft and 40ft bay widths; however, the equation very accurately predicts the force in the outer tube for the 30ft bay width. The major difference between these two configurations is the number of panels that exist for each bay width. The 20ft and 40ft SC-TMFs each have an even number of panels: 6 and 12, respectively. In contrast, the 30ft trusses have nine panels along the length of the members. Because of the alternating direction of the web diagonals, if there is an odd number of panels, the final diagonal will connect to the top chord (instead of the outer tube) at one end. This concept is depicted in Figure 7.15. In this figure, it is evident how a change in the number of panels alters where the final diagonal (on the right) is connected.

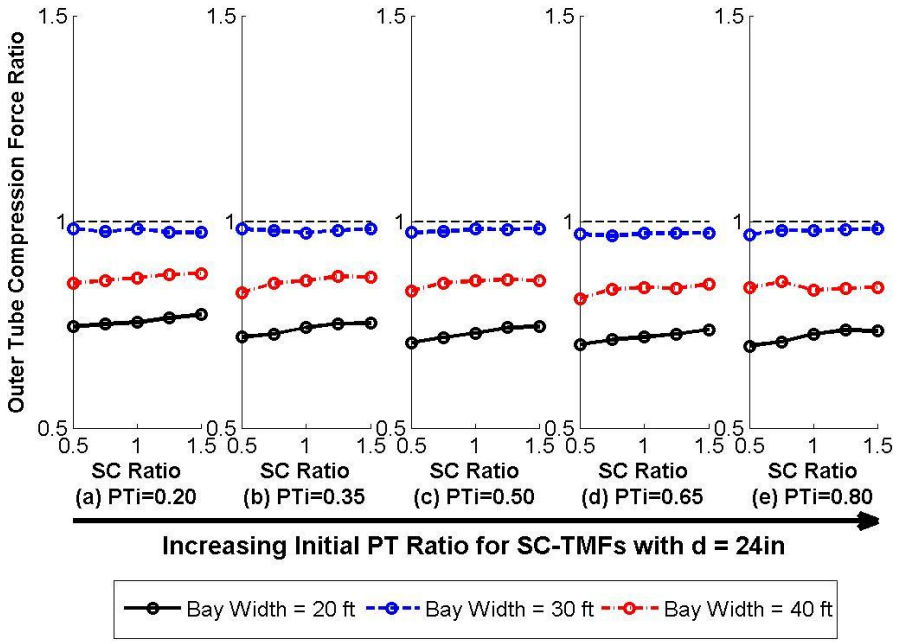

Figure 7.14: Compression Force Ratio in the Outer Tube using Equation 6.4

When there is an even number of panels (20’ and 40’ trusses shown in Figure 7.15), the final diagonal will always connect to the bottom chord outer tube at the ends of the truss. When this occurs, a portion of the load applied to the outer tube is taken by the first diagonal, reducing the maximum load that the outer tube must carry. In contrast, when the final diagonal connects to the top tube (30’ bay width as shown in Figure 7.15), the entire force is transferred through the bottom chord outer tube along the first panel. Equation 6.4 takes this fact into account and assumes that the full load is always taken by the outer tube. This is a conservative assumption, but it is recommended for more general use.

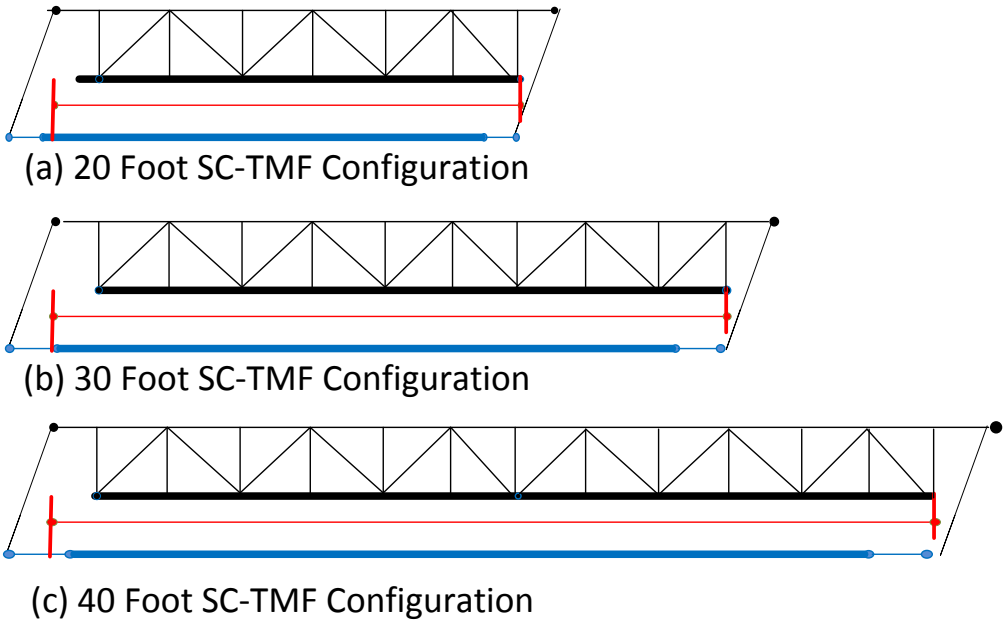

Figure 7.15: SC-TMF Configurations for (a) 20ft bay, (b) 30ft bay, and (c) 40ft bay

Chapter 8. Parametric Study Results

8.1 Interstory Drift at Post-Tensioning Yield

The interstory drift at post-tensioning yield is an important quantity because it defines the ultimate displacement the system can undergo while retaining its moment capacity and self-centering properties. If the post-tensioning is allowed to yield, some of the initial compression in the tubes will be lost, post-tensioning strands may fracture, the gap opening moment and related moment capacity will be reduced, and the self-centering capability may be compromised. For this reason, it is desirable to prevent post-tensioning yield for the interstory drifts associated with a maximum considered earthquake.

For the purposes of this discussion, a target of preventing post-tensioning yield up to 6% story drift is selected. This limit has been developed based on a combination of drift criteria. First, the prequalification of special steel moment frames, requires testing up to an interstory drift ratio of 4%. This requirement exceeds the drift limits used in design, 2% for the Design Basis Earthquake (DBE) (ASCE 2010).

The target interstory drift of 6 percent before post-tensioning yield provides a factor of safety of 1.5 on the prequalification drift requirement and a factor of safety of 3 for the DBE level ground motions. These factors of safety are included in the proposed SC-TMF design procedure until the behavior of the system after post-tensioning yield is better understood. Further nonlinear dynamic analysis of a variety of building archetypes, using models that capture post-tensioning behavior up to large strains, would help to determine how each truss will interact with the rest of the seismic force resisting system. Based on the results of such a study, the need for these factors of safety on current drift requirements could be adjusted appropriately.

8.1.1 Initial Post-Tensioning Ratio Design

Figure 8.1 through Figure 8.3 summarize the drift at which all of the models for a given truss depth experienced post-tensioning yield. The lines represent the median value for interstory drift at each initial post-tensioning ratio while the brackets show the minimum and maximum value at that post tensioning ratio. The plots have been subdivided based on the bay width and the curves are subdivided based on the depth of the truss. A horizontal line has been included at 6 percent interstory drift to visually represent the requirement discussed above.

Based on these three figures, it is evident that the interstory drift at which post-tensioning yield occurs is significantly affected by the bay width, truss depth, and initial post-tensioning ratio. The interstory drift at post-tensioning yield tends to increase with increasing bay width, which was expected because the increased length of the post-tensioning component means that the strain required to achieve the same gap openings, and therefore drift ratios, is decreased. In contrast, the interstory drift at post-tensioning yield decreases with increasing truss depth because the increased depth moves the post-tensioning component farther from the center of rotation, which requires greater gap opening and post-tensioning elongation to achieve the same level of rotation. Finally, the initial post-tensioning ratio is inversely proportional to the interstory drift at post-tensioning yield, because the increased initial post-tensioning force leaves less deformation capacity for additional displacements. In design, the bay width is generally a value that is set by the architect before structural design begins. Figure 8.1 through Figure 8.3 can be used to get an initial idea of which truss depths are reasonable for each bay width and which initial post-tensioning ratio should be utilized for that bay width and truss depth.

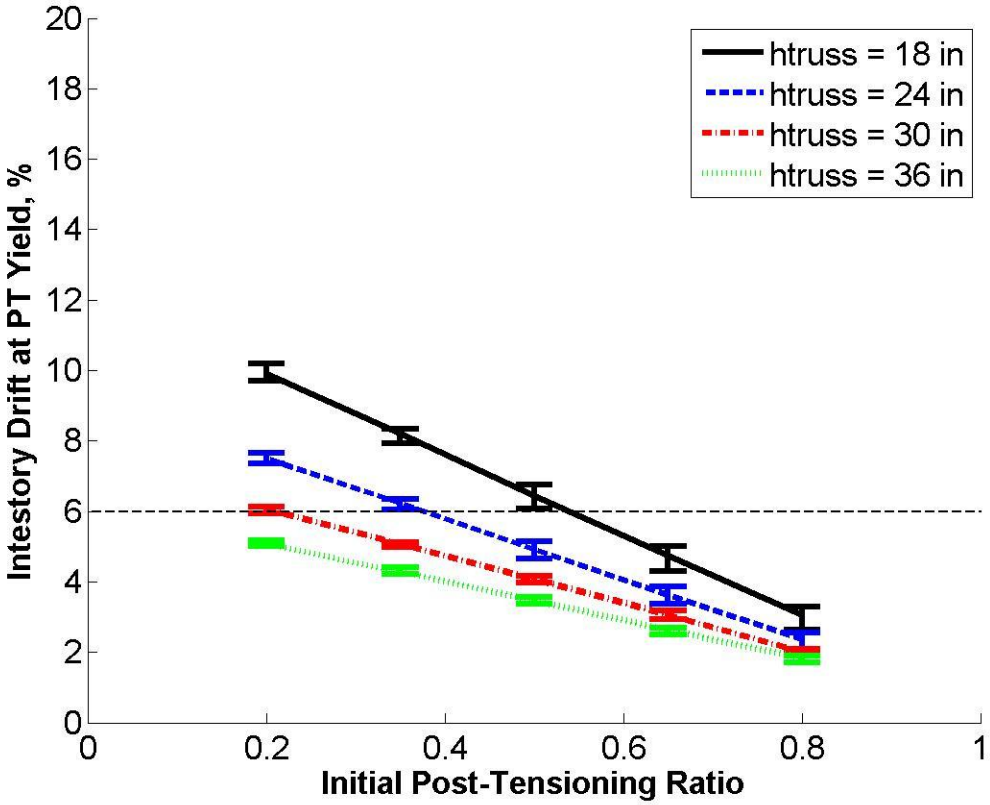

Figure 8.1: Interstory Drift at PT Yield for SC-TMF 20ft Bay Width

Figure 8.1 shows the interstory drift at post-tensioning yield for SC-TMFs with 20 foot bay widths. Based on the plot, it is recommended that 18 and 24 inch trusses are utilized when bay widths of 20ft are specified. For an 18in SC-TMF, an initial post-tensioning ratio of 0.50 can be utilized, while a 24in truss should use a ratio of 0.35 or less. A limited number of 30in trusses would have sufficient deformation capacity when the initial post-tensioning ratio is set to less than 0.20. None of the 36 in deep trusses meet the selected deformation capacity criteria.

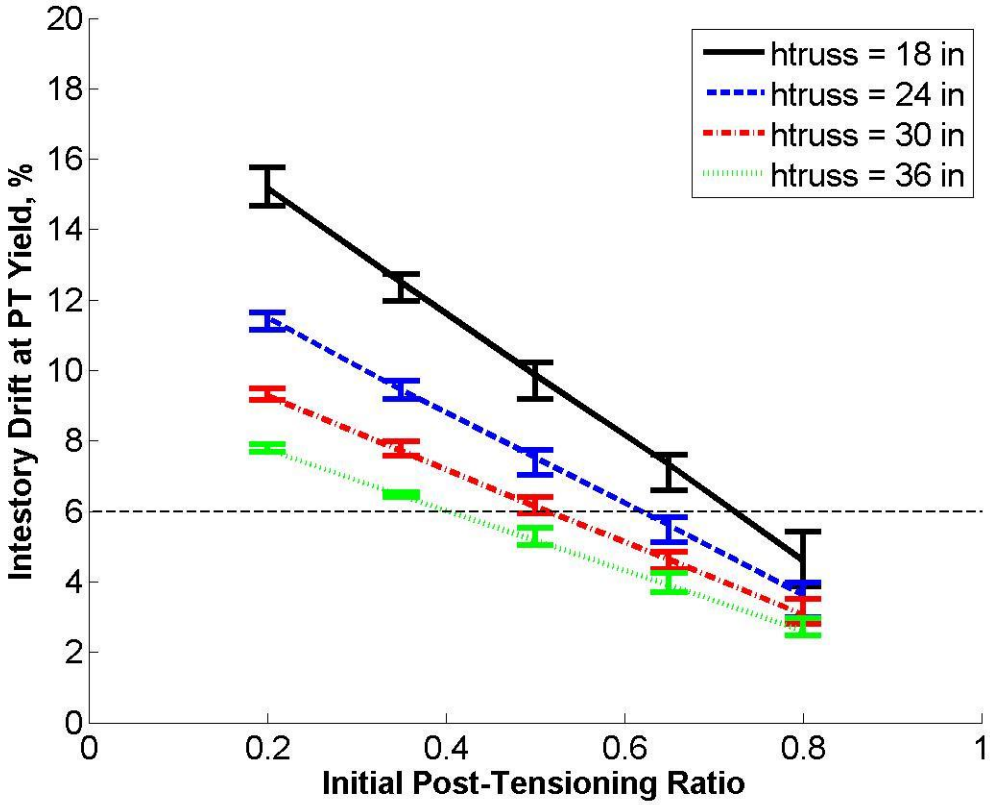

Figure 8.2: Interstory Drift at PT Yield for SC-TMF with 30ft Bay Width

Similarly, Figure 8.2 shows the interstory drift at post-tensioning yield for SC-TMFs with 30 foot bay widths. All of the truss depths have sufficient deformation capacity at various levels of initial post tensioning. Based on the models tested, it is recommended that initial post-tensioning ratios are limited to a maximum value of 0.65 for 18in SC-TMFs, 0.50 for 24 and 30 inch SC-TMF's, and 0.35 for 36in SC-TMF's. However, it is evident that some of these depths may have more deformation capacity than what is recommended. For example, it is recommended that initial post-tensioning ratio for the 24 inch deep truss is limited to 0.50, but the curve shows that it may have sufficient deformation capacity at ratios up to approximately 0.60. In these cases, it is possible to exceed the recommended ratio by interpolating along the design curves during the initial design because the deformation capacity will have to be checked later on for the specific design that is developed.

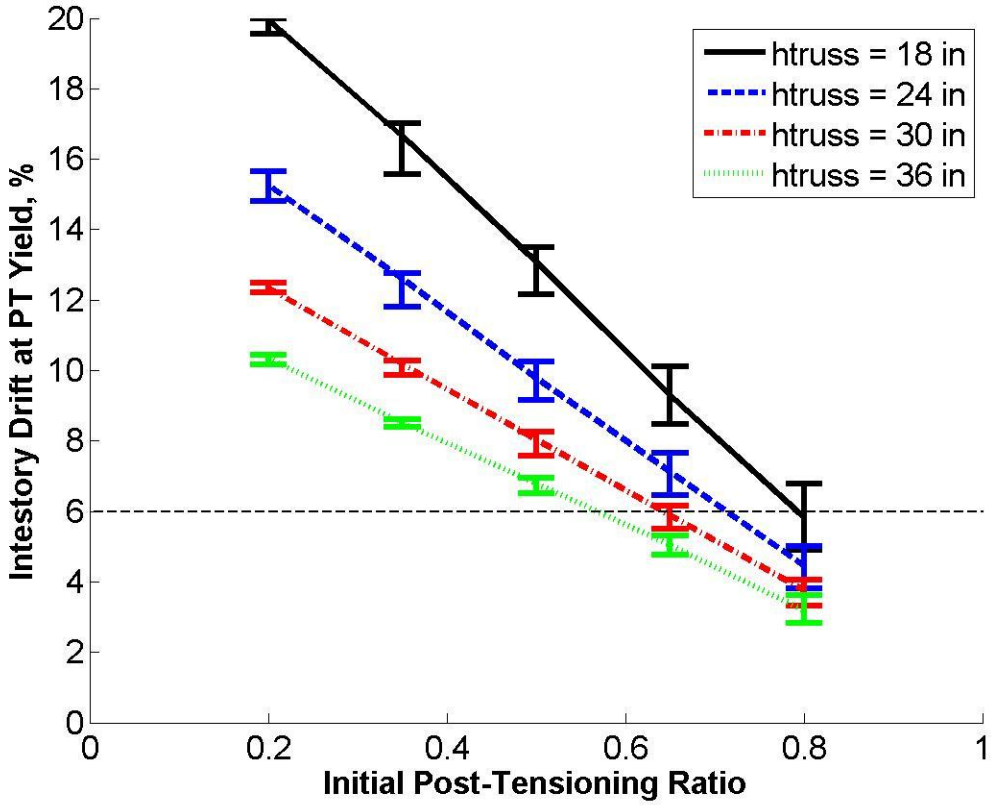

Figure 8.3: Interstory Drift at PT Yield for SC-TMF with 40 ft bay width

Finally, Figure 8.3 shows the interstory drift at post-tensioning yield for SC-TMFs with 40 foot bay widths. All of the truss depths have sufficient deformation capacity at various levels of initial post tensioning. Based on the models tested, it is recommended that initial post-tensioning ratios are limited to 0.65 for 18in SC-TMFs. However, a select set of the 18 in SC-TMF reach an adequate interstory drift at post-tensioning yield when designed with a ratio of 0.80. Initial post-tensioning ratios of 0.65 for 24 SC-TMFs, 0.50 for 30 and 36in SC-TMF's are recommended.

Table 8.1: Recommended Initial Post-Tensioning Ratio for Various Bay Widths and Truss Depths

	Recommended Maximum Initial PT Ratio for Various Bay Widths		
Truss Depth	**20 ft bay**	**30 ft bay**	**40 ft bay**
18 inch	0.50	0.65	0.65
24 inch	0.35	0.50	0.65
30 inch	0.20	0.50	0.50
36 inch	NA	0.35	0.50

The recommended interstory drifts for initial design are summarized in Table 8.1. Suggested initial post-tension ratios may be interpolated for intermediate values of truss depth and bay width.

8.1.2 Detailed Design – Initial Post Tensioning Ratio

Figure 8.4 shows the interstory drift at post-tensioning yield on a model by model basis for SC-TMF's with a self-centering ratio of 1.0. There is very little deviation between the behavior of the truss at the different design moment levels, so the medium level models are shown below. The subplots divide the models by truss depth, and each curve represents a different bay width. Similar plots for additional self-centering ratios can be found in Appendix C. Once the SC-Ratio, Truss Depth, and Bay Width have been set for a design, these plots can be used to verify that the initial post-tensioning ratio selected is adequate. Each point represents an individual model and linear interpolation can be utilized to determine more precise post-tensioning ratio for alternate design input values.

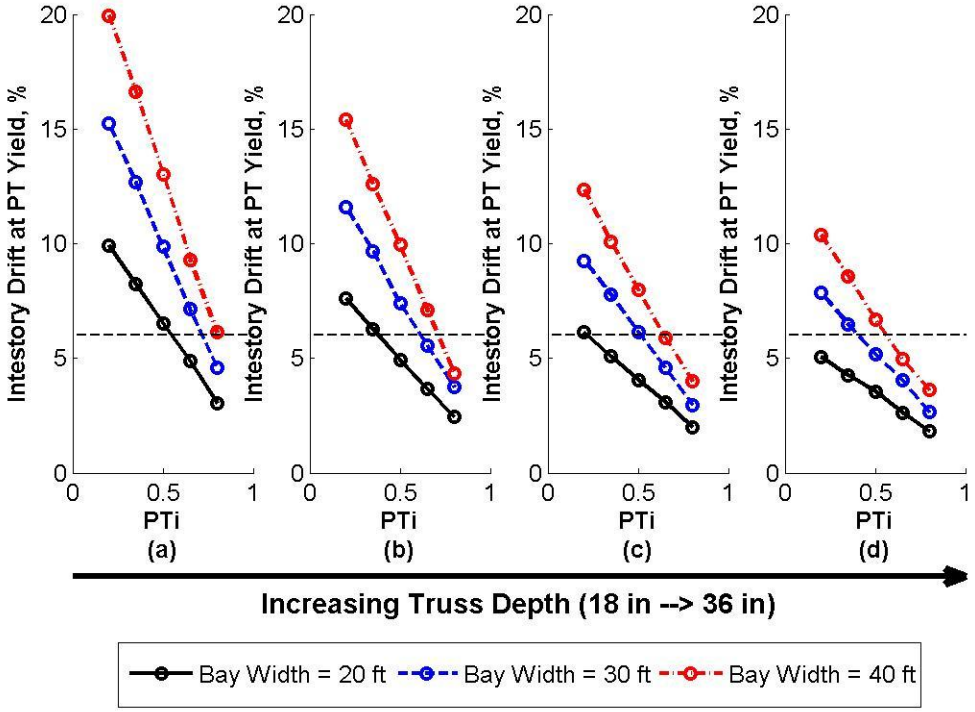

Figure 8.4: Initial Post-Tensioning Ratio for SC-TMF with SC Ratio = 1.0 and Medium Moment

8.2 Drift at Zero Force

A primary performance objective for the SC-TMF system is to nearly eliminate residual drifts following large ground motions. This is done to reduce repair costs associated with distributed plasticity that is seen in conventional seismic force resisting systems. Therefore, residual drifts are a key factor in the development of this self-centering seismic system. The target level of residual drifts is set as the limits for out of plumb described in the AISC code of standard practice (AISC 2010a) for new construction.

Values of interstory drift at zero force were recorded for the final cycle loading during the cyclic pushover analyses. This magnitude of drift represents the maximum possible residual drifts if the load were slowly removed from the peak drift ratio of 4%. Figure 8.5 shows the interstory

drift at zero force for the 24 inch SC-TMFs. Results for the remaining truss depths can be found in Appendix D. These plots show the interstory drift at zero force approaches zero when the self-centering ratio is equal to or greater than 1.0. These results seem logical because the hysteretic curves for these types of systems are the flag shaped hysteretic loops that limit drift near zero force. Example hysteretic curves have been shown above in Section 6.2. In contrast, models with self-centering ratios less than 1.0 have significantly higher levels of interstory drift when the forces are removed from the model. However, this value is not necessarily representative of residual drifts that the system might experience following dynamic earthquake motions.

Load-deformation behavior that returns to near zero drift when the forces are removed is sometimes referred to as having full self-centering. This type of self-centering occurs because the force developed by the restoring force component, such as the post-tensioning in the SC-TMF, is able to overcome the yield force of the fuse components. This creates the flag shape hysteresis that is indicative of full self-centering, eliminating drifts when the system is unloaded.

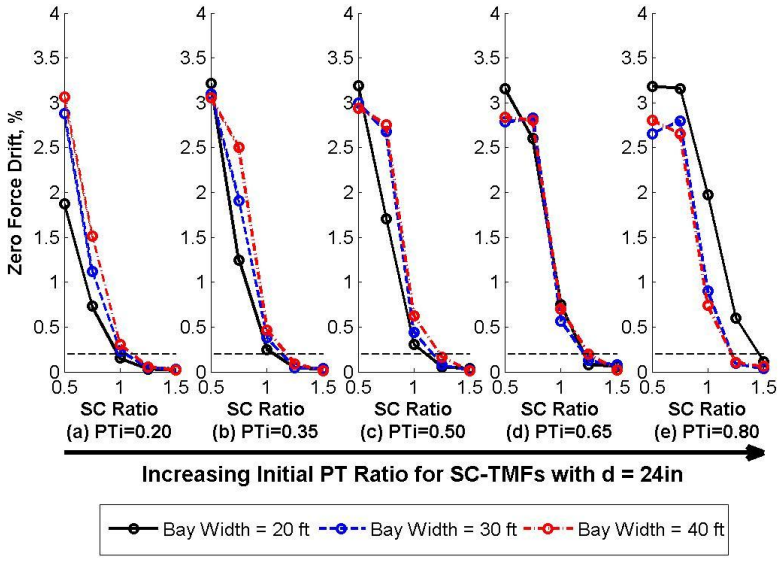

Figure 8.5: Zero Force Drift for SC-TMF with Depth = 24 inches

A second type of self-centering has been identified as probabilistic self-centering (Eatherton and Hajjar 2011). This type of self-centering occurs when a statistical probability exists that the

inelastic deformations are more likely to occur towards zero displacement than they are to occur away from zero while a system is loaded dynamically. The increased probability of yielding toward zero force is based on the fact that, when any amount of restoring force is present, the yield force in the direction of zero displacement is always less than the yield force in the opposite direction. This fact is depicted in Figure 8.6. In this figure, the initial interstory drift ratio is equal to 0.2%. The yield force that must be reached to develop yielding away from zero displacement, F_{py}, is significantly larger than the yield force that will cause deformations toward zero displacement, F_{ny}.

Figure 8.7(a) depicts the probability distribution any force is obtained in the subsequent load step during dynamic loading. The shaded portions under this curve represent the probability that the yield force is surpassed in either direction. In this example, the probability that the next load step will produce a force less than F_{ny} is 34%, while the probability of producing a force greater than F_{py} is only 14%. Figure 8.7(b) depicts how these probabilities vary with various initial interstory drifts. These curves show that at an initial drift ratio of zero, the probability of yielding in either direction is equal. However, as the initial interstory drift increases, the probability of reaching the negative yield force is increased while the probability of reaching the positive yield force is decreased. Based on these values, the probability that the system will yield toward zero displacement can be calculated. This probability is represented by the dotted curve in Figure 8.7(b). For the example with initial drift ratio of 0.2%, there is a 71% chance that the inelastic deformations will be toward zero displacement. This probability asymptotically approaches 1.0 as the initial interstory drift ratio is increased (Eatherton and Hajjar 2011).

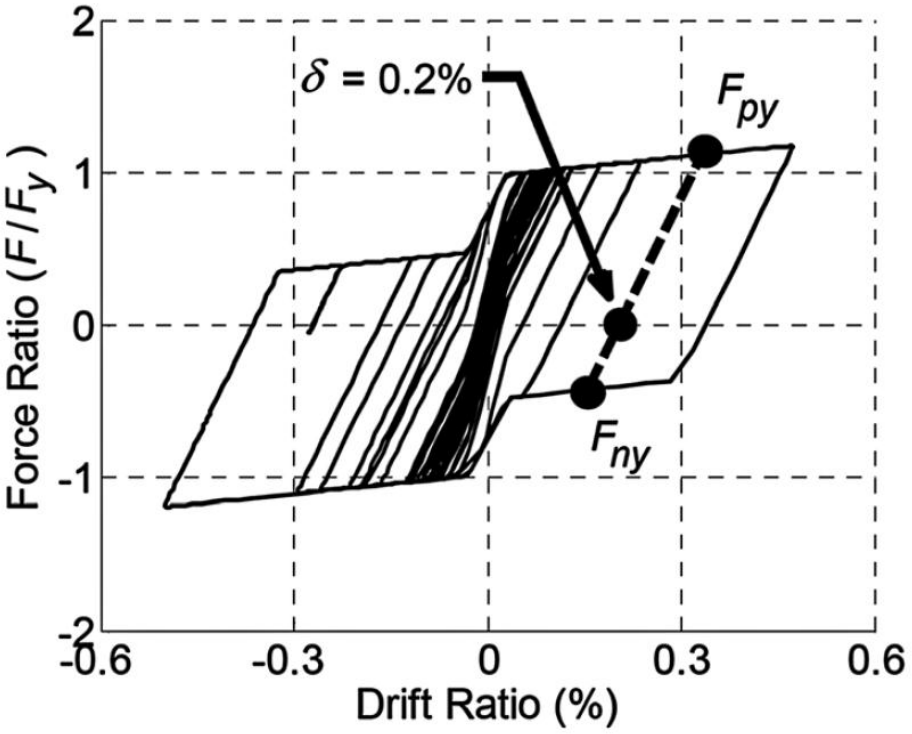

Figure 8.6: Load deformation response of a self-centering system without full self-centering behavior [from (Eatherton and Hajjar 2011)] [Used under fair use, 2012]

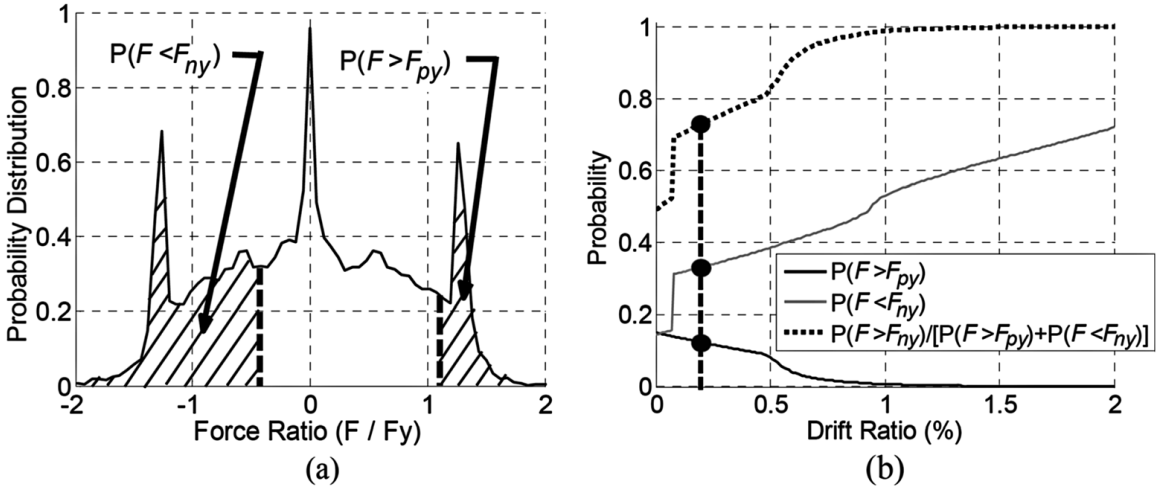

Figure 8.7: (a) Probability distribution for force ratios exceeding the yield force (b) probability curves for various drift ratios [from (Eatherton and Hajjar 2011)] [Used under fair use, 2012]

These plots ultimately show that even systems without full self-centering capability have a propensity to self-center when subjected to dynamic loading. Similar probability curves were shown for systems with varying self-centering ratios.

Because of this second type of self-centering, it is expected that systems exhibiting drift at zero force that is larger than the target, may still achieve self-centering performance. Configurations without full self-centering (self-centering ratio less than 1.0) should be further studied through nonlinear, multi-degree of freedom dynamic analyses in order to understand which ones will provide sufficient restoring force to limit residual drifts. However, based on the recorded drifts associated with zero force, it is expected that systems with self-centering ratios equal to or greater than 1.0 will likely produce self-centering behavior.

8.3 Energy Dissipation Ratio

The energy dissipation ratio is ratio that compares the energy dissipated by the flag-shaped hysteresis curve of a self-centering system during the final cycle of loading to an idealized full hysteresis curve that circumscribes the SC hysteresis curve. Two methods are currently employed in reporting this ratio. The first utilizes a bilinear hysteresis that matches the stiffness of the self-centering system just before and just after unloading. The second utilizes an elastic-perfectly-plastic, EPP, hysteretic that only matches the unloading stiffness of the self-centering system. Because there is not a consensus on how to report energy dissipation in self-centering systems, both values have been reported below.

Figure 8.8 shows the energy dissipation ratio based on a bilinear hysteretic for the 30 inch SC-TMFs. Energy dissipation ratios for the remaining truss depths are reported in Appendix E in Figure E.1 through Figure E.4. As is expected for the bilinear model, the majority of the energy dissipation ratios for systems with a self-centering ratio of 1.0 are centered near 0.5. It is also shown that the energy dissipation ratio is well above the 25% limit suggested in the literature for all configurations. This implies that all of the systems analyzed should have sufficient energy

dissipation to limit peak drifts during earthquakes to values similar to those with full hysteretic behavior.

The energy dissipation ratios are also only affected by the self-centering ratio, which makes it a much easier output to predict. The only place where this is not true is the self-centering systems with a bay width of 20ft and an initial post-tensioning ratio of 0.65 or greater. For these systems, the energy dissipation ratio is considerably higher than the rest of the models. This increase in energy dissipation is caused by the yielding of the post-tensioning in these models, which in turn reduces the system's ability to fully self-center. The loss of full self-centering capability is highlighted in Figure 8.9, which shows the three hysteretic loops for the 30 inch deep truss with a self-centering ratio of 1.0, intial post-tensioning ratio of 0.80, and bay width of 20 ft. This occurs in these systems because the short bay width, high initial post-tensioning ratio, and deep truss all contribute to an increased likelihood of post-tensioning yield at low interstory drift.

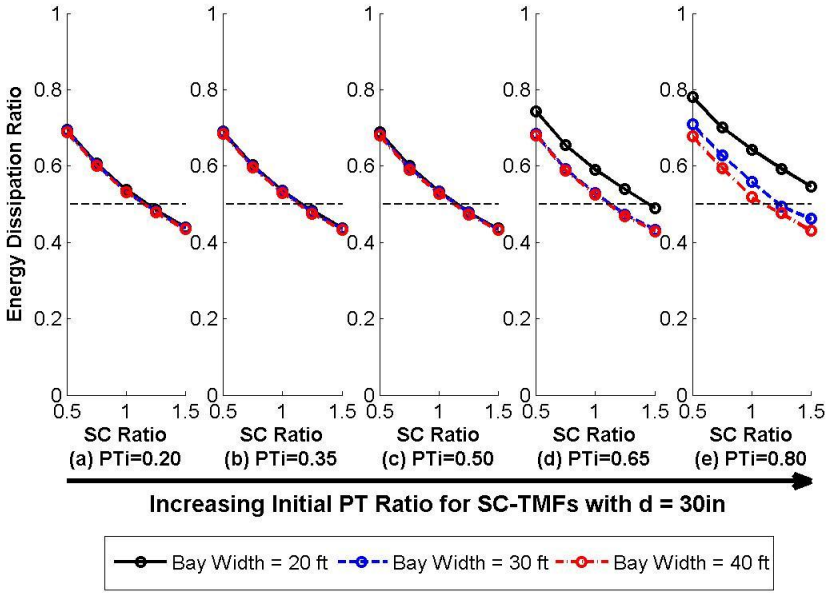

Figure 8.8: Energy Dissipation Ratio Compared to Bilinear Hysteretic for SC-TMF with Depth = 30in

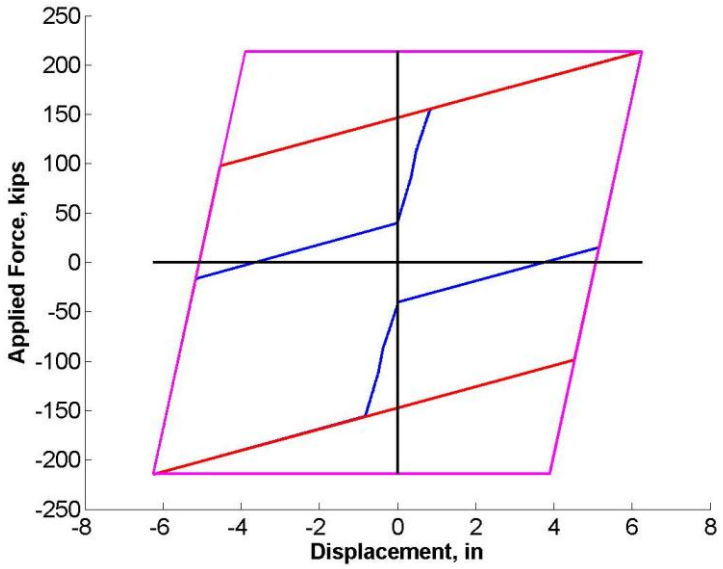

Figure 8.9: Hysteretic for 30 inch SC-TMF with SC = 1.0, PT_i = 0.80, Length = 20ft

Figure 8.10 show shows the energy dissipation ratios based on an EPP hysteretic for the 30 inch SC-TMFs. Energy dissipation ratios for the remaining truss depths are reported in Figure E.5 through Figure E.8. Figure 8.10 clearly shows that the EPP energy dissipation ratios are lower than the bilinear model. This is because the EPP hysteretic does not take into account the secondary stiffness of the system. The energy dissipation ratios are also affected by the initial post-tensioning ratio as well as the self-centering ratio. The fact that both input variables affect the energy dissipation ratio makes it much difficult to predict the energy dissipation that can be expected for the system. However, when compared to the ACI minimum of 12.5%, it is evident that the SC-TMF is able to retain sufficient energy dissipation while providing self-centering.

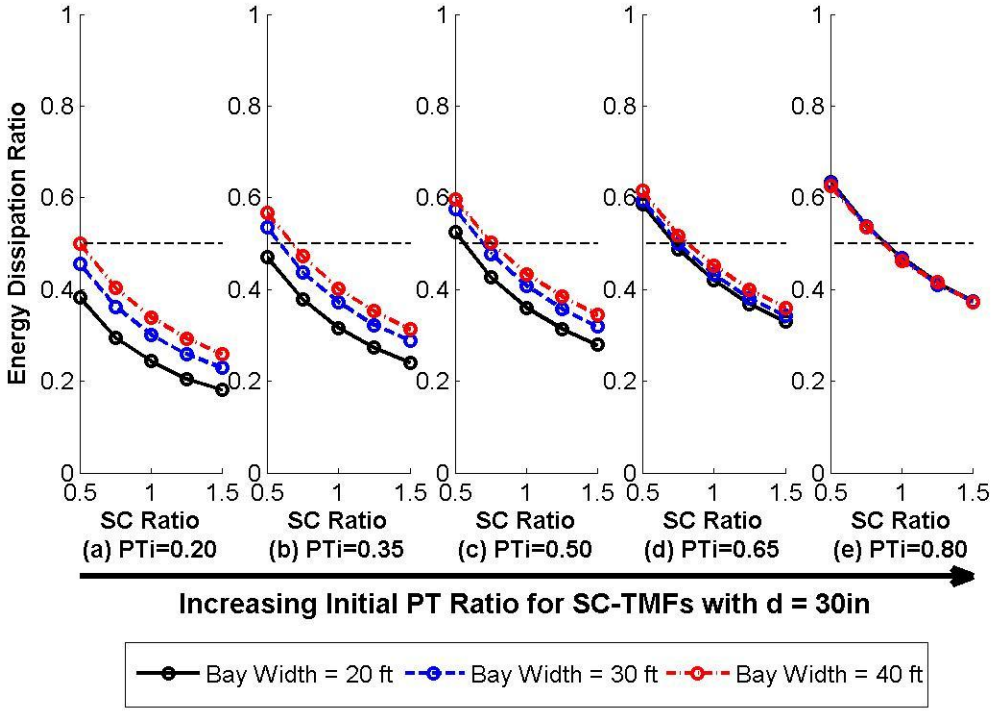

Figure 8.10: Energy Dissipation Ratio Compared to EPP Hysteretic for SC-TMF with Depth = 30in

8.4 Moment Ratio

The moment ratio is the ratio of the overturning moment applied at fuse yield compared to the design moment given in Equation 4.5. Figure 8.11 shows a sample plot of the moment ratios for models with a self-centering ratio of 1.5 and the medium design moment. The moment ratios for all other models are shown in Appendix F, Figure F.1 through Figure F.5. These figures show that nearly every model has a moment ratio at or above 1.0. This shows that the design moment is very accurate, or even a little conservative.

When the moment ratio is examined closer, it is evident that the majority of the models have a moment ratio of nearly 1.1. This is because Equation 4.5 does not take into account the full force in the post-tensioning at the point of fuse yield. The equation uses the simplifying assumption that the force in the post-tensioning at the time of fuse yield is equal to the initial

post-tensioning force. However, in order for the fuse to yield, a limited amount of gap opening, and therefore post-tensioning elongation, must occur. The post-tensioning elongation increases the force in the post-tensioning at the point of fuse yield, which increases the overturning moment required to yield the fuse components. Because the resulting design moment is conservative and is typically within approximately 10% of the computational model values, the simplifying assumption for post-tensioning force appears to be appropriate.

A limited number of models also show moment ratios less than 1.0. These were generally trusses with 30 and 40 foot bay widths and high initial post-tensioning ratios (PTi greater than or equal to 0.65). When the forces in the fuse elements are examined for these models, it is evident that the bar in tension is yielding at a later load step than the fuse in compression. This could be attributed to elastic deformations within the truss during loading of these longer trusses. This unbalanced loading could be what is causing the reduced moment ratio for these models, but further investigation is necessary to confirm this. However, every single case fell within 10% of the design value and the system will have additional capacity up through post-tensioning yield. Because the SC-TMF inherently has increased capacity compared to the design moment and the design equation is not significantly unconservative in these situations, it is recommended that the design equation is a valid estimation of capacity. These cases can be avoided by limiting the initial post-tensioning level for longer trusses. Another compensation for this fact could be increasing the phi factor that is applied to longer trusses with high initial post-tensioning when these values are developed in future research.

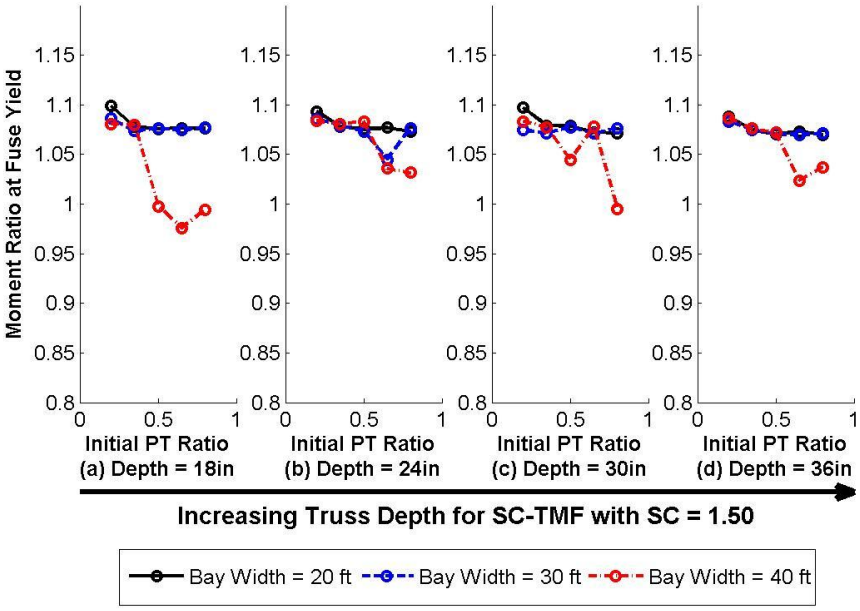

Figure 8.11: Moment Ratios for SC-TMFs with *SC* = 1.50

8.5 Energy Dissipating Bar Strain

The peak strains and cumulative strains in the energy dissipating bars were measured during the cyclic loading tests. This is important because it will identify how well the energy dissipating bars are able to accommodate the displacements that they will undergo during seismic loading. However, without component tests to understand the maximum the limits for the energy dissipating bars for peak strain or cumulative, the value of these measurements is rather limited.

Figure 8.12 shows the peak energy dissipating bars strains for the SC-TMFs with an initial post-tensioning ratio of 0.20. This plot indicates that as the depth of the truss increases, the peak strain demands also increase. This is what would be expected because, if you assume an elastic strain distribution, the deeper trusses undergo larger gap openings than shorter truss for the same level of rotation. The other input parameters appear to have very little influence on the peak strain in the system. Similar trends were seen for the remaining initial post-tensioning ratios. These plots can be found in Appendix G.

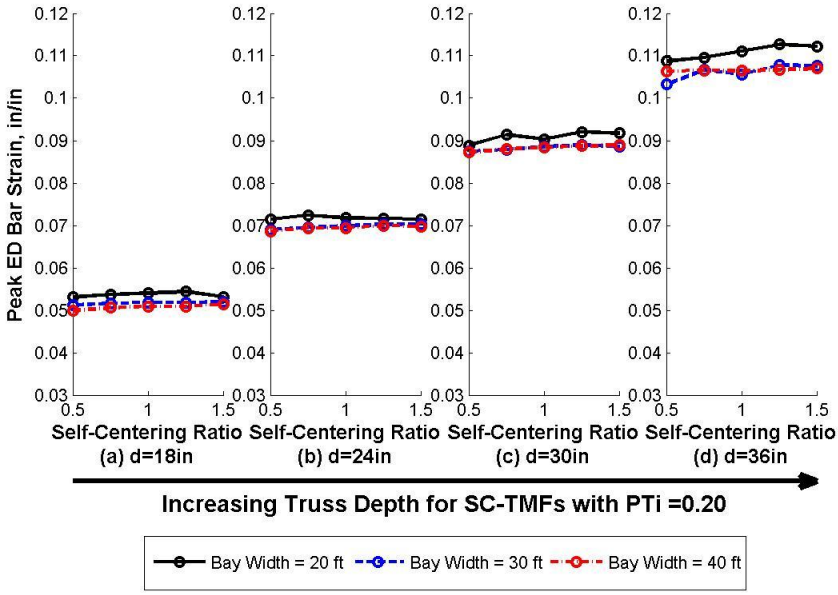

Figure 8.12: Peak Energy Dissipating Bar Strain for SC-TMFs with PT_i = 0.20

Figure 8.12 shows the cumulative energy dissipating bars strains for the SC-TMFs with an initial post-tensioning ratio of 0.20. The cumulative strain was determined by taking the peak strain from the loading in the positive and negative direction of each cycle and adding it to the total. Similar to the peak strains, this plot indicates that as the depth of the truss increases, the cumulative strains also increase. Similarly, the other input parameters have little influence on the cumulative strains in the system. Similar trends were seen for the remaining initial post-tensioning ratios. These plots can be found in Appendix H.

These results can be compared to the limitations of the energy dissipating bars following future component tests. It is important to note the all of the energy dissipating bars were modeled with the same length, 12 inches. This was done to reduce the number of possible input parameters that were considered during the parametric study. However, it would be very simple to adjust the length of the energy dissipating bar since you would only need to move the location where the DSI coupler was installed. Based on this fact, if the peak or cumulative strains are exceeding the capacity shown in the component tests, recommendations can be developed for required length of the ED bars.

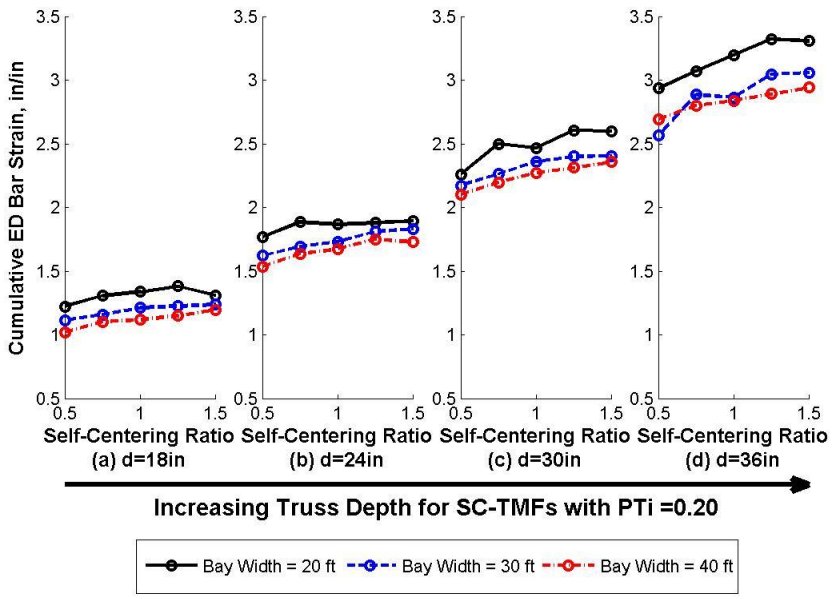

Figure 8.13: Cumulative Energy Dissipating Bar Strain for the SC-TMFs with PT_i = 0.20

Chapter 9. Conclusions

9.1 Recommended Preliminary Design Procedure

In this section the results of the initial investigations, mechanics investigations, parametric study design procedure, and parametric study results, are synthesized into a step by step recommended design procedure for the SC-TMF. This is a preliminary design procedure that is not intended for the actual implementation of a SC-TMF in a building design. There are a number of limitations of on this work that need to be addressed before a design procedure could be used in practice. These limitations include:

- The combined effects of gravity and lateral loads were not taken into consideration during these analyses.

- The influence of column flexibility was not modeled during the parametric study (columns assumed as rigid). This was done to reduce the number of possible input parameters that could affect the results. However, column flexibility could have an effect on the efficiency of the gap opening mechanism.

- The behavior of this system in tall buildings is unknown. The prototype building investigation showed that the behavior in a shorter building (4 stories) was as expected. However, taller buildings may experience higher modes that were not seen in the prototype building analysis.

- The fuse and post-tensioning elements were modeled with elastic-perfectly plastic materials. The effects of additional material properties, such as strain hardening, were not taken into consideration.

- The behavior of the system following the loss of a fuse or post-tensioning member through low cycle-fatigue, rupture, or improper installation was not investigated. These

component failure mechanisms have the potential to detrimentally affect the response of the SC-TMF.

- The chord and web elements were modeled as elastic elements because it was assumed that the capacity design will ensure that these elements remain elastic. However, the effects of any of these elements yielding could cause a significant change in global behavior of the system.

- Connections at the ends of the top chord and bottom chord inner tube where modeled as pins. The effect of a partially pinned or fully fixed connection has not been investigated.

These limitations should be investigated as part of any future research into the development of the SC-TMF. These investigations, including experimental tests and nonlinear response history analyses, may lead to the refinement or modification of this preliminary design procedure.

As a starting point, the procedure assumes that the building layout has been defined. This will dictate the bay width, story height, and available depth for structural members. Additionally, it is assumed that the design moment has been determined using an appropriate analysis method, as prescribed by ASCE 7. To complete this, appropriate values of R, C_d, Ω_o, T need to be determined for the system. It is recommended that future research perform a FEMA P-695 analysis to determine these values. However, because the behavior of the SC-TMF is comparable to that of the SMRF, the values given in ASCE 7 for the SMRF can be assumed for this preliminary design process. Once this data is known the following procedure can be followed.

Step 1: Determine truss depth and a preliminary estimate of initial post-tensioning ratio using the summary figures (Figure 8.1 through Figure 8.3) or Table 8.1 (repeated in Table 9.1) to provide sufficient interstory drift before post-tensioning yield. A preliminary target for drift is 6%, which includes a factor of safety on all drift requirements currently used in the design and prequalification of special moment frames.

Table 9.1: Recommended Maximum Initial Post-Tensioning Ratio for Various Bay Widths and Truss Depths

	Recommended Maximum Initial PT Ratio for Various Bay Widths		
Truss Depth	**20 ft bay**	**30 ft bay**	**40 ft bay**
18 inch	0.50	0.65	0.65
24 inch	0.35	0.50	0.65
30 inch	0.20	0.50	0.50
36 inch	NA	0.35	0.50

Commentary: *Note that the truss depth refers to the centerline to centerline dimension between the chords.* Table 9.1 *shows recommended upper limits on initial post-tensioning force to prevent post-tensioning yield before 6% story drift. Deeper trusses will provide a larger moment arm for the post-tensioning and fuse components, which will minimize the required area for these elements. This will in turn minimize the forces produced by these elements and limit size of the other elements in the truss. However deeper trusses create larger strains in the post-tensioning leading to less rotation capacity prior to post-tension yield.*

In general larger post-tensioning ratios lead to more economical SC-TMF designs. However, lower initial post-tensioning ratios provide the most rotation capacity prior to post-tension yielding. Finally, lower post-tensioning ratios require a greater cross-sectional area of post-tensioning for the same initial post-tensioning force, which leads to increased stiffness in the overall system.

Step 2: Establish the self-centering ratio using the plots from energy dissipation and the interstory drift at zero force.

Commentary: *Not many benefits were observed for using self-centering ratios greater than 1.0. Increased post-tensioning force implies less energy dissipation, and larger forces in the truss members. Based on previous research (Eatherton and Hajjar 2011) and the results of the*

parametric study, it is expected that self-centering ratios greater than or equal to 1.0 will result in self-centering behavior. Further analyses are required to confirm the range of self-centering ratio that limits residual drifts to the target values.

Step 3: Finalize the initial post-tensioning ratio using Figure C.1 through Figure C.5 for the appropriate combination of self-centering ratio, truss depth, and bay width.

Commentary: *This step is following up on Step 1, by verifying that the selected design will produce sufficient rotation capacity prior to post-tensioning yield. Interpolation between values tested may be utilized in order to refine the design because these plots generally show linear trends.*

Step 4: Size the post-tensioning and energy dissipating components. This is accomplished using the following procedure:

- Determine the target moment for the fuse, M_{t_fuse}, and the post-tensioning element, M_{t_pt}.

$$M_{t\_fuse} = \frac{M_u}{SC + 1.0} \qquad 8.1$$

where

M_u = factored applied moment as determined using ASCE-7

SC = self-centering ratio

$$M_{t\_pt} = M_u - M_{t\_fuse} \qquad 8.2$$

- Determine the minimum required area for the fuse component, A_{min_ED}. Assume energy dissipating bars are used in this configuration.

$$V_{n\_ED} = \frac{M_{t\_fuse}}{\phi d_{truss}} \qquad 8.3$$

where

V_{n_ED} = required nominal axial capacity of the energy dissipating bars

d_{truss} = depth of the truss from centerline to centerline of chords

ϕ = resistance factor

$$A_{\min\_ED} = \frac{V_{n\_ED}}{F_{y\_ED}} \qquad 8.4$$

where

F_{y_ED} = yield stress of energy dissipating bars (60 ksi)

- Determine the minimum required area for the post-tensioning elements

$$f_{pi} = \gamma_{pt} f_{pu} \qquad 8.5$$

where

γ_p = initial post-tensioning ratio

f_{pu} = ultimate stress of post-tensioning element (270 ksi)

$$P_{i\_req} = \frac{M_{t\_pt}}{\varphi_b d_{truss}} \qquad 8.6$$

where

P_{i_req} = required initial post-tensioning force

$$A_{\min\_pt} = \frac{P_{i\_req}}{f_{pi}} \qquad 8.7$$

Step 5: Complete a capacity based design for the inner tube, outer tube, and top chord based on the cross sectional areas defined for the post-tensioning and fuse elements.

- Design the inner tube, checking for tension and compression independently.

$$F_{IT} = 0.9\left(1 - \frac{L_{IT}}{L_{IC}}\right)F_{ptu} = 0.9\left(1 - \frac{L_{IT}}{L_{IC}}\right)\left(f_{pu}A_{pt}\right) \qquad 8.8$$

where

F_{IT} = ultimate tension force in the inner tube

L_{IT} = length of the inner tube that is in tension

L_{IC} = length of the inner tube that is in compression

f_{pu} = ultimate stress for the post-tensioning material

A_{pt} = cross sectional area of the post-tensioning

Commentary: *Equation 8.8 assumes the cross section area of the end region and the inner tube are the same. If this assumption is not accurate, a ratio of the stiffnesses of each component should be used in place of the ratio of the lengths.*

$$F_{IC} = -0.35F_{ptu} = -0.35\left(f_{pu}A_{pt}\right) \qquad 8.9$$

where

F_{IC} = ultimate compression force in the inner tube

- Design the top chord, checking for tension and compression independently.

$$F_{TC} = -0.9\left(1 - \frac{L_{IT}}{L_{IC}}\right)\left(f_{pu}A_{pt}\right) - \frac{F_{ED}}{2} \qquad 8.10$$

where

F_{TC} = ultimate compression force in the top chord

$$F_{TT} = 0.35\left(f_{pu} A_{pt} \right) + \frac{F_{ED}}{2} \qquad 8.11$$

where

F_{TT} = ultimate tension force in the top chord

- Design the outer chord for compression. Utilize the additional buckling capacity that comes from having a non-uniform axial load distribution in the compression capacity calculation.

$$F_O = \frac{F_{ED}}{2} + F_{ptu} \qquad 8.12$$

where

F_O = ultimate compression force in the outer chord

$$P_{cr} = \frac{\beta \pi^2 EI}{L^2} \qquad 8.13$$

where

β = 1.88

Commentary: *Only out of plane buckling should be checked for the design of all three tubes. Unbraced length should be assumed to be the full length of each member. Finally, effective length factor of 1.0 should be utilized because of the assumption that the members are behaving as a pinned-pinned column.*

9.2 SC-TMF Conclusions

The self-centering truss moment frame (SC-TMF) is a new structural system with improved seismic performance relative to conventional seismic systems. From the outset, the goal of this new self-centering system was to develop a new structural system with the benefits of self-centering behavior to eliminate residual drifts while concentrating inelastic behavior to replaceable structural fuses. Based on the investigations contained in the preceding chapters, the SC-TMF is a viable system that satisfies all of the performance goals.

These goals needed to be accomplished while mitigating a number of issues seen with other self-centering systems. These issues included deformation incompatibility with the gravity framing, limited deformation capacity, and unusual field construction techniques

The SC-TMF also has some significant improvements relative to currently available self-centering seismic force resisting systems. For example, the self-centering post-tensioned moment frames had issues of deformation incompatibility and unconventional field construction procedures. The issue of deformation incompatibility is solved by the SC-TMF by moving the gap openings within the truss at the bottom chord. This prevents gap openings from interacting with the diaphragm directly or through bay elongation. The SC-TMF is also a system that can be fully prefabricated and installed on site just as any other truss would be installed. Additionally, the SC-TMF only requires pin connections at the end of each chord, which simplifies the construction detailing that is required when compared to moment frames. Other self-centering systems, such as the rocking or braced frame, had issues of limited deformation capacity for certain configurations. This problem is solved by the SC-TMF, which consistently had deformation capacity well beyond the defined minimum of 6% interstory drift.

Another benefit that was shown through the investigations was that strength and stiffness were decoupled. This fact allows for a more efficient use of structural steel than conventional seismically resistant moment frames. Strength and stiffness in these moment frames are coupled together and stiffness generally controls the design. This leads to an inefficient use of steel where strength is concerned.

A set of preliminary investigations were conducted to confirm the expected structural behavior. The preliminary analyses also included nonlinear response history analyses of a four story prototype building for the 44 Near Field ground motion set that is specified in the FEMA P-695 methodology. This was done to investigate whether the SC-TMF would behave as expected during dynamic loading. As expected, the system could be easily scaled to a full building implementation with reasonable configurations. The SC-TMF exhibited peak drifts similar to those expected in a Special Moment Resisting Frame (SMRF). As an added benefit, the configurations designed for these analyses had similar levels of steel when compared with the moment frame that the designs had been based on. Finally, the trusses provided full self-centering behavior and limited residual drifts to values within the tolerances specified for new construction.

The preliminary analyses helped identify a deficiency with the fuse used in the initial configuration. Originally, a butterfly fuse plate was located at the middle of the truss connected between the top chord and the bottom chord inner tube. However, the preliminary investigations showed that elastic deformations of the truss significantly reduced the efficacy of this fuse configuration. The SC-TMF configuration was modified to use buckling restrained, energy dissipating bars as the fuse element. These components provided greater secondary stiffness and provide easier access for replacement following a strong ground motion.

To build on the preliminary investigations, a mechanics investigation was conducted. In the mechanics investigation, static pushover analyses (monotonic and cyclic) were conducted. Utilizing analysis of the new configuration, it was determined that strength and stiffness were predictable through simple mechanics based equations. Equations were developed to describe the initial stiffness, moment causing gap opening, stiffness after gap opening, moment causing fuse yield, stiffness after fuse yield, and moment causing post-tensioning yield. These equations showed that the SC-TMF follows predictable behavior during lateral loading.

Next, a parametric study was conducted to gain a better understanding of how various design decisions influence the structural behavior. Five input parameters were varied at numerous

levels, resulting in 900 independent designs. Each design was analyzed using a monotonic static pushover analysis as well as a cyclic static pushover analysis that followed the loading protocol for prequalification of moment frames for seismic design as outlined by AISC. A capacity based design and general design procedure were developed in order to implement the parametric study. The results of the study confirmed the validity of a number of design equations used in developing the models. They also helped to tweak a few of the design equations for improved accuracy. Finally, the results indicated a number of trends that can be utilized when making preliminary design decisions.

Using the results of the mechanics investigation and the parametric study, a final recommended design procedure was outlined for the continued development of the SC-TMF.

9.3 Future Work

Beyond the scope of this project is the possibility for extensive additional research on the SC-TMF. To continue the analytical research, full building designs should be developed and tested using the FEMA P-695 methodology. In addition to the computational research, an experimental program should be developed to corroborate the findings of the computational studies. This should include component tests of the fuse and post-tensioning elements. These tests can then be used to enhance the hysteretic curves used in the analyses that were conducted in this project. Next, full scale, single-story systems should be tested experimentally using a cyclic pushover. These experiments will be used to determine the validity of the findings from the parametric study and to identify additional concerns that need to be taken into account during design (ie. details of the connections or reinforcement of the end members against buckling). Finally, once the behavior of the system is fully understood and the models closely match the experimental behavior, a full FEMA P-695 study should be completed to determine the appropriate design values for the SC-TMF when it is implemented in the building design code.

Currently, an NSF sponsored research program is underway at Virginia Tech to continue to develop the SC-TMF. This program will address many of the recommendations listed above.

Works Cited

ACI (2007). Acceptance Criteria for Special Unbonded Post-Tensioned Precast Structural Walls Based on Validation Testing and Commentary. ACI ITG-5.1-07.

AISC (2010a). Code of standard Practice for Steel Buildings and Bridges (AISC 303-10), American Institute of Steel Construction.

AISC (2010b). Seismic Provisions for Structural Steel Buildings (341-10). American Institute of Steel Construction. Chicago, IL.

ASCE (2010). Minimum design loads for buildings and other structures (ASCE/SEI 7-10). Reston, VA, American Society of Civil Engineers.

ATC (1978). Tentative Provisions for the Development of Seismic Regulations of Buildings. ATC 3-06. Washington, DC, prepared by the Applied Technologies Council for the National Institute of Standards and Technology (NIST).

Basha, H. and S. Goel (1995). "Special truss moment frames with Vierendeel middle panel." Engineering Structures **17**: 352-358.

Chao, S. H. and S. C. Goel (2008). "Performance-Based Plastic Design of Special Truss Moment Frames." Engineering Journal **45**: 127-150.

Christopoulos, C., A. Filiatrault and B. Folz (2002a). "Seismic response of self-centring hysteretic SDOF systems." Earthquake Engineering & Structural Dynamics **31**: 1131-1150.

Christopoulos, C., A. Filiatrault, C.-M. Uang and B. Folz (2002b). "Posttensioned Energy Dissipating Connections for Moment-Resisting Steel Frames." Journal of Structural Engineering **128**: 1111.

Cohen, M. P. (1986). "Design solutions utilizing the staggered-steel truss system." AISC Engineering Journal **23**: 97-106.

Cronin, L. and C. Moen (2012). Flexural Capacity Prediction Method for an Open Web Joist Laterally Supported by a Standing seam Roof System. Blacksburg, VA, VIRGINIA POLYTECHNIC INSTITUTE AND STATE UNIVERSITY.

Deierlein, G., J. Hajjar, M. Eatherton, S. Billington, H. Krawinkler and X. Ma (2009). Seismically Resilient Steel Braced Frame Systems with Controlled Rocking and Energy Dissipating Fuses. NEES 7th Annual Meeting, Honolulu, Hawaii.

Deierlein, G., X. Ma, J. Hajjar, M. Eatherton, H. Krawinkler, T. Takeuchi, M. Midorikaw, T. Hikino and K. Kasai (2010). Seismic resilience of self-centering steel braced frames with

replaceable energy-dissipating fuses-part II: e-defense shake table test. Joint Conference Proceedings, 7th International Conference on Urban Earthquake Engineering (7CUEE) and 5th International Conference on Earthquake Engineering (5ICEE), Tokyo Institute of Technology, Tokyo, Japan.

Eatherton, M., J. Hajjar, G. Deierleing, H. Krawinkler, S. Billington and X. Ma (2010). Hybrid Simulation Testing of a Controlled Rocking Steel Braced Frame System. 9NCEE/10CCEE. Toronto.

Eatherton, M. R. (2010). Large-Scale Cyclic and Hybrid Simulation Testing and Development of a Controlled-Rocking Steel Building System with Replaceable Fuses. Graduate College. Urbana, Illinois, University of Illinois at Urbana-Champaign. **Doctor of Philosophy in Civil Engineering**.

Eatherton, M. R. and J. F. Hajjar (2011). "Residual Drifts of Self-Centering Systems Including Effects of Ambient Building Resistance." Earthquake Spectra, Earthquake Engineering Research Institute **Volume 27**(No. 3): 719-744.

Esposto, M., B. Faggiano and F. M. Mazzolani (2006). Numerical vs . experimental results on a PTED beam-to-column connection for seismic resistant steel frames. Proceedings of the 5th International Conference on the Behaviour of Steel Structures in Seismic Areas (STESSA 2006), Yokohama, Japan.

FEMA (2009). Quantification of Building Seismic Performance Factors. FEMA P-695. Washington, D.C, prepared by Applied Technology Council for the Federal Emergency Management Agency.

Garlock, M. and J. Li (2008). "Steel Self-Centering Moment Frames with Collector Beam Floor Diaphragms." Journal of Constructional Steel Research **Vol. 64**(No. 5): pp. 526-538.

Garlock, M. M. (2002). Design, analysis and experimental behavior of seismic resistant post-tensioned steel moment resisting frames. nisee.berkeley.edu.

Garlock, M. M., J. M. Ricles and R. Sause (2005). "Experimental Studies of Full-Scale Posttensioned Steel Connections." Journal of Structural Engineering **131**: 438.

Goel, S. C. and A. M. Itani (1994a). "Seismic-Resistant Special Truss-Moment Frames." Journal of Structural Engineering **120**: 1781-1797.

Goel, S. C. and A. M. Itani (1994b). "Seismic Behavior of Open-Web Truss-Moment Frames." Journal of Structural Engineering **120**: 1763-1780.

Gray, M., C. Christopoulos and J. Packer (2012). Full-scale testing of the cast steel yielding brace system. STESSA 2012. Mazzolani and Herrera. Santiago, Chile, Taylor & Francis Group.

Hanson, R., R. Gupta, S. Goel and G. Berg (1974). "Seismic Behavior of Staggered Truss Framing System Design Procedure for Earthquake Loading." Steel Research for Construction.

Kim, J., J. H. Lee and Y. M. Kim (2007). "Inelastic behavior of staggered truss systems." The Structural Design of Tall and Special Buildings **16**: 85-105.

Lin, Y. C., J. Ricles, R. Sause and C.-y. Seo (2009). "EARTHQUAKE SIMULATIONS ON A SELF-CENTERING STEEL MOMENT RESISTING FRAME WITH WEB FRICTION." Engineering Simulation: 1364-1373.

Ma, X. (2010). Seismic Design and Behavior of Self-Centering Braced Frame with Controlled Rocking and Energy Dissipating Fuses. Department of CEE. Stanford, California, Stanford University. **PhD**.

Ma, X., E. Borchers, A. Pena, H. Krawinkler and G. Deierlein (2010a). Design and Behavior of Steel Shear Plates With Openings as Energy-Dissipating Fuses. Internal Report, Blume Earthquake Engineering Center, Stanford University.

Ma, X., G. Deierlein, J. Hajjar, M. Eatherton, H. Krawinkler, T. Takeuchi, M. Midorikaw, T. Hikino and K. Kasai (2010b). Large-Scale Shaking Table Test of Steel Braced Frame with Controlled Rocking and Energy Dissipating Fuses. 9th National Conference of Earthquake Engineering, Toronto, Canada.

Mar, D. (2010). Design Examples Using Mode Shaping Spines for Frame and Wall Buildings. 9th National Conference of Eathquake Engineering. Toronto, Canada.

Mazzoni, S., F. McKenna, M. H. Scott and G. L. Fenves (2005). "OpenSees command language manual." Pacific Earthquake Engineering Research (PEER) Center.

MIT (1967). High-rise housing in steel - the staggered truss. Research Report (R67-7 Civil Engineering) Cambridge, Massachusetts, Department of Architecture and Civil Engineering, Massachusetts Institute of Technology. (Out of Print).

MSJC, M. S. J. C. (2008). Building Code Requirements and Specification for Masonry Structures, Masonry Society.

Nakaki, S. D., J. Stanton and S. Sritharan (1999). "An overview of the PRESSS five-story precast test building." PCI journal **44**: 26-39.

Newmark, N. and W. Hall (1982). Earthquake Spectra and Design. Earthquake Engineering Research Institute, Berkeley, CA.

NIST (2010). Evaluation of the FEMA P-695 Methodology for Quantification of Building Seismic Performance Factors. NIST GCR 10-917-8. Gaithersburg, MD, prepared by the NEHRP Consultants Joint Venture for the National Institute of Standards and Technology.

NIST (2011). Improved Structural Response Modification Factors for Seismic Design of New Buildings. NIST GCR 11-917-16, prepared by the NEHRP Consultants Joint Venture for the National Institute of Standards and Technology.

Ölmez, H. D. and C. Topkaya (2010). "A numerical study on special truss moment frames with Vierendeel openings." Journal of Constructional Steel Research.

Pekcan, G., C. Linke and A. Itani (2009). "Damage avoidance design of special truss moment frames with energy dissipating devices." Journal of Constructional Steel Research **65**: 1374-1384.

Priestley, M. J. N., S. Sritharan, J. R. Conley and S. Pampanin (1999). "Preliminary results and conclusions from the PRESSS five-story precast concrete test building." PCI journal **44**: 42-67.

Ricles, J. and R. Sause (2007). Earthquake Resistant Post-Tensioned Connections to Concrete Filled HSS Columns, ASCE.

Ricles, J., R. Sause, M. Garlock and C. Zhao (2001). "Posttensioned seismic-resistant connections for steel frames." Journal of Structural: 113-121.

Ricles, J., R. Sause, S. Peng and L. Lu (2002). "Experimental evaluation of earthquake resistant posttensioned steel connections." Journal of Structural Engineering **128**: 850.

Scalzi, J. B. (1971). "The staggered-truss system: structural considerations." AISC Engineering Journal **8**: 25-30.

Seo, C.-Y. and R. Sause (2005). "Ductility Demands on Self-Centering Systems under Earthquake Loading." ACI Structural Journal **V. 102**(No. 2): pg 275-285.

Tirca, L., C. Caprarelli and N. Danila (2012). Seismic simulation and design of low-rise CBF buildings with and without dissiative connections using OpenSees. STESSA 2012. Mazzolani and Herrera. Santiago, Chile, Taylor & Francis Group.

Valley, M. and J. Hooper (2003). Issues In the Design of a Seattle-Area Special Truss Moment Frame Building. ASCE Structures Congress and Exposition.

Vargas, R. and M. Bruneau (2006). Seismic response and design of buildings with metallic structural fuses. STESSA. M. a. Wada. London, England**:** pg 99-103.

Vasdravellis, G., B. Uy and T. Karavasilis (2012). Experimental Validation of Steel Post-Tensioned Members with hourglass pins. STESSA 2012. Mazzolani and Herrera. Santiago, Chile, Taylor & Francis Group.

Veletsos, A., N. Newmark and C. Chelapati (1965). Deformation Spectra for Elastic and Elastoplastic Systems Subjected to Ground Shock and EArthquake Motions. Third World Congress on Earthquake Engineering. New Zealand. **Vol. 2:** pp 11-663 to 611-682.

Zhou, X., Y. He, L. Xu and Q. Zhou (2009). "Experimental study and numerical analyses on seismic behaviors of staggered-truss system under low cyclic loading." Thin-Walled Structures **47**: 1343-1353.

Appendices

Appendix A. Mathmatica Solution to Fourth Order ODE

```
alpha = 0.0;

gpo = 10; gypo = 1;
endpt[po_?NumericQ, ypo_?NumericQ] :=
  NDSolve[{y''''[t] + (po * (-((1 - alpha) * y'[t]) + ((1 - ((1 - alpha) * t)) y''[t]))) == 0,
    y[0] == 0, y'[0] == 0.1, y''[0] == 0, y'''[0] == ypo},
   {y}, {t, 0, 1}, MaxSteps → 100 000];
y1[po_?NumericQ, ypo_?NumericQ, t_] := y[t] /. endpt[po, ypo][[1]]
ypp1[po_?NumericQ, ypo_?NumericQ, t_] := y''[t] /. endpt[po, ypo][[1]]
{po, ypo} = {po, ypo} /. FindRoot[{y1[po, ypo, 1], ypp1[po, ypo, 1]},
   {{po, gpo}, {ypo, gypo}}, AccuracyGoal → 5, MaxIterations → 100 000 000]
Plot[Evaluate[y[t] /. endpt[po, ypo]], {t, 0, 1}]
```

```
{18.5687, -1.52997}
```

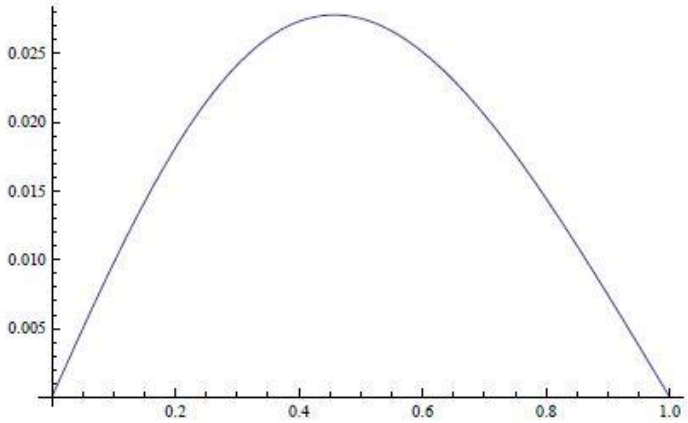


```
ListPlot[{{-1, 41.58}, {-0.8, 35.77}, {-0.6, 30.46}, {-0.4, 25.77}, {-.2, 21.8},
  {0, 18.56}, {0.2, 15.98}, {0.4, 13.93}, {0.6, 12.29}, {0.8, 10.96}, {1.0, 9.87}},
 AxesOrigin → {-1, 0}, PlotJoined → True]
```

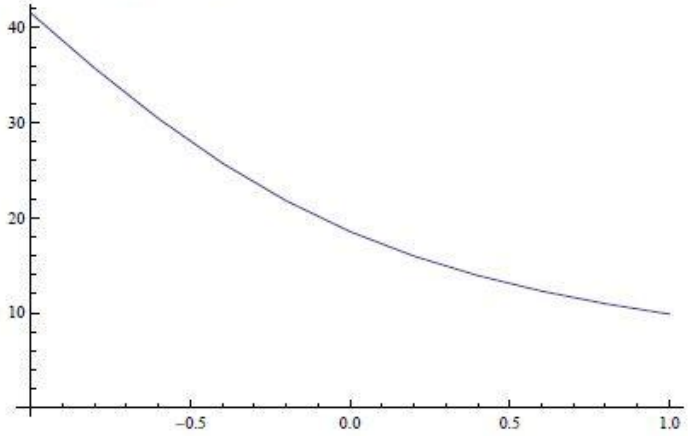

Appendix B. Figures – Capacity Based Design Force Ratios

B.1 *Inner Tube Tension Force Ratios Based on Equation* 6.3

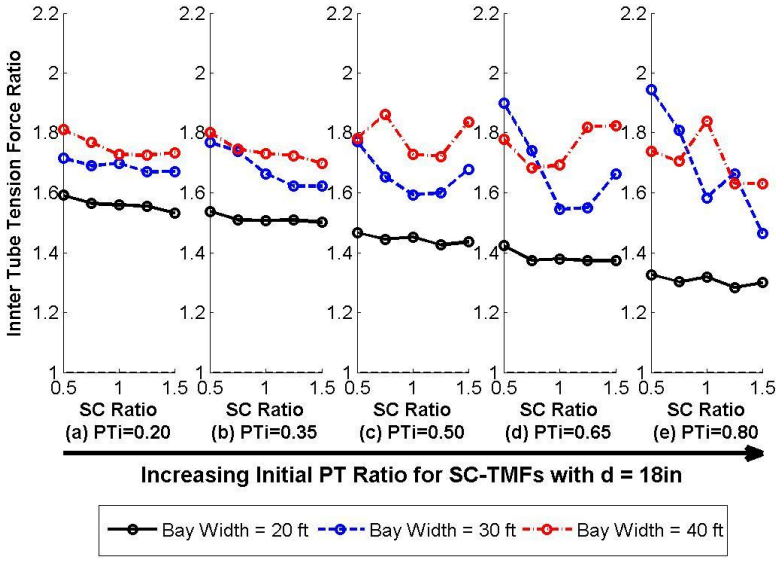

Figure B.1: Inner Tube Tension Force Ratios for 18in SC-TMFs using Equation 7.3

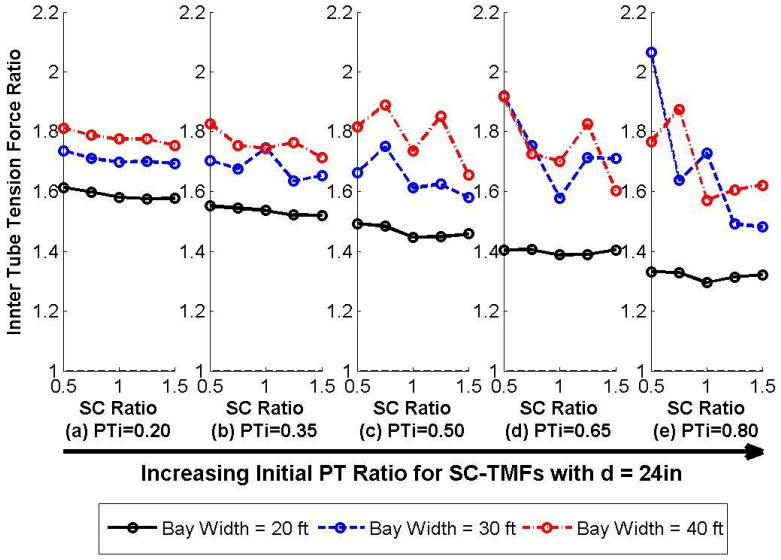

Figure B.2: Inner Tube Tension Force Ratios for 24in SC-TMFs using Equation 7.3

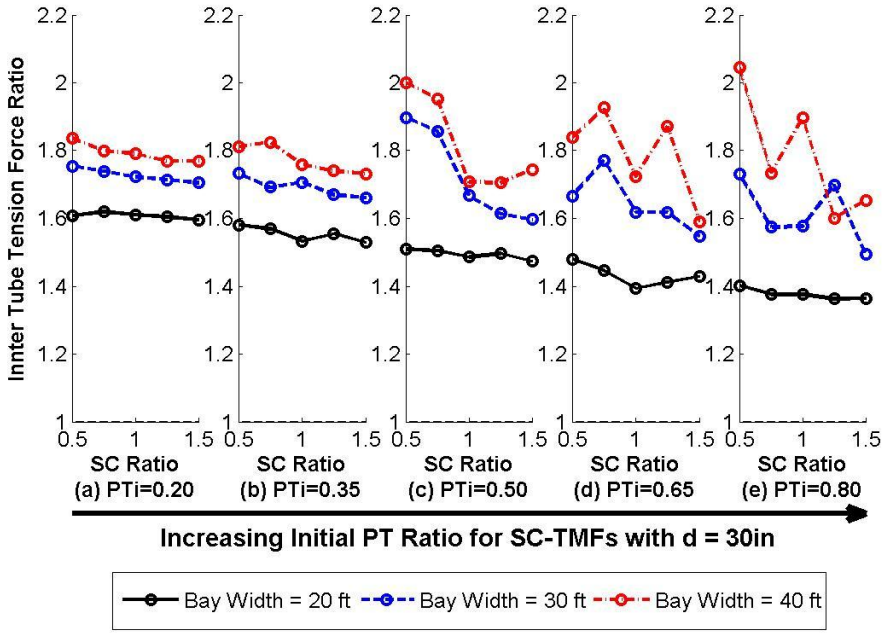

Figure B.3: Inner Tube Tension Force Ratios for 30in SC-TMFs using Equation 7.3

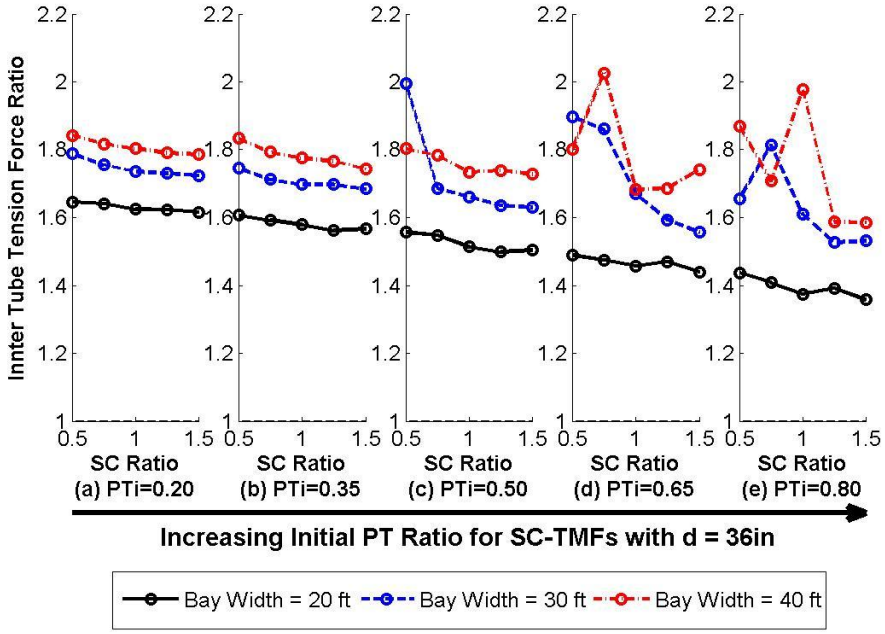

Figure B.4: Inner Tube Tension Force Ratios for 36in SC-TMFs using Equation 7.3

B.2 Inner Tube Tension Force Ratios Based on Equation 6.24

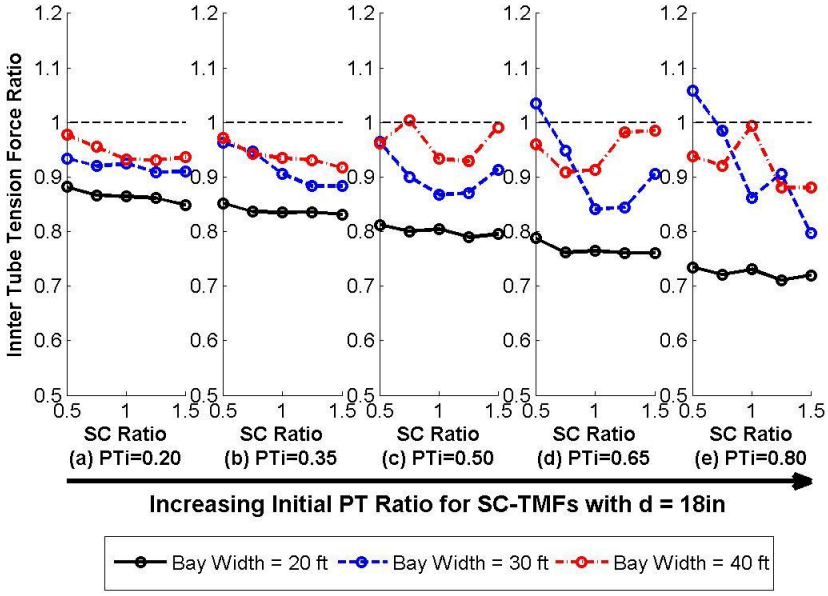

Figur B.5: Inner Tube Tension Force Ratios for 18in SC-TMFs using Equation 7.24

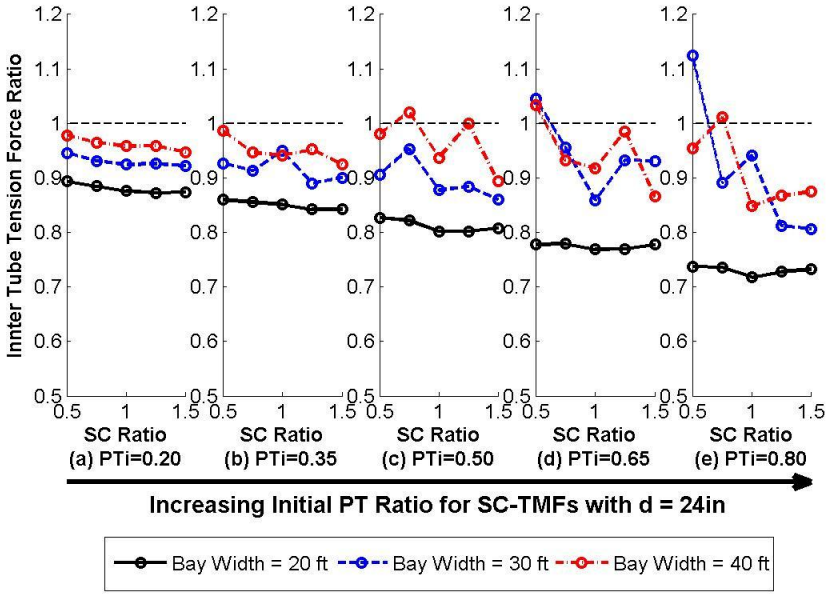

Figure B.6: Inner Tube Tension Force Ratios for 24in SC-TMFs using Equation 7.24

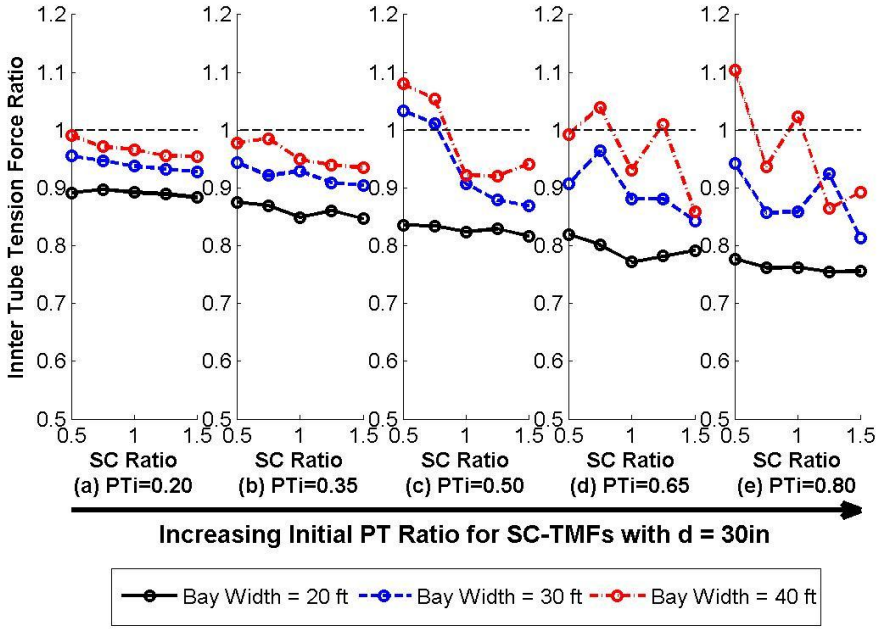

Figure B.7: Inner Tube Tension Force Ratios for 30in SC-TMFs using Equation 7.24

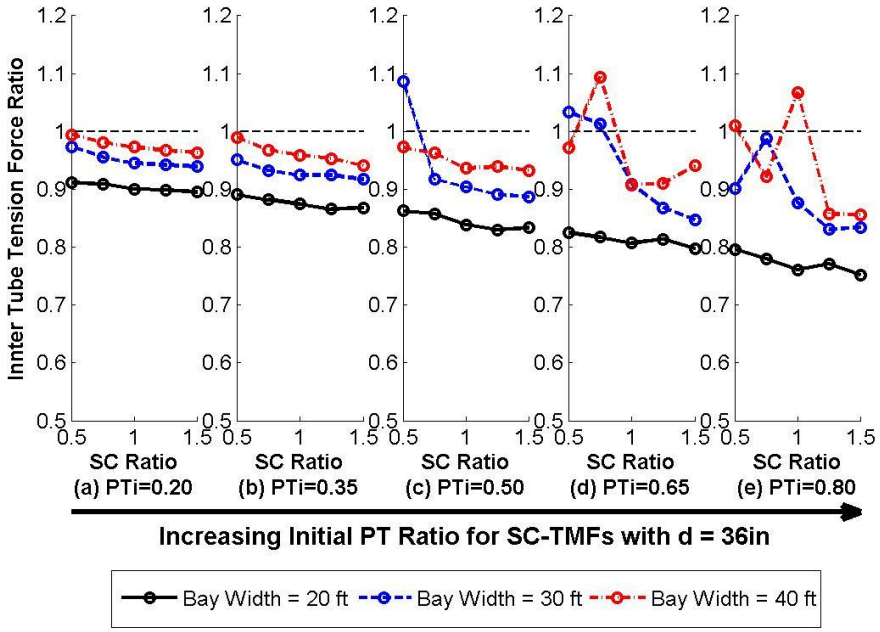

Figure B.8: Inner Tube Tension Force Ratios for 36in SC-TMFs using Equation 7.24

B.3 *Inner Tube Compression Force Ratios Based on Equation* 6.3

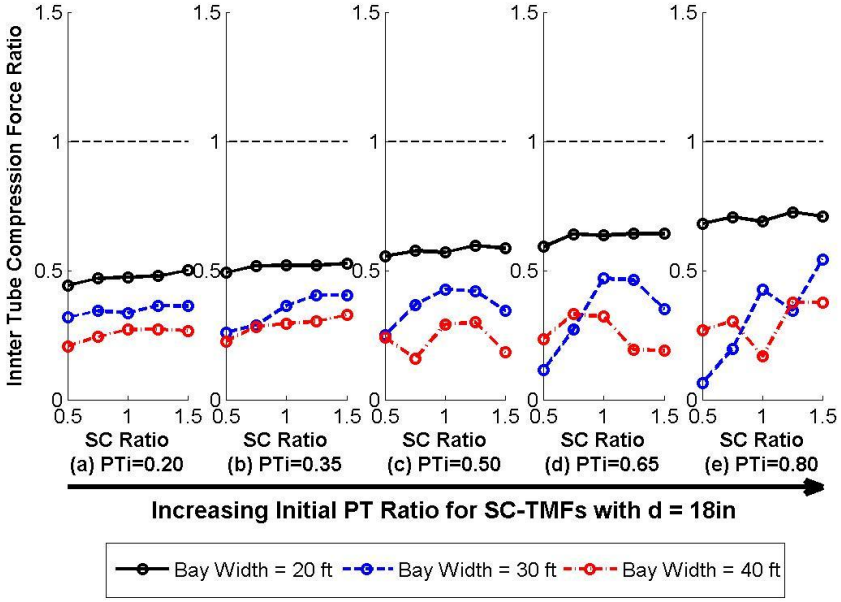

Figure B.9: Inner Tube Compression Force Ratios for 18in SC-TMFs using Equation 7.3

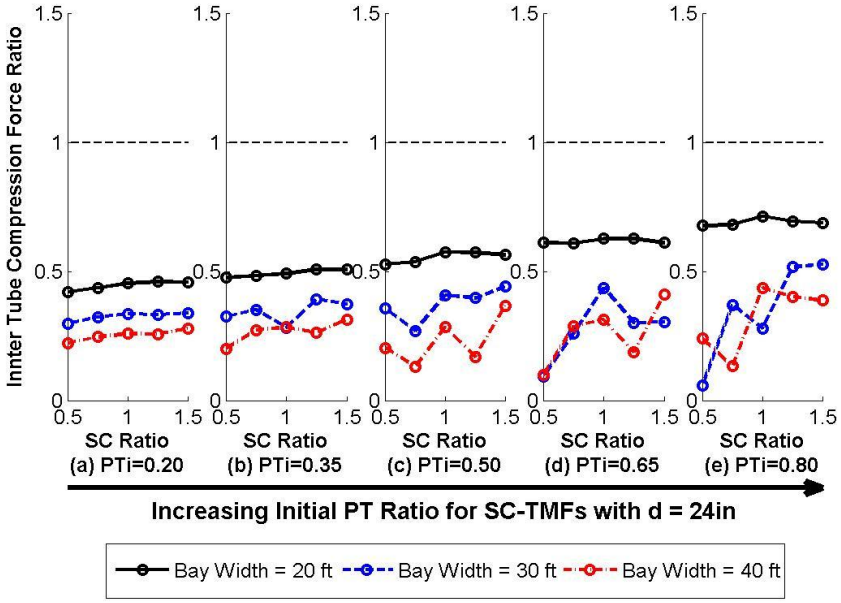

Figure B.10: Inner Tube Compression Force Ratios for 24in SC-TMFs using Equation 7.3

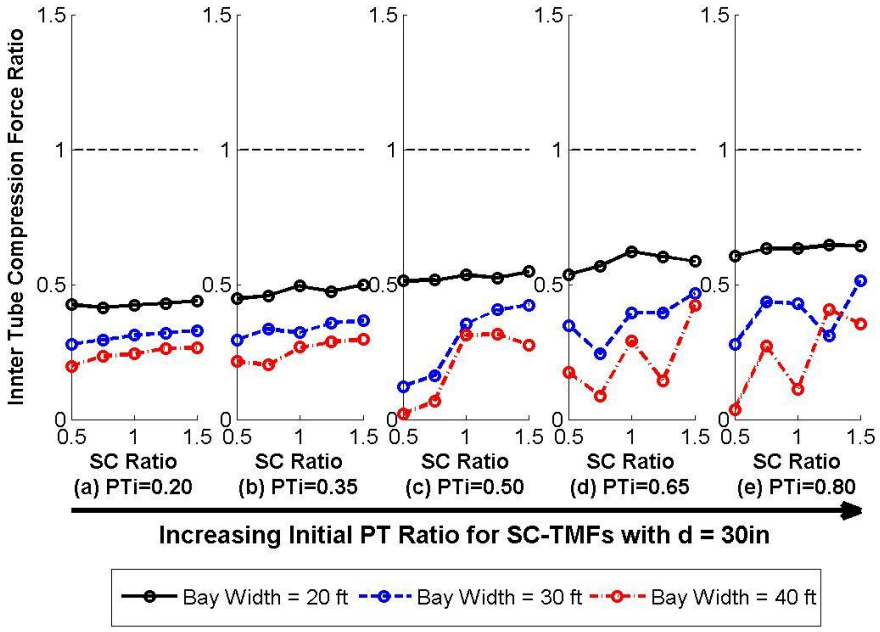

Figure B.11: Inner Tube Compression Force Ratios for 30in SC-TMFs using Equation 7.3

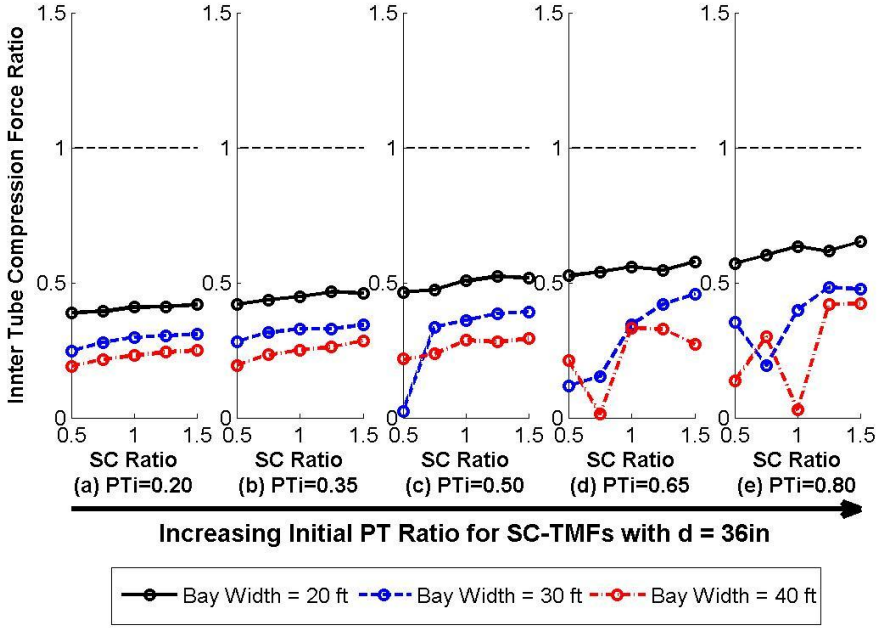

Figure B.12: Inner Tube Compression Force Ratios for 36in SC-TMFs using Equation 7.3

B.4 *Inner Tube Compression Force Ratios Based on Equation* 6.25

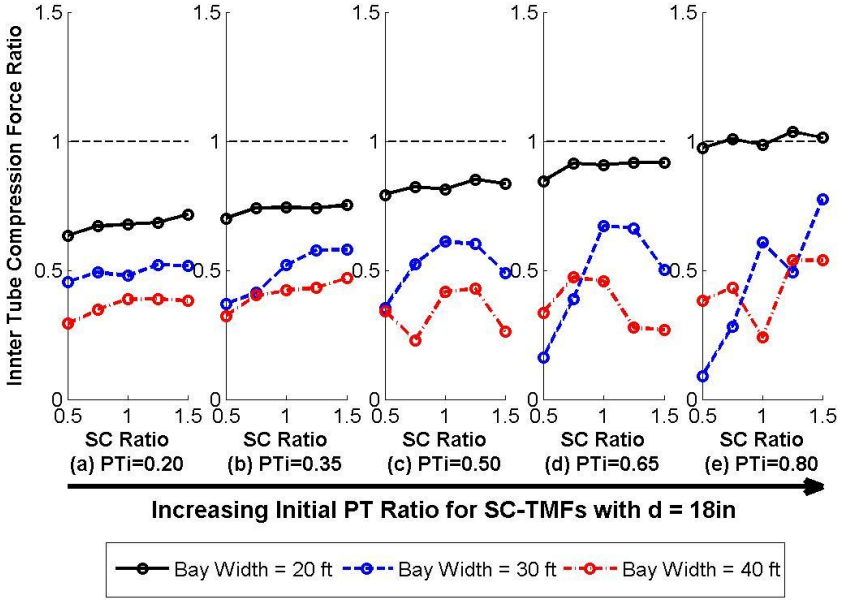

Figure B.13: Inner Tube Compression Force Ratios for 18in SC-TMFs using Equation 7.25

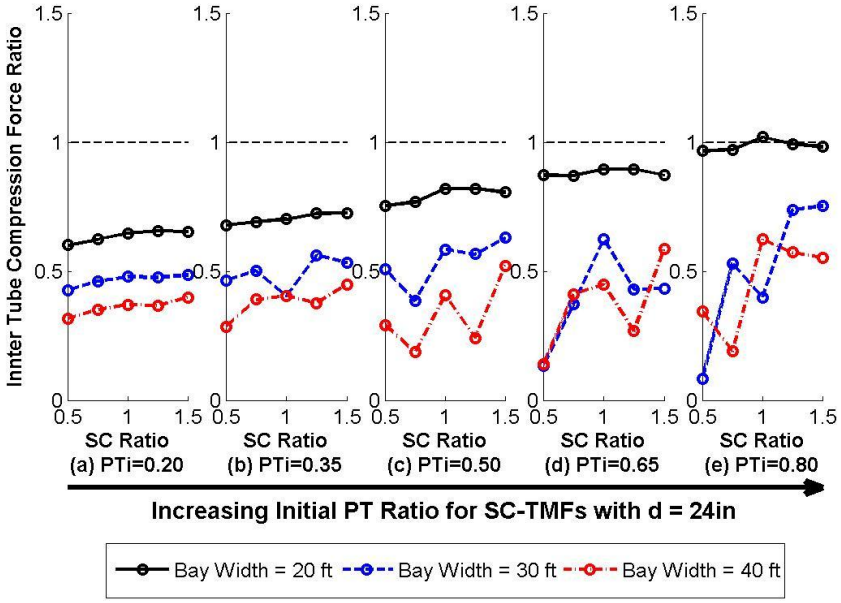

Figure B.14: Inner Tube Compression Force Ratios for 24in SC-TMFs using Equation 7.25

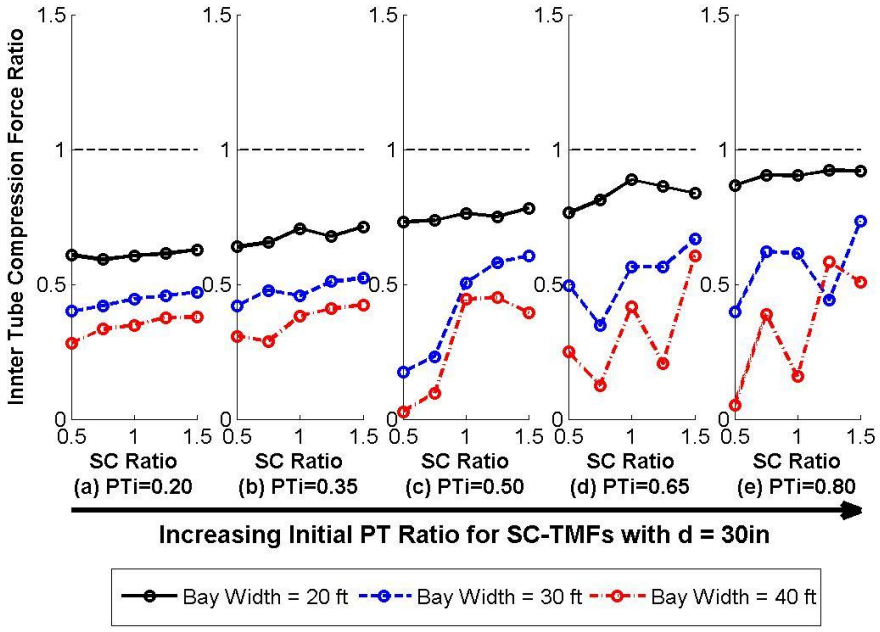

Figure B.15: Inner Tube Compression Force Ratios for 30in SC-TMFs using Equation 7.25

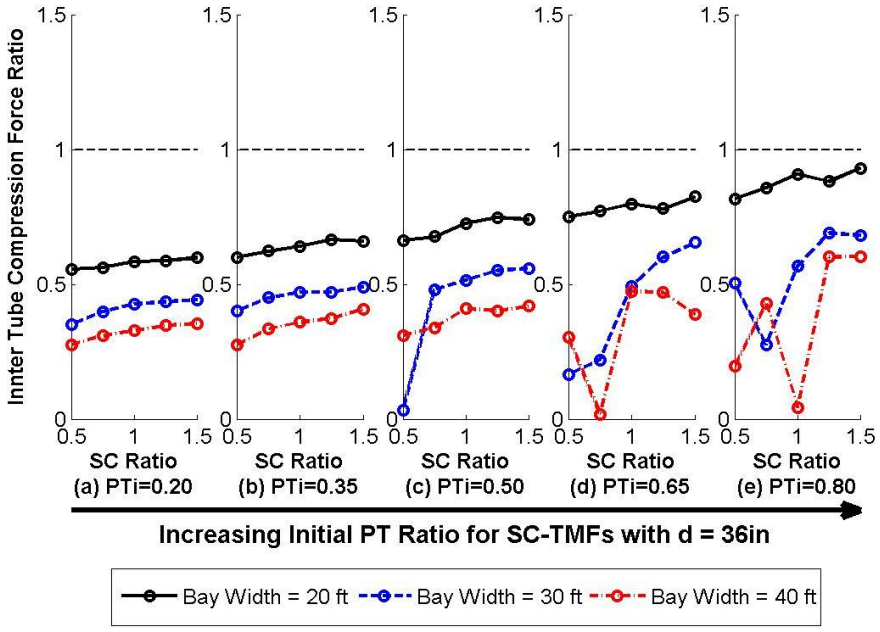

Figure B.16: Inner Tube Compression Force Ratios for 36in SC-TMFs using Equation 7.25

B.5 *Top Chord Tension Force Ratios Based on Equation* 6.2

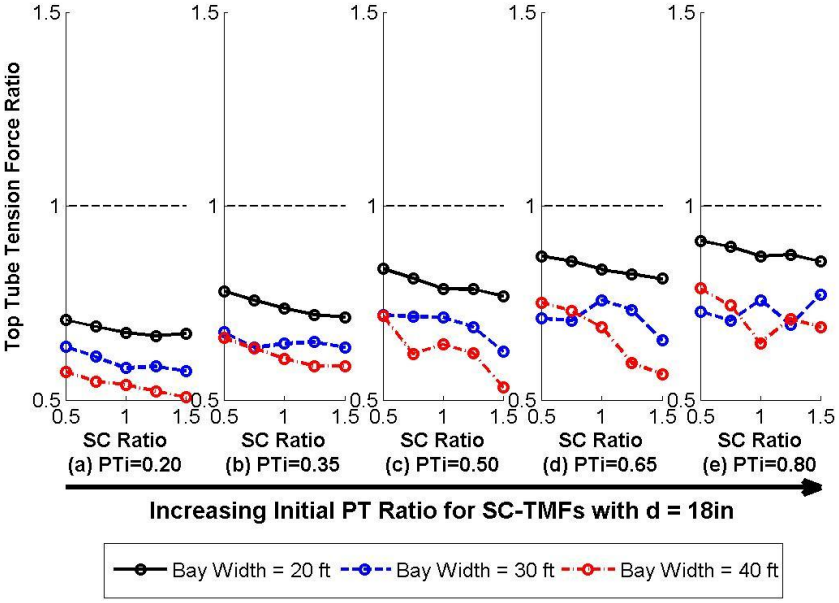

Figure B.17: Top Chord Tension Force Ratios for 18in SC-TMFs using Equation 7.2

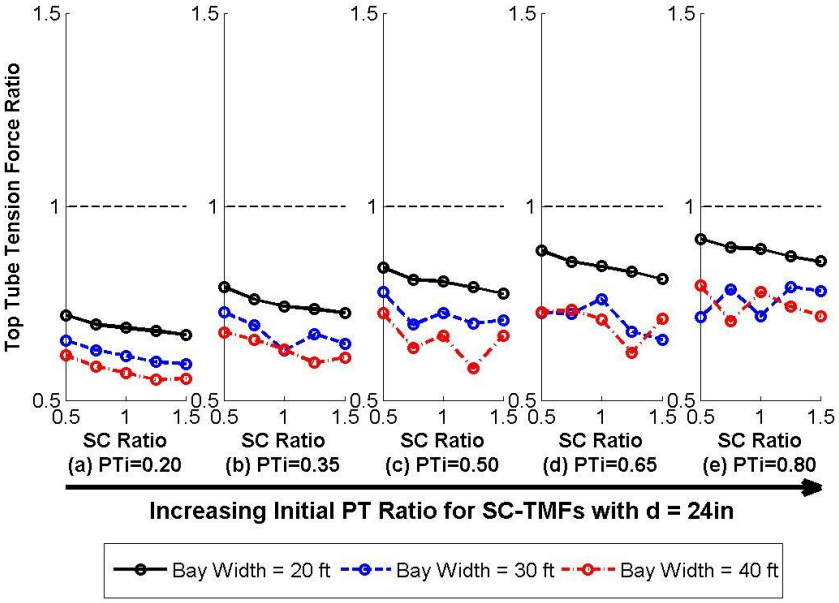

Figure B.18: Top Chord Tension Force Ratios for 24in SC-TMFs using Equation 7.2

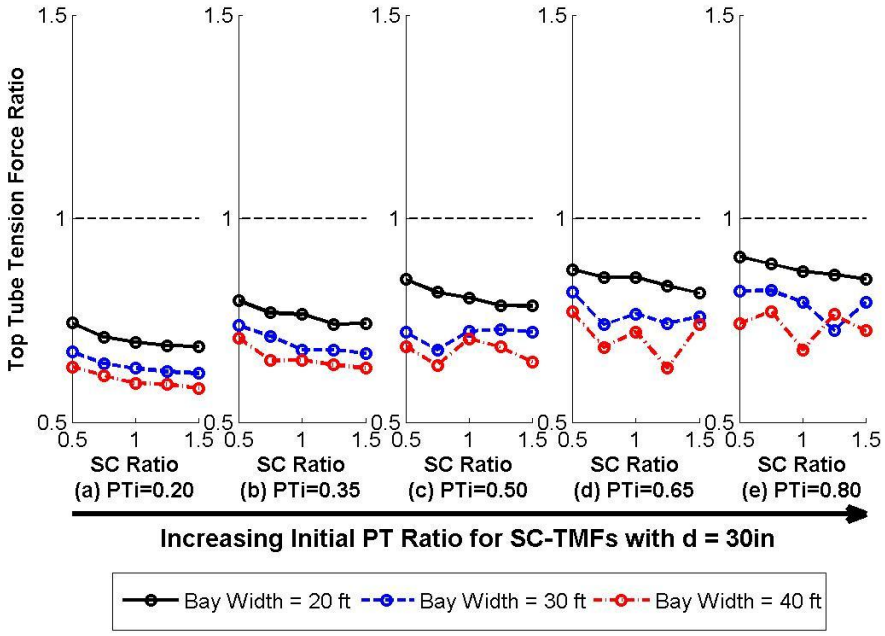

Figure B.19: Top Chord Tension Force Ratios for 30in SC-TMFs using Equation 7.2

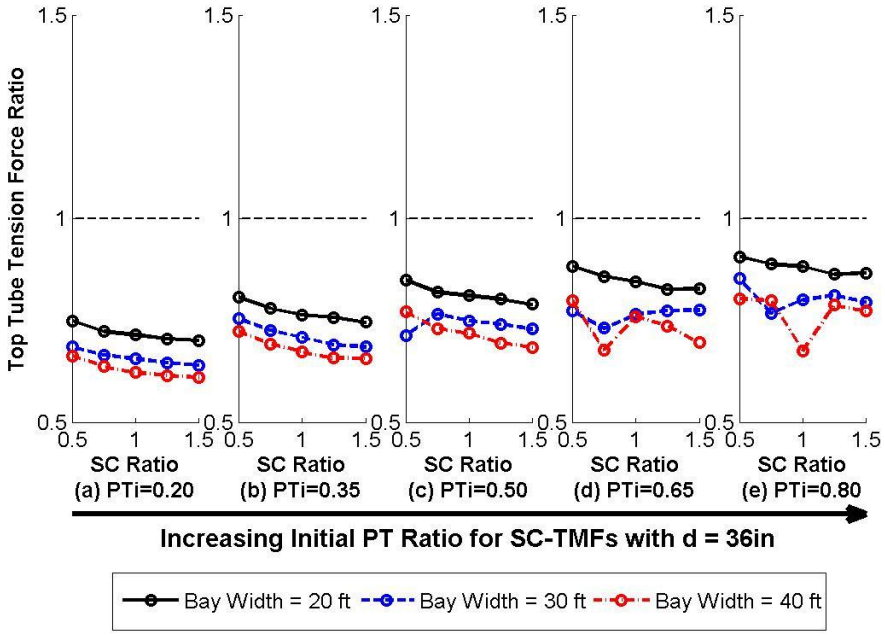

Figure B.20: Top Chord Tension Force Ratios for 36in SC-TMFs using Equation 7.2

B.6 Top Chord Tension Force Ratios Based on Equation 6.27

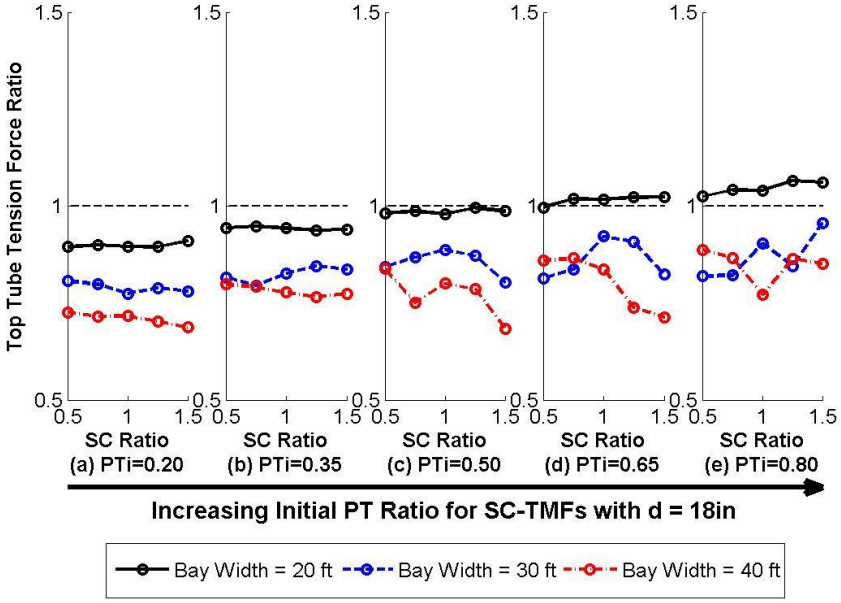

Figure B.21: Top Chord Tension Force Ratios for 18in SC-TMFs using Equation 7.27

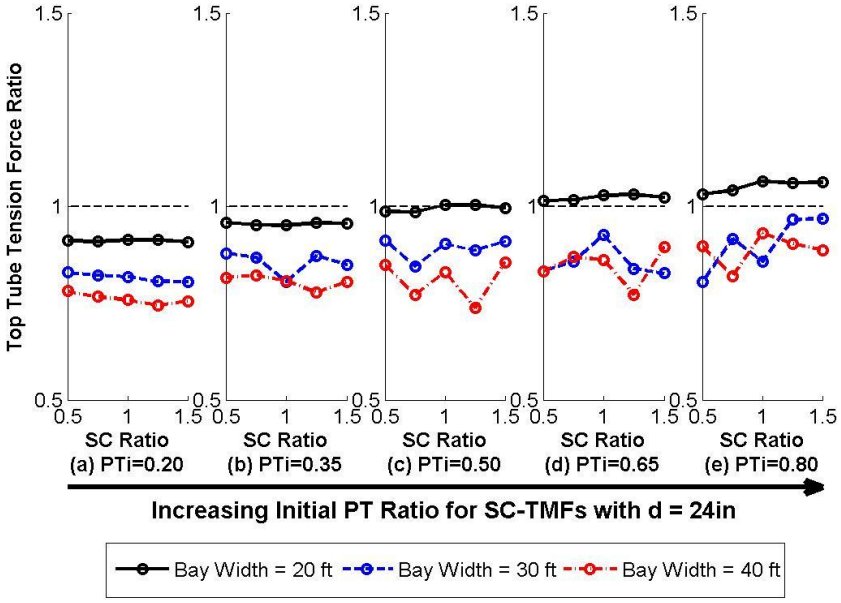

Figure B.22: Top Chord Tension Force Ratios for 24in SC-TMFs using Equation 7.27

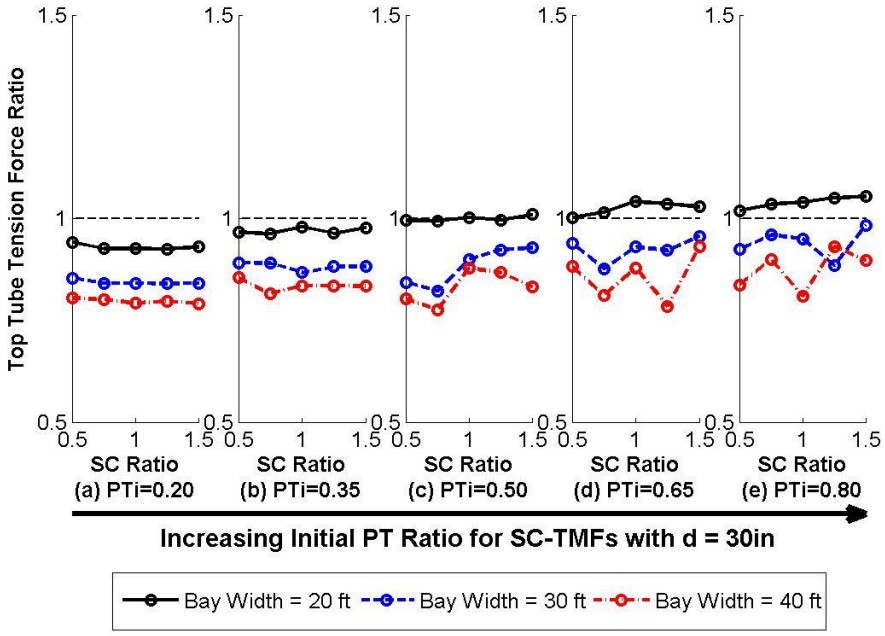

Figure B.23: Top Chord Tension Force Ratios for 30in SC-TMFs using Equation 7.27

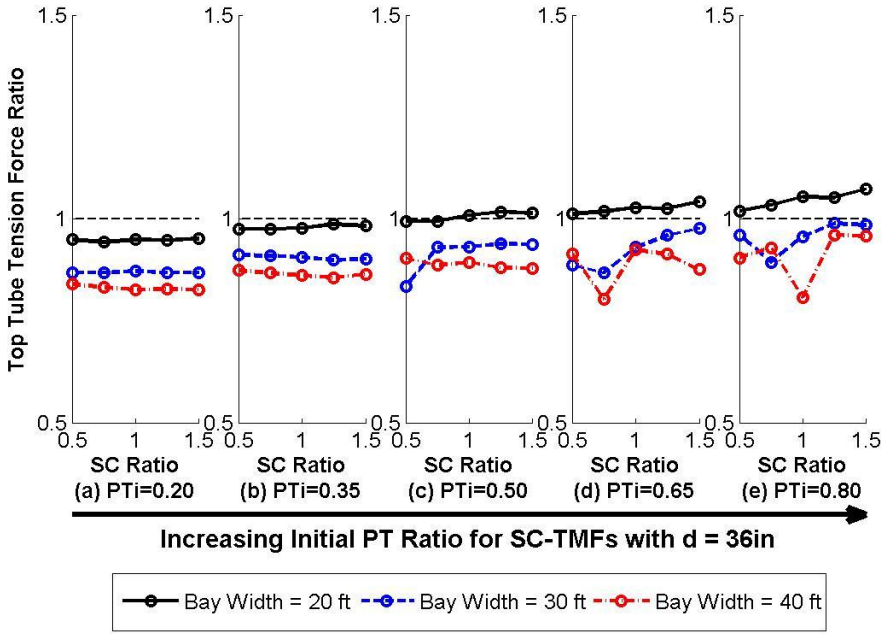

Figure B.24: Top Chord Tension Force Ratios for 36in SC-TMFs using Equation 7.27

B.7 *Top Chord Compression Force Ratios Based on Equation* 6.2

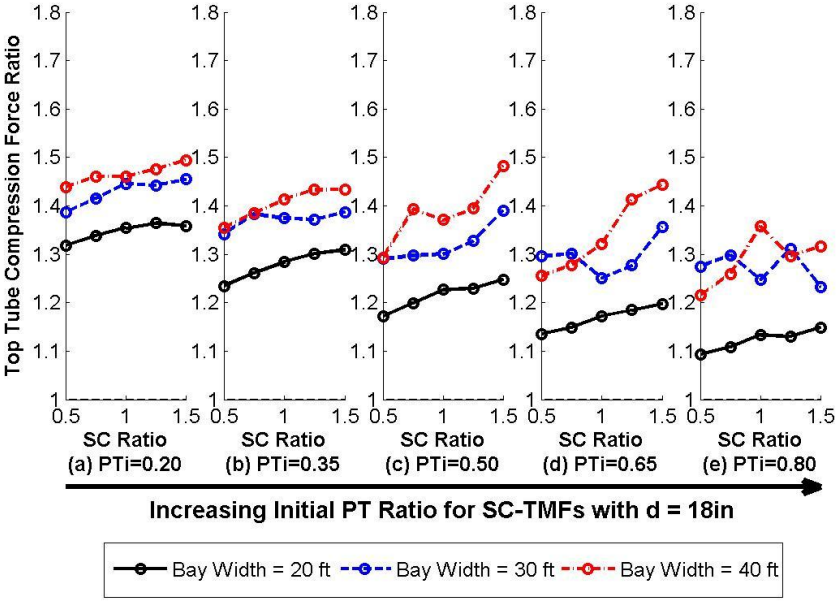

Figure B.25: Top Chord Compression Force Ratios for 18in SC-TMFs using Equation 7.2

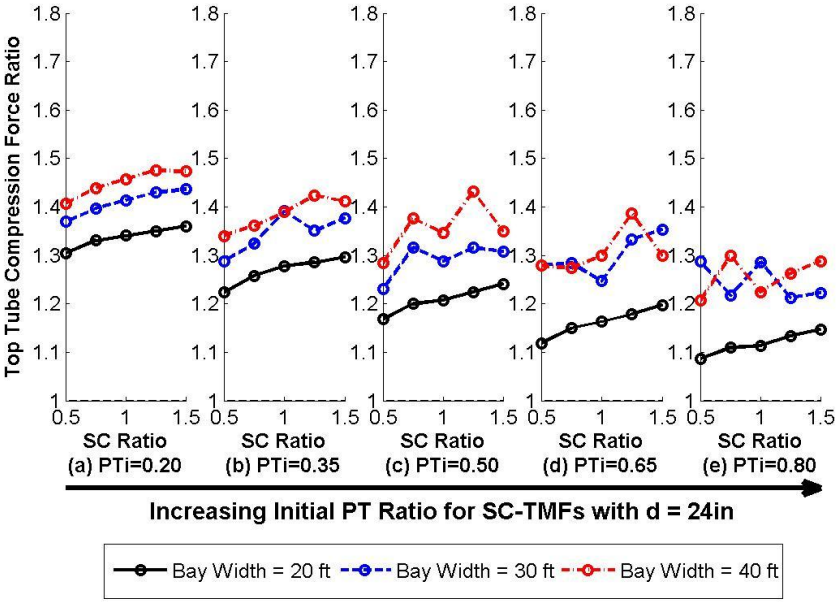

Figure B.26: Top Chord Compression Force Ratios for 24in SC-TMFs using Equation 7.2

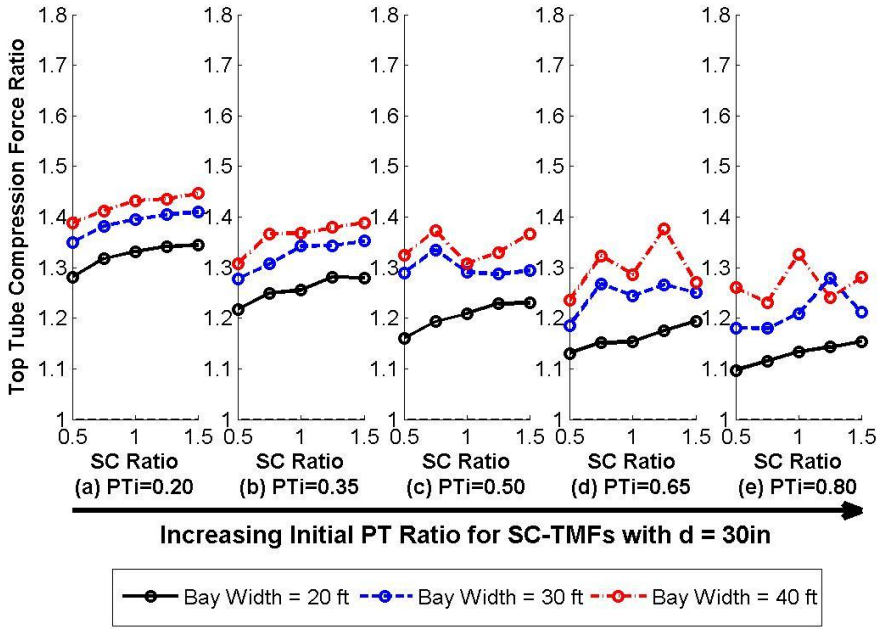

Figure B.27: Top Chord Compression Force Ratios for 30in SC-TMFs using Equation 7.2

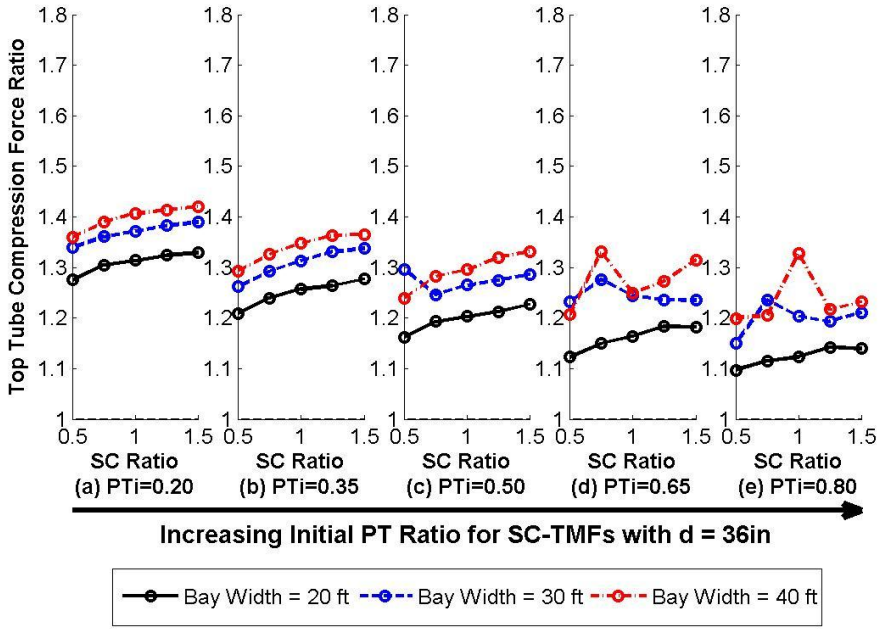

Figure B.28: Top Chord Compression Force Ratios for 36in SC-TMFs using Equation 7.2

B.8 *Top Chord Compression Force Ratios Based on Equation* 6.26

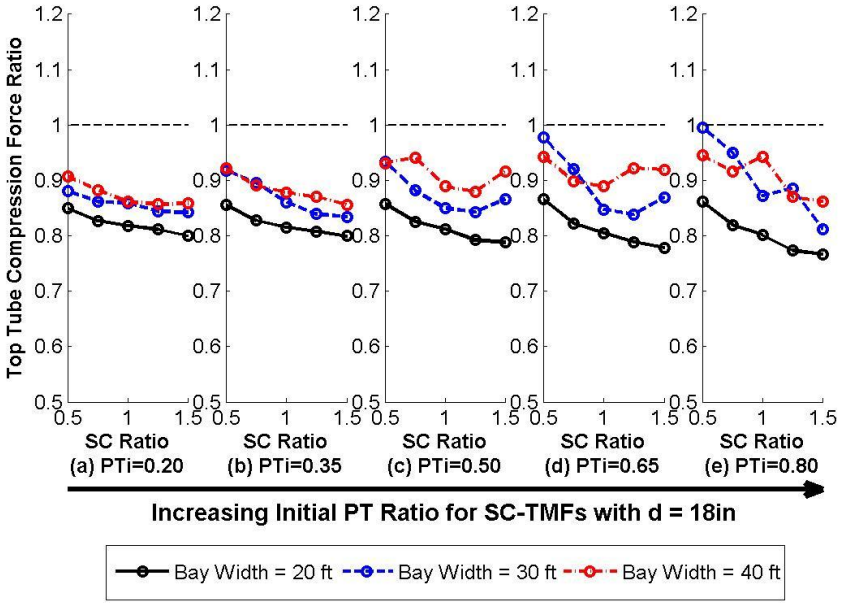

Figure B.29: Top Chord Compression Force Ratios for 18in SC-TMFs using Equation 7.26

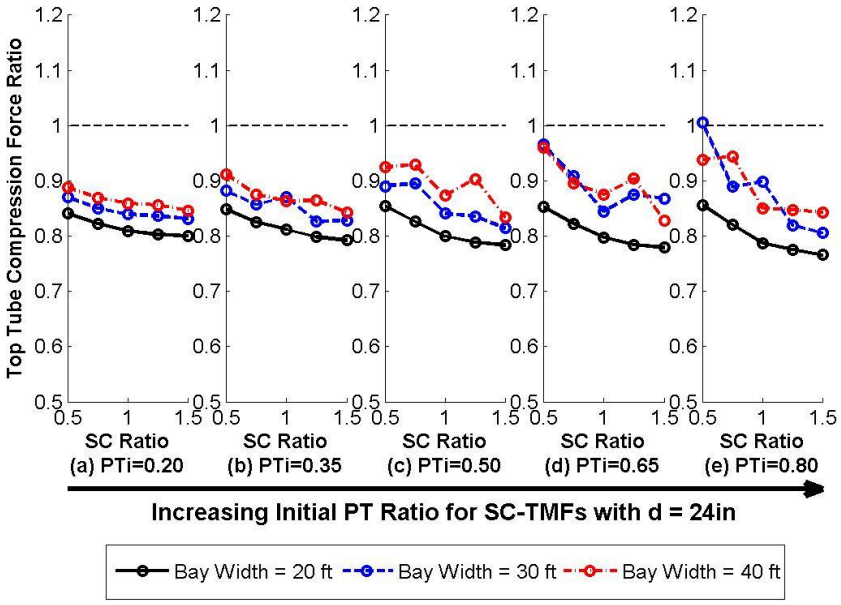

Figure B.30: Top Chord Compression Force Ratios for 24in SC-TMFs using Equation 7.26

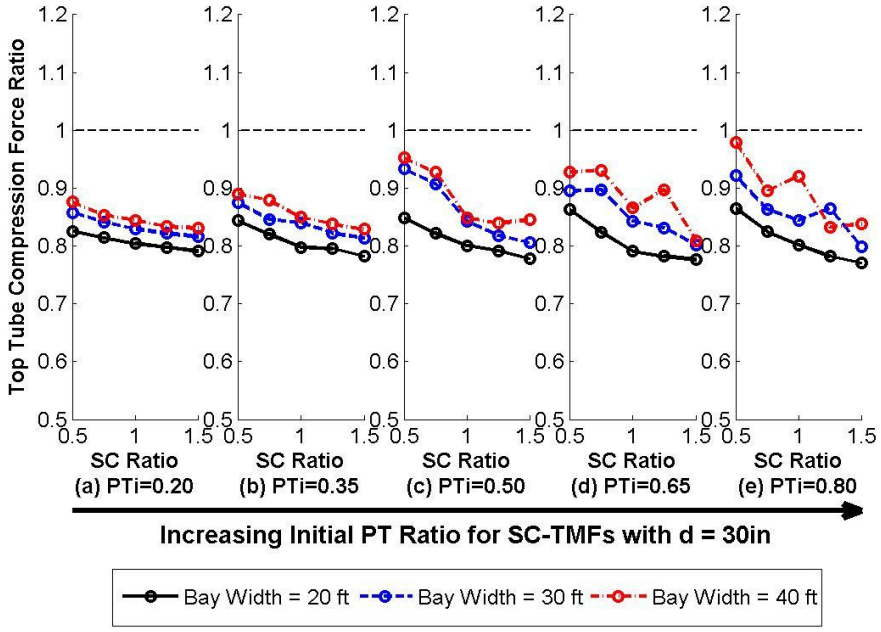

Figure B.31: Top Chord Compression Force Ratios for 30in SC-TMFs using Equation 7.26

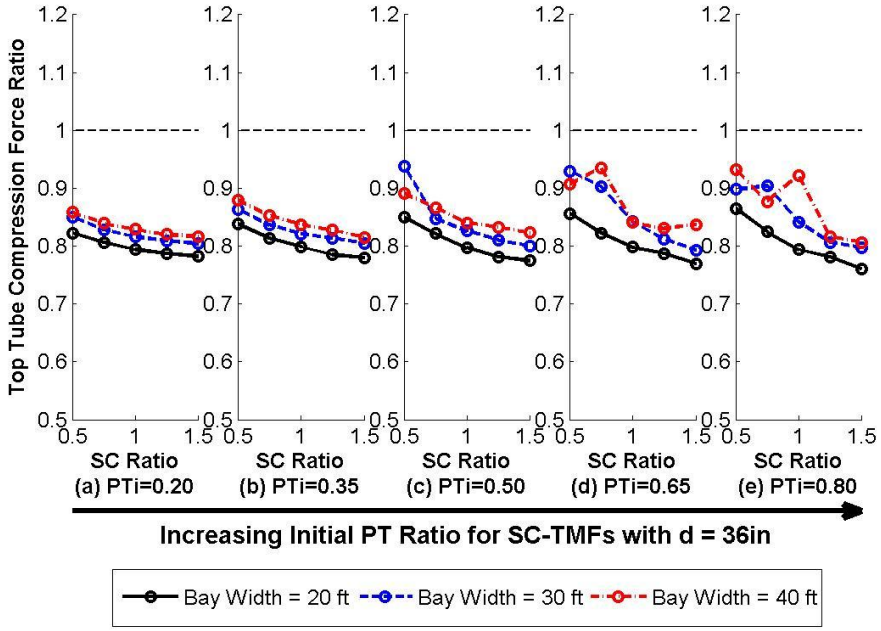

Figure B.32: Top Chord Compression Force Ratios for 36in SC-TMFs using Equation 7.26

B.9 *Outer Tube Compression Force Ratios Based on Equation* 6.4

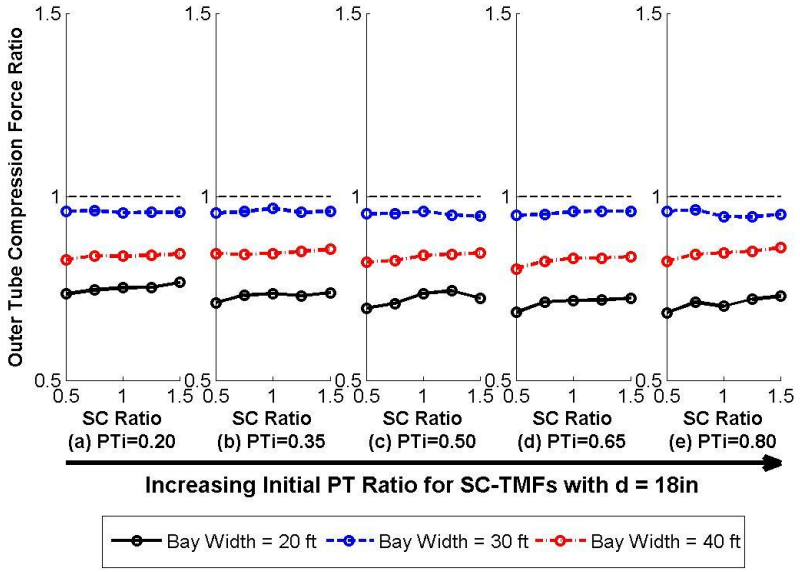

Figure B.33: Compression Force Ratio in the Outer Tube for 18in SC-TMFs using Equation 7.4

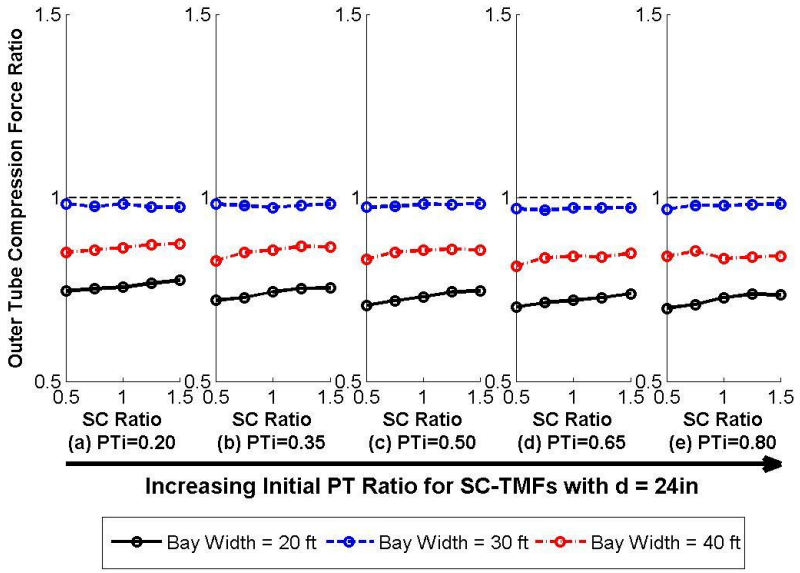

Figure B.34: Compression Force Ratio in the Outer Tube for 24in SC-TMFs using Equation 7.4

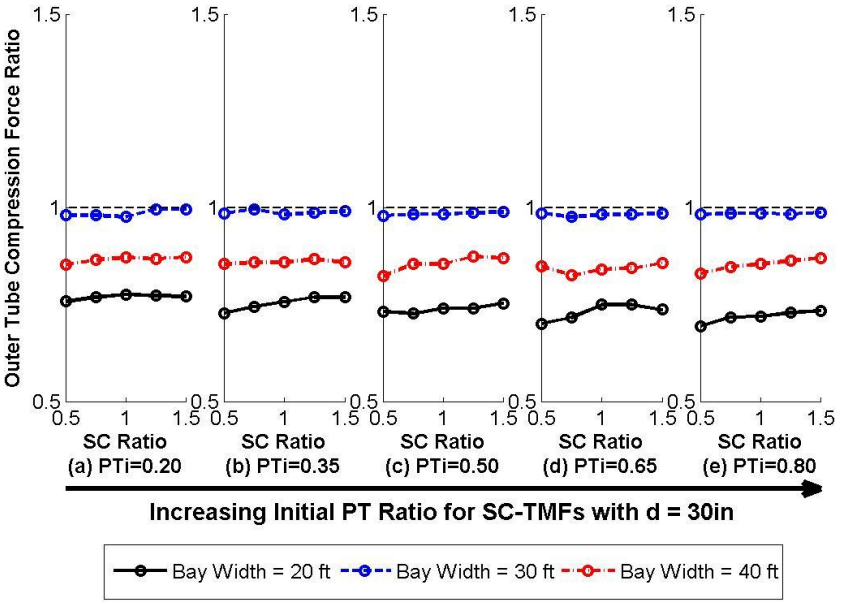

Figure B.35: Compression Force Ratio in the Outer Tube for 30in SC-TMFs using Equation 7.4

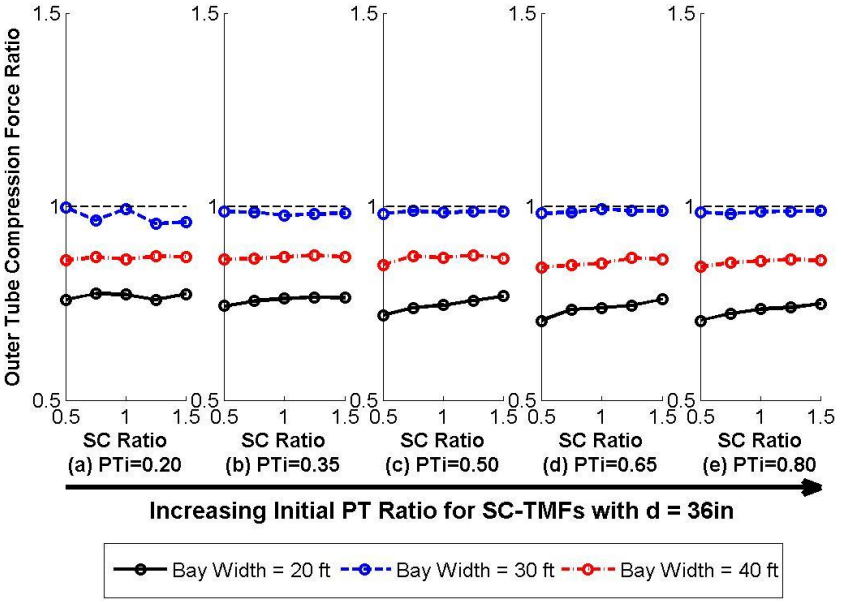

Figure B.36: Compression Force Ratio in the Outer Tube for 36in SC-TMFs using Equation 7.4

Appendix C. Figures – Interstory Drift at Post-Tensioning Yield

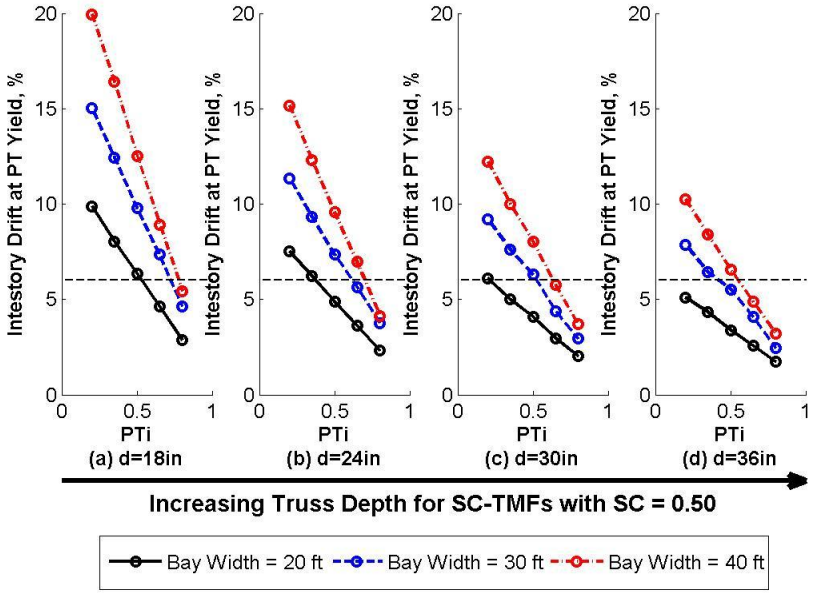

Figure C.1: Initial Post-Tensioning Ratio for SC-TMF with SC Ratio = 0.50

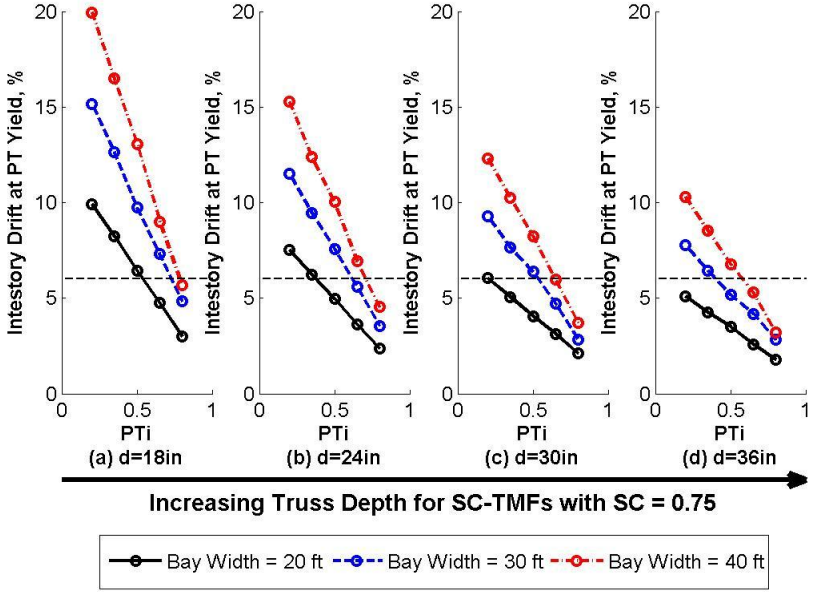

Figure C.2: Initial Post-Tensioning Ratio for SC-TMF with SC Ratio = 0.75

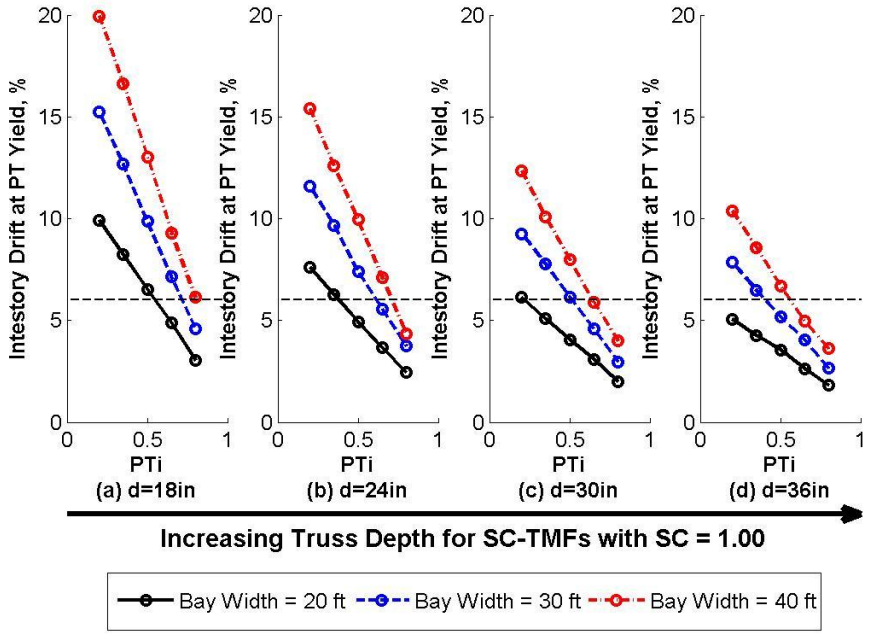

Figure C.3: Initial Post-Tensioning Ratio for SC-TMF with SC Ratio = 1.0

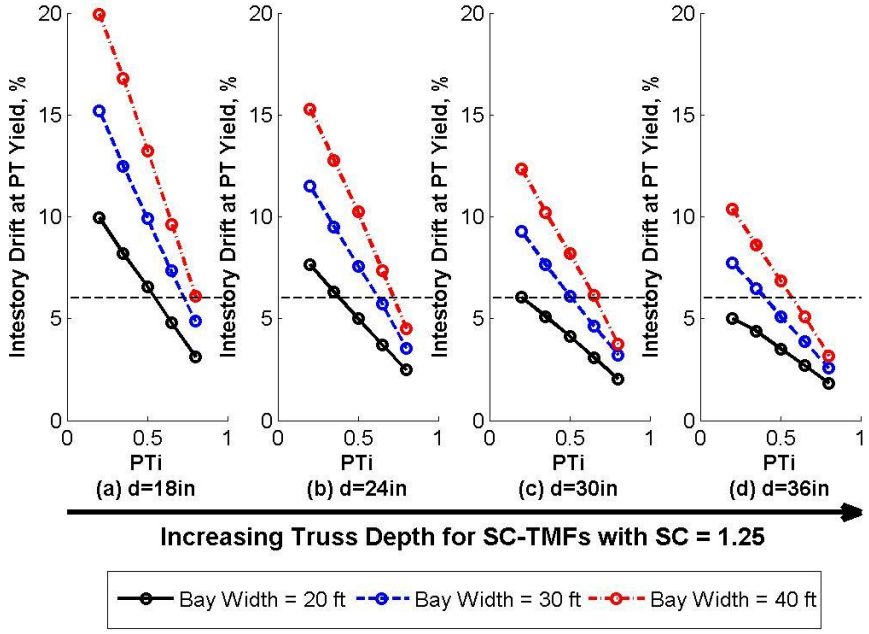

Figure C.4: Initial Post-Tensioning Ratio for SC-TMF with SC Ratio = 1.25

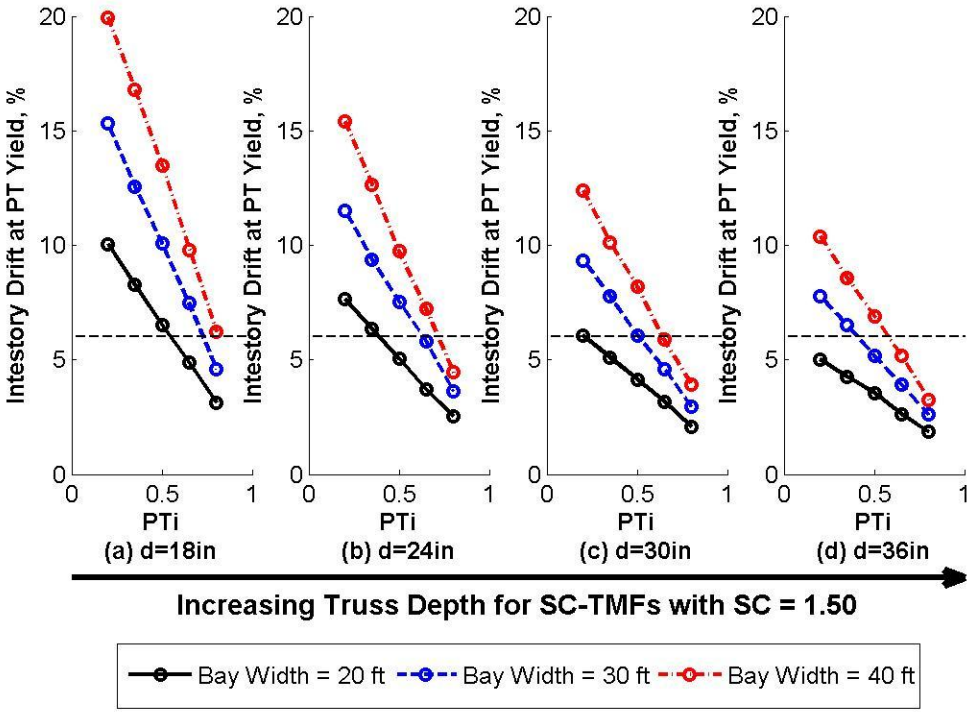

Figure C.5: Initial Post-Tensioning Ratio for SC-TMF with SC Ratio = 1.50

Appendix D. Figures – Drift at Zero Force

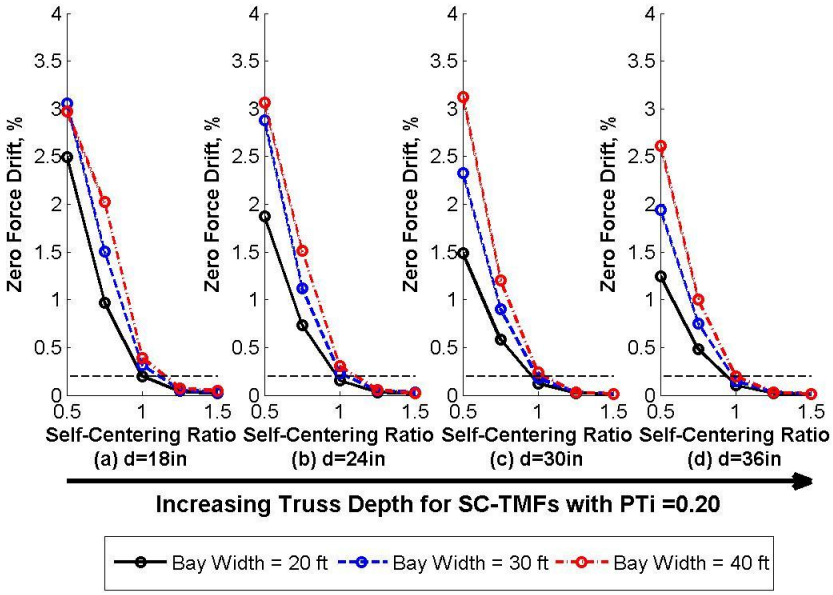

Figure D.1: Zero Force Drift for SC-TMF with PT_i = 0.20

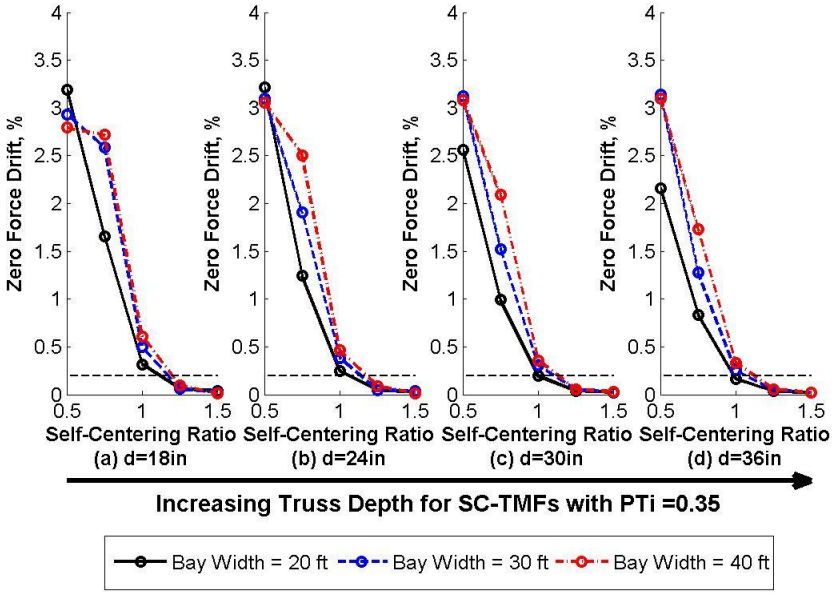

Figure D.2: Zero Force Drift for SC-TMF with PT_i = 0.35

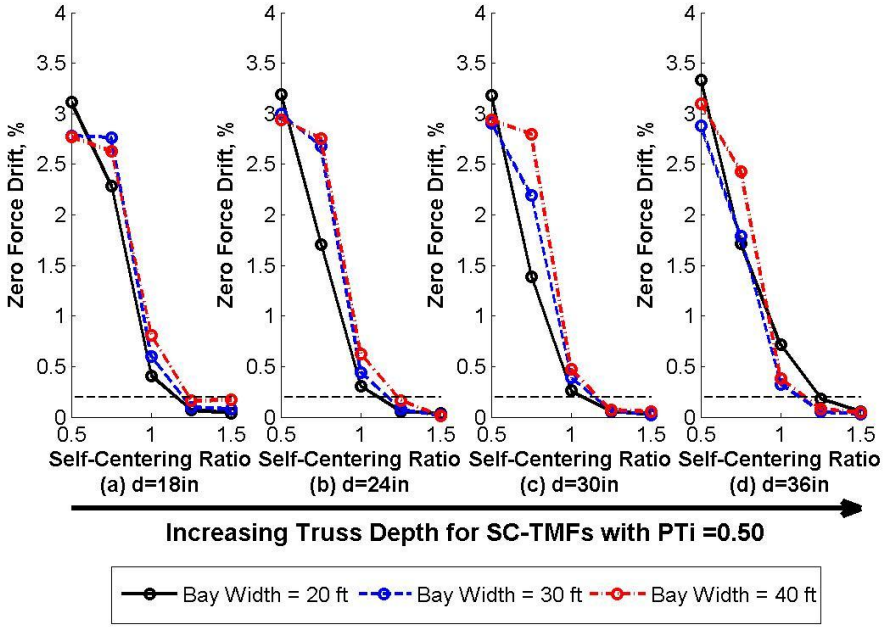

Figure D.3: Zero Force Drift for SC-TMF with $PT_i = 0.50$

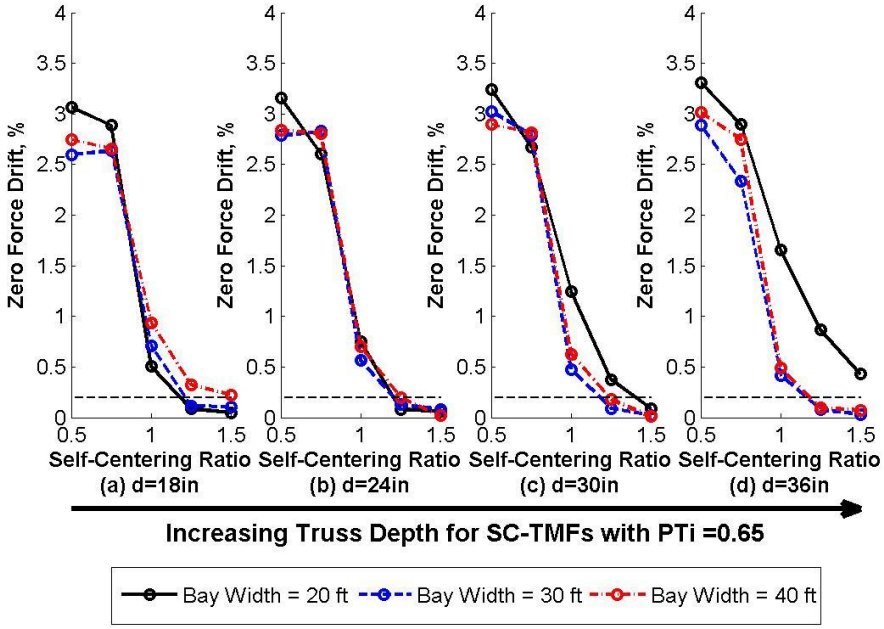

Figure D.4: Zero Force Drift for SC-TMF with $PT_i = 0.65$

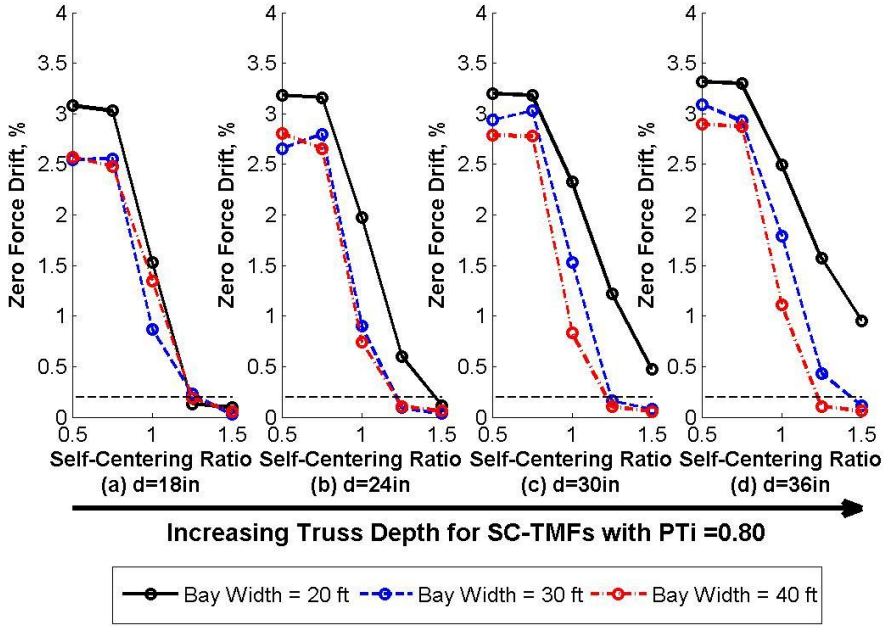

Figure D.5: Zero Force Drift for SC-TMF with PT_i = 0.80

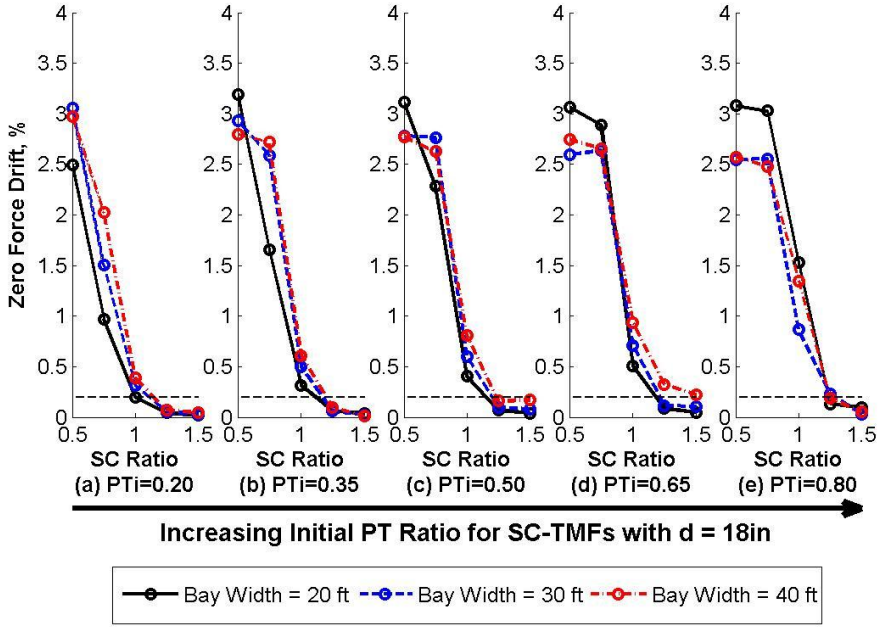

Figure D.6: Zero Force Drift for SC-TMF with Depth = 18 inches

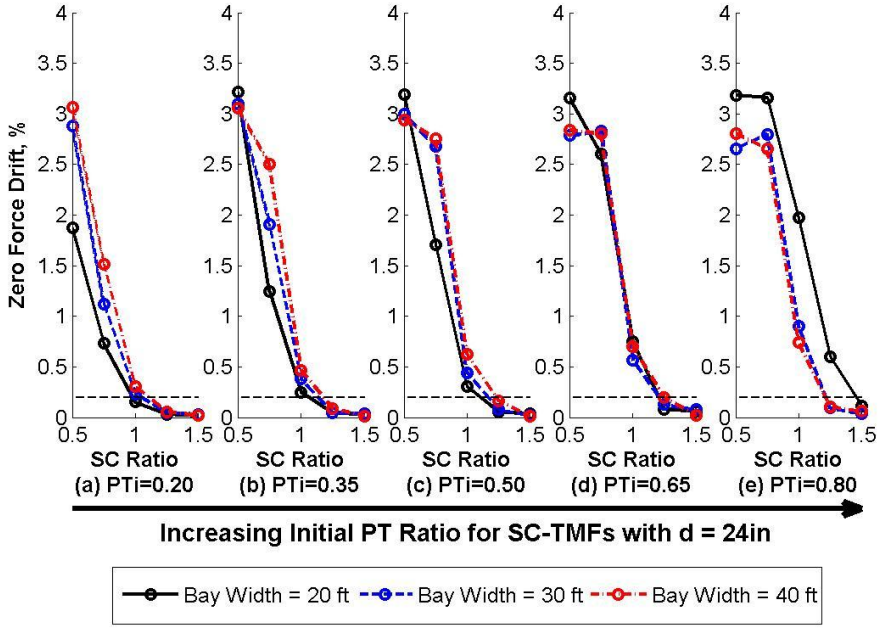

Figure D.7: Zero Force Drift for SC-TMF with Depth = 24 inches

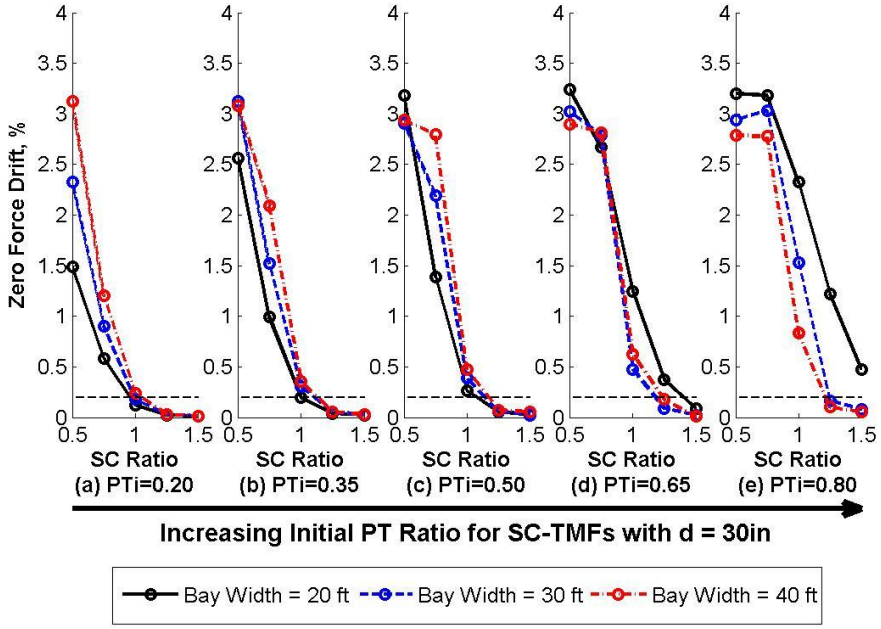

Figure D.8: Zero Force Drift for SC-TMF with Depth = 30 inches

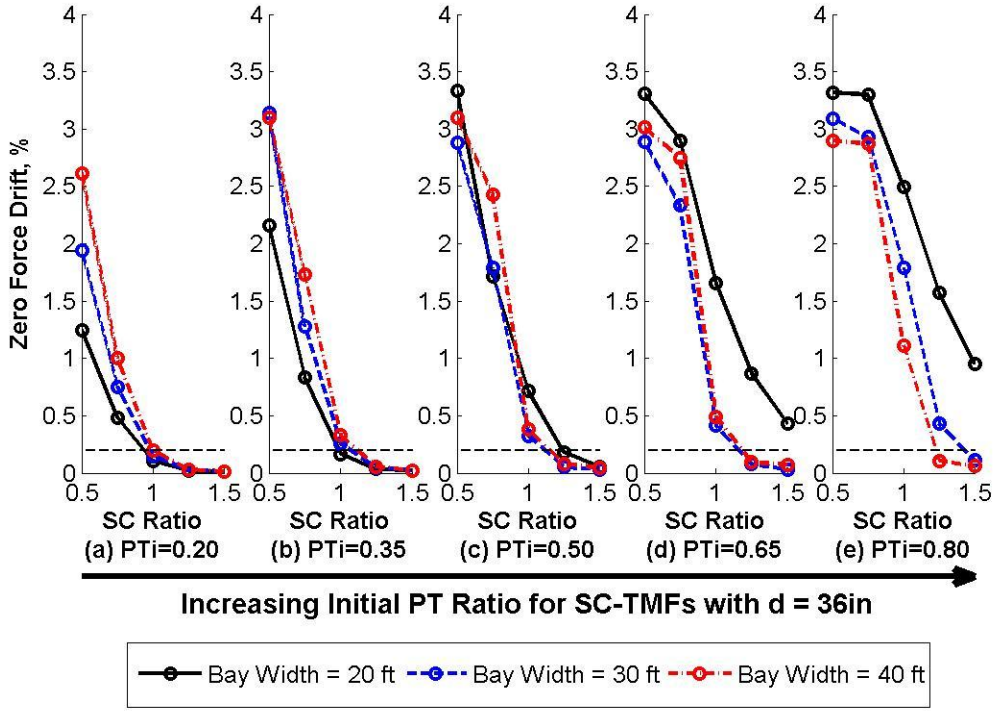

Figure D.9: Zero Force Drift for SC-TMF with Depth = 36 inches

Appendix E. Figures – Energy Dissipation Ratio

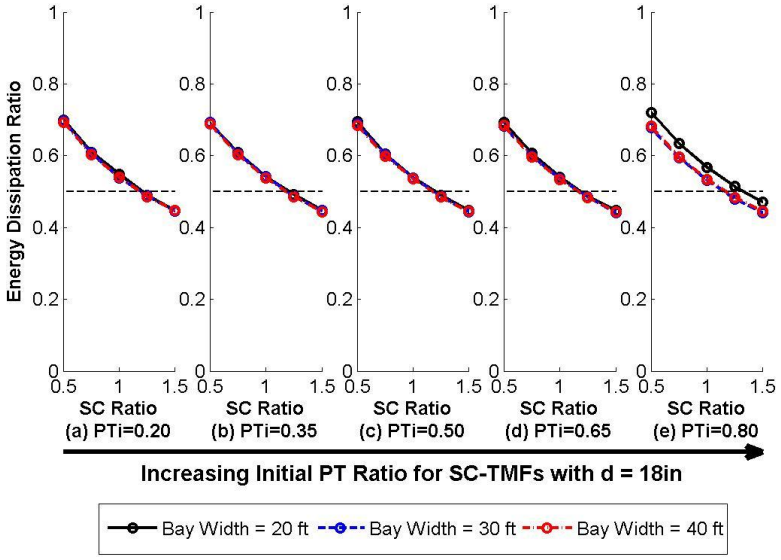

Figure E.1: Energy Dissipation Ratio Compared to Bilinear Hysteretic for SC-TMF with Depth = 18 inches

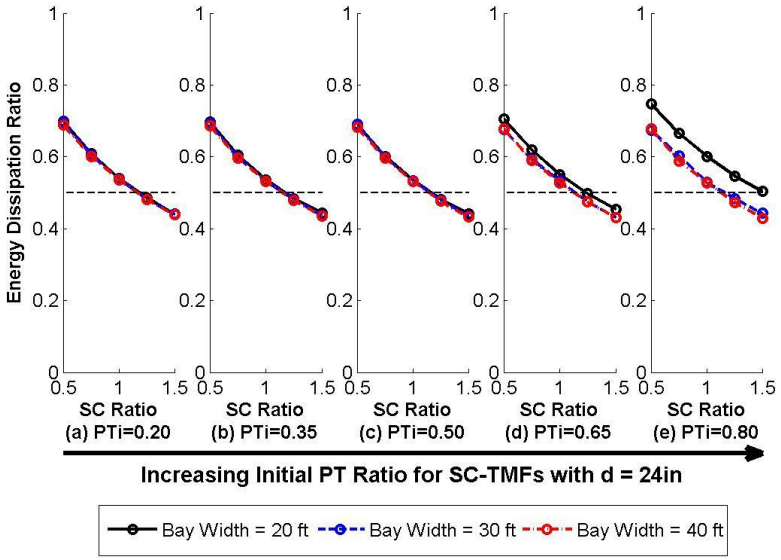

Figure E.2: Energy Dissipation Ratio Compared to Bilinear Hysteretic for SC-TMF with Depth = 24 inches

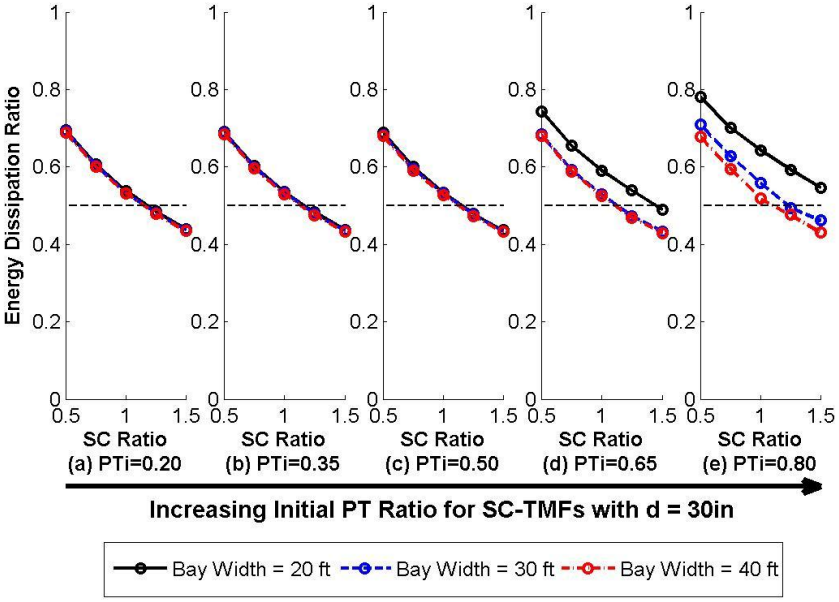

Figure E.3: Energy Dissipation Ratio Compared to Bilinear Hysteretic for SC-TMF with Depth = 30 inches

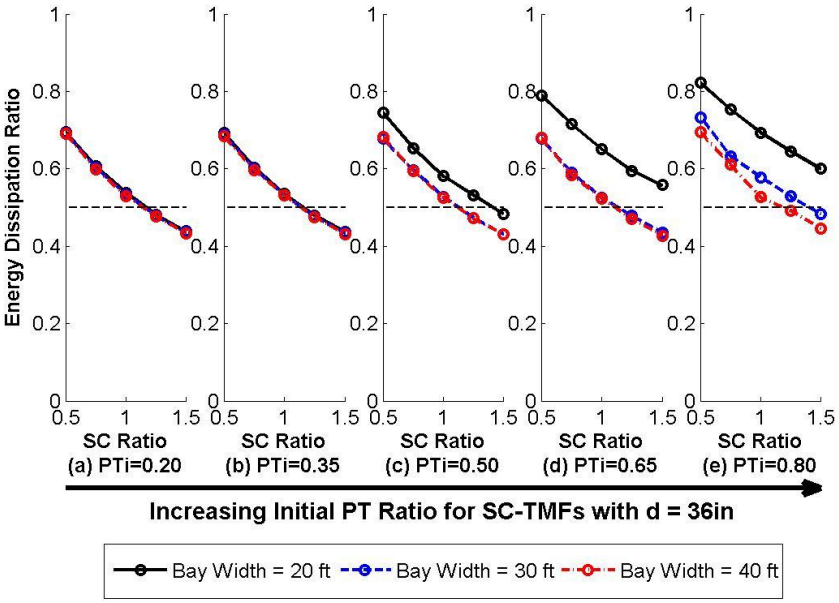

Figure E.4: Energy Dissipation Ratio Compared to Bilinear Hysteretic for SC-TMF with Depth = 36 inches

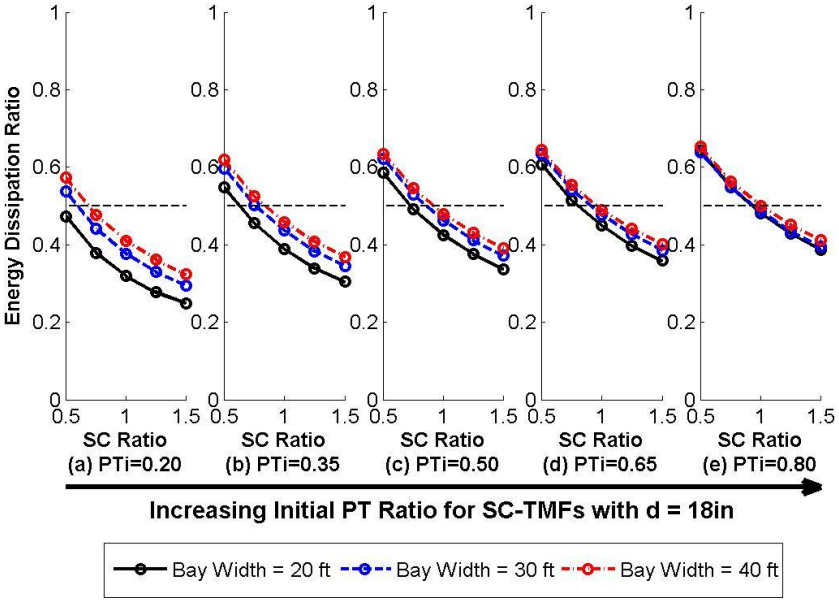

Figure E.5: Energy Dissipation Ratio Compared to EPP Hysteretic for SC-TMF with Depth = 18 inches

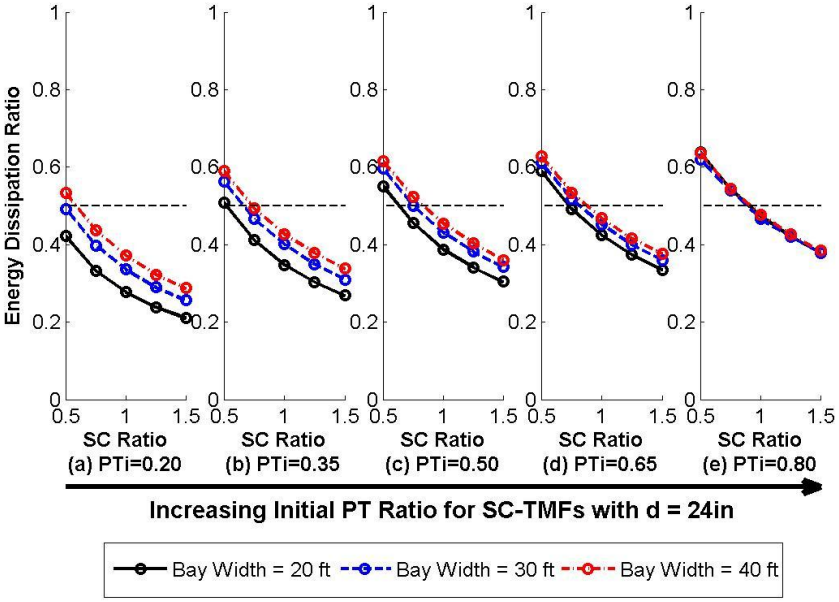

Figure E.6: Energy Dissipation Ratio Compared to EPP Hysteretic for SC-TMF with Depth = 24 inches

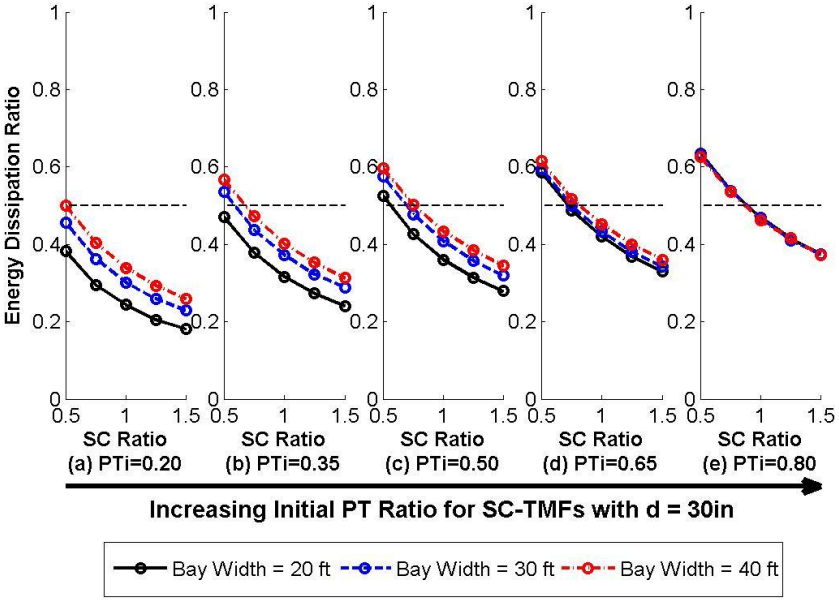

Figure E.7: Energy Dissipation Ratio Compared to EPP Hysteretic for SC-TMF with Depth = 30 inches

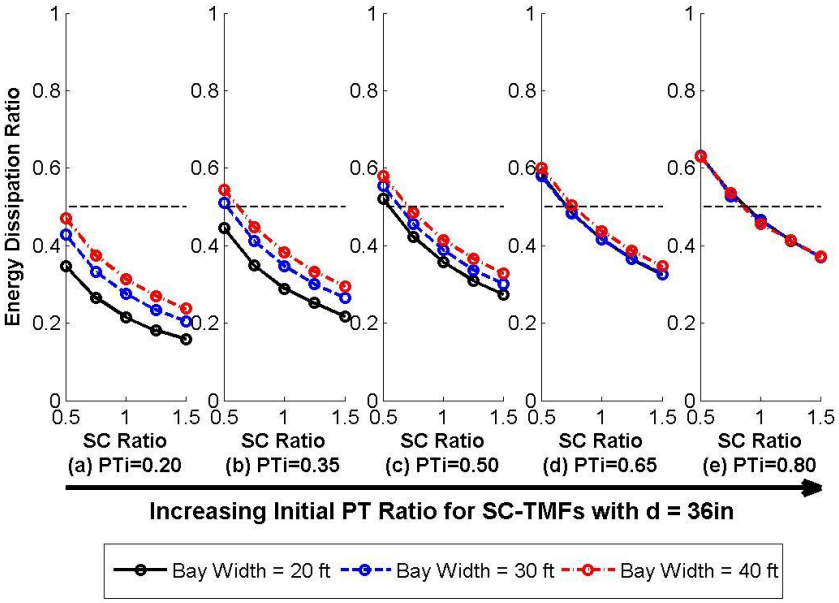

Figure E.8: Energy Dissipation Ratio Compared to EPP Hysteretic for SC-TMF with Depth = 36 inches

Appendix F. Figures – Moment Ratio

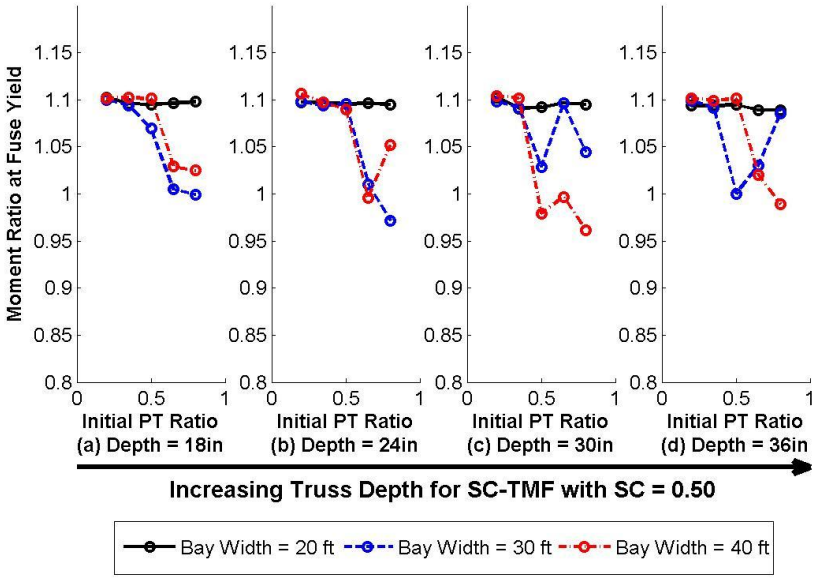

Figure F.1: Moment Ratios for SC-TMFs with SC = 0.50

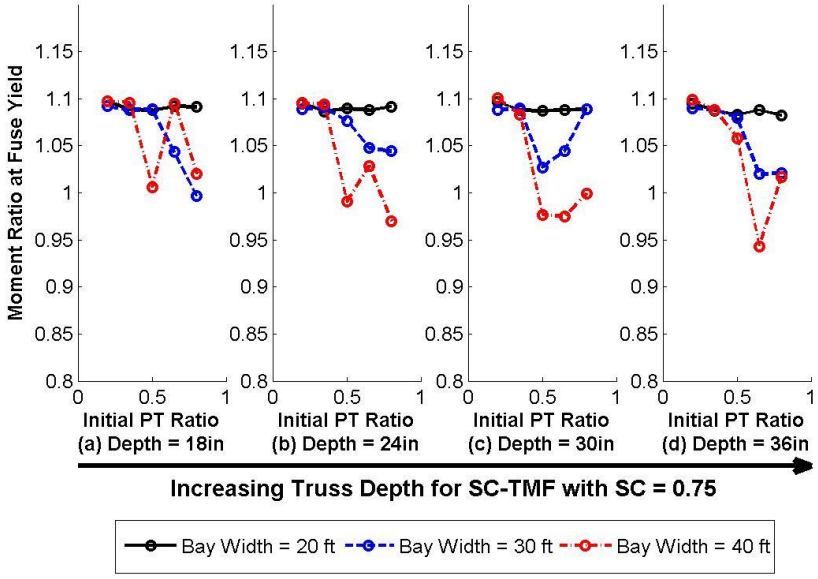

Figure F.2: Moment Ratios for SC-TMFs with SC = 0.75

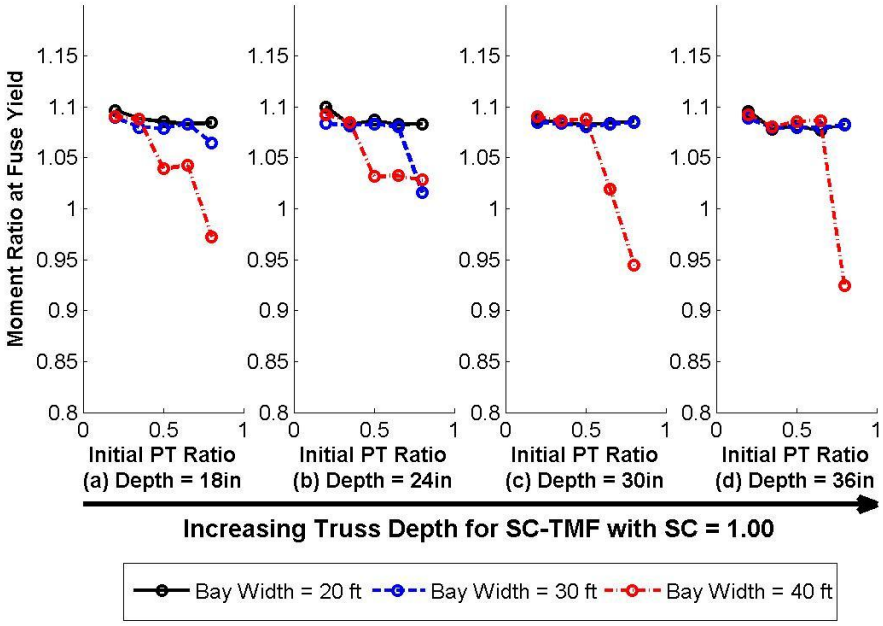

Figure F.3: Moment Ratios for SC-TMFs with SC = 1.0

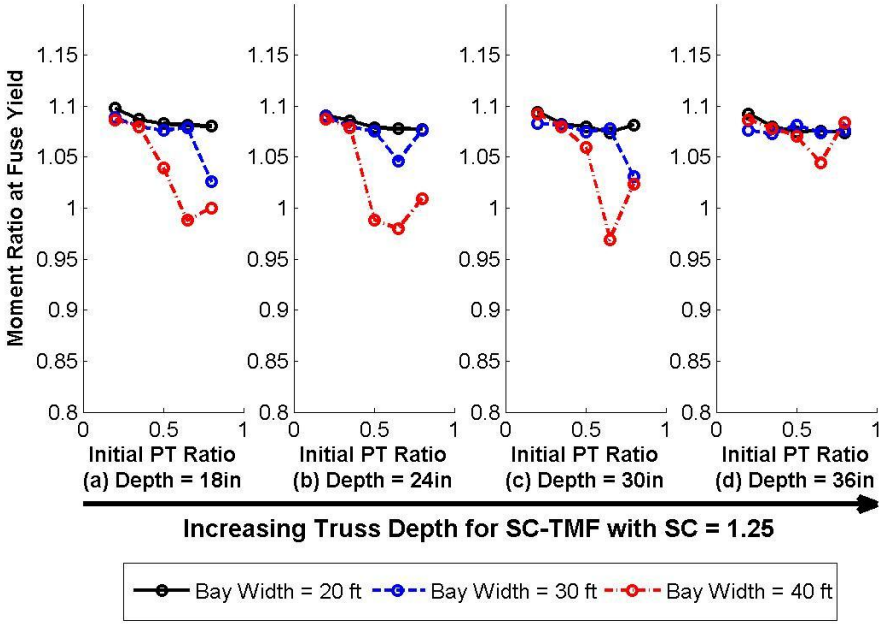

Figure F.4: Moment Ratios for SC-TMFs with SC = 1.25

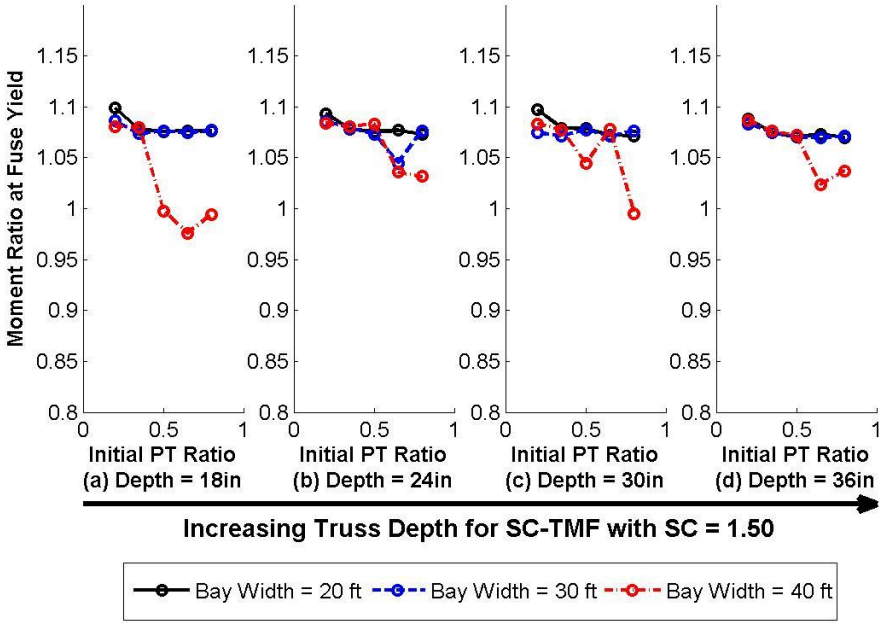

Figure F.5: Moment Ratios for SC-TMFs with SC = 1.50

Appendix G. Figures – Peak Energy Dissipating Bar Strains

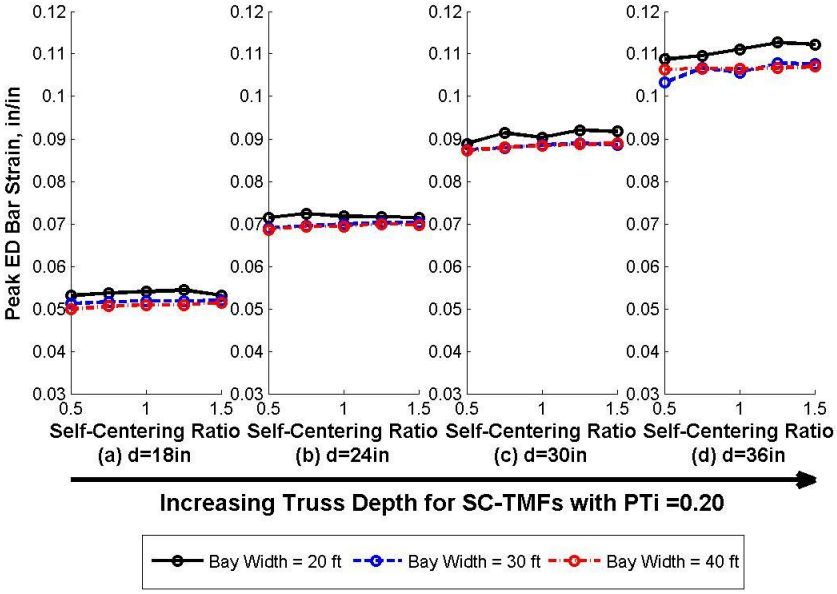

Figure G.1: Peak ED Bar Strain for SC-TMFs with PT_i = 0.20

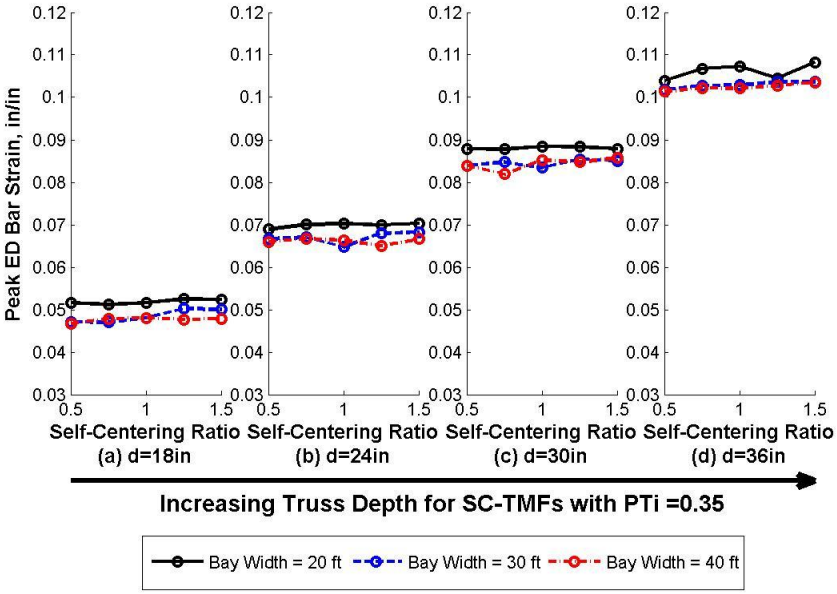

Figure G.2: Peak ED Bar Strain for SC-TMFs with PT_i = 0.35

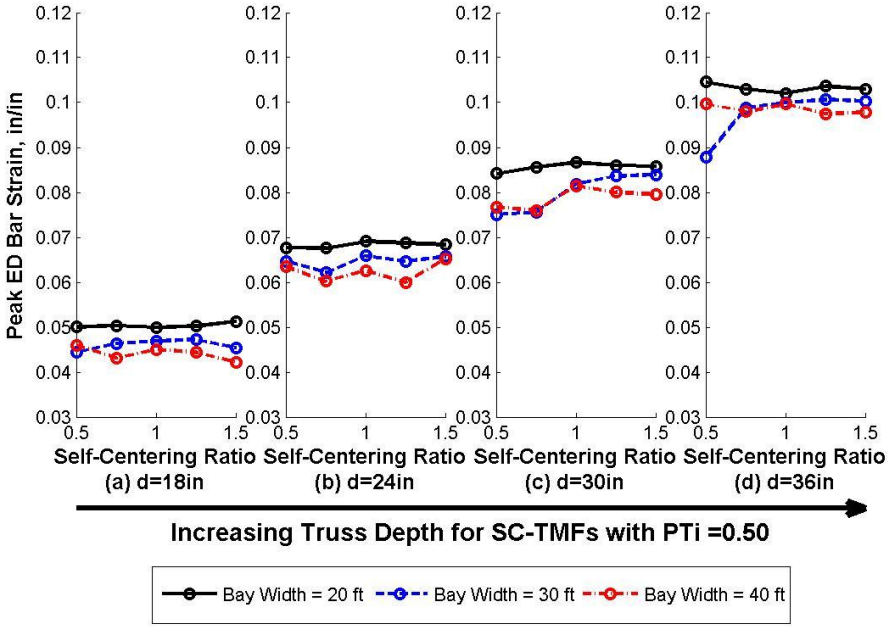

Figure G.3: Peak ED Bar Strain for SC-TMFs with PT_i = 0.50

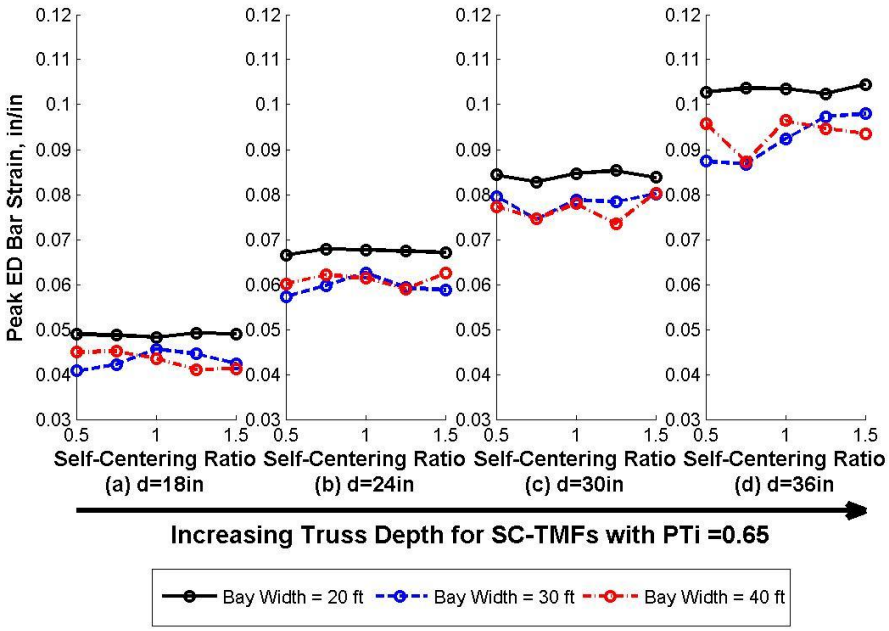

Figure G.4: Peak ED Bar Strain for SC-TMFs with PT_i = 0.65

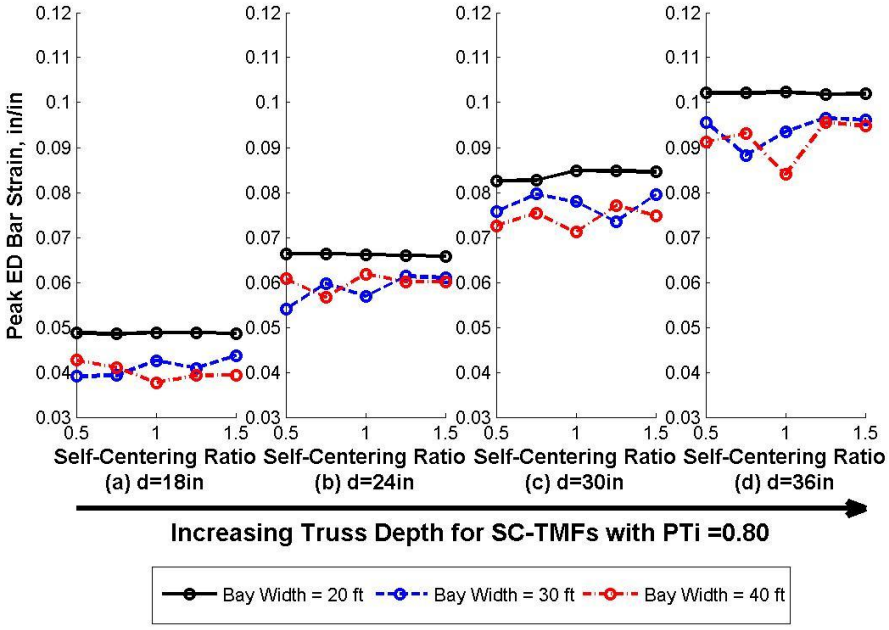

Figure G.5: Peak ED Bar Strain for SC-TMFs with $PT_i = 0.80$

Appendix H. Figures – Cumulative Energy Dissipating Bar Strains

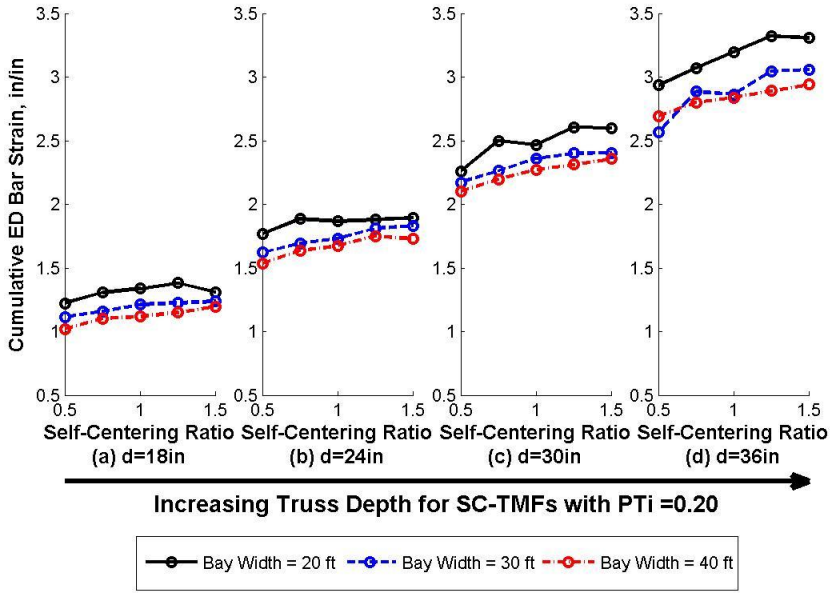

Figure H.1: Cumulative ED Bar Strain for SC-TMFs with PT_i = 0.20

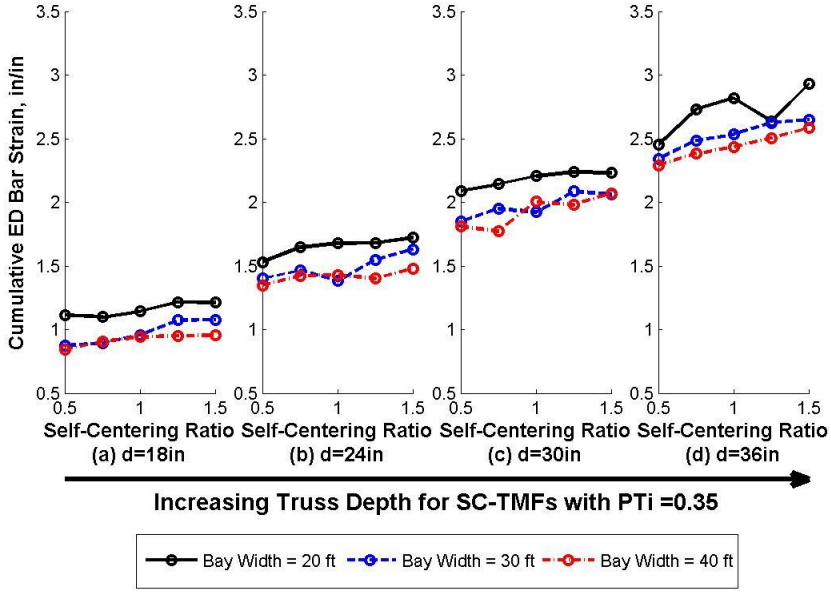

Figure H.2: Cumulative ED Bar Strain for SC-TMFs with PT_i = 0.35

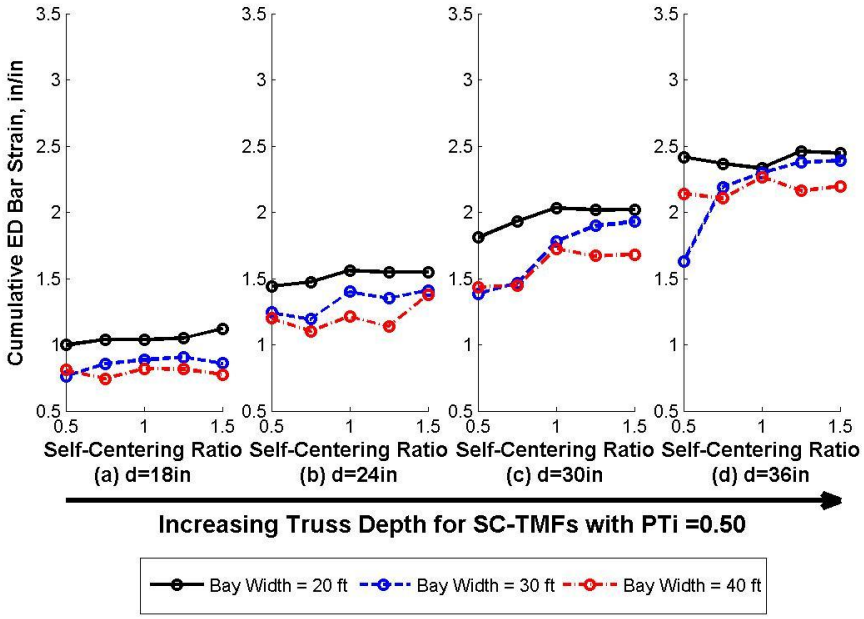

Figure H.3: Cumulative ED Bar Strain for SC-TMFs with PT_i = 0.50

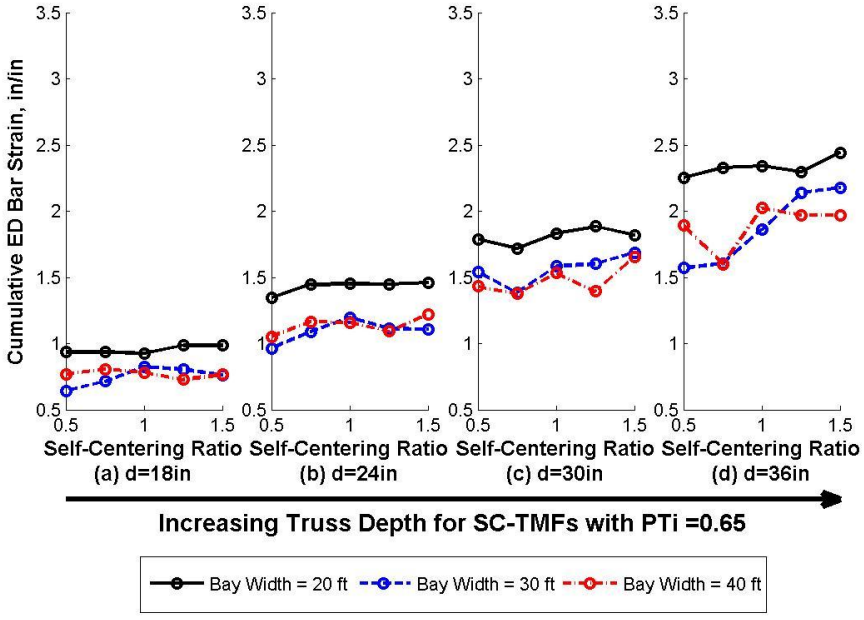

Figure H.4: Cumulative ED Bar Strain for SC-TMFs with PT_i = 0.65

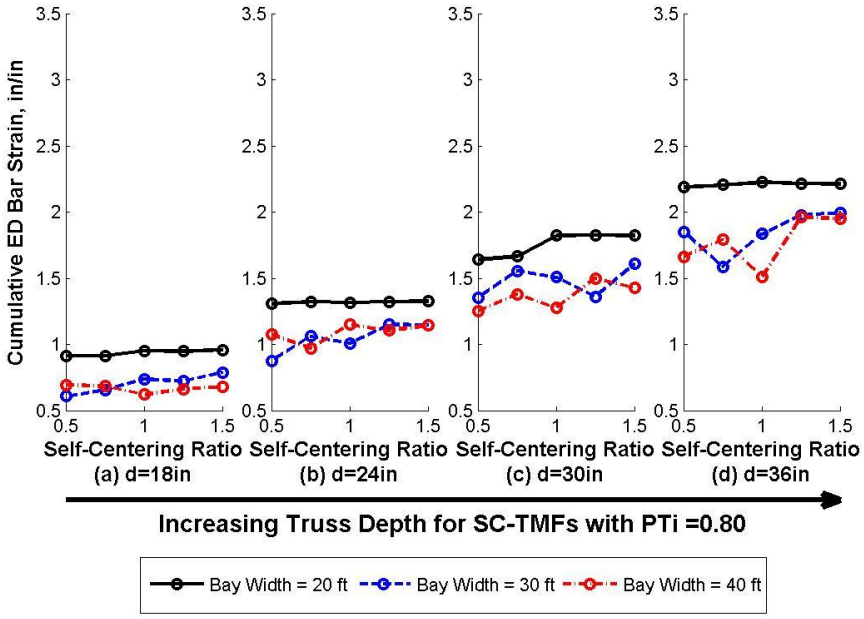

Figure H.5: Cumulative ED Bar Strain for SC-TMFs with PT_i = 0.80